

1

CAMPINAS STATE UNIVERSITY

2

DOCTORAL THESIS

3

4 **Search of Z and Higgs boson decaying into $\Upsilon + \gamma$
5 in pp collisions at CMS/LHC**

6

7 *Author:*

Felipe Torres da Silva de Araujo

Supervisor:

Dr. José Augusto Chinellato

Co-Supervisor:

Dr. Alberto Franco de Sá Santoro

8

*A thesis submitted in fulfillment of the requirements
9 for the degree of Doctor of Physics*

10

in the

11

Graduate Program of
12 "Gleb Wataghin" Institute of Physics

13

October 18, 2020

14 “Sometimes science is a lot more art than science. A lot of people don’t get that.”

15

Rick Sanchez

16 “Então, que seja doce. Repito todas as manhãs, ao abrir as janelas para deixar entrar o sol ou o
17 cinza dos dias, bem assim, que seja doce. Quando há sol, e esse sol bate na minha cara amassada do
18 sono ou da insônia, contemplando as partículas de poeira soltas no ar, feito um pequeno universo;
19 repito sete vezes para dar sorte: que seja doce que seja doce que seja doce e assim por diante. Mas,
20 se alguém me perguntasse o que deverá ser doce, talvez não saiba responder. Tudo é tão vago como
21 se fosse nada.”

22

Caio Fernando Abreu

23 CAMPINAS STATE UNIVERSITY

24 *Abstract*

25 "Gleb Wataghin" Institute of Physics

26 Doctor of Physics

27 **Search of Z and Higgs boson decaying into $\Upsilon + \gamma$ in pp collisions at CMS/LHC**

28 by Felipe Torres da Silva de Araujo

29 This thesis presents the study on searches for rare decays of Standard Model bosons to quarkonia.
30 The searches are performed on data collected during the 2016 data taking of the CMS detector, at
31 center-of-mass energy $\sqrt{s} = 13$ TeV. Standard Model Higgs and Z bosons decaying to a $\Upsilon(1S, 2S, 3S)$
32 and a photon, with subsequent decay of the $\Upsilon(1S, 2S, 3S)$ to $\mu^+ \mu^-$ are performed using integrated
33 luminosity of 35.86 fb^{-1} from proton-proton collisions. No significant excess above the background-
34 only assumption is observed. A limit at 95% confidence level, is set on the $H \rightarrow \Upsilon(1S, 2S, 3S) + \gamma$
35 decay branching fraction at $(6.8, 7.1, 6.0) \times 10^{-4}$ and on $Z \rightarrow \Upsilon(1S, 2S, 3S) + \gamma$ decay branching
36 fraction at $(2.6, 2.3, 1.3) \times 10^{-6}$, using the CL_s method. Contributions given from 2016 to 2018 to
37 the operation, maintenance and R&D for Phase-2 Upgrade of Resistive Plate Chambers (RPC) at
38 CMS are also presented.

DRAFT

39

Acknowledgements

40 I would like to thank:

- 41 • the Campinas State University for providing the institutional support for this study;
- 42 • the Rio de Janeiro State University for the cooperation with Campinas State University in
43 their high-energy physics program. This was a key factor for this study;
- 44 • the National Council for Scientific and Technological Development (CNPq) for the financial
45 support for this work;
- 46 • the European Laboratory for Particle Physics (CERN) for the construction and operation of
47 the Large Hadron Collider (LHC);
- 48 • the Compact Muon Solenoid (CMS) collaboration for the construction, operation and provi-
49 sion of the instrumental means for this study.

DRAFT

50 **Contents**

51	Abstract	iii
52	Acknowledgements	v
53	1 Introduction	1
54	2 Standard Model and rare Z and Higgs decays to quarkonia	5
55	2.1 Standard Model and Local Gauge Invariance	5
56	2.1.1 Local Gauge Invariance	6
57	2.1.2 The Standard Model	8
58	Quantum Chromodinamics	9
59	Electroweak Theory	10
60	Standard Model Lagrangian and the Higgs Sector	11
61	2.2 SM and Higgs results	14
62	2.2.1 Standard Model vector bosons at CMS	14
63	2.2.2 Higgs boson at CMS	17
64	2.3 Rare Z and Higgs decays to quarkonia	21
65	2.4 Recent results	24
66	3 Experimental Setup	27
67	3.1 The Large Hadron Collider	27
68	3.2 The Compact Muon Solenoid - CMS	29
69	3.2.1 Coordinate system	31
70	3.3 Tracker	32
71	3.4 Electromagnetic Calorimeter	33
72	3.5 Hadronic Calorimeter	34
73	3.6 Muon System	35
74	3.6.1 Drift Tubes	35
75	3.6.2 CSC	36
76	3.6.3 RPC	37
77	3.7 Trigger and Data Acquisition	37
78	3.8 Particle Flow Algorithim	37
79	4 Physics Analysis	41
80	4.1 Datasets and simulated events	42
81	4.1.1 Data samples	42

82	4.1.2 Simulated datasets	42
83	4.2 Contribution of the $\Upsilon(nS)$ polarisation	45
84	4.3 Kinematical studies using MC generator	45
85	4.4 Event selection	49
86	4.5 Trigger and physics object selection (Group I)	49
87	4.5.1 Trigger	49
88	4.5.2 Muon Identification	50
89	4.5.3 Photon Identification	51
90	4.5.4 Kinematical distributions	51
91	4.6 Kinematical selection (Group II)	61
92	4.7 Event categorization and yields	69
93	4.7.1 R9 reweighting	69
94	4.7.2 Event counting and yields	70
95	4.8 Background modeling	71
96	4.9 Signal modeling	79
97	4.10 Systematic uncertainties	85
98	4.10.1 Uncertainties on the predicted yields	85
99	4.10.2 Uncertainties that affect the signal fits	86
100	4.11 Modeling Cross checks	89
101	5 Results and conclusion	95
102	5.1 The CL_s formalism for upper limits setting at CMS	95
103	5.2 Branching fraction upper limits	98
104	6 CMS Resistive Plate Chambers - RPC	101
105	6.1 Resistive Plate Chambers	101
106	6.1.1 Principles and operation modes	101
107	6.2 CMS Resistive Plate Chambers	103
108	6.2.1 Performance	106
109	6.3 Contribution to the CMS RPC project	108
110	6.3.1 RPC Operation - Shifts and Data Certification	109
111	6.4 RPC Online Software	110
112	6.4.1 iRPC R&D	111
113	6.4.2 LS2 and the RPC Standard Maintenance	117
114	HV maintenance	117
115	LV and control maintenance	118
116	Detector commissioning	119
117	Bibliography	121

¹¹⁸ List of Figures

¹¹⁹ 1.1	Dimuon mass distribution collected with various dimuon triggers. The light gray 120 continuous distribution represents events collected with inclusive dimuon triggers with 121 high p_T thresholds. The dataset corresponding to an integrated luminosity of 13.1 122 fb^{-1} was collected during the 25 ns LHC running period at 13 TeV in 2016. Source: [7].	2
¹²³ 2.1	Elementary particles of the Standard Model, with their masses charges and spin. 124 Those particles can be divided in two classes: boson (the interaction/force carriers) 125 and the fermions, which are divided in three generations. Source: [12].	6
¹²⁶ 2.2	(a) Di-boson cross section ratio comparison to theory: Theory predictions updated 127 to latest NNLO calculations where available compared to predictions in the CMS 128 papers and preliminary physics analysis summaries. Source: [26]. (b) Summary of 129 the cross sections of pure Electroweak (EWK) interactions among the gauge bosons 130 presented as a ratio compared to theory. Source: [26].	15
¹³¹ 2.3	Summary of the cross section measurements of Standard Model processes at CMS. 132 Source: [26].	16
¹³³ 2.4	(a) Standard Model Higgs boson production cross sections at $\sqrt{s} = 13$ TeV as a 134 function of Higgs boson mass. The tH production cross section accounts for t -channel 135 and s -channel only (no tWH production). The VBF process is indicated here as 136 $q\bar{q}H$. The theoretical uncertainties are indicated as shaded bands around the lines. 137 Source: [28]. (b) Standard Model Higgs boson decay branching ratios for different 138 decay channels. The theoretical uncertainties are indicated as shaded bands around 139 the lines. Source: [28].	18
¹⁴⁰ 2.5	Example of leading order Standard Model Higgs boson production model diagrams. 141 Source: [29].	18
¹⁴² 2.6	(a) The diphoton invariant-mass distribution for the 7 and 8 TeV datasets (points), 143 with each event weighted by the predicted $S/(S + B)$ ratio of its event class. The 144 solid and dotted lines give the results of the signal-plus-background and background- 145 only fit, respectively. The light and dark bands represent the ± 1 and ± 2 standard 146 deviation uncertainties respectively on the background estimate. The inset shows 147 the corresponding unweighted invariant-mass distribution around $m_{\gamma\gamma} = 125$ GeV. 148 Source: [4]. (b) Distribution of the observed four-lepton invariant mass from the 149 combined 7 and 8 TeV data for the $H \rightarrow ZZ \rightarrow 4\ell$ analysis (points). The prediction 150 for the expected $Z+X$ and $ZZ(Z\gamma^*)$ background are shown by the dark and light 151 histogram, respectively. The open histogram gives the expected distribution for a 152 Higgs boson of mass 125 GeV. Source: [4].	19

153	2.7	Signal strength modifiers for the production modes, (a) μ^i , and for the decay channels, (b) μ^f . The thick (thin) black lines report the 1σ (2σ) confidence intervals. The thick blue and red lines report the statistical and systematic components of the 1σ confidence intervals. Source: [40].	20
154			
155			
156			
157	2.8	A summary of the measured Higgs boson mass in the $H \rightarrow ZZ \rightarrow 4l$ and $H \rightarrow \gamma\gamma$ decay channels, and for the combination of the two is presented here. The statistical (wider, yellow-shaded bands), and total (black error bars) uncertainties are indi- cated. The (red) vertical line and corresponding (grey) shaded column indicate the central value and the total uncertainty of the Run 1 + 2016 combined measurement, respectively. Source: [36].	21
158			
159			
160			
161			
162			
163	2.9	(a) T the $m_{\mu\mu}$ distribution for the weighted combination of all event categories used in the analysis. The upper panel is dominated by the gluon-gluon fusion categories with many data events but relatively small $S/(S + B)$. The lower panel shows the residuals after background subtraction, with the best-fit SM $H \rightarrow \mu\mu$ signal con- tribution with $m_H = 125.38$ GeV indicated by the red line. The measured signal strength is $1.19^{+0.41}_{-0.39}(\text{stat})^{+0.17}_{-0.16}(\text{sys})$. Source: [31]. (b) The best-fit estimates for the reduced coupling modifiers extracted for fermions and weak bosons from the resolved κ -framework model compared to their corresponding prediction from the SM. The error bars represent 68% CL intervals for the measured parameters. The lower panel shows the ratios of the measured coupling modifiers values to their SM predictions. Source: [31].	22
164			
165			
166			
167			
168			
169			
170			
171			
172			
173			
174	2.10	Example of leading order diagrams for the indirect and direct production mechanisms. In thees diagrams, the h can also be understood as a Z or a Higgs boson.	24
175			
176	2.11	Expected relative variation of the branching ratio for the $H \rightarrow \Upsilon(nS) + \gamma$ to k_b , where $k_b = g(Hb\bar{b})/g(Hb\bar{b})_{SM}$ is the ratio for the observed and expected Yukawa coupling oh $Hb\bar{b}$. Source: [44]	25
177			
178			
179	3.1	The LHC is the last ring (dark grey line) in a complex chain of particle accelerators. The smaller machines are used in a chain to help boost the particles to their final energies and provide beams to a whole set of smaller experiments. Source: [68].	28
180			
181			
182	3.2	Overview of the CMS experiment and its subdetectors. Source: [73].	30
183	3.3	Schematic cross section through the CMS tracker. Each line represents a detec- tor module. Double lines indicate back-to-back modules which deliver stereo hits. Source: [2].	32
184			
185			
186	3.4	Longitudinal section view of the ECAL and its components. Source: [2].	33
187	3.5	Longitudinal section view of the HCAL and its components. The barrel calorimeter (HB) covers the central region, inside the solenoid, the outer calorimeter covers also the central region, but it is positioned on the outside the solenoid. The endcap calorimeter (HE) covers the forward region and it is complemented by the forward calorimeter (HF), which uses Cherenkov light detectors made of radiation-hard quartz fibers. Source: [2].	35
188			
189			
190			
191			
192			
193	3.6	Longitudinal section view of the ECAL and its components. Source: [81].	36

194	3.7	The figure illustrates how the information from each subdetector is used in order to identify the different high-level objects in the Particle-Flow algorithm. Source: [85]. . .	38
195			
196	4.1	A diagram for the reconstructed invariant mass of the $\mu\mu\gamma$ final state. The blue and gray regions represent the Full Combinatorial and $\Upsilon+\gamma$ Combinatorial contributions, respectively, while the yellow and red regions represent the Resonant background and the signal region.	42
197			
198	4.2	Distributions of $\cos\theta$ of $\Upsilon \rightarrow \mu\mu$ and $\gamma^* \rightarrow \mu\mu$. The orange distribution is the $Z \rightarrow \Upsilon(1S, 2S, 3S) + \gamma$ sample before reweighting (Unpolarized); the blue and gray distributions are $Z \rightarrow \Upsilon(1S, 2S, 3S)$ sample after reweighting, for the Transverse and Longitudinal Polarization.	46
199			
200	4.3	Generator level distributions of main variables for $Z \rightarrow \Upsilon(1S, 2S, 3S) + \gamma$: Transverse momenta of the leading/trailing p_T muon and the photon, pseudorapidity (η) and ϕ of the muons and the photon, distances ΔR between the two muons and between the muons and the photon. All the distributions shown in the figure are normalized to the unity of area.	47
201			
202	4.4	Generator level distributions of main variables for $H \rightarrow \Upsilon(1S, 2S, 3S) + \gamma$: Transverse momenta of the leading/trailing p_T muon and the photon, pseudorapidity (η) and ϕ of the muons and the photon, distances ΔR between the two muons and between the muons and the photon. All the distributions shown in the figure are normalized to the unity of area.	48
203			
204	4.5	The p_T muon distributions from data and signal events for Z decaying in $\Upsilon(1S, 2S, 3S) + \gamma$ after Group I of selection cuts, where on left are presenting the trailing muons and on right are the leading muons. The plots are normalized to the unit of area. . . .	52
205			
206	4.6	The η muon distributions from data and signal events of Z decaying in $\Upsilon(1S, 2S, 3S) + \gamma$ after Group I of selection cuts, where on left are presenting the trailing muons and on right are the leading muons. The plots are normalized to the unit of area. . . .	52
207			
208	4.7	The ϕ muon distributions from data and signal events of Z decaying in $\Upsilon(1S, 2S, 3S) + \gamma$ after Group I of selection cuts, where on left are presenting the trailing muons and on right are the leading muons. The plots are normalized to the unit of area. . . .	53
209			
210	4.8	The p_T photon distributions from data and signal events for Z decaying in $\Upsilon(1S, 2S, 3S) + \gamma$ Group I of selection cuts. The plots normalized to the unit of area.	53
211			
212	4.9	The η photon distributions from data and signal events of Z decaying in $\Upsilon(1S, 2S, 3S) + \gamma$ after Group I of selection cuts. The plot is normalized to the unit of area.	53
213			
214	4.10	The ϕ photon distributions from data and signal events of Z decaying in $\Upsilon(1S, 2S, 3S) + \gamma$ after Group I of selection cuts. The plot is normalized to the unit of area.	54
215			
216	4.11	The p_T distributions for the reconstructed $\Upsilon(1S, 2S, 3S)$ in the left and for Z in the right from data and signal events for Z decaying in $\Upsilon(1S, 2S, 3S) + \gamma$ after Group I of selection cuts. The plots are normalized to the unit of area.	54
217			
218	4.12	The η distributions for $\Upsilon(1S, 2S, 3S)$ in the left and for Z in the right from data and signal events for Z decaying in $\Upsilon(1S, 2S, 3S) + \gamma$ after Group I of selection cuts. The plots are normalized to the unit of area.	54
219			

235	4.13 The ϕ distributions for $\Upsilon(1S, 2S, 3S)$ in the left and for Z in the right from data and signal events for Z decaying in $\Upsilon(1S, 2S, 3S) + \gamma$ after Group I of selection cuts. The plots are normalized to the unit of area.	55
236		
237		
238	4.14 The ΔR distributions between the photon and the leading muon (left) and the trailing muon (right) for for Z decaying in $\Upsilon(1S, 2S, 3S) + \gamma$ from data and signal events after Group I of selection cuts. The plots are normalized to the unit of area.	55
239		
240		
241	4.15 Left: The ΔR distributions between reconstructed dimuon ($\mu\mu$) system and the photon. Right: absolute value of the $\Delta\phi$ between the leading muon and the photon for for Z decaying in $\Upsilon(1S, 2S, 3S) + \gamma$ from data and signal events after Group I of selection cuts. The plots are normalized to the unit of area.	55
242		
243		
244		
245	4.16 The ratio for the transverse momentum of the reconstructed Upsilon and the reconstructed Z mass ($p_T^{\mu\mu}/M_{\mu\mu\gamma}$ - left) and the ratio for the transverse energy of the reconstructed Photon and the reconstructed Z mass ($E_T^{\mu\mu}/M_{\mu\mu\gamma}$ - right) distribution for Z decaying in $\Upsilon(1S, 2S, 3S) + \gamma$ from data and signal events after Group I of selection cuts. The plots are normalized to the unit of area.	56
246		
247		
248		
249		
250	4.17 The dimuon mass distribution of the reconstructed $\Upsilon(1S, 2S, 3S)$ from data and signal events for Z decaying after Group I of selection cuts. The plot is normalized to the number of events. "Signal" stands for the $Z \rightarrow \Upsilon(1S, 2S, 3S) + \gamma$ sample (scaled by a factor of $\times 100$) and "Background" corresponds to the peaking background ($Z \rightarrow \mu\mu\gamma_{FSR}$) sample (scaled by a factor of x3).	56
251		
252		
253		
254		
255	4.18 The p_T muon distributions from data and signal events for Higgs decaying in $\Upsilon(1S, 2S, 3S) + \gamma$ after Group I of selection cuts, where on left are presenting the trailing muons and on right are the leading muons. The plots are normalized to the unit of area. . . .	56
256		
257		
258	4.19 The η muon distributions from data and signal events of Higgs decaying in $\Upsilon(1S, 2S, 3S) + \gamma$ after Group I of selection cuts, where on left are presenting the trailing muons and on right are the leading muons. The plots are normalized to the unit of area. . . .	57
260		
261	4.20 The ϕ muon distributions from data and signal events of Higgs decaying in $\Upsilon(1S, 2S, 3S) + \gamma$ after Group I of selection cuts, where on left are presenting the trailing muons and on right are the leading muons. The plots are normalized to the unit of area. . . .	57
262		
263		
264	4.21 The p_T photon distributions from data and signal events for Higgs decaying in $\Upsilon(1S, 2S, 3S) + \gamma$ Group I of selection cuts. The plot is normalized to the unit of area.	57
266		
267	4.22 The η photon distributions from data and signal events of Higgs decaying in $\Upsilon(1S, 2S, 3S) + \gamma$ after Group I of selection cuts. The plot is normalized to the unit of area.	58
268		
269	4.23 The ϕ photon distributions from data and signal events of Higgs decaying in $\Upsilon(1S, 2S, 3S) + \gamma$ after Group I of selection cuts. The plot is normalized to the unit of area.	58
270		
271	4.24 The p_T distributions for $\Upsilon(1S, 2S, 3S)$ in the left and for Higgs in the right from data and signal events for Higgs decaying in $\Upsilon(1S, 2S, 3S) + \gamma$ after Group I of selection cuts. The plots are normalized to the unit of area.	58
272		
273		
274	4.25 The η distributions for $\Upsilon(1S, 2S, 3S)$ in the left and for Higgs in the right from data and signal events for Higgs decaying in $\Upsilon(1S, 2S, 3S) + \gamma$ after Group I of selection cuts. The plots are normalized to the unit of area.	59
275		
276		

277	4.26 The ϕ distributions for $\Upsilon(1S, 2S, 3S)$ in the left and for Higgs in the right from data 278 and signal events for Higgs decaying in $\Upsilon(1S, 2S, 3S) + \gamma$ after Group I of selection 279 cuts. The plots are normalized to the unit of area.	59
280	4.27 The ΔR distributions between the photon and the leading muon (left) and the trailing 281 muon (right) for Higgs decaying in $\Upsilon(1S, 2S, 3S) + \gamma$ from data and signal events 282 after Group I of selection cuts. The plots are normalized to the unit of area.	59
283	4.28 Left: The ΔR distributions between reconstructed dimuon ($\mu\mu$) system and the 284 photon. Right: absolute value of the $\Delta\phi$ between the leading muon and the photon 285 for for Higgs decaying in $\Upsilon(1S, 2S, 3S) + \gamma$ from data and signal events after Group 286 I of selection cuts. The plots are normalized to the unit of area.	60
287	4.29 The ratio for the transverse momentum of the reconstructed Upsilon and the recon- 288 structed Higgs mass ($p_T^{\mu\mu}/M_{\mu\mu\gamma}$ - left) and the ratio for the transverse energy of the 289 reconstructed Photon and the reconstructed Higgs mass ($E_T^{\mu\mu}/M_{\mu\mu\gamma}$ - right) distribu- 290 tion for Higgs decaying in $\Upsilon(1S, 2S, 3S) + \gamma$ from data and signal events after Group 291 I of selection cuts. The plots are normalized to the unit of area.	60
292	4.30 The dimuon mass distribution of the reconstructed $\Upsilon(1S, 2S, 3S)$ from data and signal 293 events for Higgs decaying after Group I of selection cuts. This plot is normalized the 294 expected number of events. The plot is normalized to the number of events. "Signal" 295 stands for the $H \rightarrow \Upsilon(1S, 2S, 3S) + \gamma$ sample (scaled by a factor of $\times 60000$) and 296 "Background" corresponds to the peaking background (Higgs Dalitz Decay) sample 297 (scaled by a factor of $\times 400$).	60
298	4.31 The p_T muon distributions from data and signal events for Z decaying in $\Upsilon(1S, 2S, 3S)$ 299 + γ after Group I of selection cuts, where on left are presenting the trailing muons 300 and on right are the leading muons. The plots are normalized to the number of 301 events. Signal sample is scaled by a factor of $\times 100$	61
302	4.32 The η muon distributions from data and signal events of Z decaying in $\Upsilon(1S, 2S, 3S)$ 303 + γ after Group I of selection cuts, where on left are presenting the trailing muons 304 and on right are the leading muons. The plots are normalized to the number of 305 events. Signal sample is scaled by a factor of $\times 100$	62
306	4.33 The ϕ muon distributions from data and signal events of Z decaying in $\Upsilon(1S, 2S, 3S)$ 307 + γ after Group I of selection cuts, where on left are presenting the trailing muons 308 and on right are the leading muons. The plots are normalized to the number of 309 events. Signal sample is scaled by a factor of $\times 100$	62
310	4.34 The p_T photon distributions from data and signal events for Z decaying in $\Upsilon(1S, 2S, 3S)$ 311 + γ all (Group I+II) selection cuts. The plot is normalized to the number of events. 312 Signal sample is scaled by a factor of $\times 100$	62
313	4.35 The η photon distributions from data and signal events of Z decaying in $\Upsilon(1S, 2S, 3S)$ 314 + γ after all (Group I+II) selection cuts. The plot is normalized to the number of 315 events. Signal sample is scaled by a factor of $\times 100$	63
316	4.36 The ϕ photon distributions from data and signal events of Z decaying in $\Upsilon(1S, 2S, 3S)$ 317 + γ after all (Group I+II) selection cuts. The plot is normalized to the number of 318 events. Signal sample is scaled by a factor of $\times 100$	63

319	4.37 The p_T distributions for $\Upsilon(1S, 2S, 3S)$ in the left and for Z in the right from data 320 and signal events for Z decaying in $\Upsilon(1S, 2S, 3S) + \gamma$ after all (Group I+II) selection 321 cuts. The plots are normalized to the number of events. Signal sample is scaled by 322 a factor of $\times 100$).	63
323	4.38 The η distributions for $\Upsilon(1S, 2S, 3S)$ in the left and for Z in the right from data and 324 signal events for Z decaying in $\Upsilon(1S, 2S, 3S) + \gamma$ after all (Group I+II) selection 325 cuts. The plots are normalized to the number of events. Signal sample is scaled by 326 a factor of $\times 100$).	64
327	4.39 The ϕ distributions for $\Upsilon(1S, 2S, 3S)$ in the left and for Z in the right from data and 328 signal events for Z decaying in $\Upsilon(1S, 2S, 3S) + \gamma$ after all (Group I+II) selection 329 cuts. The plots are normalized to the number of events. Signal sample is scaled by 330 a factor of $\times 100$).	64
331	4.40 The ΔR distributions between the photon and the leading muon (left) and the trailing 332 muon (right) for $\Upsilon(1S, 2S, 3S)$ from data and signal events for Z decaying after all 333 (Group I+II) selection cuts. The plots are normalized to the number of events. Signal 334 sample is scaled by a factor of $\times 100$).	64
335	4.41 The ratio for the transverse momentum of the reconstructed Upsilon and the re- 336 constructed Z mass ($p_T^{\mu\mu}/M_{\mu\mu\gamma}$ - left) and the ratio for the transverse energy of the 337 reconstructed Photon and the reconstructed Z mass ($E_T^{\mu\mu}/M_{\mu\mu\gamma}$ - right) distribution 338 for $\Upsilon(1S, 2S, 3S)$ from data and signal events for Z decaying after all (Group I+II) 339 selection cuts. The plots are normalized to the number of events. Signal sample is 340 scaled by a factor of $\times 100$).	65
341	4.42 The p_T muon distributions from data and signal events for Higgs decaying in $\Upsilon(1S, 2S, 3S)$ 342 $+ \gamma$ after Group I of selection cuts, where on left are presenting the trailing muons 343 and on right are the leading muons. The plots are normalized to the number of 344 events. Signal sample is scaled by a factor of $\times 600000$).	65
345	4.43 The η muon distributions from data and signal events of Higgs decaying in $\Upsilon(1S, 2S, 3S)$ 346 $+ \gamma$ after Group I of selection cuts, where on left are presenting the trailing muons 347 and on right are the leading muons. The plots are normalized to the number of 348 events. Signal sample is scaled by a factor of $\times 600000$).	65
349	4.44 The ϕ muon distributions from data and signal events of Higgs decaying in $\Upsilon(1S, 2S, 3S)$ 350 $+ \gamma$ after Group I of selection cuts, where on left are presenting the trailing muons 351 and on right are the leading muons. The plots are normalized to the number of 352 events. Signal sample is scaled by a factor of $\times 600000$).	66
353	4.45 The p_T photon distributions from data and signal events for Higgs decaying in 354 $\Upsilon(1S, 2S, 3S) + \gamma$ all (Group I+II) selection cuts. The plot is normalized to the 355 number of events. Signal sample is scaled by a factor of $\times 600000$).	66
356	4.46 The η photon distributions from data and signal events of Higgs decaying in $\Upsilon(1S, 2S, 3S)$ 357 $+ \gamma$ after all (Group I+II) selection cuts. The plot is normalized to the number of 358 events. Signal sample is scaled by a factor of $\times 600000$).	66

359	4.47 The ϕ photon distributions from data and signal events of Higgs decaying in $\Upsilon(1S, 2S, 3S) + \gamma$ after all (Group I+II) selection cuts. The plot is normalized to the number of events. Signal sample is scaled by a factor of c).	67
360		
361		
362	4.48 The p_T distributions for $\Upsilon(1S, 2S, 3S)$ in the left and for Higgs in the right from data and signal events for Higgs decaying in $\Upsilon(1S, 2S, 3S) + \gamma$ after all (Group I+II) selection cuts. The plots are normalized to the number of events. Signal sample is scaled by a factor of $\times 600000$).	67
363		
364		
365		
366	4.49 The η distributions for $\Upsilon(1S, 2S, 3S)$ in the left and for Higgs in the right from data and signal events for Higgs decaying in $\Upsilon(1S, 2S, 3S) + \gamma$ after all (Group I+II) selection cuts. The plots are normalized to the number of events. Signal sample is scaled by a factor of $\times 600000$).	67
367		
368		
369		
370	4.50 The ϕ distributions for $\Upsilon(1S, 2S, 3S)$ in the left and for Higgs in the right from data and signal events for Higgs decaying in $\Upsilon(1S, 2S, 3S) + \gamma$ after all (Group I+II) selection cuts. The plots are normalized to the number of events. Signal sample is scaled by a factor of $\times 600000$).	68
371		
372		
373		
374	4.51 The ΔR distributions between the photon and the leading muon (left) and the trailing muon (right) for $\Upsilon(1S, 2S, 3S)$ from data and signal events for Higgs decaying after all (Group I+II) selection cuts. The plots are normalized to the number of events. Signal sample is scaled by a factor of $\times 600000$).	68
375		
376		
377		
378	4.52 The ratio for the transverse momentum of the reconstructed Upsilon and the reconstructed Higgs mass ($p_T^{\mu\mu}/M_{\mu\mu\gamma}$ - left) and the ratio for the transverse energy of the reconstructed Photon and the reconstructed Higgs mass ($E_T^{\mu\mu}/M_{\mu\mu\gamma}$ - right) distribution for $\Upsilon(1S, 2S, 3S)$ from data and signal events for Higgs decaying after all (Group I+II) selection cuts. The plots are normalized to the number of events. Signal sample is scaled by a factor of $\times 600000$).	68
379		
380		
381		
382		
383		
384	4.53 Data and MC of the R9 variable, before and after the reweighting. Barrel (left) and Endcap (right).	69
385		
386	4.54 Peaking background for the $Z \rightarrow \Upsilon(1S, 2S, 3S) + \gamma$ analysis. $\mu\mu$ mass distribution (left) and $\mu\mu\gamma$ invariant mass distribution (right). From top to bottom categories: Inclusive, EB High R9, EB Low R9, EE.	73
387		
388		
389	4.55 Υ control sample fit with Chebychev 1 st order for the background support and 3 gaussian for the three $\Upsilon(1S, 2S, 3S)$ peaks.	74
390		
391	4.56 $Z \rightarrow \Upsilon(1S, 2S, 3S) + \gamma$ Background Modeling: $\mu\mu$ distribution. Inclusive (top left); EB High R9 (top right), EB Low R9 (bottom left), EE (bottom right). The pdfs projections are plotted with respect to the overall best choice of the statistica test.	77
392		
393		
394	4.57 $Z \rightarrow \Upsilon(1S, 2S, 3S) + \gamma$ Background Modeling: $\mu\mu\gamma$ distribution. Inclusive (top left); EB High R9 (top right), EB Low R9 (bottom left), EE (bottom right). The plotted pdfs corresponds to the best choice by the statistical test for each family. The signal region, from 80 GeV to 100 GeV was blinded.	77
395		
396		
397		
398	4.58 Peaking Background for the $H \rightarrow \Upsilon(1S, 2S, 3S) + \gamma$ analysis. $m_{\mu\mu}$ invariant mass distribution (left) and $m_{\mu\mu\gamma}$ invariant mass distribution (right).	78
399		

400	4.59 $H \rightarrow \Upsilon(1S, 2S, 3S) + \gamma$ Background Modeling: $m_{\mu\mu}$ distribution. The <i>pdfs</i> projections 401 are plotted with respect to the overall best choice of the statistical test.	78
402	4.60 $H \rightarrow \Upsilon(1S, 2S, 3S) + \gamma$ Background Modeling: $\mu\mu\gamma$ distribution. The plotted <i>pdfs</i> 403 corresponds to the best choice by the statistical test for each family. The signal 404 region, from 115 GeV to 135 GeV was blinded.	78
405	4.61 Signal Modeling for the $Z \rightarrow \Upsilon(1S, 2S, 3S) + \gamma$ analysis for Inclusive category. $m_{\mu\mu}$ 406 mass distribution (left) and $m_{\mu\mu\gamma}$ mass distribution (right). From top to bottom: 407 $\Upsilon(1S)$, $\Upsilon(2S)$, $\Upsilon(3S)$	80
408	4.62 Signal Modeling for the $Z \rightarrow \Upsilon(1S, 2S, 3S) + \gamma$ analysis for EB High R9 category. 409 $m_{\mu\mu}$ mass distribution (left) and $m_{\mu\mu\gamma}$ mass distribution (right). From top to bottom: 410 $\Upsilon(1S)$, $\Upsilon(2S)$, $\Upsilon(3S)$	81
411	4.63 Signal Modeling for the $Z \rightarrow \Upsilon(1S, 2S, 3S) + \gamma$ analysis for EB Low R9 category. 412 $m_{\mu\mu}$ mass distribution (left) and $m_{\mu\mu\gamma}$ mass distribution (right). From top to bottom: 413 $\Upsilon(1S)$, $\Upsilon(2S)$, $\Upsilon(3S)$	82
414	4.64 Signal Modeling for the $Z \rightarrow \Upsilon(1S, 2S, 3S) + \gamma$ analysis for EE category. $m_{\mu\mu}$ mass 415 distribution (left) and $m_{\mu\mu\gamma}$ mass distribution (right). From top to bottom: $\Upsilon(1S)$, 416 $\Upsilon(2S)$, $\Upsilon(3S)$	83
417	4.65 Signal Modeling for the $H \rightarrow \Upsilon(1S, 2S, 3S) + \gamma$. $m_{\mu\mu}$ mass distribution (left) and 418 $m_{\mu\mu\gamma}$ mass distribution (right). From top to bottom: $\Upsilon(1S)$, $\Upsilon(2S)$, $\Upsilon(3S)$	84
419	4.66 Examples of the toy datasets fit ($M_{\mu\mu}$), for the Z decay analysis, after the toy dataset 420 refit, for 1S, 2S and 3S (left to right), with μ_{true} equals to 20, 50, 100, 1000 (top to 421 bottom). The red lines corresponds to the background model (B), the green lines to 422 signal model (S), the blue lines to the total (S+B) and the dots is the toy dataset.	89
423	4.67 Examples of the toy datasets fit ($M_{\mu\mu\gamma}$), for the Z decay analysis, after the toy dataset 424 refit, for 1S, 2S and 3S (left to right), with μ_{true} equals to 20, 50, 100, 1000 (top to 425 bottom). The red lines corresponds to the background model (B), the green lines to 426 signal model (S), the blue lines to the total (S+B) and the dots is the toy dataset.	90
427	4.68 Examples of the toy datasets fit ($M_{\mu\mu}$), for the Higgs decay analysis, after the toy 428 dataset refit, for 1S, 2S and 3S (left to right), with μ_{true} equals to 100000, 200000, 429 300000, 1000000 (top to bottom). The red lines corresponds to the background model 430 (B), the green lines to signal model (S), the blue lines to the total (S+B) and the 431 dots is the toy dataset.	91
432	4.69 Examples of the toy datasets fit ($M_{\mu\mu\gamma}$), for the Higgs decay analysis, after the toy 433 dataset refit, for 1S, 2S and 3S (left to right), with μ_{true} equals to 100000, 200000, 434 300000, 1000000 (top to bottom). The red lines corresponds to the background model 435 (B), the green lines to signal model (S), the blue lines to the total (S+B) and the 436 dots is the toy dataset.	92
437	4.70 Distribution of pulls ($\frac{\mu_{fit} - \mu_{true}}{\sigma_{fit}}$), for the Z decay analysis, after the toy dataset refit, 438 for 1S, 2S and 3S (left to right), with μ_{true} equals to 20, 50, 100, 1000 (top to bottom).	93
439	4.71 Distribution of pulls ($\frac{\mu_{fit} - \mu_{true}}{\sigma_{fit}}$), for the Higgs decay analysis, after the toy dataset 440 refit, for 1S, 2S and 3S (left to right), with μ_{true} equals to 100000, 200000, 300000, 441 1000000 (top to bottom).	94

442	5.1 Example of $f(\tilde{q}_\mu \mu, \hat{\theta}_\mu^{\text{obs}})$ $f(\tilde{q}_\mu \mu = 0, \hat{\theta}_{\mu=0}^{\text{obs}})$ distributions generated with toy MC. Source: [134].	97
443		
444	5.2 Example of $f(\tilde{q}_\mu \mu, \hat{\theta}_\mu^{\text{obs}})$ $f(\tilde{q}_\mu \mu = 0, \hat{\theta}_{\mu=0}^{\text{obs}})$ distributions generated with toy MC. In the figure, q must be read as \tilde{q} . The green area shows the p_{s+b} defined in 5.7, while the yellow one shows p_b defined in 5.8. Source: [131].	98
445		
446		
447	6.1 The Avalanche production process inside a RPC gap. (Top) The initial process and the secondary electron/ion generation. (Bottom) The overall charge distribution of an Avalanche between the electrodes. Source: [138].	102
448		
449		
450	6.2 Streamer formation process. The distorted electric field around the high positive charge concentration enhances the ionization process, initiating secondary avalanches. Source: [138].	103
451		
452	6.3 RPC chamber on installed on station RE+4 of CMS Endcap. Source: [140].	104
453		
454	6.4 R- ϕ (left) and R-Z (right) projections of the barrel Muon System.	105
455		
456	6.5 R-Z projections of the endcap Muon System (positive Z side). This is the same configuration for the 36 ϕ sectors.	106
457		
458	6.6 RPC efficiencies (per chamber) over Run2 Integrated Luminosity for Barrel (left) and Endcap (right). Red lines indicates technical stops (TS) while grey ones indicates Year-End-Technical stops (YETS). The drop in the efficiency around 110 pb^{-1} is related to a known operation mistake. Source: [151].	107
459		
460		
461	6.7 RPC cluster size (CLS - per chamber) over Run2 Integrated Luminosity for Barrel (left) and Endcap (right). Red lines indicates technical stops (TS) while grey ones indicates Year-End-Technical stops (YETS). The drop in the cluster size around 110 pb^{-1} is related to a known operation mistake. Source: [151].	107
462		
463		
464	6.8 Ohmic current history of W+0, RE+1, RE+4 and RE-4. The blank regions, from time to time, corresponds to technical stops (TS), when the detector is off. Source: [151].	108
465		
466		
467	6.9 (a) Luminosity delivered by the LHC, recorded one by CMS and the certified (vali- dated), from the 22nd of April, 2016 to the 27th of October, 2016. (b) Efficiency of the certification process for each subsystem, from the 22nd of April, 2016 to the 27th of October, 2016. Total CMS efficiency is above 90%. Source: [152]	109
468		
469		
470		
471	6.10 Upgrade of the RPC online software.	110
472		
473	6.11 Example of the updated screens, using Trigger Supervisor 5.	111
474		
475	6.12 η projection of the Muon System subdetectors. In purple, is labeled the iRPCS to be installed during the CMS upgrade.	111
476		
477	6.13 FEB configured 8 channels modes. Group should be understood as wire pad. Left: Logical diagram for OR2. Right: Logical diagram for AND2.	113
478		
479	6.14 FEB configured 2 channels modes. Left: Logical diagram for OR8. Group should be understood as wire pad. Right: Logical diagram for OR4AND2.	113
480		
481	6.15 Left: Setup mounted for commissioning. Two MWPC chamber on the top (chambers A and B) and two (chambers C and D) on the bottom with a RPC R&D in the middle. Right: Rack with all the services for the operation of these chambers.	114

482	6.16	Coincidence rate of two chambers with respect to an arbitrary distance between 483 the two top planes. Measured in 10 minutes, for 2 logical combinations (OR8 and 484 OR4AND2). Applied high voltage: 2.65 kV. Threshold: 7 pC. Active area: readout 485 of 160 mm x 160 mm per chamber.	115
486	6.17	Individual rates (chambers A, B, C and D) and coincidence rates for two chambers 487 (A AND B, C AND D), for without γ source (blue), a shielded γ source (orange) and 488 an unshielded γ source (green). Source sitting on top of chamber A. Applied high 489 voltage: 2.65 kV. Threshold: 7 pC. Active area: readout of 160 mm x 320 mm per 490 chamber. Logical combination: AND2	116
491	6.18	Left: Proposed adapter the chamber patch panel which make it possible to replace 492 a tripolar by a jupiter HV connector. Right: Try out of the proposed HV connector 493 replacement.	118
494	6.19	RPC Front-end board (FEB) used in the barrel chambers.	119
495	6.20	RPC FEB Commissioning Analyzer.	120

496 List of Tables

497 2.1	Relative strength (with respect to the strong force) and effective range of action for 498 the four fundamentals interactions.	5
499 2.2	Summary of cross section and branching ratio for $H/Z \rightarrow \Upsilon(1S, 2S, 3S) + \gamma \rightarrow$ 500 $\mu^+ \mu^- + \gamma$ analysis. The effective cross-section will be discussed in section 4.1.2.	23
501 2.3	Observed upper limits, by the ATLAS experiment, on the branching fractions for the 502 Higgs and Z decays (last result). Detailed comparisons with the results obtained in 503 this study will be presented in chapter 5.	25
504 2.4	Observed upper limits, by CMS, on the branching fractions for the Higgs and Z 505 decays. The number are compatible with the ones obtained by ATLAS. The results 506 presented for different polarization scenarios of the J/Ψ	26
507 4.1	Datasets simulated (MC) for 2016 conditions. Assuming that $\sigma(pp \rightarrow H)$, taking into 508 consideration all the simulated Higgs production modes, is 55.13 pb [105] and $\sigma(pp \rightarrow$ 509 $Z \rightarrow \mu\mu$) is 57094.5 pb , including the next-to-next-to-leading order (NNLO) QCD 510 contributions, and the next-to-leading order (NLO) electroweak corrections from fewz 511 3.1 [106] calculated using the NLO PDF set NNPDF3.0, with the phase space selec- 512 tion in invariant mass of the dimuon system of $m_{\mu\mu} > 50\text{ GeV}$. For the Higgs Dalitz 513 σ , we consider only the gluon fusion contribution ($\sigma_{ggF} = 48.6\text{ pb}$) [105]. The Higgs 514 Dalitz Decay BR_{SM} and the $Z \rightarrow \mu\mu\gamma_{FSR}$ were obtained with MCFM 6.6 [107] (as 515 in the CMS search for Higgs Dalitz Decay in at $\sqrt{s} = 8\text{ TeV}$ [108]) and with MAD- 516 GRAPH 5 _MC@NLO, respectively. The $BR_{\Upsilon(1S,2S,3S) \rightarrow \mu\mu}^{PDG} = (2.48, 1.93, 2.18) \times 10^{-2}$ 517 is quoted from Particle Data Group report (PDG) [13]. The "Effective σ " for the 518 signal samples is $\sigma(pp \rightarrow Z(H)) \times BR_{SM} \times BR_{\Upsilon(nS) \rightarrow \mu\mu}^{PDG}$	44
519 4.2	Summary of the impact of reweighted of polarization contribution using several sce- 520 narios.	45
521 4.3	Conditions for a muon to pass the strict tracker requirements.	50
522 4.4	Number of events for the Z decay, before and after the full selection, per categorization 523 scenarios.	70
524 4.5	Number of events for the H decay, before and after the full selection.	70
525 4.6	Modeling for each background source and mass component.	71
526 4.7	Modeling for each signal source and mass component.	79
527 4.8	A summary table of systematic uncertainties in the Z boson decaying in $\Upsilon(1S, 2S, 3S) +$ 528 γ , affecting the final yields of the MC samples.	87
529 4.9	A summary table of systematic uncertainties in the Higgs boson decaying in $\Upsilon(1S, 2S, 3S) +$ 530 γ , affecting the final yields of the MC samples.	88

531	4.10 A summary table of systematic uncertainties in the Z (H) decaying in $\Upsilon(1S, 2S, 3S) +$	
532	γ , affecting the signal fits.	88
533	5.1 Summary table for the limits on branching ratio of $Z \rightarrow \Upsilon(1S, 2S, 3S)\gamma$ and $H \rightarrow$	
534	$\Upsilon(1S, 2S, 3S)\gamma$ decays.	99
535	5.2 Summary table for the limits on branching ratio of $Z \rightarrow \Upsilon(1S, 2S, 3S)\gamma$, for the two	
536	possible categorization scenarios.	99

537 1 Introduction

538 The Standard Model (SM) have been proven successful over the last decades by its accordance
 539 with results from many collider experiments, the Large Electron–Positron Collider (LEP) [1] and
 540 its experiments created the experimental conditions to the discovery of the electroweak bosons, W^\pm
 541 and Z . The Tevatron experiments (D0 and CDF) allowed the discovery of the top quark. These
 542 were 3 of the four heaviest components of the SM. The missing piece was the, so called, Higgs
 543 Boson, or any other explanation to the mass of the other SM particles.

544 In 2012, during CMS' Run1, at center-of-mass energy $\sqrt{s} = 13$ TeV, researchers from CMS [2] and
 545 ATLAS [3], two collaborations with experiments located at the Large Hadron Collider (LHC), a 27
 546 km long circular proton-proton collider build and operated by CERN, announced the discovery a
 547 new particle [4, 5], with characteristics compatibles with the Brout-Englert-Higgs boson, completing
 548 the SM picture proposed up to fifty years ago. In 2013, Francois Englert and Peter Higgs were
 549 awarded with the Noble Prize for "*for the theoretical discovery of a mechanism that contributes to
 550 our understanding of the origin of mass of subatomic particles, and which recently was confirmed
 551 through the discovery of the predicted fundamental particle, by the ATLAS and CMS experiments at
 552 CERN's Large Hadron Collider*" [6].

553 On top of the success of the Higgs program at CMS, there is much to be understood, e.g. pin down
 554 the coupling constants of the Higgs boson with all three generations of quarks and leptons, its mass
 555 and its full width, evaluate non-zero CP-odd components in Higgs interactions, investigate double
 556 Higgs production and its self-coupling constant and possible extensions of the SM close to the Higgs
 557 sector and explore rare decays of Higgs. The former one, specially rare decays involving quarkonia,
 558 such as $H \rightarrow M\gamma$, where M is a meson state, are a very good scenario to investigate the Higgs
 559 interaction with other SM particles other than the direct decay. This one would be overwhelmed
 560 by the immense background coming from QCD events. The same analogy can be extended to the
 561 Z boson, which also serves as a benchmark for the Higgs study.

562 The present study corresponds to $35.86 fb^{-1}$ of data taken by CMS during 2016, during the Run2,
 563 at center-of-mass energy $\sqrt{s} = 13$ TeV, in which an upper limit on the branching fraction for
 564 $H/Z \rightarrow \Upsilon(1S, 2S, 3S)(\rightarrow \mu\mu) + \gamma$ is determined.

565 Because of its narrow resolution, muons play a special role not only for this study, but for CMS,
 566 in general. Not only the Higgs studies heavily depends of muonic final states (for decay channels,
 567 such as $H \rightarrow \mu\mu$ and $H \rightarrow ZZ \rightarrow 4l$ and identification of the production modes), but also muon
 568 final states are very important to a whole broad of physics process accessible at CMS/LHC. The
 569 Figure 1.1 presents the the distribution of dimuon invariant mass reconstructed from different double
 570 muon triggers, with different requirements in pseudorapidity and transverse momentum. It is clear

571 how the muons at CMS broaden the set of interesting process giving access to light quark hadrons
 572 to high transverse momentum phenomena.

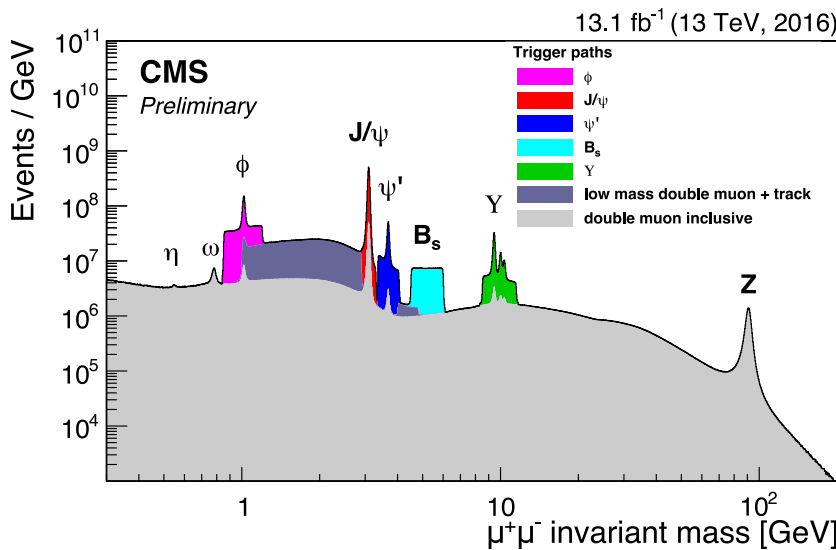


Figure 1.1: Dimuon mass distribution collected with various dimuon triggers. The light gray continuous distribution represents events collected with inclusive dimuon triggers with high p_T thresholds. The dataset corresponding to an integrated luminosity of 13.1 fb^{-1} was collected during the 25 ns LHC running period at 13 TeV in 2016. Source: [7].

573 In this scenario, a contribution to the muon system of CMS is a meaningfully one to the col-
 574 laboration. In this document it is described the contributions given to Resistive Plate Chamber
 575 (RPC) subdetector, including its commissioning, instrumentation for its upgrade, operation and
 576 maintenance.

577 This document is organized as follows: Chapter 1 is this introduction. Chapter 2 is devoted to
 578 a review of the theoretical foundations of this study and the motivations for the study of Rare
 579 Z and Higgs decays involving quarkonia. Chapter 3 is a review of the collider and experimental
 580 setup, LHC and CMS respectively. Chapter 4 is a detailed description of the data sample and the
 581 applied analysis procedure, as well as the statistical modeling and the branching fraction upper limit
 582 extraction. Chapter 5 is a reviews of the Resistive Plate Chamber technology for muon detection
 583 at CMS and the details of the contributions given to this subdetector.

584 Wherever figures and tables' sources are not provided, the source is the author himself.

585 In this document, the convention of natural units is implicitly used: the vacuum speed of light (c),
 586 the reduced Planck constant (\hbar) and electric permittivity (ϵ_0) are normalized to unity. In this way,
 587 SI units are:

- 588 • mass ($[m]$) = GeV,
- 589 • energy ($[E]$) = GeV,
- 590 • momemtum ($[p]$) = GeV,
- 591 • mass ($[m]$) = GeV,
- 592 • time ($[t]$) = 1/GeV,

- 593 • length ($[s]$) = 1/GeV.

594 The Einstein summation convention is also followed. In the notation, $y = A^i B_i$ stands for $y =$
595 $\sum_{i=0}^n A^i B_i = A^1 B_1 + A^2 B_2 + A^3 B_3 + \dots + A^n B_n$.

DRAFT

DRAFT

596 2 Standard Model and rare Z and Higgs 597 decays to quarkonia

598 2.1 Standard Model and Local Gauge Invariance

599 Physics understands matter and how it interacts in terms of two components: fundamental forces
 600 and elementary particles. From the weakest to the strongest, the fundamental forces are: Gravita-
 601 tional, Weak, Electromagnetic and Strong. All share common characteristics like, being mediated
 602 by particles ¹, being relevant within some effective range and have a associate a charge-like quan-
 603 tity (i.e. an intrinsic characteristic of the object) that defines whether or not, particles might be
 604 subjected to a specific interaction.

605 Along with the fundamental interactions, the Standard Model [8–11] (or simply *SM*) defines every
 606 existing matter in the Universe as a set of fundamental quantum objects, with properties that pre-
 607 scribes their interaction. Those objects are said to be fundamental since, in the context of the SM,
 608 they are the smallest possible components of matter. We shall refer to them as *Fundamental Parti-*
 609 *cles*. There four of those mediating particles (force carriers), gluon (g - for the strong interaction),
 610 photon (γ - for the electromagnetic interaction), Z (neutral) and W^\pm (for weak interaction), all of
 611 them being vector bosons (spin 1). Besides the interaction mediators, described at Table 2.1, the
 612 fundamental particles are divided in two groups (*quarks* and *leptons*), with three generations, each.
 613 These are not force carriers, but elementary particles, endowed with charge-like characteristics that
 614 allow them to interact by exchange the vector bosons. Those are the building blocks of Matter in
 615 our Universe.

616 Figure 2.1 summarizes their properties. Table 2.1 presents the relative strength and effective range,
 617 for each one of the four fundamental interactions. It is important to stress that, the gravitational
 618 force is not study subject of the Standard Model.

Table 2.1: Relative strength (with respect to the strong force) and effective range of action for the four fundamentals interactions.

	Mediator	Relative Strength	Effective Range
Gravitational	Graviton	10^{-41}	∞
Weak	W and Z	10^{-16}	10^{-18} m
Electromagnetic	Photon	10^{-3}	∞
Strong	Gluon	1	10^{-15} m

¹There is no evidence of the existence of the Graviton (force carrier associated to the gravitational force), even though, it is theorized by models that wish to comprehend gravity in a quantum perspective.

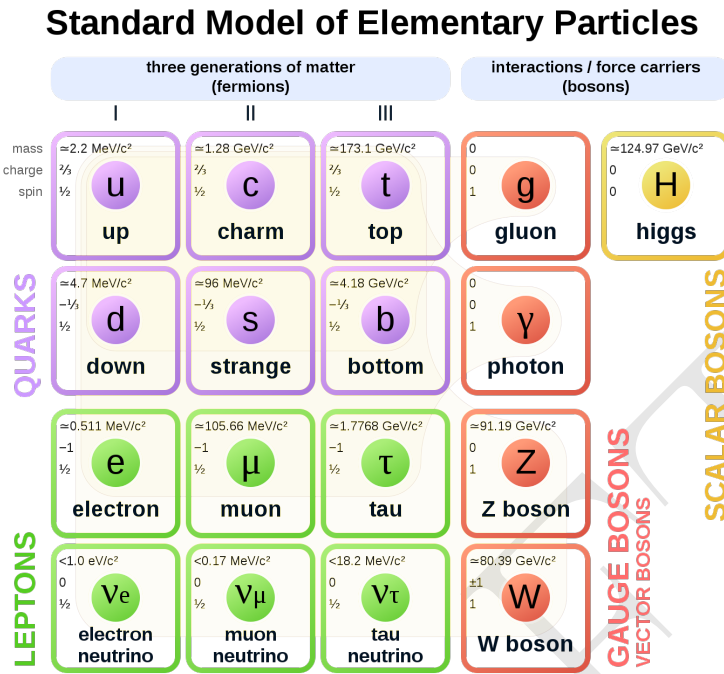


Figure 2.1: Elementary particles of the Standard Model, with their masses charges and spin. Those particles can be divided in two classes: boson (the interaction/force carriers) and the fermions, which are divided in three generations. Source: [12].

619 There are six quarks, up and down (u and d - first generation), charm and strange (c and s - second
620 generation), top and bottom (t and b - third generation), in increasing invariant mass order of the
621 generations. Since they interact through all the three fundamental forces of the SM, they are said
622 to possess electrical charge (for the electromagnetic interaction), flavour (for the weak interaction)
623 and color (for the strong). Their generational counterparts, the leptons, don't interact via strong
624 force, that is why they are said to have only flavour and electric charge. The leptons are electron
625 and electron neutrino (e and ν_e - first generation), muon and muon neutrino (μ and ν_μ - second
626 generation) and tau and tau neutrino (τ and ν_τ - third generation). The neutrinos, within the
627 SM, are massless, even though, experimental measurements have shown that they actually have
628 mass [13]. Neutrinos are also electrically neutral, meaning that they only interact through weak
629 interactions.

630 Figure 2.1 also presents the Higgs Boson (H) which is part of the SM and shall be discussed later.

631 2.1.1 Local Gauge Invariance

632 Within the Standard Model, the theoretical basis that describe the fundamental interactions are
633 derived from a common principle: the local gauge invariance. According to Salam and Ward [14]:

634 "Our basic postulate is that it should be possible to generate strong, weak and electro-
635 magnetic interaction terms [...], by making local gauge transformations on the kinetic-
636 energy terms in the free Lagrangian for all particles."

637 Taking the Quantum Electrodynamics (QED) as an example: the quantum field theory that de-
 638 scribes the electromagnetic interactions, consider the Dirac equation, in the covariant form, for a
 639 particle with mass m , charge $-e$ and spin $1/2$, i.e. a electron:

$$(i\gamma^\mu \partial_\mu + m)\psi(x) = 0, \quad (2.1)$$

640 where $\psi(x)$ is a spinor, describing the wave-function and γ^μ are gamma-matrices. This equation
 641 can be obtained from the lagrangian \mathcal{L} ² of a free particle, in the form of

$$\mathcal{L}_0 = i\bar{\psi}(x)\gamma^\mu \partial_\mu \psi(x) - m\bar{\psi}\psi(x), \quad (2.2)$$

642 when applied to the Euler-Lagrange equation.

643 It is clear that, the Dirac Equation (2.1) and its lagrangian (2.2) are invariant under a global phase
 644 transformation.

$$\psi(x) \rightarrow \psi'(x) = \exp(-ie\alpha)\psi(x), \quad (2.3)$$

645 where α is a constant (global phase shift).

646 The same is not true when α is not a constant, but actually a local phase transformation, a gauge
 647 transform.

$$\psi(x) \rightarrow \psi'(x) = \exp(-ie\alpha(x))\psi(x) \quad (2.4)$$

648 In this case, the derivative of $\alpha(x)$ will introduce a new term that would break the invariance. To
 649 recover it, the covariant derivative operator should be modified as follows:

$$\partial_\mu \rightarrow D_\mu = \partial_\mu - ieA_\mu. \quad (2.5)$$

650 This modification introduces the concept of the gauge field A_μ , associated to a particle of spin 1
 651 and zero mass, the photon. This term should transform under gauge, in the following manner:

$$A_\mu \rightarrow A'_\mu = A_\mu - \partial_\mu \alpha(x). \quad (2.6)$$

652 Modifications 2.5 and 2.6 are sufficient not only to make the free particle Dirac Equation and its
 653 lagrangian gauge transformation invariant (Equations 2.7 and 2.8), but also it naturally gives rise
 654 to an interaction term associated to the gauge field A_μ .

$$(i\gamma^\mu \partial_\mu + m)\psi(x) = -e\gamma_\mu A_\mu(x)\psi(x) \quad (2.7)$$

²Even though, the \mathcal{L} actually represents the lagrangian density, in this document we shall refer to it as simply lagrangian.

$$\begin{aligned}\mathcal{L} \rightarrow \mathcal{L}' &= i\bar{\psi}'(x)\gamma^\mu D_\mu\psi'(x) - m\bar{\psi}'\psi'(x) \\ \mathcal{L}' &= \mathcal{L}_0 + e\bar{\psi}(x)\gamma^\mu A_\mu\psi(x) = \mathcal{L}\end{aligned}\tag{2.8}$$

655 Interesting to notice that the \mathcal{L}_0 term, on 2.8, corresponds to the electron kinetic energy plus its
 656 mass contribution (the free particle lagrangian), while the second corresponds to the interaction of
 657 the electron ($\psi(x)$) and the electromagnetic field. On this basis, e is said to be the generator of the
 658 electromagnetic four-potential, A_μ . One could add the energy contribution of the electromagnetic
 659 field itself, by adding a term like:

$$\mathcal{L}_{EM} = -\frac{1}{4}F_{\mu\nu}F^{\mu\nu},\tag{2.9}$$

where:

$$F_{\mu\nu} = \partial_\mu A_\nu - \partial_\nu A_\mu\tag{2.10}$$

660 is the electromagnetic field tensor.

661 It can be proven that applying 2.10 on the Euler-Lagrange equations, this will give us the Maxwell's
 662 Equations for the vacuum, $\partial_\mu F^{\mu\nu} = 0$ ³. One could also expect that a field mass contribution in as
 663 below, could be introduced, as well.

$$\frac{1}{2}m_{photon}^2 A_\mu A^\mu\tag{2.11}$$

664 This one would break the gauge invariance, therefore we can imply that the photon should be
 665 massless.

666 The QED is said to be a gauge theory with the symmetry group $U(1)$. The $U(1)$ description comes
 667 from Lie Algebra, where 2.5 and 2.6 are transformations of gauge α (in one dimension) to which
 668 the system is symmetric (invariant), then unitary and generated by a 1×1 matrix (e).

669 2.1.2 The Standard Model

670 Taking profit of the Local Gauge Invariance as path to introduce interactions in a quantum field
 671 theory (QFT), such as for the QED, the Standard Model can be defined as a QFT of the gauge
 672 group $SU_C(3) \times SU_L(2) \times U_Y(1)$. All the experimental results we have, so far (Section 2.2), give us
 673 support to this definition.

674 In this context there are 8 spin 1 bosons (called gluons) for the $SU_C(3)$ component, which corre-
 675 sponds to the strong interaction, plus 4 bosons, W^\pm , Z and the photon for the other components
 676 (weak and electromagnetic interactions).

677 Hadrons are defined as colorless particles that interact strongly. They are bound states of quarks,
 678 which also interact via strong force and have non-neutral color. Hadrons are divided in mesons

³A non-vacuum covariant form of the Maxwell's Equations would be $\partial_\mu F^{\mu\nu} = j^\nu$.

679 (spin integer) and barions (spin non-integer). Leptons are those particles that do not interact via
 680 gluons.

681 **Quantum Chromodinamics**

682 Quantum Chromodynamics (QCD) is the $SU_C(3)$ component of the SM, where SU stands for special
 683 unitary group, to which the $\det(e^{i\lambda_i}) = 1$, where λ_i are the Gell-Mann matrices (the 8 generators
 684 of the $SU(3)$). It corresponds to the field of gluons, responsible for the strong interaction acting
 685 on a charge-like degree of freedom: colour (c). Gluons follow the same fashion as photons, they
 686 are massless and have spin 1, but contrary to electromagnetism, the QCD is a non-abelian gauge
 687 theory. This means that the force carriers (gluons) can interact with each other (self-coupling). In
 688 other words, gluons are charged (coloured). In a more formal manner, the generators of this group
 689 are non-commutative, as follows.

$$[T_a, T_b] = \left[\frac{\lambda_a}{2}, \frac{\lambda_b}{2} \right] = i \sum_{c=1}^8 f_{ab}^c \lambda_c, \quad (2.12)$$

690 where f_{ab}^c are antisymmetric structure constants.

691 From a experimental perspective, the idea of colour begins with the observation of Λ^{++} [15]. It
 692 could be only be composed by three up quarks, which would break Pauli Exclusion Principle ⁴. This
 693 observation demanded the inclusion of another degree of freedom, the colour, typically refereed as
 694 RED, BLUE, GREEN and its anti-colours.

695 The QCD lagrangian for a quark of colour c , just the QED lagrangian for a electron of charge $-e$,
 696 is ⁵:

$$\mathcal{L}_{QCD} = \bar{\psi}_c(x) (i\gamma^\mu D_\mu - m) \psi_c(x) - \frac{G_{\mu\nu}^c G_c^{\mu\nu}}{4}, \quad (2.13)$$

where

$$D_\mu = \partial_\mu + ig_s T_c G_\mu^c \quad (2.14)$$

and

$$G_{\mu\nu}^c = \partial_\mu G_\nu^c - \partial_\nu G_\mu^c - g_s f_{ab}^c G_\mu^a G_\nu^b \quad (2.15)$$

697 This lagrangian is local gauge invariant when the strength tensor 2.15 as:

$$G_\mu^c \rightarrow G_\mu^{c'} = G_\mu^c - \frac{1}{g_s} \partial_\mu \alpha_c(x) - f_{ab}^c \alpha_a(x) G_\mu^b \quad (2.16)$$

698 Coloured particles, such as quarks and gluons, are subjected to the phenomenon of Colour Con-
 699 finement, which prohibits the direct observation of these particles. These can only be observed in
 700 colourless bound states (hadrons). A isolated quark or gluon will immediately interact with the

⁴Two or more fermion can not be in the same quantum state.

⁵The total QD lagrangian would the sum over all possible states.

vacuum and initiates a hadronization process until a set of stable colourless particle is produced. As a consequence of the Colour Confinement and the self-coupling property of gluons, a bound state of gluons, Glueballs [16], is possible, even though there are no experimental clear evidences of its existence. This is one of the few open topics in the SM.

QCD is a perturbation theory ($\mathcal{L} = \mathcal{L}_{\text{Free Particle}} + \mathcal{L}_{\text{Interaction}}$) which demands renormalization⁶. In a qualitative way, one could imagine that, as larger the distance on interaction is, more sea vacuum gluon pairs can contribute to the net colour charge, due to the self-coupling, increasing the total interaction strength. To cope the Colour Confinement and the self-coupling, one would redefine the strong coupling constant as $g_s = \sqrt{4\pi\alpha_s}$ (from 2.14, 2.15 and 2.16), where $\alpha_s(Q^2) \propto \frac{\Lambda_{QCD}^2}{\ln Q^2}$. In this situation, the coupling strength is related to the transferred momentum Q^2 , in such a way that, in a highly energetic interaction (high Q^2 , hence short distance) the coupling is weaker and the quarks and gluons involved, behave like a quasi-free particles, allowing the use of perturbation theory. This effect is known as Asymptotic Freedom, and its scale have already been measured by the LHC experiments [13].

715 Electroweak Theory

The $SU_L(2) \times U_Y(1)$ represents the Electroweak component of the SM. It is the unification of the Weak and Electromagnet interaction, under the same theory. Here two new degrees of freedom are introduced, L and Y . The former one is related to the chirality of $SU(2)$ and the latter is the weak hypercharge. The generators of groups are the Pauli Matrices (T_i)⁷, form the $SU_L(2)$ and the electromagnetic generator structure for $U_Y(1)$ (but for Y , instead of $-e$, as before). Since:

$$\begin{aligned}[T_a, T_b] &= i\epsilon^{abc}T_c, \\ [T_a, Y] &= 0\end{aligned}\tag{2.17}$$

where ϵ^{abc} is the Levi-Civita tensor, $SU_L(2)$ is also a non-abelian group.

The connection between electric charge Q and the weak charge is $\frac{Y}{2} = Q - T_3$, as such, QED ($U_{EM}(1)$), as defined in Section 2.1.1 is derived from $U_Y(1)$.

In the Electroweak Theory, fermions can have left-handed or right-handed components of their wave-functions, according to their chirality. Left-handed components transform as doublets of (T, T_3) with eigenvalues $(1/2, \pm 1/2)$ under $SU_L(2)$ and the right-handed components transform as singlets ($T = 0$). Weak interactions act only on left-handed fermions. That is the reason for the L subscript in the electroweak symmetry group definition.

⁶A techniques to deal with infinites that might arrive when calculating quantities in a QFT. In summary the total probability for the theory is required to re-sum to unity.

⁷The usual σ_i representation for the Pauli Matrices usually is reserved for the $SU_{spin}(2)$ group.

729 **Standard Model Lagrangian and the Higgs Sector**

The SM lagrangian is given by:

$$\mathcal{L}_{SM} = \mathcal{L}_{gauge} + \mathcal{L}_{fermions} + \mathcal{L}_{Yukawa} + \mathcal{L}_{Higgs}, \quad (2.18)$$

730 where \mathcal{L}_{gauge} describes gauge fields of the QCD and Electroweak theories,

$$\mathcal{L}_{gauge} = -\frac{1}{4} \sum_{c=1}^8 G_{\mu\nu}^c G_c^{\mu\nu} - \frac{1}{4} \sum_{a=1}^3 W_{\mu\nu}^a W_a^{\mu\nu} - \frac{1}{4} B_{\mu\nu} B^{\mu\nu}. \quad (2.19)$$

731 The first term is related to the $SU_C(3)$ component of the SM and last two terms are related to
732 $SU_L(2) \times U_Y(1)$ components, respectively. The summations are related to all generators in the
733 symmetry group, 8 and 3 + 1, for QCD Electroweak. Following the same structure as in 2.15:

$$\begin{aligned} W_{\mu\nu}^a &= \partial_\mu W_\nu^a - \partial_\nu W_\mu^a - g\epsilon_{abc}W_\mu^b W_\nu^c, \\ B_{\mu\nu} &= \partial_\mu B_\nu - \partial_\nu B_\mu \end{aligned} \quad (2.20)$$

For the fermionic term of the lagrangian, we have:

$$\mathcal{L}_{fermions} = \sum_j i\bar{\psi}_L^j \not{D}^L \psi_L^j + \sum_k i\bar{\psi}_R^k \not{D}^R \psi_R^k, \quad (2.21)$$

734 where the first term is summed over all T doublets (left-handed components) and the second one,
735 over all T singlets (right-handed components). The slash notation was introduced, in which $\not{d} =$
736 $\gamma^\mu a_\mu$. Here, we define the covariant derivatives as:

$$\begin{aligned} D_\mu^L &= \partial_\mu + ig \sum_{a=1}^3 T_L^a W_\mu^a + ig' \frac{Y}{2} B_\mu + ig_s T_c G_\mu^c \\ D_\mu^R &= \partial_\mu + ig' \frac{Y}{2} B_\mu + ig_s T_c G_\mu^c \end{aligned} \quad (2.22)$$

737 It is important to notice that, the weak interaction term (W_μ) is absent in the right-handed component and the QCD term of the covariant derivative is only applied to quarks. Leptons are colourless.
738
739 Since, the electroweak components of the SM are not related to flavour and charge, but rather weak
740 hypercharge and left-handed chirality, the boson that we observe experimentally (Z , W^\pm and γ)
741 are not directly related to the fields W_μ^a and B_μ . They are linear combination of them, as follows
742 (assuming $T_L^a = \sigma^a/2$, where σ^a are the Pauli Matrices):

$$W_\mu^\pm = \frac{1}{\sqrt{2}} W_\mu^1 \mp i W_\mu^2 \quad (2.23)$$

$$\begin{aligned} Z_\mu &= \cos\theta_w W_\mu^3 - \sin\theta_w B_\mu, \\ A_\mu &= \sin\theta_w W_\mu^3 + \cos\theta_w B_\mu, \end{aligned} \quad (2.24)$$

743 where θ_w is a measurable of the theory [13].

744 The SM lagrangian terms, presented so far, are clearly gauge invariant, under the proper transfor-
 745 mations. Even though this is sufficient to define the interactions, two problems arise, related to
 746 mass: the spin 1 gauge boson are, by construction, massless, which is in conflict for the measure-
 747 ments we have for Z and W^\pm [13]; if one include a mass term for the fermions, as expected from the
 748 previous discussion on the QED and QCD, this would break the gauge invariance of the symmetry.

749 To overcome these problem, another field (ϕ) is introduced. By its interaction with Electroweak
 750 bosons (Z and W^\pm), they gain mass. Also, at the same time, a Yukawa coupling term, between the
 751 new field and the fermion, is capable to give them mass, naturally. The simplest way to achieve
 752 this is by introducing a scalar field double in $SU_L(2)$, the Higgs field.

$$\phi = \begin{pmatrix} \phi^+ \\ \phi^0 \end{pmatrix} \quad (2.25)$$

753 Therefore, the Higgs contribution to the SM lagrangian is:

$$\mathcal{L}_{Higgs} = (D_\mu \phi)^\dagger (D_\mu \phi) - V(\phi), \quad (2.26)$$

where

$$D_\mu = \partial^\mu + ig \sum_{a=1}^3 T_L^a W_\mu^a + ig' \frac{Y}{2} B_\mu \quad (2.27)$$

and

$$V(\phi) = \mu^2 \phi^\dagger \phi + \lambda (\phi^\dagger \phi)^2. \quad (2.28)$$

754 The key idea behind the introduction of this field, is that, at ground state, the $SU_L(3) \times U_Y(1)$
 755 symmetry is "spontaneously" broken, hence the name usually given to this procedure Spontaneously
 756 Symmetry Break [17–22]. In this case, to preserve unitarity and to ensure the $V(\phi)$ has a global
 757 minimum, $\lambda > 0$. and μ^2 needs to be negative, in order to give mass to Z and W^\pm , otherwise, we
 758 would be adding just a scalar field of mass μ with self-coupling of strength λ , but the SM bosons
 759 would still be massless.

760 In this case, the minimum value for $V(\phi)$ is a set of degenerated states in a circle of radius $\langle \phi \rangle =$
 761 $\sqrt{\frac{-\mu^2}{2\lambda}} = \frac{v}{\sqrt{2}}$, $v = \sqrt{-\mu^2/\lambda}$ is the vacuum expectation value (VEV). Without loss of generality, one
 762 can choose a direction:

$$\phi = \frac{1}{\sqrt{2}} \begin{pmatrix} 0 \\ v \end{pmatrix} \quad (2.29)$$

⁷⁶³ assigning hypercharge $Y = 1$.

⁷⁶⁴ Once again, taking profit of the perturbation theory around the ground state (VEV), one could
⁷⁶⁵ define ⁸:

$$\phi = \frac{1}{\sqrt{2}} \begin{pmatrix} 0 \\ v + H \end{pmatrix} \quad (2.30)$$

⁷⁶⁶ Expanding the potential $V(\phi)$, as is 2.28, one gets:

$$V = \mu^2 H^2 + \frac{\mu^2}{v} H^3 + \frac{\mu^2}{4v^2} H^4, \quad (2.31)$$

⁷⁶⁷ hence, a new scalar boson (the Higgs boson) is included in the theory with mass $\sqrt{2\mu^2}$ and
⁷⁶⁸ self-couplings terms.

In the same way, expanding 2.27 and assuming $T_L^a = \sigma^a/2$:

$$(D_\mu \phi)^\dagger (D_\mu \phi) = \frac{1}{2} (\partial_\mu H)^2 + \frac{1}{8} g^2 (v + H)^2 |W_\mu^1 + iW_\mu^2|^2 + \frac{1}{8} (v + H)^2 |gW_\mu^3 - g'B_\mu|^2. \quad (2.32)$$

⁷⁶⁹ Defining the SM bosons fields as:

$$\begin{aligned} W_\mu^\pm &= \frac{1}{\sqrt{2}} (W_\mu^1 \mp iW_\mu^2) \\ Z_\mu &= \frac{gW_\mu^3 - g'B_\mu}{\sqrt{g^2 + g'^2}} \\ A_\mu &= \frac{gW_\mu^3 + g'B_\mu}{\sqrt{g^2 + g'^2}}, \end{aligned} \quad (2.33)$$

⁷⁷⁰ one can naturally infer that the introduction of the Higgs fields gave the SM bosons mass values of:
⁷⁷¹ $M_W = vg/2$, $M_Z = v\sqrt{(g^2 + g'^2)}$ and $M_A = 0$. In this context, the Weinberg angle, θ_W , is related
⁷⁷² to the SM coupling constants as:

$$\begin{aligned} \cos\theta_W &= \frac{g'}{\sqrt{g^2 + g'^2}} \\ \sin\theta_W &= \frac{g}{\sqrt{g^2 + g'^2}}. \end{aligned} \quad (2.34)$$

⁸A even more general redefinition of the Higgs field would be possible ($\phi = (\phi^+, v + H + i\chi)$), but the one proposed presents no loss of generality.

773 The missing piece of the SM lagragian (2.18) is the Yukawa components, \mathcal{L}_{Yukawa} , and how it gives
 774 the fermion masses. The procedure is quite straightforward. Start including a Yukawa coupling for
 775 each fermion to either ϕ or $\tilde{\phi} = i\sigma_2\phi^\dagger$ (this one with $Y = -1$). Taking the electron as an example:

$$\begin{aligned}\mathcal{L}_{Yuk}^e &= -\lambda_e \bar{L}\phi e_R + h.c. \\ \mathcal{L}_{Yuk}^e &= -\frac{1}{\sqrt{2}}\lambda_e(\bar{\nu}^e, \bar{e}_L) \begin{pmatrix} 0 \\ v + H \end{pmatrix} e_R + h.c \\ \mathcal{L}_{Yuk}^e &= -\frac{1}{\sqrt{2}}\lambda_e(v + H)\bar{e}_L e_R + h.c,\end{aligned}\tag{2.35}$$

776 where λ_e is the coupling constant between the Higgs boson and the electron. This tell us that
 777 $m_e = \frac{\lambda_e v}{\sqrt{2}}$.

778 Similar procedure can be used for all the fermion of the SM.

779 2.2 SM and Higgs results

780 The Standard Model have been proven extremely successful in describing what it is proposed to
 781 do. The discovery of the two highest invariant mass particles of the SM, the top quark [23, 24], by
 782 the CDF and 0 collaboration, at FERMILAB, and the Higgs Boson [4, 5], by CMS and ATLAS,
 783 at CERN, fill the two missing pieces of the SM puzzle, presented at Figure 2.1. In general, SM
 784 measurements presents very good agreement between theory and experiment, even when the Higgs
 785 boson is taken into account, once it mass has been established, the subsequent results tend to
 786 be found restricted within the expectations and constrained by the statistics and experimental
 787 sensitivity.

788 In this section, we shall briefly review some of the most relevant SM results from LHC, with special
 789 focus to Z and Higgs boson, subjects of the study.

790 2.2.1 Standard Model vector bosons at CMS

791 The success of the Standard Model relies mostly on its excellent agreement between its predictions
 792 and the measurements, even though there are still many open questions on fundamental particle
 793 physics [25], such as: How can we explain the number of fundamental particles known so far? Why
 794 matter and antimatter appear in the Universe in different proportions? What is the astrophysical
 795 dark matter? How could we unify the fundamental interactions? How to quantize gravity?

796 The Figures 2.2b, 2.2a and 2.3 presents a summary of relevant CMS results on SM measurements.
 797 The former one presents the ratio between the observed and expected cross section ($\sigma_{exp}/\sigma_{theo}$)
 798 for different di-boson production at NNLO calculations and pure electroweak processes, while the
 799 later have a summary of cross section measurements made by CMS. When theory and experiment

800 agreement is not exact, one has to take into account the experimental limitations of one experiment,
 801 such as CMS and the many possible electroweak phenomena to be studied.

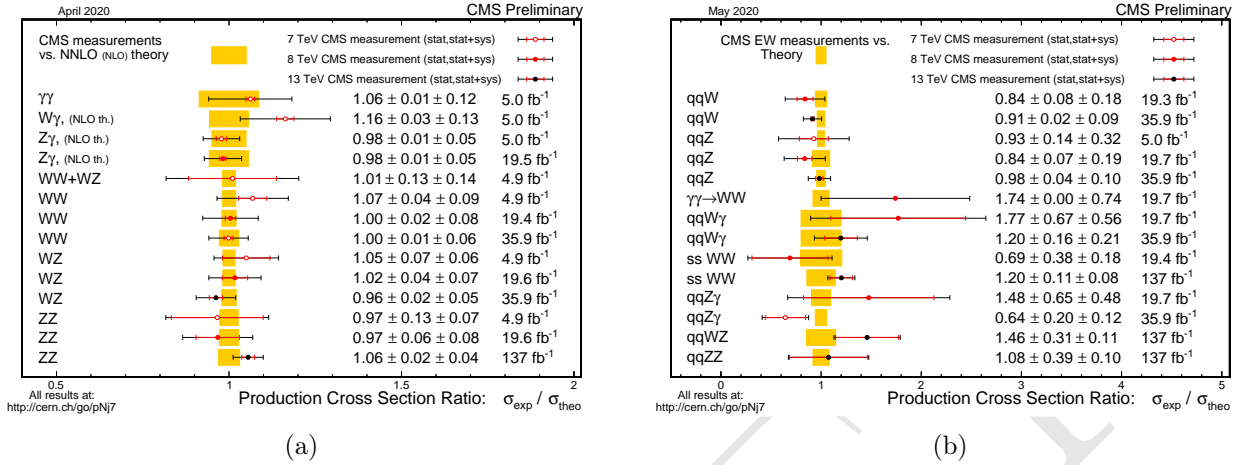


Figure 2.2: (a) Di-boson cross section ratio comparison to theory: Theory predictions updated to latest NNLO calculations where available compared to predictions in the CMS papers and preliminary physics analysis summaries. Source: [26]. (b) Summary of the cross sections of pure Electroweak (EWK) interactions among the gauge bosons presented as a ratio compared to theory. Source: [26].

802 The open questions above are not subjected to the SM scope, but even within the SM there still
 803 relevant precision measurements [27] that are important to understand the validity of the SM and
 804 what other questions lies about the SM, at the threshold of the LHC experiments precision.

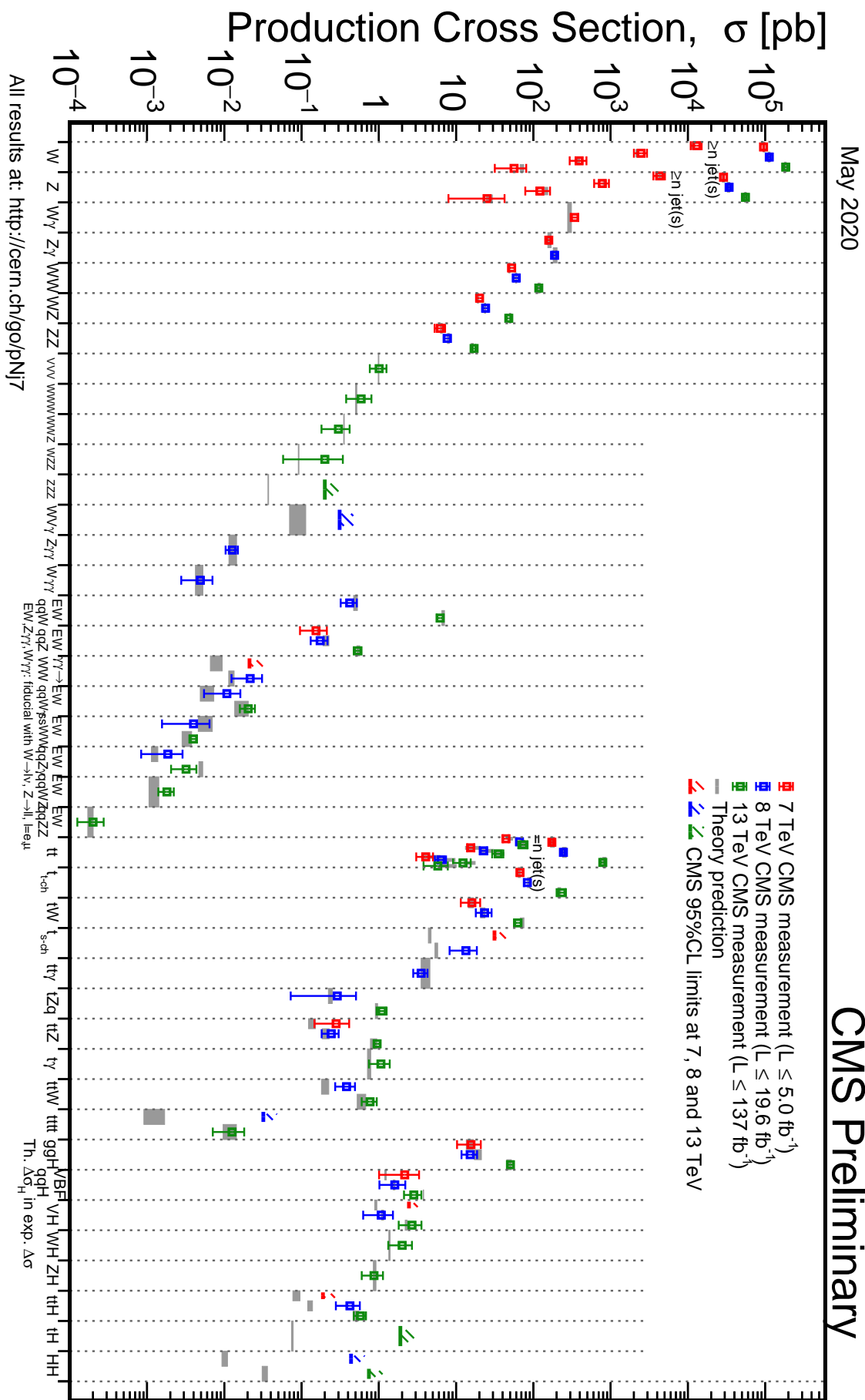


Figure 2.3: Summary of the cross section measurements of Standard Model processes at CMS. Source: [26].

2.2.2 Higgs boson at CMS

The Higgs may be produced at LHC proton-proton collisions by the following process, called **Production Modes**. *state-of-art* SM cross section predictions were computed by the "LHC Higgs Cross Section Working Group" [28] and are presented as a function of the the Higgs mass is presented at Figure 2.4a and examples of leading order Feynmann diagrams of them are presented at Figure 2.5, for the highest cross section production modes.

The **Gluon Fusion - ggF** - is the result of a gluon-gluon interaction which is mediated by a heavy quark loop. Each quark contributing is suppressed by $1/m_q^2$. It is by far the one with highest cross section. Its final state is composed only by a Higgs boson, which makes it harder to identify, since there are no other auxiliary final state particle to tag it. In this decay, QCD radiative corrections are very important and have been included the results of Figure 2.4a up to N3LO (next-to-next-to-next-to-leading order, while electroweak corrections are computed up to NNLO. The **Associated Vector Boson Production - VH** - a SM vector boson (Z or W) irradiate a Higgs. Due to its clear electroweak signature (a final state with a Higgs and a vector boson), this production mode enhances the signal, when the Higgs decay has a large contribution from QCD background, e.g. $H \rightarrow b\bar{b}$. This process is also called Higgs-Strahlung.

The third process is the **Vector Boson Fusion - VBFH** - in which the two quarks from the initial state scatter by the emission a pair of vector bosons (ZZ or $W\pm W\mp$). Those would interact (fuse) and produce a Higgs in the final, associated with two back-to-back jets, from the initial state quarks. The **Associated $t\bar{t}$ Production - ttH** - and **Associated $b\bar{b}$ Production - bbH** are very similar process (especially in the scale of $\sqrt{s} = 13$ TeV, where their cross sections almost match), where the coupling of the heavy quark to the Higgs boson, contrary to what happens in the ggF production, it is not with a virtual state of then.

The **Associated Single Top Production - tH** - is the production mode with the smallest cross section, due to its destructive interference with other process. Without loss of generality, it is not considered in this study.

The Higgs allowed **Decay Channel**, in the context of the Standard Model, is also a closet set, which have also been subject of study of the "LHC Higgs Cross Section Working Group" [28]. Figure 2.4b presents their expected branching ratios.

The largest branching fraction is the decay to a $b\bar{b}$ pair, which is, at $\sqrt{s} = 13$ TeV, more than the double of the next channel. The large cross section does not imply in being the most sensible channel for the Higgs observation. One has to take into account the experimental sensitivity to this final state (which rely on b-tagging techniques) and its enormous QCD background. Tagging on specific production modes is usually explored in this kind of study [30] to enhance the signal to background ratio. Similar to $b\bar{b}$, decays to other SM dileptons are also usually studied, such as dimuons [31], $\tau\tau$ [32] and $c\bar{c}$ [33].

Other decays include the VV state, where V is a electroweak vector boson (Z [34], W^\pm [35] and γ [36]). Even tough the branching fraction for these ones are relatively smaller, they offer a clear signature for event selection, with reduced QCD background. It is important to notice that $H \rightarrow Z\gamma$

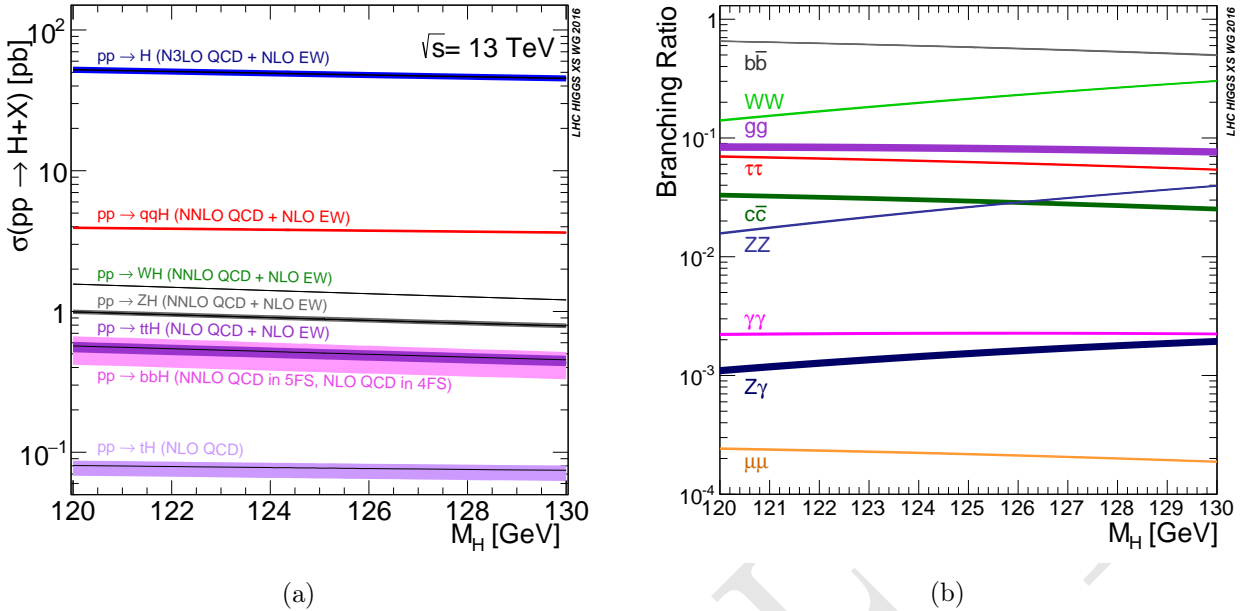


Figure 2.4: (a) Standard Model Higgs boson production cross sections at $\sqrt{s} = 13$ TeV as a function of Higgs boson mass. The tH production cross section accounts for t -channel and s -channel only (no tWH production). The VBF process is indicated here as qqH . The theoretical uncertainties are indicated as shaded bands around the lines. Source: [28]. (b) Standard Model Higgs boson decay branching ratios for different decay channels. The theoretical uncertainties are indicated as shaded bands around the lines. Source: [28].

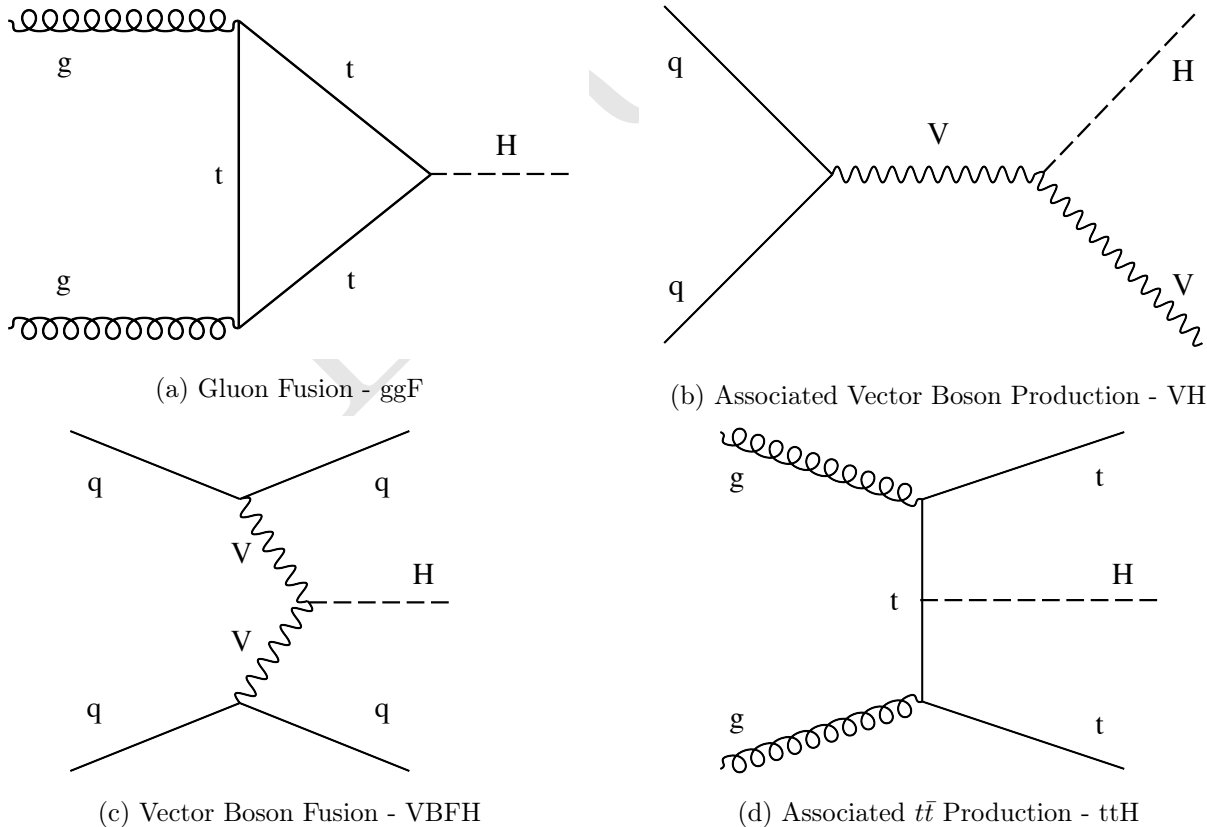


Figure 2.5: Example of leading order Standard Model Higgs boson production model diagrams. Source: [29].

also play a role in this decay mode. CMS (and ATLAS) has a very good sensitivity for leptonic final states of these bosons and for a direct measurement of photons, with resolutions to the order of 1% for the Higgs. Other channels will have resolutions larger than 10% [13].

Gluonic Higgs decays ($H \rightarrow gg$) are allowed in the Standard Model, but they would be overwhelmed by the QCD background. This is considered to be measurable only in the context of a e^+e^- detector [37].

As already mentioned on Section ??, the Higgs have been found at CMS and ATLAS in 2012, with Run1 data at $\sqrt{s} = 7$ and 8 TeV, by investigating the $H \rightarrow ZZ \rightarrow 4l$ and $H \rightarrow \gamma\gamma$ decays. Figures 2.6a and 2.6b present the reconstructed final state invariant masses that lead to its discovery. Since then, a broad program have been carried out by both, ATLAS and CMS, to extend the understanding of the Higgs boson to all accessible decays, production modes and also its properties and differential cross section.

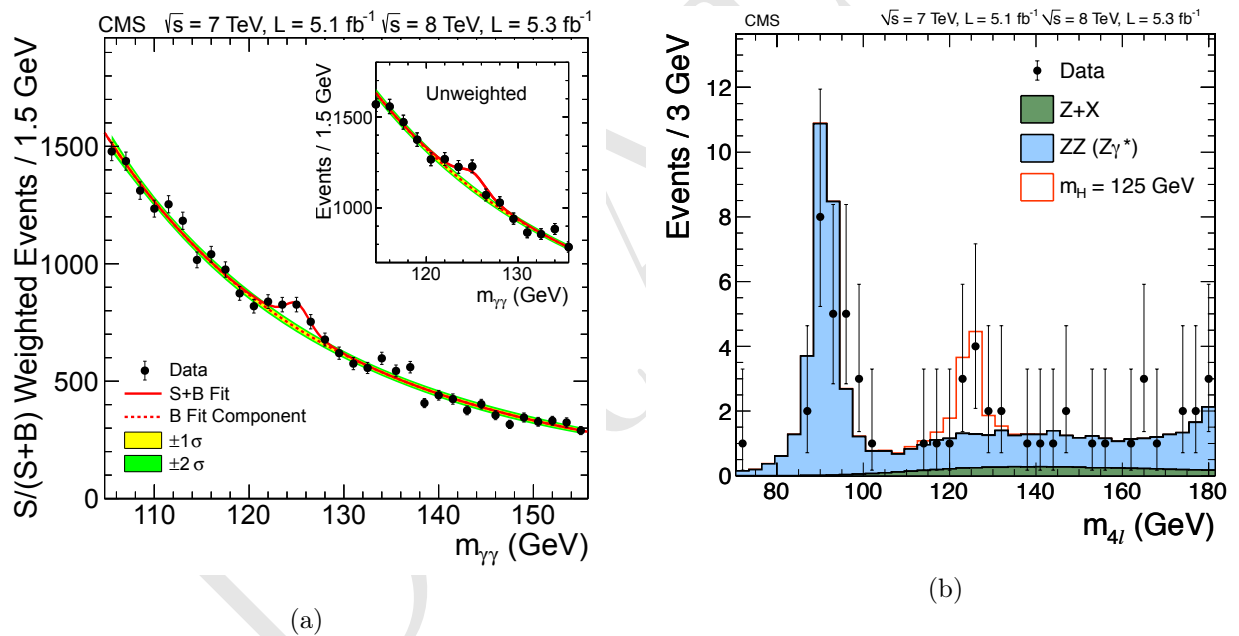


Figure 2.6: (a) The diphoton invariant-mass distribution for the 7 and 8 TeV datasets (points), with each event weighted by the predicted $S/(S + B)$ ratio of its event class. The solid and dotted lines give the results of the signal-plus-background and background-only fit, respectively. The light and dark bands represent the ± 1 and ± 2 standard deviation uncertainties respectively on the background estimate. The inset shows the corresponding unweighted invariant-mass distribution around $m_{\gamma\gamma} = 125$ GeV. Source: [4]. (b) Distribution of the observed four-lepton invariant mass from the combined 7 and 8 TeV data for the $H \rightarrow ZZ \rightarrow 4l$ analysis (points). The prediction for the expected $Z+X$ and $ZZ(Z\gamma^*)$ background are shown by the dark and light histogram, respectively. The open histogram gives the expected distribution for a Higgs boson of mass 125 GeV. Source: [4].

A complete list of Higgs publications and public result from CMS can be found at [38, 39]. With the Higgs measurements being carried out per decay channel, a important effort of combination of these results in performed independently by each collaboration, as well as joint combinations. Some of the Higgs boson measurements by CMS are summarized.

860 The signal strength modifier is the ratio of the measured cross section or branching ratio over the
 861 expected one.

$$\mu^i = \frac{\sigma^i}{\sigma_{SM}^i} \quad \mu^f = \frac{\mathcal{B}^i}{\mathcal{B}_{SM}^i}, \quad (2.36)$$

862 where σ^i and \mathcal{B}^i stand for the measured cross section and branching ratio of a certain production
 863 mode or decay channel, respectively. Figure 2.7 presents the most updated measurements of μ^i and
 864 μ^f during Run2. The overall combined strength modifier is $\mu = 1.02^{+0.07}_{-0.06}$ [40], for $m_H = 125.09$
 865 GeV, which shows very good agreement with the SM expectation.

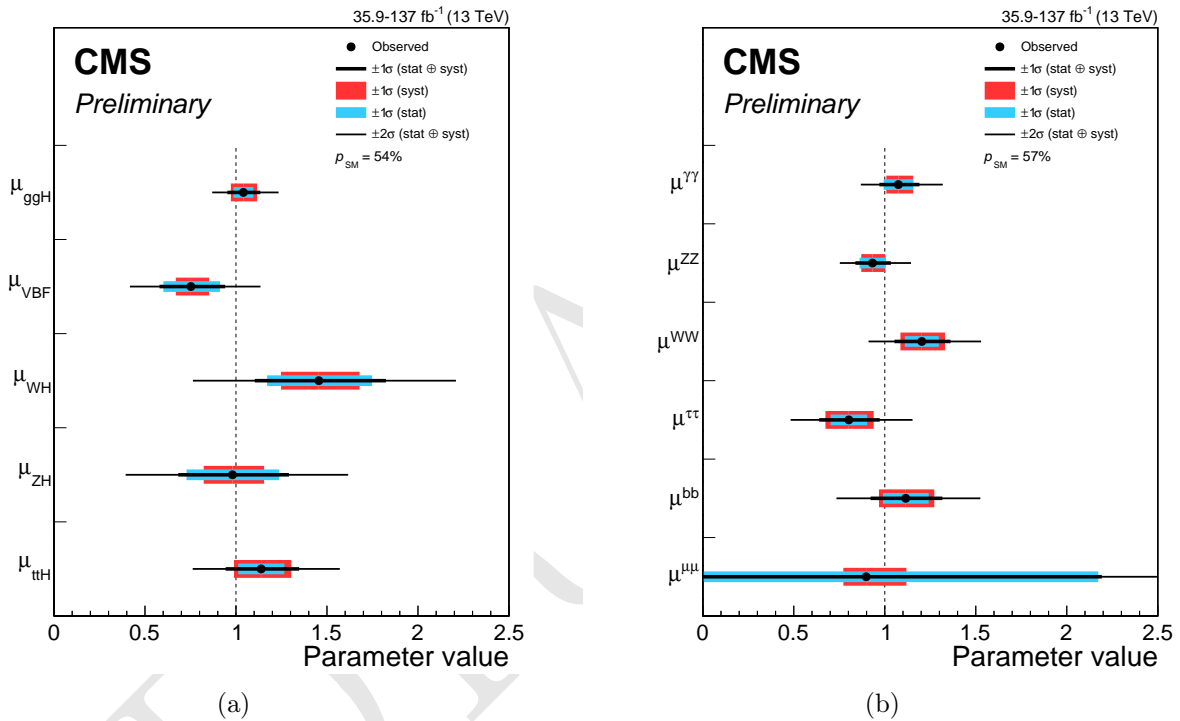


Figure 2.7: Signal strength modifiers for the production modes, (a) μ^i , and for the decay channels, (b) μ^f . The thick (thin) black lines report the 1σ (2σ) confidence intervals. The thick blue and red lines report the statistical and systematic components of the 1σ confidence intervals. Source: [40].

866 The Higgs mass was also subject of many study, here we quote the results on Figure 2.8 [36], for
 867 Run1 and partial Run2 datasets, for both $H \rightarrow ZZ \rightarrow 4l$ and $H \rightarrow \gamma\gamma$ decays. The combined
 868 measurement is $m_H = 125.38 \pm 0.14$ GeV. This is the *state-of-art* value for the Higgs mass.

869 Other properties studied comprehends its quantum numbers. The Landau-Yang theorem [41, 42]
 870 rules out the spin-1 possibility, based on its observation on the $\gamma\gamma$ channel. All the tests conducted,
 871 so far, support the $J^P = 0^+$ hypothesis [43].

872 A recent very relevant Higgs result published by CMS is the evidence of the $H \rightarrow \mu\mu$ decay [31]. In
 873 this paper it is reported an excess on data, with respect to the background only hypothesis, with
 874 3σ of significance. This is the first evidence of the Higgs coupling to second generation fermions.
 875 Figure 2.9a presents a weighted invariant mass distribution of the dimuon system ($m_{\mu\mu}$) for all the
 876 categories included in this analysis.

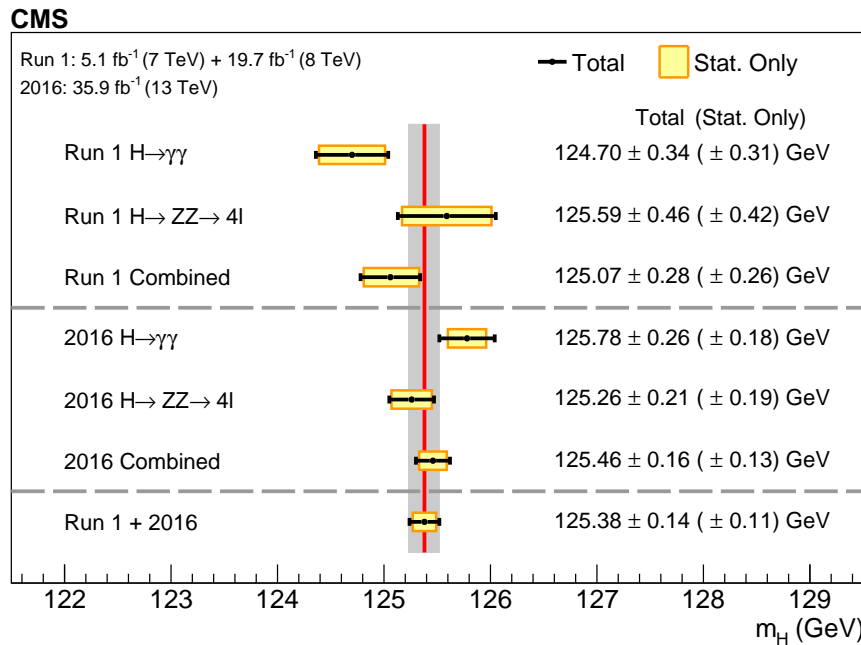


Figure 2.8: A summary of the measured Higgs boson mass in the $H \rightarrow ZZ \rightarrow 4l$ and $H \rightarrow \gamma\gamma$ decay channels, and for the combination of the two is presented here. The statistical (wider, yellow-shaded bands), and total (black error bars) uncertainties are indicated. The (red) vertical line and corresponding (grey) shaded column indicate the central value and the total uncertainty of the Run 1 + 2016 combined measurement, respectively. Source: [36].

877 The same note also updates the coupling constant modifier by combining the new results for $H \rightarrow \mu\mu$
 878 with previous Higgs results from Run2 [40]. The measured parameters are presented at Figure 2.9b
 879 and they also present very good agreement with the SM prediction, where the coupling constants
 880 to fermions is proportional to the fermion mass (M_f), while for electroweak boson, it is proportional
 881 to the square of the boson mass (M_V). The fit results are scaled to the reduced coupling strength
 882 modifiers, defined as $y_V = \sqrt{\kappa_V} \frac{m_V}{\nu}$ and $y_f = \kappa_f \frac{m_f}{\nu}$, where ν is the vacuum expectation value of
 883 the Higgs field of 246.22 GeV.

884 2.3 Rare Z and Higgs decays to quarkonia

885 The rare decays of the Higgs boson [4, 5] to a quarkonium state and a photon provide a unique
 886 sensitivity to the magnitude of the Yukawa couplings of the Higgs boson to quarks [44–46]. These
 887 couplings are difficult to access on hadronic collisions through direct decay of Higgs in quark-
 888 antiquark, due to the immense background from QCD [47].

889 Among the channels available to explore Yukawa’s couplings of light quarks [45, 46] are those with
 890 heavy-quarkonia. The rare modes of decay of the Z boson have attracted attention focused on
 891 establishing its sensitivity to New Physics [48], being configured as an alternative environment to
 892 investigate the Yukawa couplings of the Higgs boson.

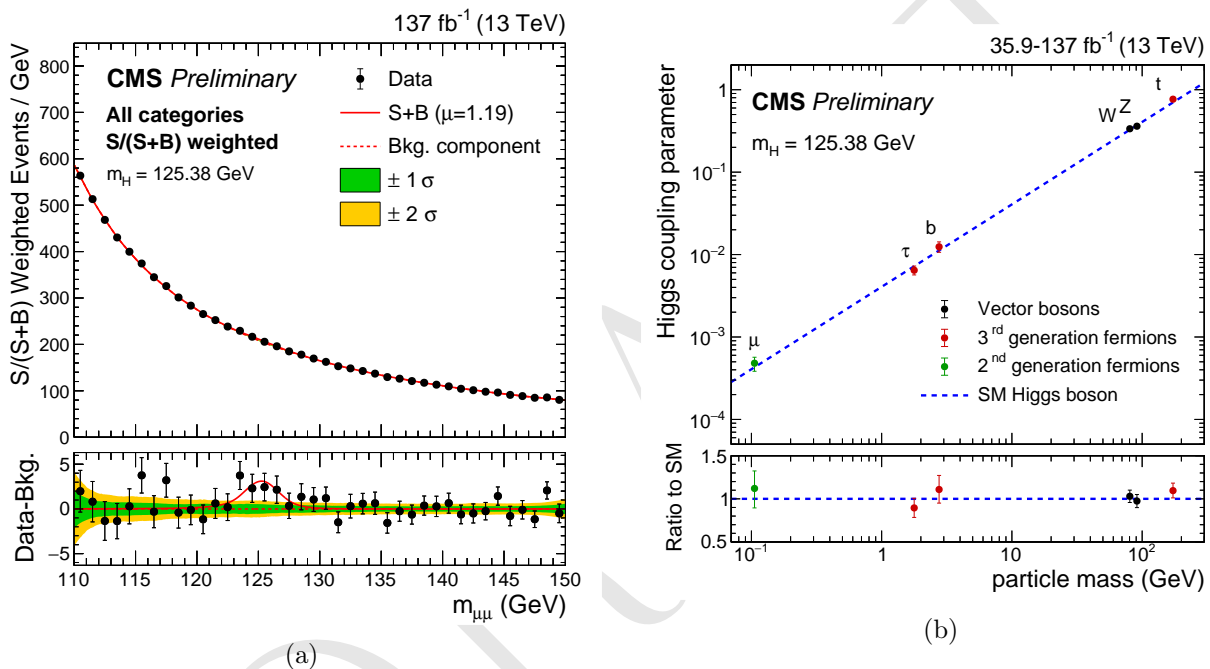


Figure 2.9: (a) The $m_{\mu\mu}$ distribution for the weighted combination of all event categories used in the analysis. The upper panel is dominated by the gluon-gluon fusion categories with many data events but relatively small $S/(S+B)$. The lower panel shows the residuals after background subtraction, with the best-fit SM $H \rightarrow \mu\mu$ signal contribution with $m_H = 125.38$ GeV indicated by the red line. The measured signal strength is $1.19^{+0.41}_{-0.39}(\text{stat})^{+0.17}_{-0.16}(\text{sys})$. Source: [31]. (b) The best-fit estimates for the reduced coupling modifiers extracted for fermions and weak bosons from the resolved κ -framework model compared to their corresponding prediction from the SM. The error bars represent 68% CL intervals for the measured parameters. The lower panel shows the ratios of the measured coupling modifiers values to their SM predictions. Source: [31].

Also, the exclusive rare decays of vector bosons (Z , W) provide a favorable environment for testing the factorization of QCD, thus allowing an approach in a context where the power of corrections are definitely under control. The main focus of this kind of analysis are the hadronic radioactive decays, $Z \rightarrow M\gamma$, where M can be a pseudoscalar or a vector meson ($J/\psi, \phi, \Upsilon_n$).

They offer the perfect way to explore some of the leading order properties of the light-cone distribution amplitudes (LCDAs) [49] of several mesons, but they present a difficulty, considering that in the LHC energy scale the branching ratio of these processes is very small. There are theoretical predictions [50, 51] that point out a branching ratio for several decay channels in the Standard Model, as shown in the Table 2.2.

Table 2.2: Summary of cross section and branching ratio for $H/Z \rightarrow \Upsilon(1S, 2S, 3S) + \gamma \rightarrow \mu^+ \mu^- + \gamma$ analysis. The effective cross-section will be discussed in section 4.1.2.

Physics Processes	Branching Ratio (BR_{SM}):
$H \rightarrow \Upsilon(1S) + \gamma$	5.22×10^{-9}
$H \rightarrow \Upsilon(2S) + \gamma$	1.42×10^{-9}
$H \rightarrow \Upsilon(3S) + \gamma$	9.10×10^{-10}
$Z \rightarrow \Upsilon(1S) + \gamma$	4.88×10^{-8}
$Z \rightarrow \Upsilon(2S) + \gamma$	2.44×10^{-8}
$Z \rightarrow \Upsilon(3S) + \gamma$	1.88×10^{-8}

Recent studies on exclusive Higgs boson decays [52–54] in final states containing a simple vector meson and a photon have caused interest in these physics topics. It was proposed to use these decays as a possible way to explore non-standard Yukawa couplings of the Higgs boson. Such measures are quite challenging in the LHC environment. The observation of hadronic decays of vector bosons provides could provide a new frontier for the nature of heavy quarkonia production in hadronic collisions.

Along the same lines, the simple exploration of rare SM decays, even in scenarios where anomalous couplings are, in principle, ruled out by direct measurements [55], as in the case of this analysis ($H \rightarrow \Upsilon(nS) + \gamma$), are still important as a stress test of the SM and as reference for future measurements. Specially the later one, when you consider that the small predicted cross sections from Table 2.2, most probably, would imply that an observation of this decay would be unlikely even in the HL-LHC [56].

This measurement is sensitive to the direct and indirect production (Figure 2.10). The *direct* process consists in the decay of boson (Higgs or Z) to a quark anti-quark pair, in which, one of the quarks radiates a photon and the pair hadronizes to a meson (a $\Upsilon(nS)$, for this study), while in *indirect* process, the decay happens to a $\gamma\gamma^*(Z)$, with the subsequent decay of the $\gamma^*(Z)$ to a quark anti-quark that hadronizes.

Clearly, only the direct process is sensible to the Yukawa coupling of the boson with the quarks, but, since both processes are indistinguishable in their final state, the in direct process needs to be taken into account. In this study, a dimuon final state is used to tag the $\Upsilon(nS)$.

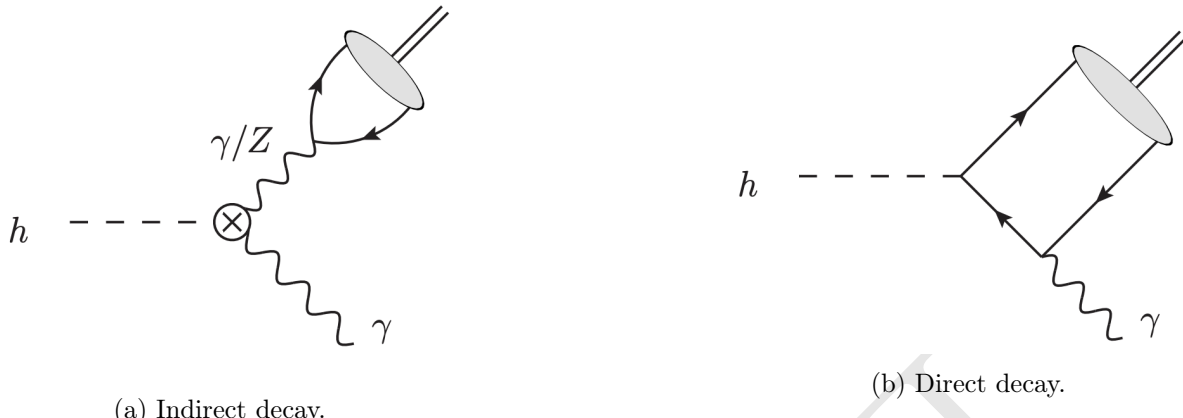


Figure 2.10: Example of leading order diagrams for the indirect and direct production mechanisms. In these diagrams, the h can also be understood as a Z or a Higgs boson.

Even though there is different theoretical predictions for the cross section of this process and its twin brother ($H \rightarrow J/\Psi + \gamma$), each one taking into account different levels of complexity, the 2013 paper [44], from G. Bodwin, F. Petriello, S. Stoynev and M. Velasco, summarizes very well and in a simpler manner, the most relevant phenomenological results on these decays. For the decay to $J/\Psi + \gamma$, the quantum interference with the indirect amplitude, enhances the directed production, leading to a larger, and potentially observable, cross section. This is not true for the $\Upsilon(nS) + \gamma$ decay, since the interference is destructive, diminishing the cross sections.

Another interesting aspect of this study is that, for both $Hc\bar{c}$ and $Hb\bar{b}$ direct coupling measurements are not sensible to the sign of the Yukawa coupling, while the presence of the indirect process in the $H \rightarrow M + \gamma$ (M standing for J/Ψ or $\Upsilon(nS)$) decays resolve this ambiguity.

Finally, since the $\Upsilon(nS) + \gamma$ decay has a much smaller cross section, because of the destructive quantum interference between direct and indirect production mechanisms, a small deviation in the $Hb\bar{b}$ Yukawa coupling, can lead a large increase in the expected branching ratio, making this channel sensible any non-Standard Model process that might interfere in this final state. This becomes clear when we look to Figure 2.11.

2.4 Recent results

The ATLAS experiment [3] already have two results on this decays [57, 58]. The first one corresponds to data taken from 2015, while the former one, corresponds to data from 2016 (the same data taking period to which this study refers).

The what concerns the most updated result, the study corresponded to 36.1 fb^{-1} at $\sqrt{s} = 13 \text{ TeV}$ and no significant excess was found by the experiment. Upper limits for the were obtained, assuming the Standard Model branching fractions predictions, at 95% confidence level, according to table 2.3.

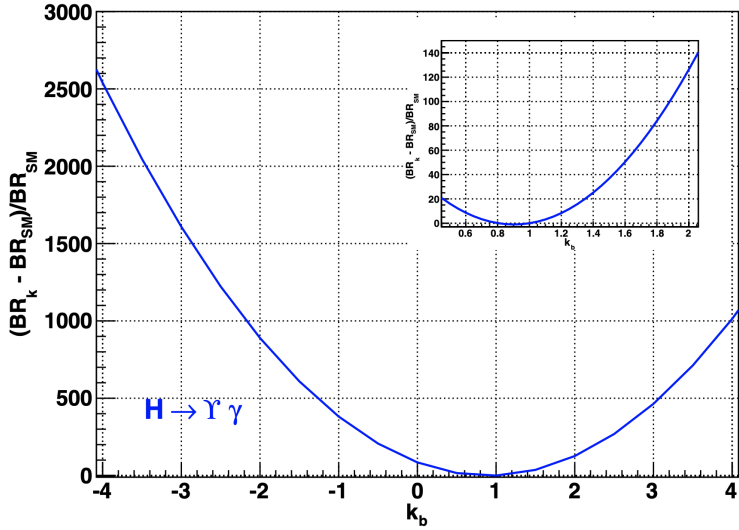


Figure 2.11: Expected relative variation of the branching ratio for the $H \rightarrow \Upsilon(nS) + \gamma$ to k_b , where $k_b = g(Hb\bar{b})/g(Hb\bar{b})_{SM}$ is the ratio for the observed and expected Yukawa coupling of $Hb\bar{b}$. Source: [44]

Table 2.3: Observed upper limits, by the ATLAS experiment, on the branching fractions for the Higgs and Z decays (last result). Detailed comparisons with the results obtained in this study will be presented in chapter 5.

Decay	$\mathcal{B}F$ at 95% CL
$H \rightarrow J/\Psi + \gamma$	$< 4.5 \times 10^{-4}$
$H \rightarrow \Psi(2S) + \gamma$	$< 2.0 \times 10^{-3}$
$H \rightarrow \Upsilon(1S) + \gamma$	$< 4.9 \times 10^{-4}$
$H \rightarrow \Upsilon(2S) + \gamma$	$< 5.9 \times 10^{-4}$
$H \rightarrow \Upsilon(3S) + \gamma$	$< 5.7 \times 10^{-4}$
<hr/>	
$Z \rightarrow J/\Psi + \gamma$	$< 2.3 \times 10^{-6}$
$Z \rightarrow \Psi(2S) + \gamma$	$< 4.5 \times 10^{-6}$
$Z \rightarrow \Upsilon(1S) + \gamma$	$< 2.8 \times 10^{-6}$
$Z \rightarrow \Upsilon(2S) + \gamma$	$< 1.7 \times 10^{-6}$
$Z \rightarrow \Upsilon(3S) + \gamma$	$< 4.8 \times 10^{-6}$

945 It is worth it to mention that the ATLAS papers present a broader analysis, including the decays
 946 to $J/\Psi + \gamma$ and $\Psi(2S) + \gamma$.

947 CMS [59] also have a result on $J/\Psi + \gamma$ and $\Psi(2S) + \gamma$ decay channel, of the Higgs and Z boson [60].
 948 The observed upper limit on the branching fraction for these decays are presented in table 2.4.

Table 2.4: Observed upper limits, by CMS, on the branching fractions for the Higgs and Z decays. The number are compatible with the ones obtained by ATLAS. The results presented for different polarization scenarios of the J/Ψ .

Channel	Polarization	$\mathcal{B}F$ at 95% CL
$Z \rightarrow J/\Psi + \gamma$	Unpolarized	$< 1.4 \times 10^{-6}$
	Transverse	$< 1.5 \times 10^{-6}$
	Longitudinal	$< 1.2 \times 10^{-6}$
$H \rightarrow J/\Psi + \gamma$	Transverse	$< 7.6 \times 10^{-4}$

949 No result on the Z and Higgs decays to $\Upsilon(nS) + \gamma$ have been published by CMS, yet.

950 The results presented here, are a subset of a broader topic related to the rare decays of Standard
 951 Model (SM) boson, involving quarkonia. Sticking only to CMS results, we can cite:

- 952 • Search for Higgs and Z boson decays to J/ψ or Υ pairs in proton-proton collisions at $\sqrt{s} =$
 953 13 TeV [61].
- 954 • Observation of the $Z \rightarrow \psi\ell^+\ell^-$ decay in pp collisions at $\sqrt{s} = 13$ TeV [62]. This one specifically,
 955 is the first observation a such decay, involving a Z boson.
- 956 • Search for decays of the 125 GeV Higgs boson into a Z boson and a ρ or ϕ meson [63].

957 3 Experimental Setup

958 This chapter describes the experimental setup used in this study, for the sake of brevity, it is provided
959 a brief descriptions of the Large Hadron Collider (LHC), the Compact Muons Solenoid (CMS), and
960 its subdetectors, and the process of high-level physics objects processing and reconstruction.

961 3.1 The Large Hadron Collider

962 The Large Hadron Collider (LHC) is the world largest and powerful particle accelerator for protons
963 and heavy-ions ever build. It is located in a complex of other accelerator operated by the European
964 Organization for Nuclear Research (CERN), in the border of between Switzerland and France.
965 The LHC is built in the same 26.7 km extension tunnel with depth varying from 45 m to 170
966 m below the surface (the LHC plane is tilted 1.4% for construction reasons), once used by Large
967 Electron–Positron Collider. The CERN complex is a composition of many accelerators, for proton
968 and heavy-ions, used to provide beams of particles for smaller experiments and as a sequence of
969 injectors for the LHC. Figure 3.1 presents the many components of the LHC complex of accelerators.
970 A detailed description of the LHC can be found at [64–67].

971 A LHC section is composed of two vacuum pipes, in which the bunch of particles travels in opposite
972 directions. This means that both beams are magnetically coupled by the same super-conducting
973 magnetic system, saving space and allowing the use of the pre-built LEP tunnel. The particle
974 acceleration is made by Resonant Cavities [69]. Those cavities apply to each beam a set of radio-
975 frequencies (RF) used to transfer energy by means of a 2 MV electric potential per cavity, at a
976 revolution frequency of 400.789 MHz. The acceleration is applied to bunches of particles. The
977 bunch configuration depends of the injection mode (configurable), but a typical pp injection would
978 be composed by 2808 bunches of 1.1×10^{11} protons each. Proper timing of the bunches injection
979 and the RF is a key factor for an efficient energy transfer inside the RF cavities. The cavities also
980 are operated in low temperatures of 4.5 K, to ensure superconducting properties and reduce energy
981 losses.

982 The nominal time spacing between each bunch (bunch crossing - BX) is 25 ns. This defines the
983 clock frequency of the LHC at $f_{LHC} = 400$ MHz. This frequency is propagated to all experiments
984 and used as a reference for timing and synchronization.

985 In certain positions, called the interaction points (IP), those two bunches are allowed to cross, possi-
986 bility the particle collisions. The experiments on the LHC are located in those interaction points.
987 ATLAS (A Toroidal LHC ApparatuS) [3] and CMS (Compact Muon Solenoid, better explained in

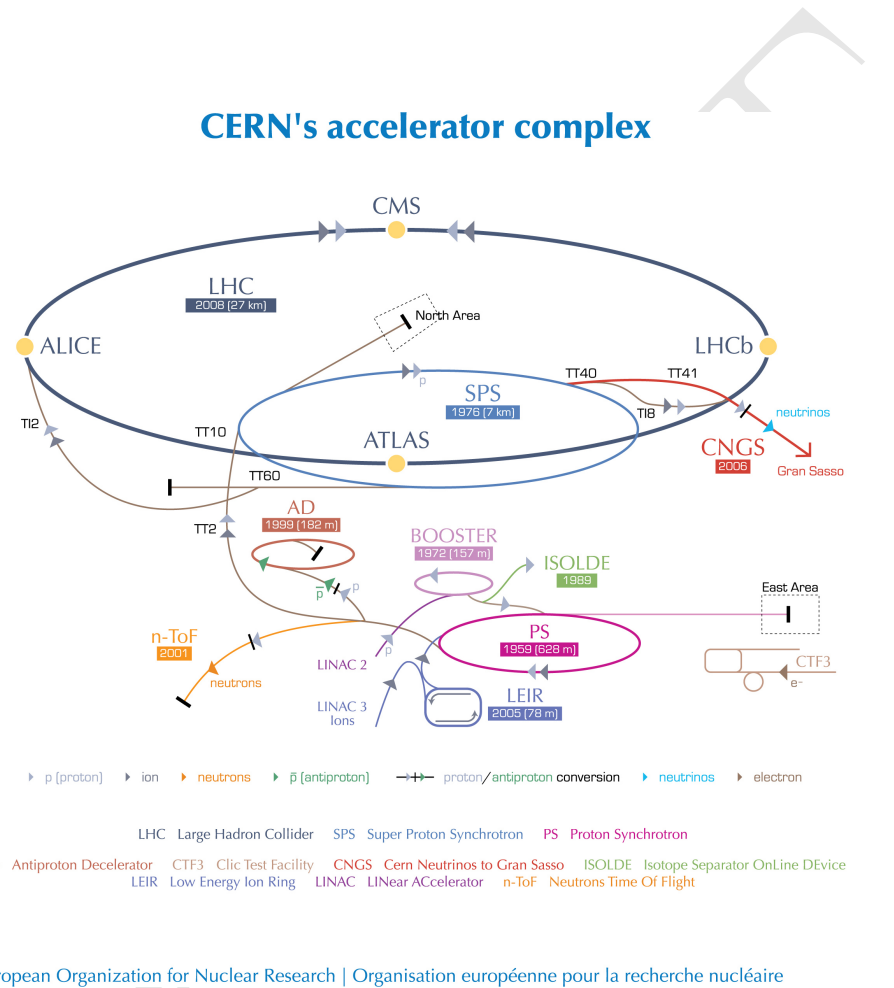


Figure 3.1: The LHC is the last ring (dark grey line) in a complex chain of particle accelerators. The smaller machines are used in a chain to help boost the particles to their final energies and provide beams to a whole set of smaller experiments. Source: [68].

the next section), at P1 and P5, respectively, are so called general proposes experiments, with focus on different aspects of a particle interactions in the LHC energy scale, including extensive test of known Standard Model process (in high and low transverse momentum regime), including the Higgs sector and Heavy Flavour Physics (phenomena involving the hadrons composed by c and b quarks), exploration of Beyond Standard Model (BSM) phenomena, as well as an competitive program in heavy-ions collisions. The LHCb (Large Hadron Collider beauty) [70] is a experiment devoted, mostly, to precision measurements of CP violation and rare decays of B hadrons. The ALICE (A Large Ion Collider Experiment) [71] experiment is dedicated to the study of p - Pb and Pb - Pb collisions and processes such as QCD, strongly interacting matter and the quark-gluon plasma at extreme values of energy density and temperature.

The number of events of a certain kind i , per unit of time, is given by Equation 3.1.

$$\frac{dN^i}{dt} = \sigma^i \mathcal{L}, \quad (3.1)$$

where σ^i is the cross-section for a certain process i and \mathcal{L} is the instantaneous luminosity delivered by the LHC.

In order to accumulate as much statistics as possible, in the shortest amount of time (for the most efficiently use of the resources available, including person-power), the luminosity is a key factor in the exploration of the collisions. This is dependent of the number of particles per bunch, number of bunches per beam, revolution frequency, form factors of the bunches, crossing angles at the interaction points and correction factors to address relativistic and electromagnetic associated phenomena. For pp collisions, the LHC aims peak luminosities of, for ATLAS and CMS, around $2 \times 10^{34} \text{ cm}^{-2} \text{ s}^{-1}$. For future upgrades of the LHC (called HL-LHC [72]), the peak luminosity might increase 10 times, allowing an accumulated luminosity ¹ of 3000 fb^{-1} .

The LHC can collide protons with center-of-mass energy \sqrt{s} up to 14 TeV. Different energy configurations have been used so far, historically increasing the energy. For the operation cycle used in this study (Run2, from 2015 to 2018), the machine was producing collisions at $\sqrt{s} = 13 \text{ TeV}$. For the next operation cycle (Run3), to start in 2022, it is expected that the LHC might reach the 14 TeV energy values.

3.2 The Compact Muon Solenoid - CMS

The Compact Muon Solenoid (CMS) is a multiple purpose experiment used to investigated pp as well as lead-lead collisions at the LHC. It is operated by the CMS Collaborations, composed by around 5000 researches and 20 institutes ². The CMS is located in the city of Cessy, France, 100 below the surface. The CMS apparatus has an overall length of 22m, a diameter of 15m, and weighs 14 000 tonnes. A detailed description of the CMS detector, can be found in [2]. Figure 3.2 presents a sketch of CMS and its subdetectors.

¹Accumulated (or integrated) luminosity is defined as $L = \int \mathcal{L} dt$.

²It is important to stress that CMS is a collaboration of institutes, not researches.

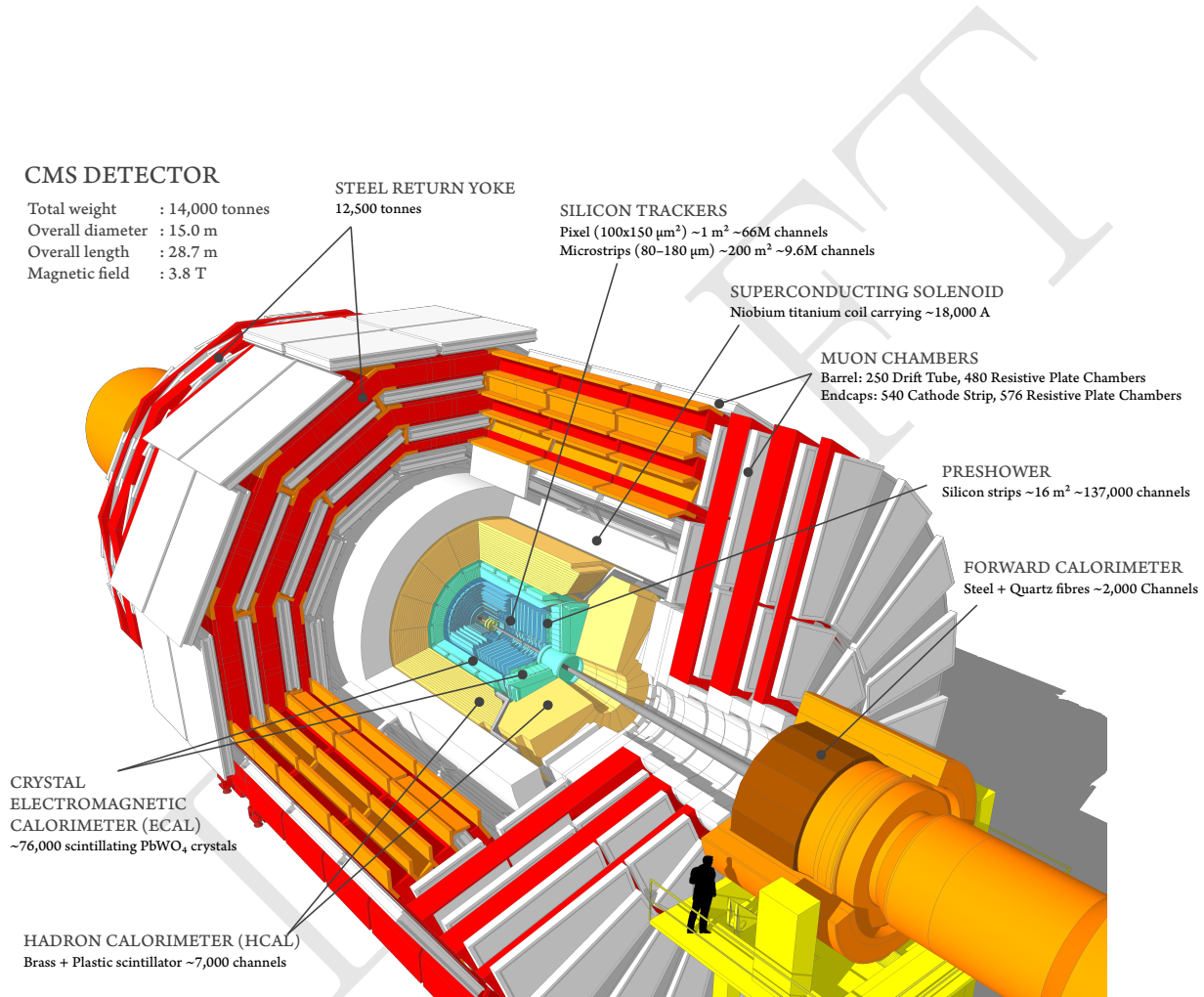


Figure 3.2: Overview of the CMS experiment and its subdetectors. Source: [73].

1021 The central feature of the CMS apparatus is a superconducting solenoid of 6 m internal diameter,
 1022 providing a magnetic field of 3.8 T. Within the solenoid volume are a silicon pixel and strip tracker,
 1023 a lead tungstate crystal electromagnetic calorimeter (ECAL), and a brass and scintillator hadron
 1024 calorimeter (HCAL), each composed of a barrel and two endcap sections. Forward calorimeters ex-
 1025 tend the pseudorapidity coverage provided by the barrel and endcap detectors. Muons are detected
 1026 in gas-ionization chambers embedded in the steel flux-return yoke outside the solenoid.

1027 The following sections describes the subdetectors, mentored above, and the CMS coordinate system,
 1028 as well as some important variables.

1029 3.2.1 Coordinate system

1030 CMS uses a right-handed coordinate system, with the origin at the nominal interaction point, the
 1031 x axis pointing to the centre of the LHC ring, the y axis pointing up (perpendicular to the LHC
 1032 plane), and the z axis along the anticlockwise-beam direction. The polar angle θ is measured from
 1033 the positive z axis and the azimuthal angle ϕ is measured in the x - y plane.

1034 It is important to define some key variables for CMS, in this study. The rapidity is defined as in
 1035 Equation 3.2, bellow.

$$y = \frac{1}{2} \ln \left(\frac{E + p_z}{E - p_z} \right), \quad (3.2)$$

1036 where E is the energy of the object and p_z is the momentum ov the objects along the z direction.
 1037 The difference between the rapidity of two objects is known for being a lorentz invariant under a
 1038 boost.

1039 A usually more suitable variable is the pseudorapidity, which is the rapidity in the relativistic limit
 1040 of $E \gg m$.

$$\eta = -\ln \left[\tan \left(\frac{\theta}{2} \right) \right], \quad (3.3)$$

1041 where θ is the angle between the transverse plane to the beam line (x - y plane) and the positive z
 1042 direction. The convenience of using the pseudorapidity is its direct connection with the geometry
 1043 of the event by the θ angle.

1044 Spatial distance, at CMS, usually is measured based on the η - ϕ space. In this sense the distance
 1045 ΔR between two objects is defined as:

$$\begin{aligned} \Delta R &= \sqrt{(\Delta\eta)^2 + (\Delta\phi)^2} \\ &= \sqrt{(\eta_1 - \eta_2)^2 + (\phi_1 - \phi_2)^2} \end{aligned} \quad (3.4)$$

1046 One last important variable is the transverse momentum component, computed as in Equation 3.5

$$\begin{aligned} p_T &= \sqrt{p_x^2 + p_y^2} \\ &= |\mathbf{p}| \cos(\theta) \end{aligned} \quad (3.5)$$

1047 3.3 Tracker

1048 The tracker is the closest subdetector to the interaction point, with 5.8 m length and 2.5 m
 1049 diameter cylinder. The silicon tracker measures charged particles within the pseudorapidity range
 1050 $|\eta| < 2.5$. The challenge of this subdetector is to cope with the high efficiency demanded for the
 1051 secondary vertices identification for long lived particles and initial momentum measurement, the
 1052 required radiation hardness for being close to the interaction point and the expected resolution
 1053 demanded to deal with the high multiplicity of a pp collisions, specially in the high pileup ³ regime.
 1054 It consists of 1440 silicon pixel and 15 148 silicon strip detector modules, as in Figure 3.3. For
 1055 non-isolated particles of $1 < p_T < 10$ GeV and $|\eta| < 1.4$, the track resolutions are typically 1.5% in
 1056 p_T and 25–90 (45–150) μm in the transverse (longitudinal) impact parameter [74].

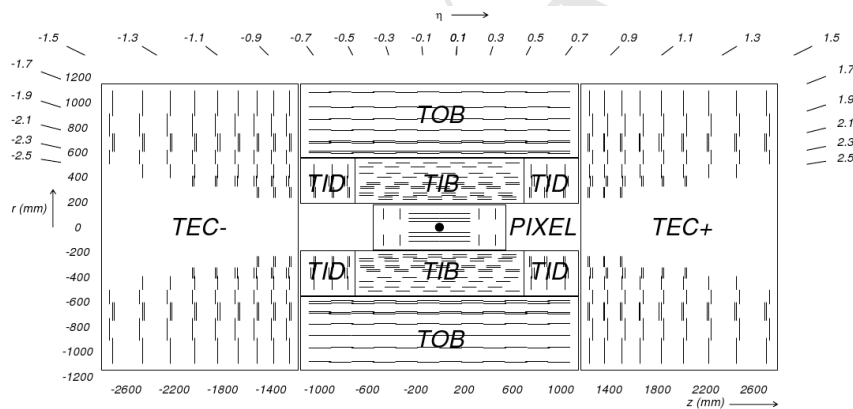


Figure 3.3: Schematic cross section through the CMS tracker. Each line represents a detector module. Double lines indicate back-to-back modules which deliver stereo hits. Source: [2].

1057 The pixel detector consists of 3 layers ⁴ on the barrel region and 4 layers on the endcap ⁵. The pixel
 1058 is located in a region of 20 cm from the beam pipe.

1059 Each pixel sensor has 100 by $150 \mu\text{m}^2$. The silicon strips detector covers a area of $\approx 200\text{m}^2$ with
 1060 9.3×10^6 channels. It is the largest silicon detector covered area ever built. It is divided in Tracker
 1061 Inner Barrel (TIB), with length of 130 cm covering the central part of the detector, the Tracker

³Each LHC collision recorded by CMS, is composed not by a single pp interaction, but by bunches of protons crossing each other. In this case, a hard interaction is actually surrounded by many soft interaction between adjacent protons. The extra activity produced in these interactions, and caught by the detector, is called **pileup** and has its signal mixed with the hard one.

⁴After 2017, the pixel received one more layer, but this irrelevant to the context of this study, since the data analyzed was collected during 2016.

⁵From 2017, another layer on each side was added.

- 1062 Inner Disks (TID) at the inner endcap, both are surrounded by the Tracker Outer Barrel (TOB)
 1063 on the barrel, and the Tracker Endcap (TEC).
 1064 The tracker is essential for a proper muon measurement in this study.

1065 **3.4 Electromagnetic Calorimeter**

1066 The Electromagnetic Calorimeter (ECAL) is responsible for absorb (and measure) the energy of
 1067 photons and electrons produced as final state particles of the collisions. The ECAL consists of
 1068 75 848 lead tungstate ($PbWO_4$) crystals, which provide coverage in pseudorapidity $|\eta| < 1.48$ in a
 1069 barrel region (EB, $2.2 \times 2.2 cm^2$ and a length of 23 cm) and $1.48 < |\eta| < 3.0$ in two endcap regions
 1070 (EE, $2.86 \times 2.86 cm^2$ front cross section and 22 cm long). Preshower detectors consisting of two
 1071 planes of silicon sensors interleaved with a total of $3X_0$ of lead are located in front of each EE
 1072 detector [75], as shown in Figure 3.4.

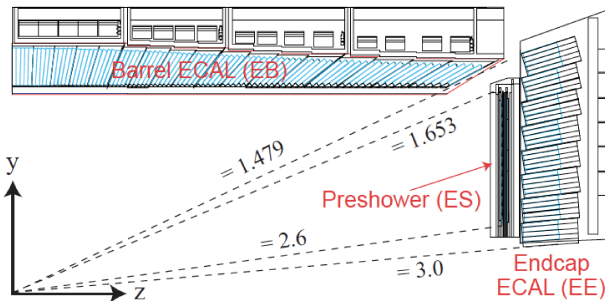


Figure 3.4: Longitudinal section view of the ECAL and its components. Source: [2].

1073 When a electron (or photon) enters the high density region of the lead tungstate crystals ($8.3 g/cm^3$),
 1074 it initiates a cascade effect of pair production and photon emission via bremsstrahlung. The intensity
 1075 of light produce is proportional to the energy of the particle adsorbed. With radiation length ⁶ of
 1076 0.89 cm and a small Molière radius (2.2 cm) the ECAL was built with compact size and its fine
 1077 granularity. The preshower, located in front of the endcap ECAL (EE), is used to distinguish from
 1078 high momentum photons and pair of photons coming from π^0 decays, highly boosted, in such a way
 1079 that they would be indistinguishable one from the other. Its first layer is composed oh the lead
 1080 tungstate crystal, followed by silicon strip sensor, that allow to measure the shape of the initiated
 1081 cascade on the first layer and correlate this with the source of the radiation.

1082 Each ECAL crystal is isolated by a carbon fiber layer and it is connected to two photodetectors
 1083 with a gain of 50. Their signal is collected by a ADC (Analog to Digital Converter) which catches
 1084 the charge from the photodetectors and convert it to a digital signal.

1085 In the barrel section of the ECAL, an energy resolution of about 1% is achieved for unconverted
 1086 or late-converting photons that have energies in the range of tens of GeV. The remaining barrel
 1087 photons have a resolution of about 1.3% up to a pseudorapidity of $|\eta| = 1$, rising to about 2.5% at
 1088 $|\eta| = 1.4$. In the endcaps, the resolution of unconverted or late-converting photons is about 2.5%,

⁶Distance an electron or a photon travels until its energy is reduced by a factor of $1/e$.

1089 while the remaining endcap photons have a resolution between 3 and 4% [76]. When combining
 1090 information from the entire detector, the jet energy resolution amounts typically to 15% at 10 GeV,
 1091 8% at 100 GeV, and 4% at 1 TeV, to be compared to about 40%, 12%, and 5% obtained when the
 1092 ECAL and Hadronic Calorimeter (HCAL) alone are used.

1093 Due to its responsibility on photon and electrons identification, the ECAL had a very important
 1094 role on the Higgs observation, specially concerning its relation with the $\gamma\gamma$ and 4-leptons finals
 1095 states of the discovery.

1096 3.5 Hadronic Calorimeter

1097 The Hadronic Calorimeter (HCAL) is devoted to absorb and measure the energy of final states
 1098 hadrons. Together with the ECAL, it plays a key role on the jet reconstruction and missing energy
 1099 measurement. It is the last subdetector until the magnet coil and, as much as possible, tries to cover
 1100 the largest pseudorapidity region in order to enhance the missing transverse energy identification. It
 1101 is composed by layers of brass and steel, interleaved with plastic scintillators, with 3.7 mm thickness
 1102 each, in order to leave as much as possible space for the absorptive materials. This allows, once a
 1103 hadron hit the material, the formation of hadronic cascades. These cascades are detected by the
 1104 scintillators which emits light proportional to the amount of energy deposited.

1105 The HCAL is divided in 4 components, the HB (barrel) 9 m long in the central region

1106 In the region $|\eta| < 1.74$, the HCAL cells have widths of 0.087 in pseudorapidity and 0.087 in azimuth
 1107 (ϕ), corresponding to 5 to 10 interaction lengths. In the η - ϕ plane, and for $|\eta| < 1.48$, the HCAL
 1108 cells map on to 5×5 arrays of ECAL crystals to form calorimeter towers projecting radially outwards
 1109 from close to the nominal interaction point. For $|\eta| > 1.74$, the coverage of the towers increases
 1110 progressively to a maximum of 0.174 in $\Delta\eta$ and $\Delta\phi$. Within each tower, the energy deposits in
 1111 ECAL and HCAL cells are summed to define the calorimeter tower energies, which are subsequently
 1112 used to provide the energies and directions of hadronic jets. Figure 3.5 shows a longitudinal view
 1113 of the HCAL.

1114 Jets are reconstructed offline from the energy deposits in the calorimeter towers, clustered using the
 1115 anti- k_T algorithm [77, 78] with a distance parameter of 0.4. In this process, the contribution from
 1116 each calorimeter tower is assigned a momentum, the absolute value and the direction of which are
 1117 given by the energy measured in the tower, and the coordinates of the tower. The raw jet energy
 1118 is obtained from the sum of the tower energies, and the raw jet momentum by the vectorial sum of
 1119 the tower momenta, which results in a nonzero jet mass. The raw jet energies are then corrected to
 1120 establish a relative uniform response of the calorimeter in η and a calibrated absolute response in
 1121 transverse momentum p_T .

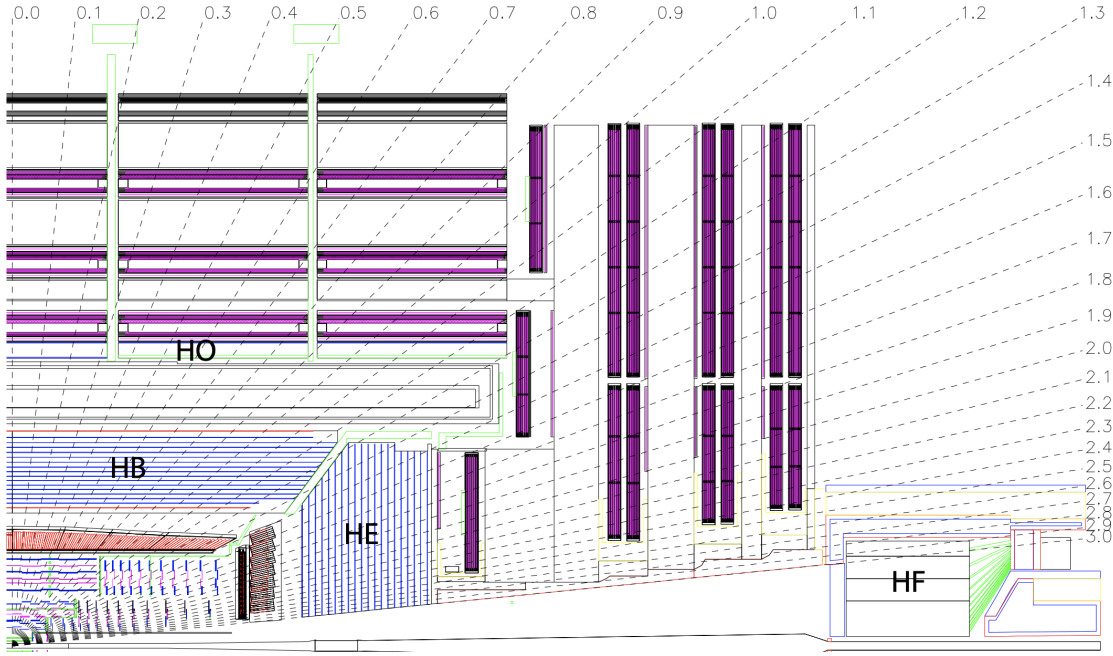


Figure 3.5: Longitudinal section view of the HCAL and its components. The barrel calorimeter (HB) covers the central region, inside the solenoid, the outer calorimeter covers also the central region, but it is positioned on the outside the solenoid. The endcap calorimeter (HE) covers the forward region and it is complemented by the forward calorimeter (HF), which uses Cherenkov light detectors made of radiation-hard quartz fibers. Source: [2].

3.6 Muon System

Muons at CMS [79] are measured in the pseudorapidity range $|\eta| < 2.4$, with detection planes made using three technologies: drift tubes, cathode strip chambers, and resistive plate chambers, as presented in Figure 3.6. The single muon trigger efficiency exceeds 90% over the full η range, and the efficiency to reconstruct and identify muons is greater than 96%. Matching muons to tracks measured in the silicon tracker results in a relative transverse momentum resolution, for muons with p_T up to 100 GeV, of 1% in the barrel and 3% in the endcaps. The p_T resolution in the barrel is better than 7% for muons with p_T up to 1 TeV [80].

The muon detection system has around 1 million channels. For Run3, the muon system is being expanded and upgraded, by the inclusion of new chamber with the Gas Electron Multiplier (GEM) [82] technology.

3.6.1 Drift Tubes

The Drift Tubes (DT) [83] is a gaseous detector (85% Ar and 15% CO₂) installed in the central region of CMS (Barrel), covering the region of $|\eta| < 1.2$. The barrel is divided in 5 wheels, along z , W+2, W+1, W0, W-1 and W-2. Each wheel is composed by four concentric stations along r , MB 1 to MB4, and each station is divided in 12 sectors along ϕ , S01 to S12. In total, there are 205 DT

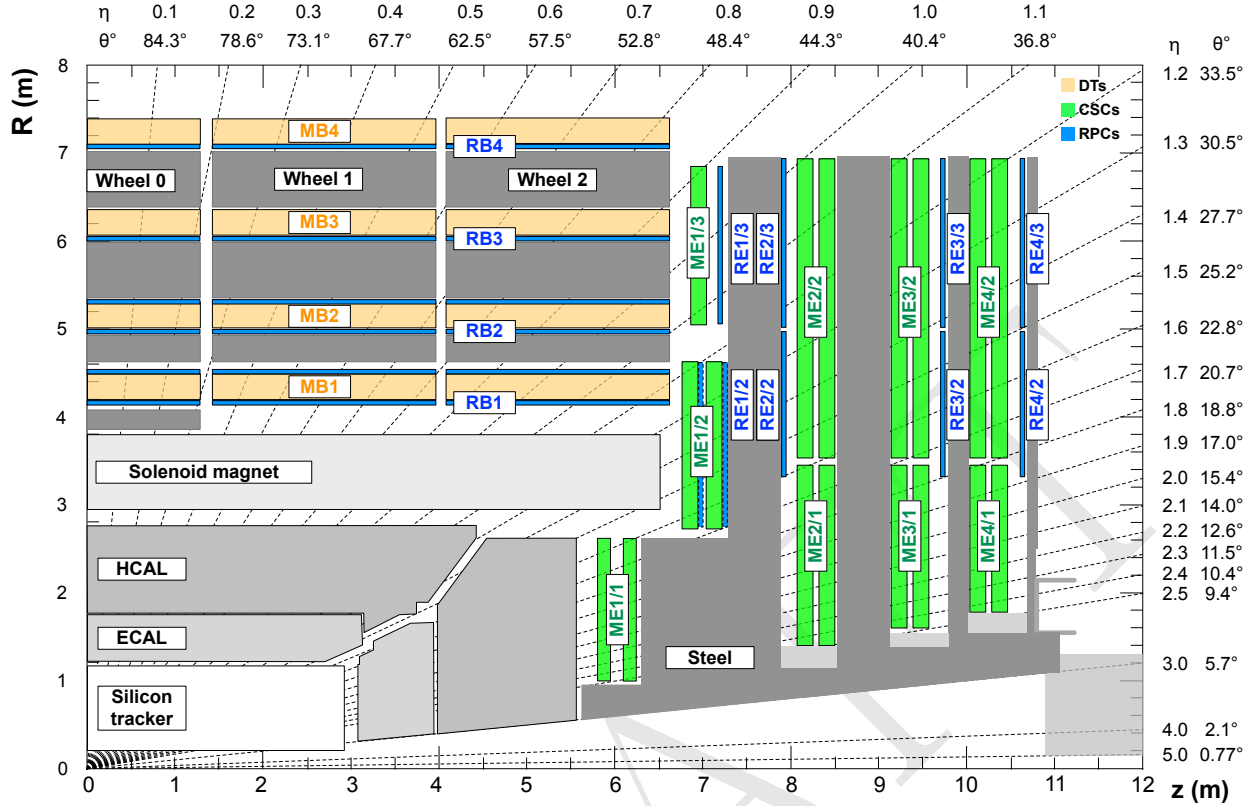


Figure 3.6: Longitudinal section view of the ECAL and its components. Source: [81].

1138 chambers. Each tube has $50 \mu\text{m}$ tick (diameter) gold-plated stainless steel wire, as well as, kept at
 1139 positive voltage, and aluminum electrodes. The signal is read on the golden wire only.

1140 The tubes are arranged in layers and occupy the whole length of the chamber. The tubes are
 1141 arranged in coaxial layers. Each set of three layers, forms a Super-Layer (SL).The first and the
 1142 last SL are aligned in the, so called, $r - \phi$ direction, while the middle one, in the $r - z$ direction,
 1143 transversal to the previous one. This arrangement give the DTs, the possibility to measure the
 1144 passage of a muon in η and ϕ direction, with a resolution of $100 \mu\text{m}$.

1145 3.6.2 CSC

1146 The Cathode Strip Chamber (CSC) is also a gaseous detector (50% CO₂, 40% Ar, and 10% CF₄) of
 1147 the Muon System which covers the endcap region, up to $|\eta| < 2.4$ composed by wires perpendicular
 1148 to η (radial measurement) and strips along η , the former operating at 3.9 to 3.6 kV. With 8.4 to 16
 1149 mm strip width and a wire-distance of 2.5 to 3.16 mm depending on their location, they provide a
 1150 75 to 150 μm resolution.

1151 They are installed in four layers (or disk) on each side of CMS, with each disk divided in up to
 1152 three rings.

1153 **3.6.3 RPC**

- 1154 The Resistive Plate Chambers (RPC) is the only muon detection technology present in both barrel
1155 and endcap. It has very good timing resolution and it is used mostly for triggering.
1156 Due to the particularities of the study, especially the contributions given to the RPC project of
1157 CMS, Chapter 6 is devoted exclusively to this subdetector.

1158 **3.7 Trigger and Data Acquisition**

- 1159 The LHC collides protons at 40 MHz. To process and save this amount of information would be
1160 unmanageable. To deal with the high rate of readouts generated by the collisions and nuclear back-
1161 ground (around 950 TB/s) CMS uses a two-tiered trigger system [84]. The first level (L1), composed
1162 of custom hardware processors, uses information from the calorimeters and muon detectors, in the
1163 form of the so called trigger-primitives, to select events at a rate of around 100 kHz within a time
1164 interval of less than 4 μ s. The L1 trigger relies on the processing of the optical links, coming
1165 CMS subdetector by FPGAs (Field Programmable Gate Array) processors. This combination of
1166 technologies allows the maximum speed in the readout information processing.
1167 The second level, known as the high-level trigger (HLT), consists of a farm of processors running a
1168 version of the full event reconstruction software optimized for fast processing, and reduces the event
1169 rate to around 1 kHz before data storage.
1170 Both triggers systems are designed to quickly identify the events ⁷ that have a specific set of
1171 signatures of interesting physics, to the context of CMS. As an example, events with characteristics
1172 of the historically widely studied soft-diffraction, are mostly (but not fully) discarded.
1173 Once a event is read by CMS, it is categorized in one or many of the defined "triggers". Each trigger
1174 is composed by a minimum sets of requirements, e.g. a single isolated muon trigger is defined as "at
1175 least one muon, well isolated from any other detector relevant activity, above a minimum transverse
1176 momentum threshold". If a event falls into a L1 trigger definition and passes the prescaling ⁸ of
1177 that trigger, a "L1 Accept" (L1A) optical signal is propagated to all subdetectors readout hardware
1178 and the information is injected into the Data Acquisition (DAQ) system and saved at the local
1179 computing cluster, the HLT. This decision process takes around 3.2 μ s. Saved events are processed
1180 by an optimized version of the Particle-Flow algorithm and if it again falls into one the the HLT
1181 triggers paths (definitions) it is saved for future analysis.

1182 **3.8 Particle Flow Algorithm**

- 1183 The global event reconstruction (also called particle-flow event reconstruction [85]) aims to re-
1184 construct and identify each individual particle in an event, with an optimized combination of all

⁷A Event can be understood the set of information from the detector channels, extracted in one readout cycle.

⁸Each trigger has its prescaling. For example, a prescaling 30 means that only once every 30 times that this trigger is activated, the event will in be processed and forwarded into the data acquisition chain.

subdetector information. In this process, the identification of the particle type (photon, electron, muon, charged hadron, neutral hadron) plays an important role in the determination of the particle direction and energy. Photons (e/γ coming from Z decays or from electron bremsstrahlung) are identified as ECAL energy clusters not linked to the extrapolation of any charged particle trajectory to the ECAL. Electrons are identified as a primary charged particle track and potentially many ECAL energy clusters corresponding to this track extrapolation to the ECAL and to possible bremsstrahlung photons emitted along the way through the tracker material. Muons are identified as tracks in the central tracker consistent with either a track or several hits in the muon system, and associated with calorimeter deposits compatible with the muon hypothesis. Charged hadrons are identified as charged particle tracks neither identified as electrons, nor as muons. Finally, neutral hadrons are identified as HCAL energy clusters not linked to any charged hadron trajectory, or as a combined ECAL and HCAL energy excess with respect to the expected charged hadron energy deposit. Figure 3.7 show the identification process for each high-level physics object, as previously described.

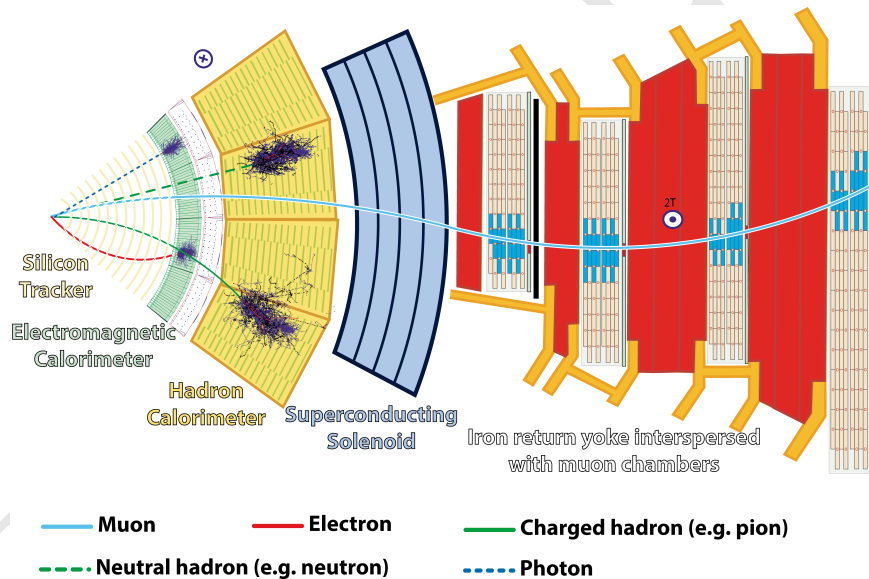


Figure 3.7: The figure illustrates how the information from each subdetector is used in order to identify the different high-level objects in the Particle-Flow algorithm. Source: [85].

The energy of photons is obtained from the ECAL measurement. The energy of electrons is determined from a combination of the track momentum at the main interaction vertex, the corresponding ECAL cluster energy, and the energy sum of all bremsstrahlung photons attached to the track. The energy of muons is obtained from the corresponding track momentum. The energy of charged hadrons is determined from a combination of the track momentum and the corresponding ECAL and HCAL energies, corrected for the response function of the calorimeters to hadronic showers. Finally, the energy of neutral hadrons is obtained from the corresponding corrected ECAL and HCAL energies.

The candidate vertex with the largest value of summed physics-object p_T^2 is taken to be the primary pp interaction vertex. For each event, hadronic jets are clustered from these reconstructed particles using the infrared and collinear safe anti- k_T algorithm [77, 78] with a distance parameter of 0.4. Jet

momentum is determined as the vectorial sum of all particle momenta in the jet, and is found from simulation to be, on average, within 5 to 10% of the true momentum over the whole p_T spectrum and detector acceptance. Additional proton-proton interactions within the same or nearby bunch crossings (pileup) can contribute additional tracks and calorimetric energy depositions to the jet momentum. To mitigate this effect, charged particles identified to be originating from pileup vertices are discarded and an offset correction is applied to correct for remaining contributions. Jet energy corrections are derived from simulation to bring the measured response of jets to that of particle level jets on average. In situ measurements of the momentum balance in dijet, photon + jet, $Z + \text{jet}$, and multijet events are used to account for any residual differences in the jet energy scale between data and simulation [86]. The jet energy resolution amounts typically to 15–20% at 30 GeV, 10% at 100 GeV, and 5% at 1 TeV [86]. Additional selection criteria are applied to each jet to remove jets potentially dominated by anomalous contributions from various subdetector components or reconstruction failures.

Anomalous high- p_T^{miss} events can be due to a variety of reconstruction failures, detector malfunctions or non collisions backgrounds. Such events are rejected by event filters that are designed to identify more than 85–90% of the spurious high- p_T^{miss} events with a mistagging rate less than 0.1% [87].

Hadronic decays of top quarks are identified using the ratio between 3-subjettiness and 2-subjettiness [88], $\tau_{32} = \tau_3/\tau_2$, and the groomed jet mass. The groomed jet mass is calculated after applying a modified mass-drop algorithm [89, 90], known as the *soft drop* algorithm [91], to anti- k_T jets with a distance parameter of 0.8 and parameters $\beta = 0$, $z_{\text{cut}} = 0.1$, and $R_0 = 0.8$. The variables are calibrated in a top quark-antiquark enriched sample [92].

In the barrel section of the ECAL, an energy resolution of about 1% is achieved for unconverted or late-converting photons in the tens of GeV energy range. The remaining barrel photons have a resolution of about 1.3% up to a pseudorapidity of $|\eta| = 1$, rising to about 2.5% at $|\eta| = 1.4$. In the endcaps, the resolution of unconverted or late-converting photons is about 2.5%, while the remaining endcap photons have a resolution between 3 and 4% [76].

The electron momentum is estimated by combining the energy measurement in the ECAL with the momentum measurement in the tracker. The momentum resolution for electrons with $p_T \approx 45$ GeV from $Z \rightarrow ee$ decays ranges from 1.7% to 4.5%. It is generally better in the barrel region than in the endcaps, and also depends on the bremsstrahlung energy emitted by the electron as it traverses the material in front of the ECAL [75].

Muons have their momentum computed by curvature of their tracks in the muon system solo or the matched track in the muon system and the tracker.

DRAFT

¹²⁴³ 4 Physics Analysis

¹²⁴⁴ The analysis here presented corresponds to the search for rare decays of $H \rightarrow \Upsilon + \gamma$, where the
¹²⁴⁵ Υ might appear in the states $1S$, $2S$ or $3S$, and shall decay to a pair of muons (from here on,
¹²⁴⁶ called dimuon system) and the γ will be identified as a offline reconstructed photon. The decay
¹²⁴⁷ to the dimuon channel offers a very efficient triggering for this process, characteristic of CMS. The
¹²⁴⁸ analogous process of the Z boson decays to the same channel is also studied, as a benchmark for
¹²⁴⁹ the Higgs decay.

¹²⁵⁰ The main process contributing to the accessible phase space of these decays are described in Fig-
¹²⁵¹ ure 4.1, in which the different process are represented in a diagram for the reconstructed invariant
¹²⁵² masses of the muon-muon-photon system ($\mu\mu\gamma$ - horizontal axis) and the muon-muon system ($\mu\mu$
¹²⁵³ - vertical axis). The vicinity of the H/Z mass and Υ mass regions are represented in the midpoint
¹²⁵⁴ for each axis. The backgrounds can be divided in **Resonant** and **Non-Resonant** backgrounds.
¹²⁵⁵ The Non-Resonant might come from two sources, a Full Combinatorial background is composed by
¹²⁵⁶ the combination of two non-correlated muons with a photon in the final state of the event. This is
¹²⁵⁷ expected to be spread all over the phase space and in the diagram, it is represented by the color blue.
¹²⁵⁸ The $\Upsilon + \gamma$ Combinatorial background is a combination of two correlated muons (e.g.: the decay of
¹²⁵⁹ a Υ to a dimuon muon system) combined with a photon from a secondary process (e.g.: Multiple
¹²⁶⁰ Particle Interaction - MPI, pileup, a jet mis-identified as a photon). This should be concentrated
¹²⁶¹ in the region around the $\Upsilon(1S, 2S, 3S)$ and it is represented by the gray region.

¹²⁶² The Resonant background is composed by the processes where the boson (Higgs or Z) decays to
¹²⁶³ a $\mu\mu\gamma$ final state without going trough the the intermediate meson state. For the Z decays, this
¹²⁶⁴ background is modeled based on a Drell-Yan to dimuon decays, with a final state radiated (FSR)
¹²⁶⁵ photon ($Z \rightarrow \mu\mu\gamma_{FSR}$), while for the Higgs decay, a Higgs Dalitz decay ($H \rightarrow \mu\mu\gamma$) is used. The
¹²⁶⁶ Resonant background (also called Peaking Background) is represented in the diagram by the region
¹²⁶⁷ in yellow. The Signal is represented by the red region on the diagram.

¹²⁶⁸ Around these representations, the a 2-dimensional model of the reconstructed invariant masses
¹²⁶⁹ ($m_{\mu\mu\gamma}$ and $m_{\mu\mu}$) is constructed for each contributing process and tested against the collected data
¹²⁷⁰ by the experiment, by means of a unbinned maximum likelihood fit. No significant excess above
¹²⁷¹ the background-only model is observed and a upper limit of the signal branch fraction is extracted.
¹²⁷² The following sections describes the data and simulated samples used in this analysis, the event
¹²⁷³ selection applied in order to enhance the signal to background ratio and the process to construct
¹²⁷⁴ the statistical models used in the upper limits extraction.

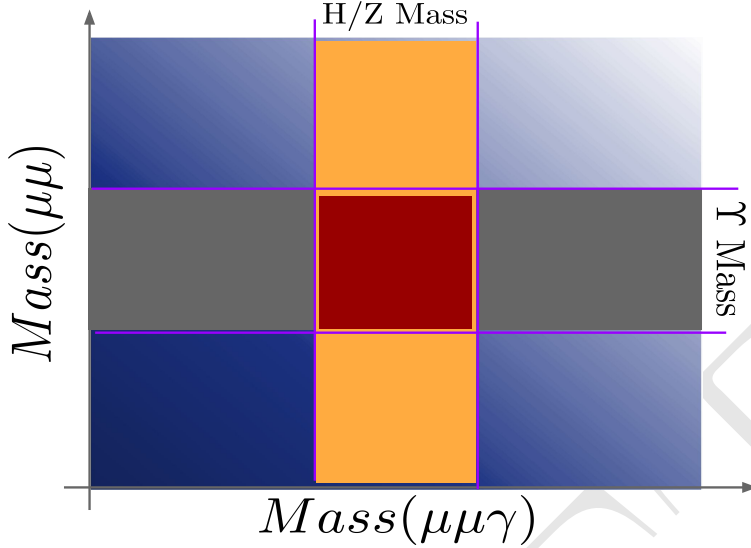


Figure 4.1: A diagram for the reconstructed invariant mass of the $\mu\mu\gamma$ final state. The blue and gray regions represent the Full Combinatorial and $\Upsilon + \gamma$ Combinatorial contributions, respectively, while the yellow and red regions represent the Resonant background and the signal region.

1275 4.1 Datasets and simulated events

1276 4.1.1 Data samples

1277 The data sample used in this analysis consists of the 2016 13 TeV run with 25 ns bunch separation
1278 recorded by CMS. This data sample is composed only by events that were certified from all CMS
1279 subsystems and reconstruction specialist as good for physics analysis.

1280 This data sample corresponds to 35.86 fb^{-1} of integrated luminosity [93].

1281 4.1.2 Simulated datasets

1282 Data simulation at CMS is done by the use of Monte Carlo (from here on, simply called MC)
1283 simulations generates pseudo-random events, constrained by the physics of the related process to
1284 which we are interested, including the effect of the produced particles interacting with the detector.
1285 The simulation starts with the **hard-scattering** process, at parton (constituents of the proton)
1286 level, done usually, by matrix element generators, which impose to the incoming and outgoing
1287 partons, the dynamics of the simulated process, according to some pre-defined theoretical model.
1288 Along the hard interaction simulation, the **fragmentation** process takes place. Since the the matrix
1289 element generator provide information on the parton level, it is necessary to extract the momentum
1290 distribution of the parton as a function of the Q^2 (transferred momentum) of the process. To do
1291 so, MC generators use the PDFs (parton distribution functions) to sample those values, accordingly.
1292 The matrix element formalism also allows the simulation of the process, taking into account, different
1293 orders of perturbations, like NLO (next-to-leading order), NNLO (next-to-next-to-leading order),
1294 and so on.

1295 After the hard-scattering, the **showering** process simulates the radiation emission by gluons and
 1296 quarks in the initial and final states. Along the hard interaction, the other proton constituents
 1297 may also interact through soft interaction. This part of the simulation is called **multiple parton**
 1298 **interaction** (MPI). The last components of the simulation is the **hadronization** and the **decay**
 1299 **of heavy hadrons and leptons**. The former one, imposes the QCD confinement to low energy
 1300 quarks and gluons¹, while the latter one, implements specific models to decays heavy hadrons and
 1301 leptons, like B hadrons and taus.

1302 Usually, different generators are used to simulate a process. Each specialized in one or more steps.

1303 A summary of the signal and background MC samples used is presented in Table 4.1. These
 1304 simulated data are comparable with the proton-proton collision using 2016 data conditions and the
 1305 **pileup**² events are added to the simulated event in this step. The pileup events distribution used is
 1306 modeled as a Poisson pdf (probability distribution function) with mean of 23 events, as recommended
 1307 by CMS. Detector response in the MC samples is simulated using a detailed description of the CMS
 1308 detector, based on GEANT4 [94].

1309 The signal MC samples are simulated for the Higgs bosons decaying to $\Upsilon(nS)(\rightarrow \mu\mu) + \gamma$ channels
 1310 with POWHEG v2.0 [95–97], at next-to-leading order (NLO) of Feynman graphs computation, for
 1311 the following production modes: gluon-gluon fusion (ggF), vector boson fusion (VBF), associated
 1312 production (VH) and associated top production (ttH), with cross-section summarized at table 4.1.
 1313 A extensive review of these production modes can be found at [98]. The PYTHIA 8 generator [99,
 1314 100] is used for hadronization and fragmentation with underlying event tune CUETP8M1 [101].
 1315 The parton distribution functions (pdf) NNPDF3.0 [102] are used.

1316 For Z decaying to $\Upsilon(nS)(\rightarrow \mu\mu) + \gamma$ channels, the signal samples are simulated with MADGRAPH
 1317 5 _MC@NLO 2.6.0 matrix element generator [103] at next leading order and the PYTHIA 8 genera-
 1318 tor [99, 100] for hadronization and fragmentation with underlying event tune CUETP8M1 [101].

1319 The Drell-Yan process, $pp \rightarrow Z \rightarrow \mu\mu\gamma_{FSR}$, results in the same final state as the signal. This
 1320 process exhibits a peak in the three-body invariant mass, $m_{\mu\mu\gamma}$, at the Z boson mass, m_Z , and it is
 1321 a resonant background for this channel, therefore referred to as a Peaking Background.

1322 It is taken into account when deriving the upper limit on the branching fraction for $Z \rightarrow \Upsilon(nS) + \gamma \rightarrow$
 1323 $\mu\mu + \gamma$. The MADGRAPH 5 _MC@NLO 2.6.0 matrix element generator [103] at leading order,
 1324 interfaced with PYTHIA 8.226 for parton showering and hadronization with tune CUETP8M1 [101],
 1325 is used to generate a sample of these resonant background events. The photons in these events are

¹QCD forbids coloured objects to exist in non-asymptotic states. They must decays to more complex systems, until they form stable colorless states.

²Each LHC collision recorded by CMS, is composed not by a single pp interaction, but by bunches of protons crossing each other. In this case, a hard interaction is actually surrounded by many soft interaction between adjacent protons. The extra activity produced in these interactions, and caught by the detector, is called **pileup** and has its signal mixed with the hard one. Since, during the data taking, the number of pileup interactions varies according to the instantaneous luminosity, the MC are mixed some soft interaction only sample, called Minimum Bias. The number of mixed soft interaction (pileup events) is governed by a Poisson distribution with a pre-defined mean. The MC samples are then reweighted to match the same distribution of primary vertexes for the corresponding Data. Systematics related to this procedure will be discussed later.

1326 all produced as final-state radiation from the $Z \rightarrow \mu\mu$ decay and therefore the $m_{\mu\mu\gamma}$ distribution
 1327 peaks at the Z boson mass and there is no continuum contribution.

1328 Similarly, the Higgs boson Dalitz decay [104], $H \rightarrow \gamma^*\gamma \rightarrow \mu\mu + \gamma$, is a Peaking Background
 1329 (resonant) to $H \rightarrow \Upsilon(nS) \rightarrow \mu\mu + \gamma$. It is simulated at NLO with MADGRAPH 5 _MC@NLO 2.6.0
 1330 matrix element generator [103] at next-to-leading order and the PYTHIA 8 generator [99, 100] for
 1331 hadronization and fragmentation with underlying event tune CUETP8M1 [101]. This Higgs Dalitz
 1332 Decay sample, was generated only for the ggF production mode, but its cross-section was rescaled
 1333 to the full Higgs cross-section. This process will present a small contribuition of selected events, so
 1334 this approximation should be sufficient for the Higgs Peaking Background modeling.

1335 There are also background processes that do not give resonance peaks in the three-body invariant
 1336 mass spectrum. They are modeled from data, as it will be explained latter in more details.

Table 4.1: Datasets simulated (MC) for 2016 conditions. Assuming that $\sigma(pp \rightarrow H)$, taking into consideration all the simulated Higgs production modes, is 55.13 pb [105] and $\sigma(pp \rightarrow Z \rightarrow \mu\mu)$ is 57094.5 pb , including the next-to-next-to-leading order (NNLO) QCD contributions, and the next-to-leading order (NLO) electroweak corrections from fewz 3.1 [106] calculated using the NLO PDF set NNPDF3.0, with the phase space selection in invariant mass of the dimuon system of $m_{\mu\mu} > 50 \text{ GeV}$. For the Higgs Dalitz σ , we consider only the gluon fusion contribution ($\sigma_{\text{ggF}} = 48.6 \text{ pb}$) [105]. The Higgs Dalitz Decay BR_{SM} and the $Z \rightarrow \mu\mu\gamma_{FSR}$ were obtained with MCFM 6.6 [107] (as in the CMS search for Higgs Dalitz Decay in at $\sqrt{s} = 8 \text{ TeV}$ [108]) and with MADGRAPH 5 _MC@NLO, respectively. The $BR_{\Upsilon(1S,2S,3S) \rightarrow \mu\mu}^{PDG} = (2.48, 1.93, 2.18) \times 10^{-2}$ is quoted from Particle Data Group report (PDG) [13]. The "Effective σ " for the signal samples is $\sigma(pp \rightarrow Z(H)) \times BR_{SM} \times BR_{\Upsilon(nS) \rightarrow \mu\mu}^{PDG}$.

Physics Processes	Branching Ratio (BR_{SM})	Effective σ (in pb)	Generator	Sample Type
$H \rightarrow \Upsilon(1S) + \gamma$	5.22×10^{-9}	7.14×10^{-9}	POWHEG 2.0	Signal
$H \rightarrow \Upsilon(2S) + \gamma$	1.42×10^{-9}	1.51×10^{-9}	POWHEG 2.0	Signal
$H \rightarrow \Upsilon(3S) + \gamma$	9.10×10^{-10}	1.10×10^{-9}	POWHEG 2.0	Signal
$Z \rightarrow \Upsilon(1S) + \gamma$	4.88×10^{-8}	6.80×10^{-5}	MADGRAPH 5	Signal
$Z \rightarrow \Upsilon(2S) + \gamma$	2.44×10^{-8}	2.69×10^{-5}	MADGRAPH 5	Signal
$Z \rightarrow \Upsilon(3S) + \gamma$	1.88×10^{-8}	2.34×10^{-5}	MADGRAPH 5	Signal
H Dalitz Decay	3.83×10^{-5}	2.13×10^{-3}	MADGRAPH 5	Peaking Background
$Z \rightarrow \mu\mu\gamma_{FSR}$	—	7.93×10^{-2}	MADGRAPH 5	Peaking Background

1337 The number of simulated events is is rescaled by the Effective σ , from table 4.1, in order to match
 1338 35.86 fb^{-1} of integrated luminosity, from the recorded data. Being $N = \sigma\mathcal{L}$, N in the number of
 1339 events for a process, σ is the cross-section and \mathcal{L} is the integrated luminosity, the reweighting factor,
 1340 for a simulated sample is:

$$w_{MC} = \frac{\sigma\mathcal{L}}{N_{sim}}, \quad (4.1)$$

1341 where N_{sim} is the number of simulated events for a specific process.

1342 The simulated sample are also corrected by the data pileup distribution, since the pileup distribution
 1343 of MC is different from the pileup distribution of data. The way to correct the MC is to assign a

1344 weight to each bin of the MC pileup distribution, with respect to the data. The rescaling is defined
1345 as the ratio between normalized pileup (PU) distribution for Data and MC.

$$w_{PU}(n) = \frac{P_{PU}^{Data}(n)}{P_{PU}^{Sim}(n)}, \quad (4.2)$$

1346 where n is the number of interaction per bunch crossing (pileup).

1347 4.2 Contribution of the $\Upsilon(nS)$ polarisation

1348 Measurements of quarkonium polarization observables may yield information about quarkonium
1349 production mechanisms that are not available from the study of unpolarized cross sections alone.
1350 The three polarization states of a $J = 1$ quarkonium can be specified in terms of a particular
1351 coordinate system in the rest frame of the quarkonium. This coordinate system is often called the
1352 "spin-quantization frame".

1353 In a hadron collider, $\Upsilon(1S, 2S, 3S)$ are reconstructed through their electromagnetic decays into
1354 a lepton pair. The information about the polarization of the quarkonium state is encoded in the
1355 angular distribution of the leptons. This angular distribution is usually described in the quarkonium
1356 rest frame with respect to a particular spin-quantization frame [109]. The polarization of the
1357 $\Upsilon(1S, 2S, 3S)$ is not simulated for signal MC sample and we only apply a reweighting scale factor to
1358 each event and so we can emulate the polarization effects [110]. Figure 4.2 present the distributions
1359 of $\cos \Theta$ of $\Upsilon \rightarrow \mu\mu$, where Θ is the angle between the positive muon and the Υ in the Z (Higgs) rest-
1360 frame. At Table 4.2 we show the the analytical functions used to describe the extremes scenarios
1361 (Unpolarized, Transverse Polarization and Longitudinal Polarization) reweighting, presented in this
1362 analysis.

1363 It is worth stating that, for the Higgs decay, on the Transverse Polarization is considered. For
1364 the Z decay, because of its spin nature, the Unpolarized scenario is used as the nominal one, and
1365 the effects of the two other extremes (Transverse Polarization and Longitudinal Polarization) are
1366 quoted as systematics.

Table 4.2: Summary of the impact of reweighted of polarization contribution using several scenarios.

J_Z	Polarisation Scenario	Analytic Description
± 1	Transverse	$3/4 \times (1 + (\cos \Theta)^2)$
0	Longitudinal	$3/2 \times (1 - (\cos \Theta)^2)$

1367 4.3 Kinematical studies using MC generator

1368 Using the PYTHIA 8.226 generator, the Monte Carlo signals are produced for Higgs (Z) boson events
1369 decaying in $(\Upsilon(1S, 2S, 3S)) + \gamma$, which are highly boosted. Observing the kinematic generator level
1370 distributions in Figure 4.3 for Z boson and Figure 4.4 for Higgs boson, we could conclude that the

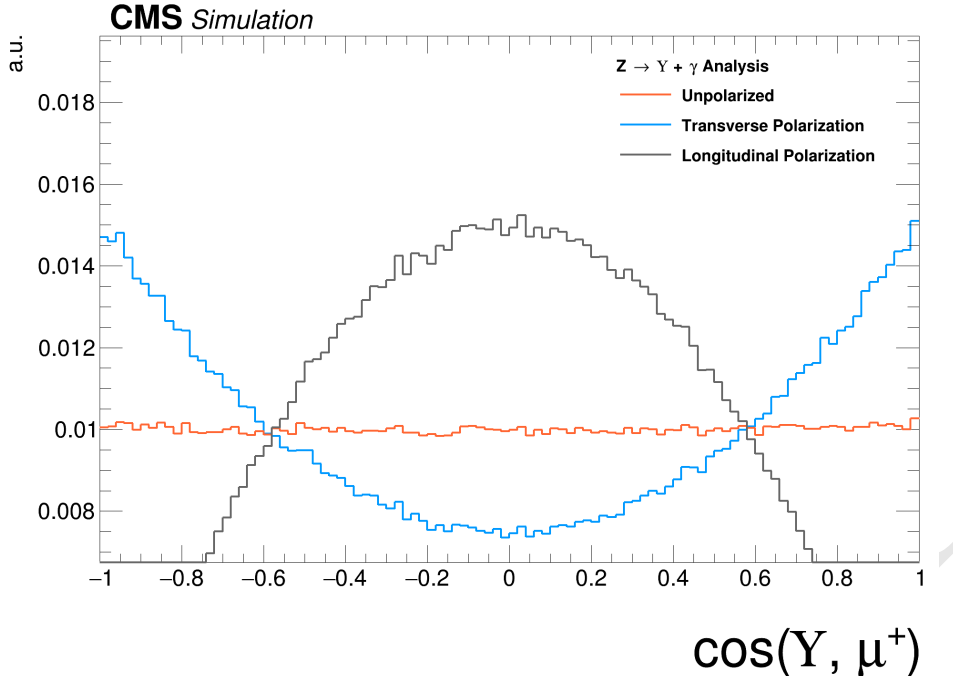


Figure 4.2: Distributions of $\cos\theta$ of $\Upsilon \rightarrow \mu\mu$ and $\gamma^* \rightarrow \mu\mu$. The orange distribution is the $Z \rightarrow \Upsilon(1S, 2S, 3S) + \gamma$ sample before reweighting (Unpolarized); the blue and gray distributions are $Z \rightarrow \Upsilon(1S, 2S, 3S)$ sample after reweighting, for the Transverse and Longitudinal Polarization.

1371 high- E_T (transverse energy, with respect to the beam line) photon will be back-to-back to the Υ
 1372 particles being possible to apply an isolation selection to identify a photon in this kinematic topology.
 1373 Also, we can observe those transverse momenta of the leading/trailing p_T (transverse momentum,
 1374 with respect to the beam line) muon ³ and the photon and distances $\Delta R = \sqrt{\Delta\eta^2 + \Delta\phi^2}$ between
 1375 the two muons and between the muons and the photon are a good variable that can be used to
 1376 discriminate the contribution between signal and background events. The leading muon transverse
 1377 momentum can be greater than 45(30) GeV and trailing muon is greater than 10(20) GeV in Higgs(Z)
 1378 decay. ΔR distributions of the two muons and between the muons and the photon in the both cases
 1379 show that the two muons are very close and the photon is back-to-back in relation of dimuon system.
 1380 Another feature of this kinematic topology is that the production vertex between muons produced
 1381 in Υ decaying events and the high- E_T photon is very well defined.

³In this study we define leading muon and the muon, decaying from the Υ , with highest p_T . Trailing muon is the one with the second hight p_T .

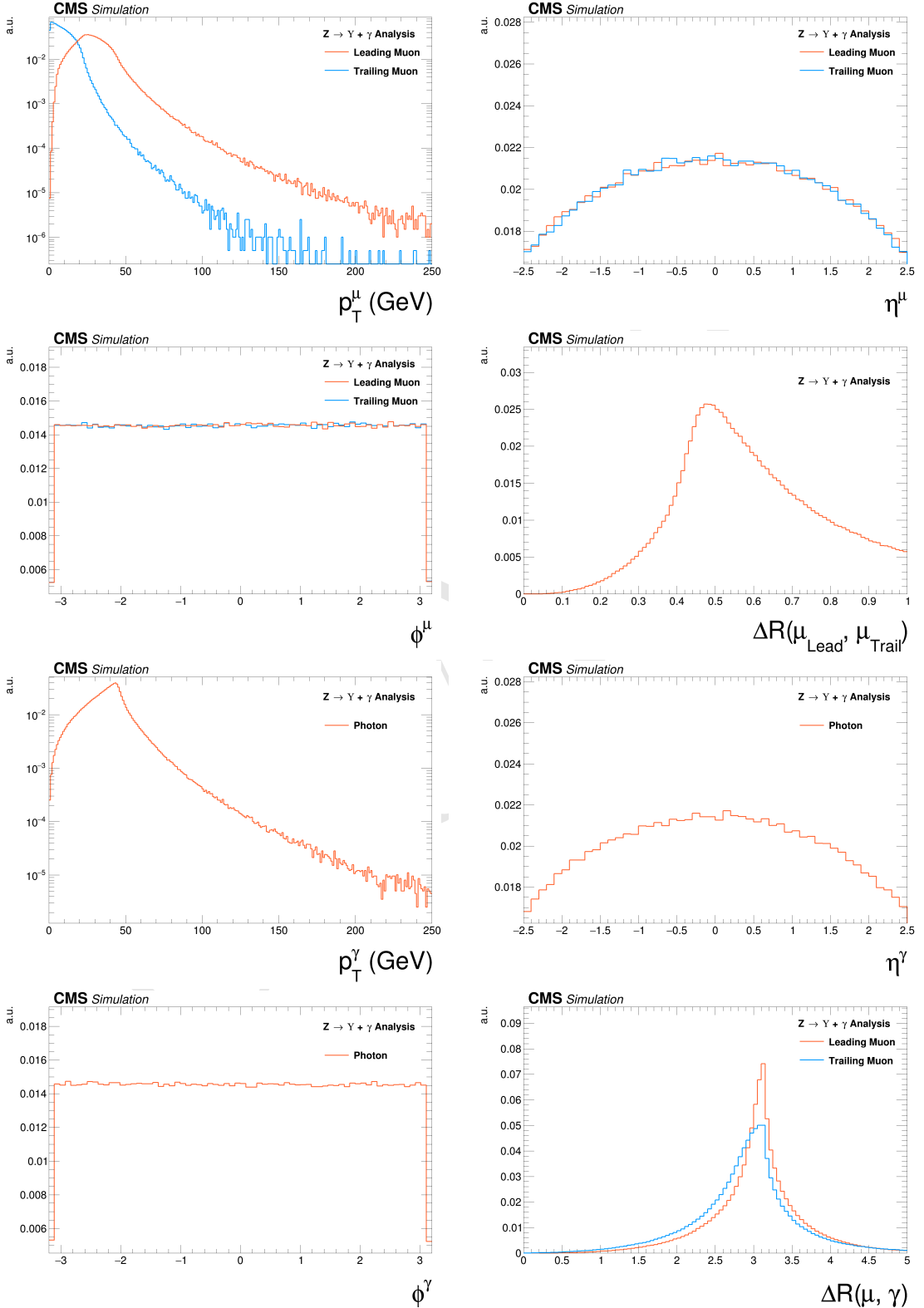


Figure 4.3: Generator level distributions of main variables for $Z \rightarrow \Upsilon(1S, 2S, 3S) + \gamma$: Transverse momenta of the leading/trailing p_T muon and the photon, pseudorapidity (η) and ϕ of the muons and the photon, distances ΔR between the two muons and between the muons and the photon. All the distributions shown in the figure are normalized to the unity of area.

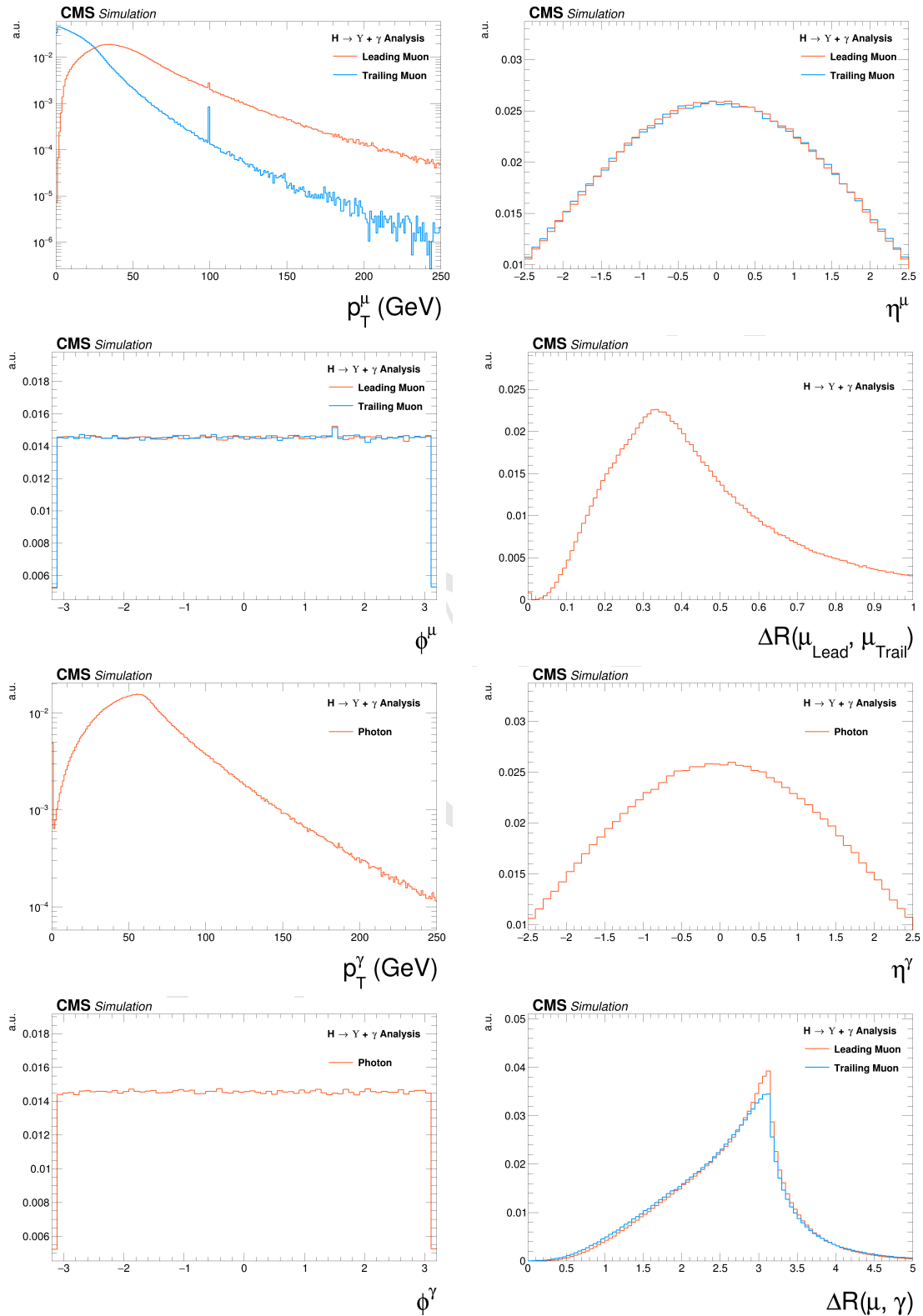


Figure 4.4: Generator level distributions of main variables for $H \rightarrow \Upsilon(1S, 2S, 3S) + \gamma$: Transverse momenta of the leading/trailing p_T muon and the photon, pseudorapidity (η) and ϕ of the muons and the photon, distances ΔR between the two muons and between the muons and the photon. All the distributions shown in the figure are normalized to the unity of area.

1382 4.4 Event selection

1383 The event selection is divided in two steps. At first, a set of cuts related to trigger and physics object
 1384 (muons and photons) selection is applied. High level physics objects at CMS are reconstructed based
 1385 of the Particle Flow (PF) algorithm [111]. This selection is called, within this analysis, Group I.
 1386 For the events that pass the Group I selection, another set of cuts is applied, this time focusing on
 1387 kinematical (phase space) event selection, in order to enhance the signal to background ratio. This
 1388 later set is called, within this analysis, Group II. After full selection, three exclusive categories are
 1389 defined, based on the photon's η region and its energy spread shape within the ECAL cells (R9).
 1390 After the full selection, a background and signal modeling process is applied, based on the invariant
 1391 mass distributions, which will be explained in the next section.

1392 4.5 Trigger and physics object selection (Group I)

1393 4.5.1 Trigger

1394 In this study, the same trigger requirements are applied to both data and simulated samples. For
 1395 the first trigger level (L1), events are selected if they present at least one muon with transverse
 1396 momentum greater than 5 GeV and an isolated ⁴ photon or electron with transverse momentum
 1397 greater than 18 GeV (at L1, there is no differentiation between photons and electrons). At the
 1398 software level of the trigger system (HLT), the events are required to have at least one muon with
 1399 transverse momentum greater than 17 GeV and a photon with transverse momentum greater than
 1400 30 GeV.
 1401 In order to compensate any difference in the trigger performance between simulated and data sam-
 1402 ples, for every selected MC a proper scale factor is applied, based on the the p_T of the reconstructed
 1403 muon and photon. These scale factor computed by the ratio between efficiency of the trigger for
 1404 the Data sample over the efficiency for a MC sample. These efficiencies are calculated with the
 1405 tag-and-probe method, exploring the the resonance of a final state composted by two muon and
 1406 one photon in the vicinity of the Z boson invariant mass. To this final state, a selections was
 1407 applied to ensure that the photon comes from a Final State Radiation process, allowing us to use
 1408 the tag-and-probe method.
 1409 Considering the similarity of this analysis with the $H/Z \rightarrow J/\psi + \gamma$ analysis [60], not only in therm
 1410 of data samples, but also for triggering and physics object selection, the same scale factors were
 1411 applied. More details are given in the same paper.

⁴The concept of isolation will be detailed later, but in summary, it means a object which has very small activity (above a certain threshold of energy/momentum) around it. In hadron-hadron collider, isolation is a characteristics of hard interactions.

4.5.2 Muon Identification

Ahead of any selection, a standard CMS "Ghost Cleaning" procedure is applied to all reconstructed muons in order to avoid that a single physical muon is reconstructed as two or more. For this procedure, reconstructed muons sharing 50% or more segments in the system are arbitrated.

After the cleaning, a muon is chosen when it passes a two step identification: the **Loose ID** and the **Tight ID**. Below the muon identification procedure is summarized .

For the Loose ID, each muon is required to:

- have transverse momentum greater than 5 GeV, in order to cope with Particle Flow requirements;
- be within the muon system acceptance: $|\eta| < 2.4$;
- to have a three dimensional impact parameter uncertainty smaller than 4;
- to have transverse distance smaller than 0.5 cm ($d_{xy} < 0.5$), with respect to the primary vertex (PV);
- to have longitudinal distance greater than 1.0 cm ($d_z < 1$), with respect to the primary vertex (PV).

Muons reconstructed only in the muon system, without a correspondence with the tracker, are rejected. The last three requirements of the Loose ID are imposed in order to suppress muons from in-flight decays.

The primary vertex itself, is determined as the reconstructed vertex with the biggest sum of p_T^2 in the event. This sum is performed, considering all the charged PF candidates clustered by the jet finding algorithms [77, 78] and the MET, which is defined as the p_T vector sum of all the charged and neutral PF candidates associated to that vertex.

For the Tight ID, muons with transverse momentum $p_T < 200$ GeV, are required to have been reconstructed with the Particle Flow (PF) algorithm. If they have $p_T > 200$ GeV, they should be reconstructed with the Particle Flow (PF) algorithm or satisfy the strict tracker requirements (defined in table 4.3).

Table 4.3: Conditions for a muon to pass the strict tracker requirements.

Requirement	Technical definition
Muon station matching	Muon is matched to segments in at least two stations in the muon system
Good p_T measurement	$\frac{p_T}{\sigma_{p_T}} < 0.3$
Vertex compatibility ($x - y$)	$d_{xy} < 2$ mm
Vertex compatibility (z)	$d_z < 5$ mm
Pixel hits	At least one pixel hit
Tracker hits	Hits in at least six tracker layers

1438 To mitigate spurious signal in the detector that would mimic a muon, the leading muon (the one
1439 with highest p_T) is required to be isolated within a cone of radius $\Delta R = \sqrt{\Delta\eta^2 + \Delta\phi^2} < 0.3$ in
1440 the $\eta - \phi$ plane. The isolation is evaluated in terms of $\mathcal{I}^\mu < 0.35$, defined as:

$$\mathcal{I}^\mu \equiv \left(\sum p_T^{\text{charged}} + \max \left[0, \sum p_T^{\text{neutral}} + \sum p_T^\gamma - p_T^{\text{PU}}(\mu) \right] \right) / p_T^\mu. \quad (4.3)$$

1441 The $\sum p_T^{\text{charged}}$ is the scalar sum of the transverse momenta of charged hadrons originating from the
1442 chosen primary vertex of the event. The $\sum p_T^{\text{neutral}}$ and $\sum p_T^\gamma$ are the scalar sums of the transverse
1443 momenta for neutral hadrons and photons, respectively. Since the isolation variable is particularly
1444 sensitive to energy deposits from pileup interactions, a $p_T^{\text{PU}}(\mu)$ contribution is subtracted, where
1445 $p_T^{\text{PU}}(\mu) \equiv 0.5 \times \sum_i p_T^{\text{PU},i}$, where i runs over the momenta of the charged hadron PF candidates
1446 not originating from the primary vertex, and the factor of 0.5 corrects for the different fraction of
1447 charged and neutral particles in the cone.

1448 One should keep in mind that this muon identification is the same as the one used by the $H \rightarrow$
1449 $ZZ^* \rightarrow 4l$ [112]. This was done in order to keep in phase with other Higgs analysis inside the
1450 collaboration. After the muon identification, an appropriate scale factor is applied to the MC
1451 events based on the leading muon p_T and η , in order to correct any possible discrepancy between
1452 data and simulated samples. The scale factors were taken from the $H \rightarrow ZZ^* \rightarrow 4l$ analysis.

1453 In order to cope with trigger requirements, the leading muon should have $p_T > 20$ GeV and the
1454 trailing muon $p_T > 4$ GeV.

1455 4.5.3 Photon Identification

1456 For the photon identification and selection, standard CMS . The Multivariate (MVA) Photon iden-
1457 tification is used with a working point of 90%, together with a electron veto procedure, to avoid
1458 misidentification of electrons as photons. Kinematically, the photons are requested to have trans-
1459 verse energy, with respect to the beam line, $E_T > 33$ GeV and reconstructed within the CMS
1460 acceptance for photons $|\eta_{SC}| < 2.5^5$, excluding the Electromagnetic Calorimeter (ECAL) Barrel-
1461 Endcap intersections.

1462 The threshold of 33 GeV for the photon transverse energy is driven by the trigger requirements.
1463 The selecte photon, per event, is the one with highest E_T .

1464 4.5.4 Kinematical distributions

1465 The selection described so far, is called Group I. The plots shown below are related to selected
1466 events after this set.

1467 Figures 4.5 to 4.10 presents the p_T , η and ϕ distributions for the leading muon, trailing muon and
1468 the photon, for the Z decaying in $\Upsilon(1S, 2S, 3S) + \gamma$.

5SC stands for Super Cluster of the reconstructed photon. It is the set of cell in the Electromagnetic Calorimeter used for the photon observation.

Figures 4.11 to 4.13 presents the p_T , η and ϕ distributions for reconstructed $\Upsilon(nS)$ ($\mu\mu$ system) and the reconstructed boson ($\mu\mu\gamma$ system).

Figures 4.14 to 4.17 presents the $\Delta R = \sqrt{\Delta\eta^2 + \Delta\phi^2}$ between the photon and the muons, the ΔR distributions between reconstructed dimuon ($\mu\mu$) system and the photon, the absolute value of the $\Delta\phi$ between the leading muon and the photon, the ratio for the transverse momentum of the reconstructed Upsilon and the reconstructed Z mass ($p_T^{\mu\mu}/M_{\mu\mu\gamma}$), the ratio for the transverse energy of the reconstructed Photon and the reconstructed Z mass ($E_T^{\mu\mu}/M_{\mu\mu\gamma}$) and dimuon mass distribution of the reconstructed $\Upsilon(nS)$.

Figures 4.18 to 4.30 present the same variables, but for the Higgs decaying in $\Upsilon(1S, 2S, 3S) + \gamma$ channel.

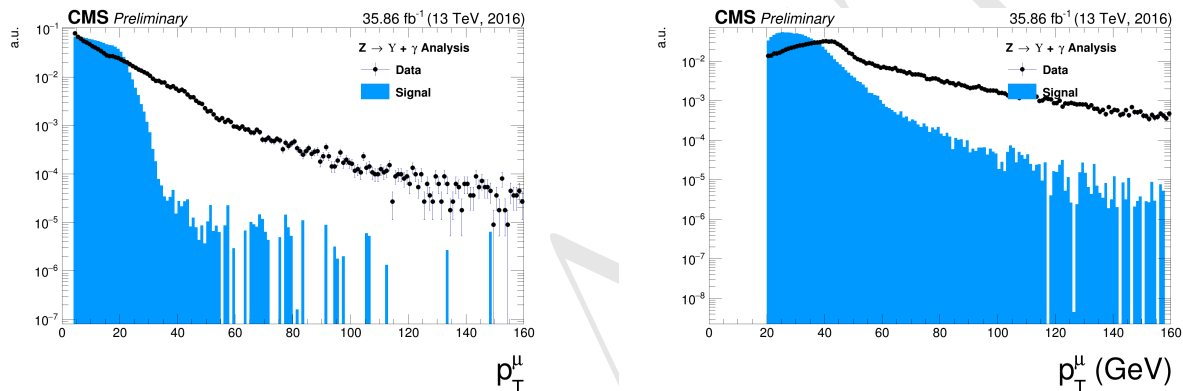


Figure 4.5: The p_T muon distributions from data and signal events for Z decaying in $\Upsilon(1S, 2S, 3S) + \gamma$ after Group I of selection cuts, where on left are presenting the trailing muons and on right are the leading muons. The plots are normalized to the unit of area.

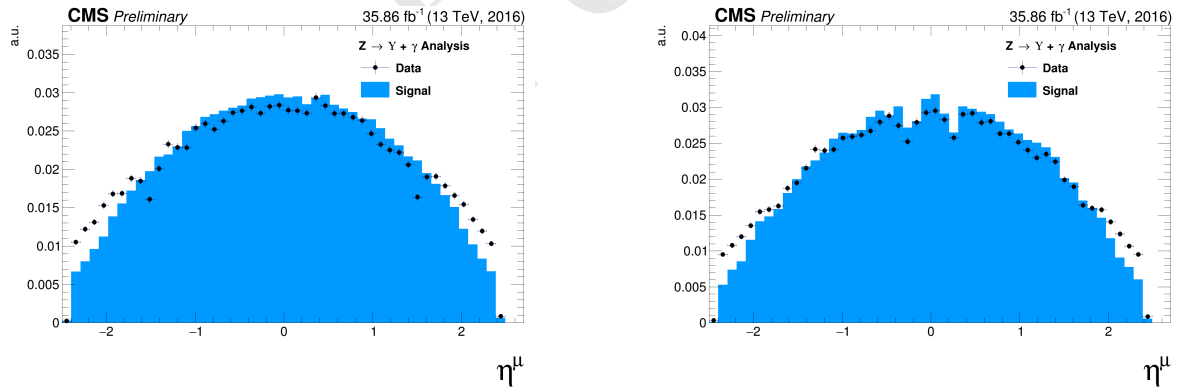


Figure 4.6: The η muon distributions from data and signal events of Z decaying in $\Upsilon(1S, 2S, 3S) + \gamma$ after Group I of selection cuts, where on left are presenting the trailing muons and on right are the leading muons. The plots are normalized to the unit of area.

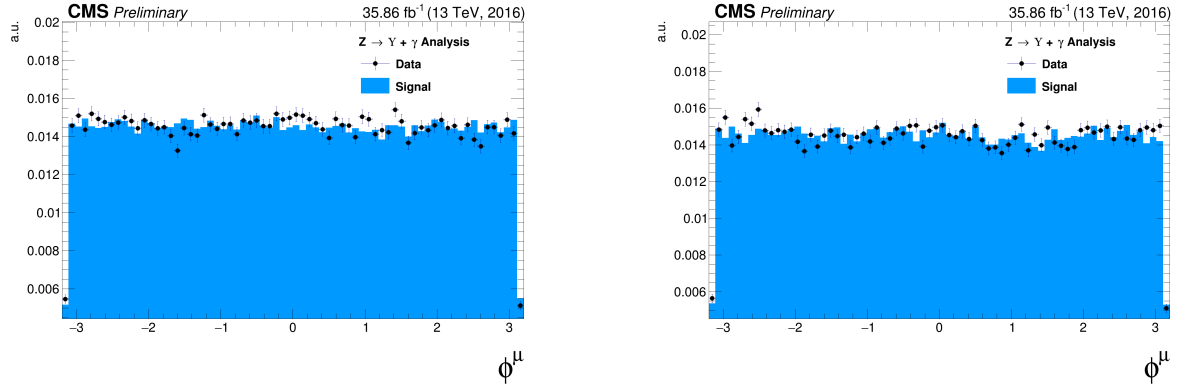


Figure 4.7: The ϕ muon distributions from data and signal events of Z decaying in $\Upsilon(1S, 2S, 3S) + \gamma$ after Group I of selection cuts, where on left are presenting the trailing muons and on right are the leading muons. The plots are normalized to the unit of area.

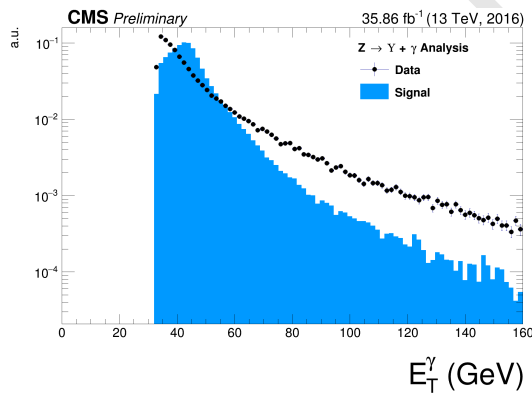


Figure 4.8: The p_T photon distributions from data and signal events for Z decaying in $\Upsilon(1S, 2S, 3S) + \gamma$ Group I of selection cuts. The plots normalized to the unit of area.

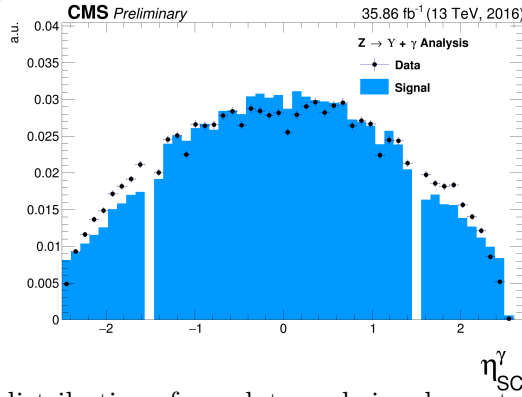


Figure 4.9: The η photon distributions from data and signal events of Z decaying in $\Upsilon(1S, 2S, 3S) + \gamma$ after Group I of selection cuts. The plot is normalized to the unit of area.

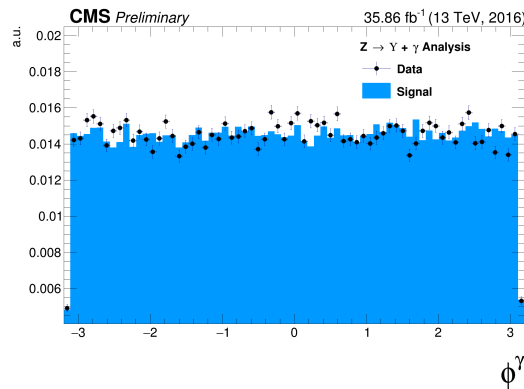


Figure 4.10: The ϕ photon distributions from data and signal events of Z decaying in $\Upsilon(1S, 2S, 3S) + \gamma$ after Group I of selection cuts. The plot is normalized to the unit of area.

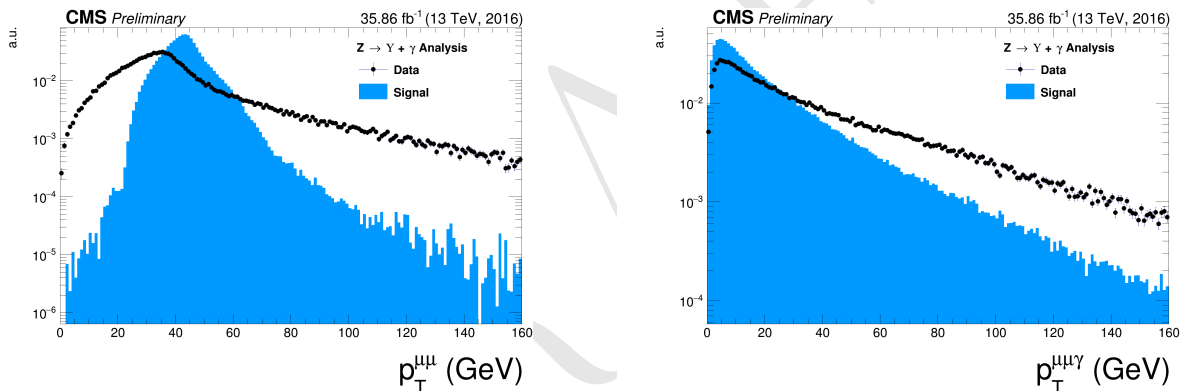


Figure 4.11: The p_T distributions for the reconstructed $\Upsilon(1S, 2S, 3S)$ in the left and for Z in the right from data and signal events for Z decaying in $\Upsilon(1S, 2S, 3S) + \gamma$ after Group I of selection cuts. The plots are normalized to the unit of area.

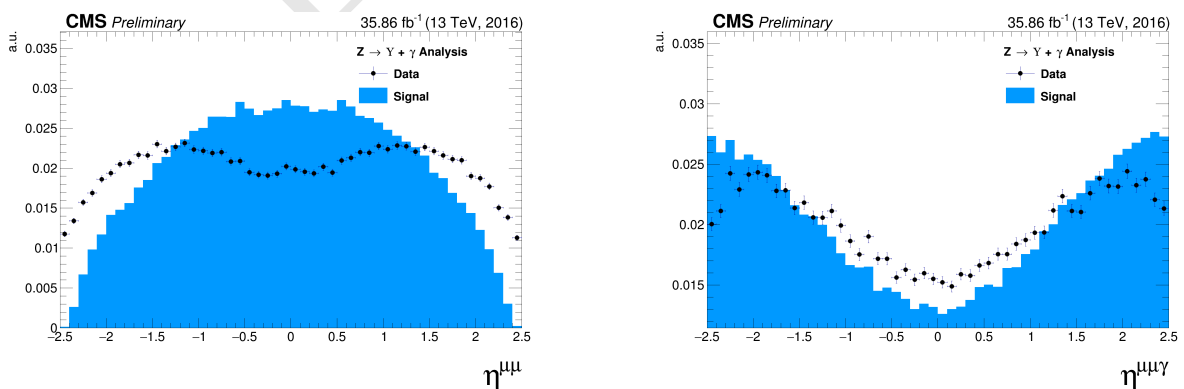


Figure 4.12: The η distributions for $\Upsilon(1S, 2S, 3S)$ in the left and for Z in the right from data and signal events for Z decaying in $\Upsilon(1S, 2S, 3S) + \gamma$ after Group I of selection cuts. The plots are normalized to the unit of area.

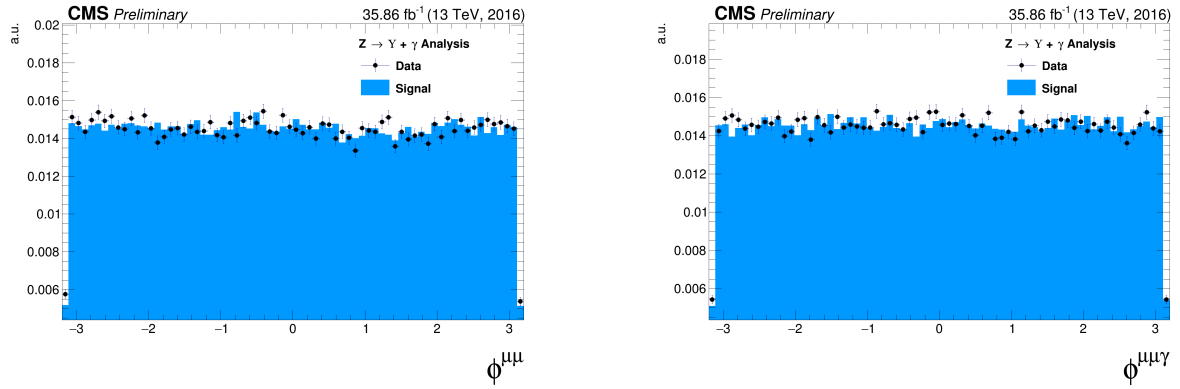


Figure 4.13: The ϕ distributions for $\Upsilon(1S, 2S, 3S)$ in the left and for Z in the right from data and signal events for Z decaying in $\Upsilon(1S, 2S, 3S) + \gamma$ after Group I of selection cuts. The plots are normalized to the unit of area.

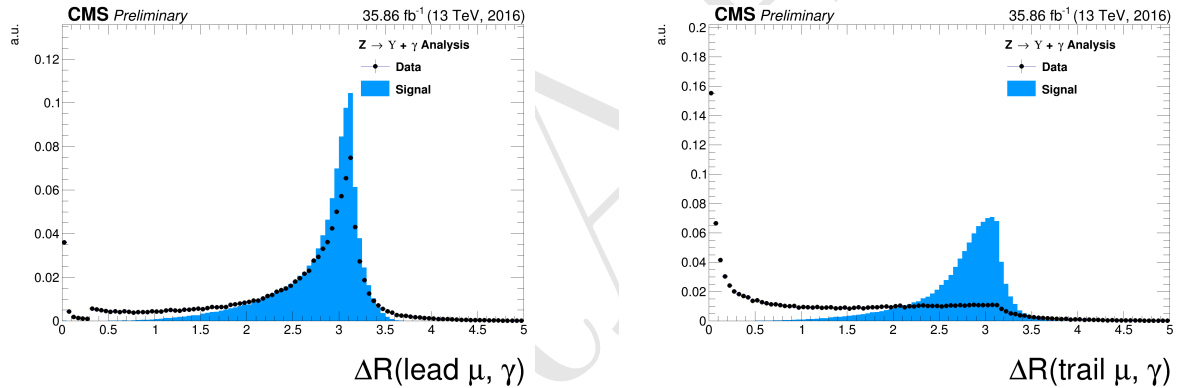


Figure 4.14: The ΔR distributions between the photon and the leading muon (left) and the trailing muon (right) for for Z decaying in $\Upsilon(1S, 2S, 3S) + \gamma$ from data and signal events after Group I of selection cuts. The plots are normalized to the unit of area.

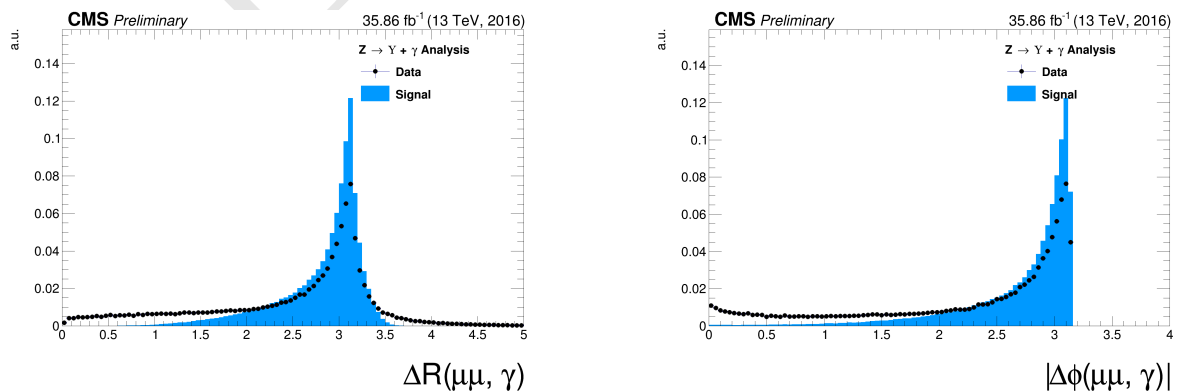


Figure 4.15: Left: The ΔR distributions between reconstructed dimuon ($\mu\mu$) system and the photon. Right: absolute value of the $\Delta\phi$ between the leading muon and the photon for for Z decaying in $\Upsilon(1S, 2S, 3S) + \gamma$ from data and signal events after Group I of selection cuts. The plots are normalized to the unit of area.

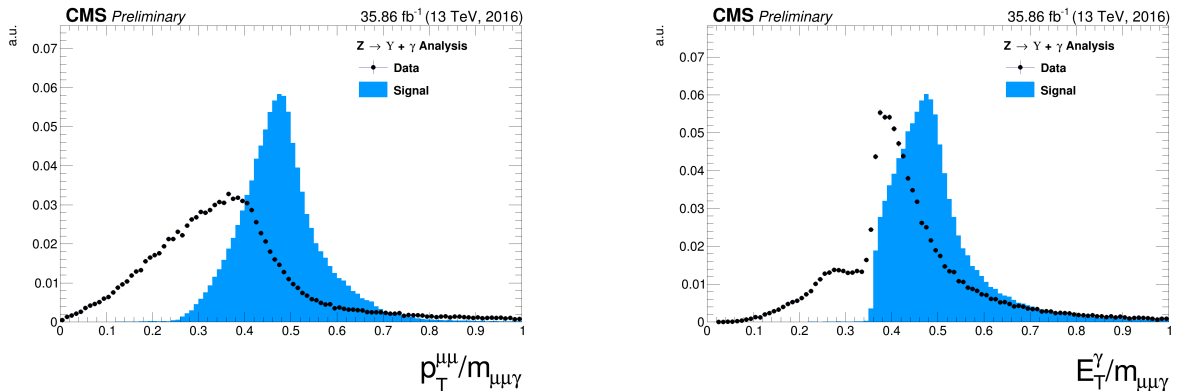


Figure 4.16: The ratio for the transverse momentum of the reconstructed Upsilon and the reconstructed Z mass ($p_T^{\mu\mu}/M_{\mu\mu\gamma}$ - left) and the ratio for the transverse energy of the reconstructed Photon and the reconstructed Z mass ($E_T^\gamma/M_{\mu\mu\gamma}$ - right) distribution for Z decaying in $\Upsilon(1S, 2S, 3S) + \gamma$ from data and signal events after Group I of selection cuts. The plots are normalized to the unit of area.

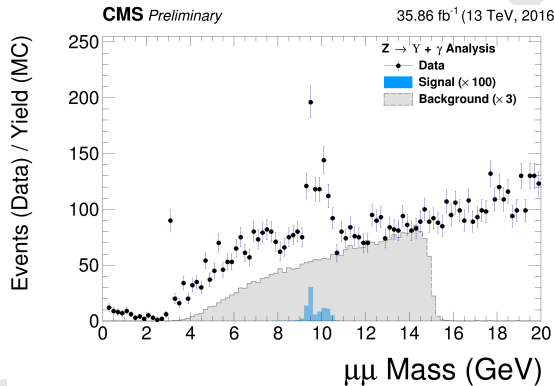


Figure 4.17: The dimuon mass distribution of the reconstructed $\Upsilon(1S, 2S, 3S)$ from data and signal events for Z decaying after Group I of selection cuts. The plot is normalized to the number of events. "Signal" stands for the $Z \rightarrow \Upsilon(1S, 2S, 3S) + \gamma$ sample (scaled by a factor of $\times 100$) and "Background" corresponds to the peaking background ($Z \rightarrow \mu\mu\gamma_{FSR}$) sample (scaled by a factor of $\times 3$).

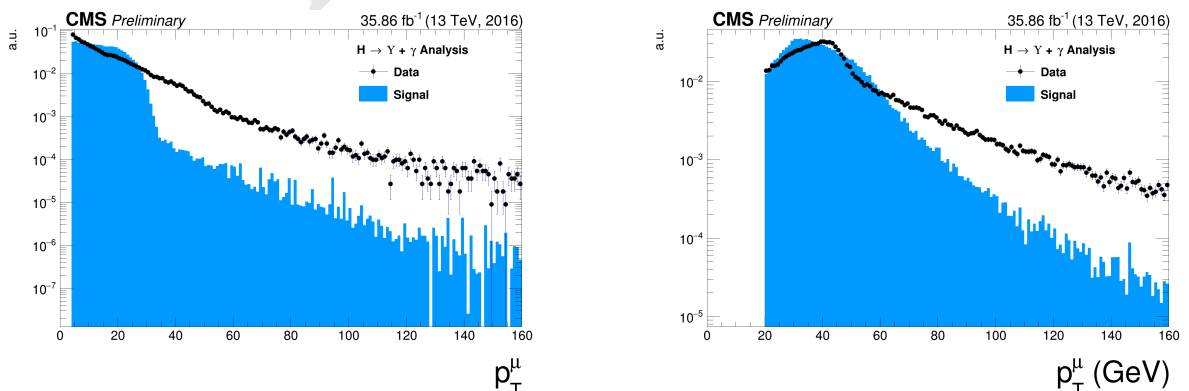


Figure 4.18: The p_T muon distributions from data and signal events for Higgs decaying in $\Upsilon(1S, 2S, 3S) + \gamma$ after Group I of selection cuts, where on left are presenting the trailing muons and on right are the leading muons. The plots are normalized to the unit of area.

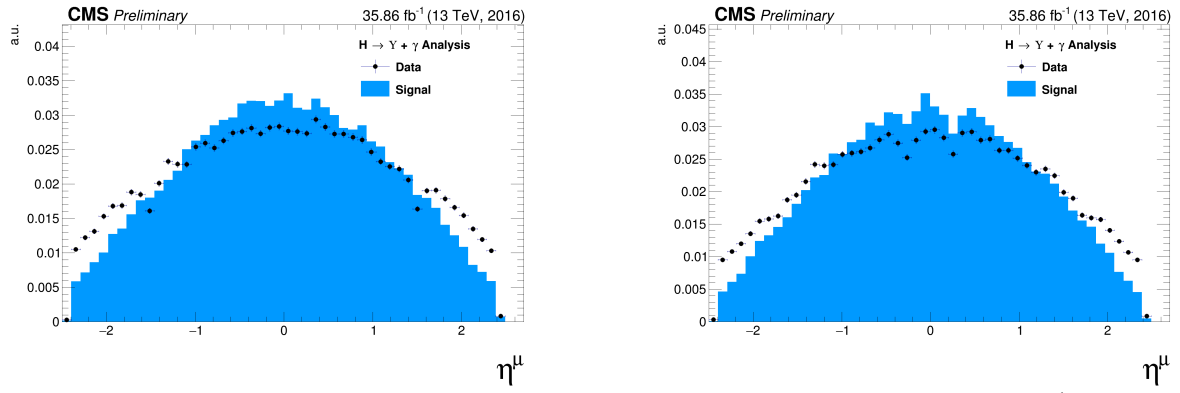


Figure 4.19: The η muon distributions from data and signal events of Higgs decaying in $\Upsilon(1S, 2S, 3S) + \gamma$ after Group I of selection cuts, where on left are presenting the trailing muons and on right are the leading muons. The plots are normalized to the unit of area.

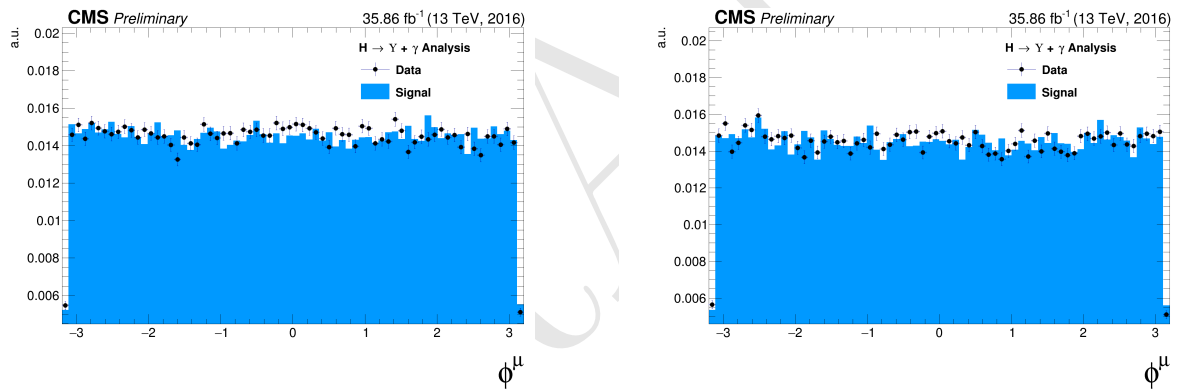


Figure 4.20: The ϕ muon distributions from data and signal events of Higgs decaying in $\Upsilon(1S, 2S, 3S) + \gamma$ after Group I of selection cuts, where on left are presenting the trailing muons and on right are the leading muons. The plots are normalized to the unit of area.

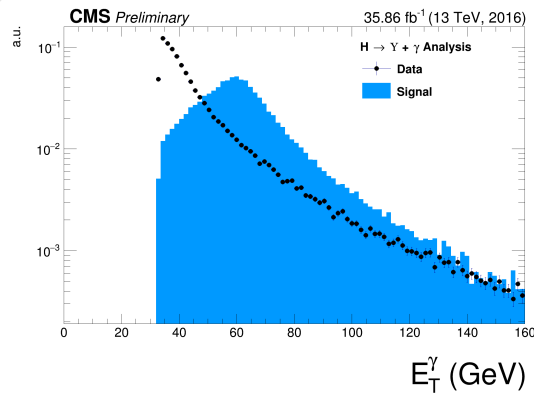


Figure 4.21: The p_T photon distributions from data and signal events for Higgs decaying in $\Upsilon(1S, 2S, 3S) + \gamma$ Group I of selection cuts. The plot is normalized to the unit of area.

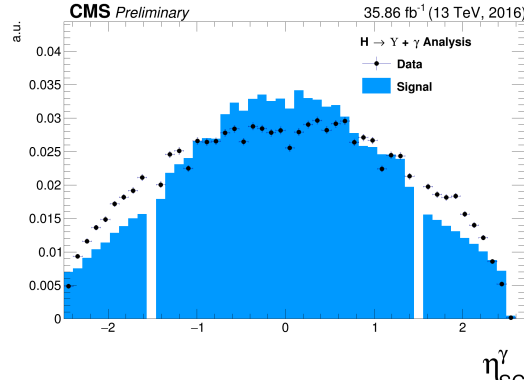


Figure 4.22: The η photon distributions from data and signal events of Higgs decaying in $\Upsilon(1S, 2S, 3S) + \gamma$ after Group I of selection cuts. The plot is normalized to the unit of area.

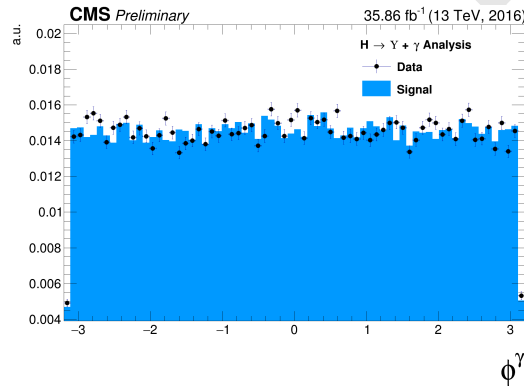


Figure 4.23: The ϕ photon distributions from data and signal events of Higgs decaying in $\Upsilon(1S, 2S, 3S) + \gamma$ after Group I of selection cuts. The plot is normalized to the unit of area.

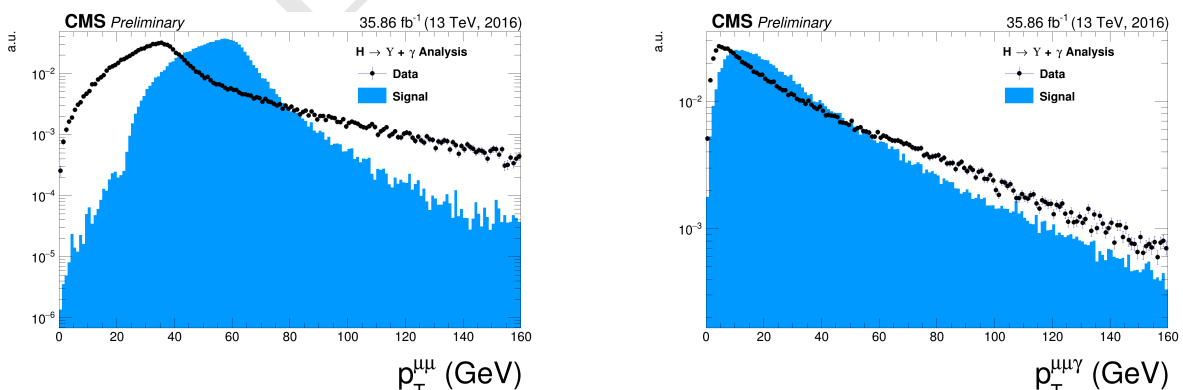


Figure 4.24: The p_T distributions for $\Upsilon(1S, 2S, 3S)$ in the left and for Higgs in the right from data and signal events for Higgs decaying in $\Upsilon(1S, 2S, 3S) + \gamma$ after Group I of selection cuts. The plots are normalized to the unit of area.

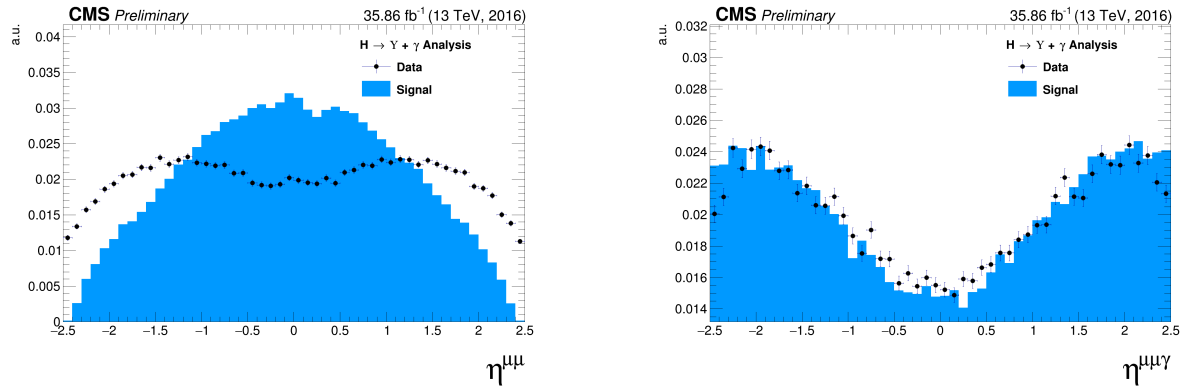


Figure 4.25: The η distributions for $\Upsilon(1S, 2S, 3S)$ in the left and for Higgs in the right from data and signal events for Higgs decaying in $\Upsilon(1S, 2S, 3S) + \gamma$ after Group I of selection cuts. The plots are normalized to the unit of area.

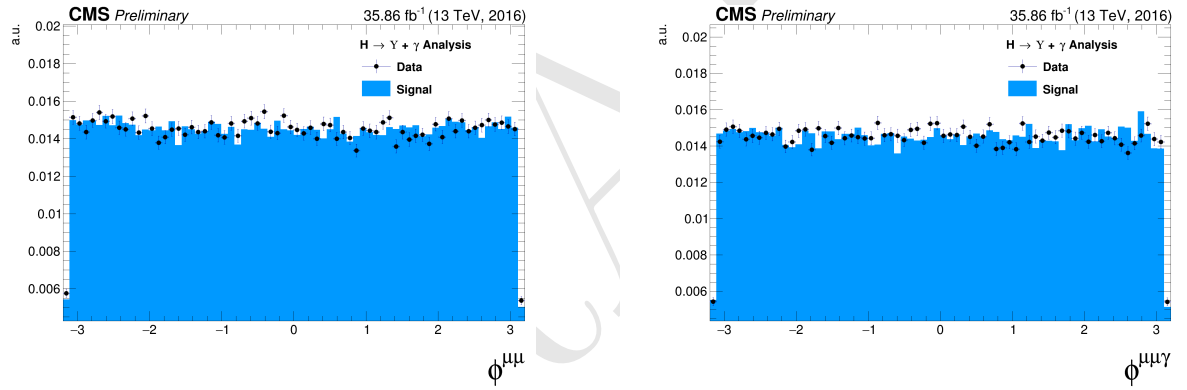


Figure 4.26: The ϕ distributions for $\Upsilon(1S, 2S, 3S)$ in the left and for Higgs in the right from data and signal events for Higgs decaying in $\Upsilon(1S, 2S, 3S) + \gamma$ after Group I of selection cuts. The plots are normalized to the unit of area.

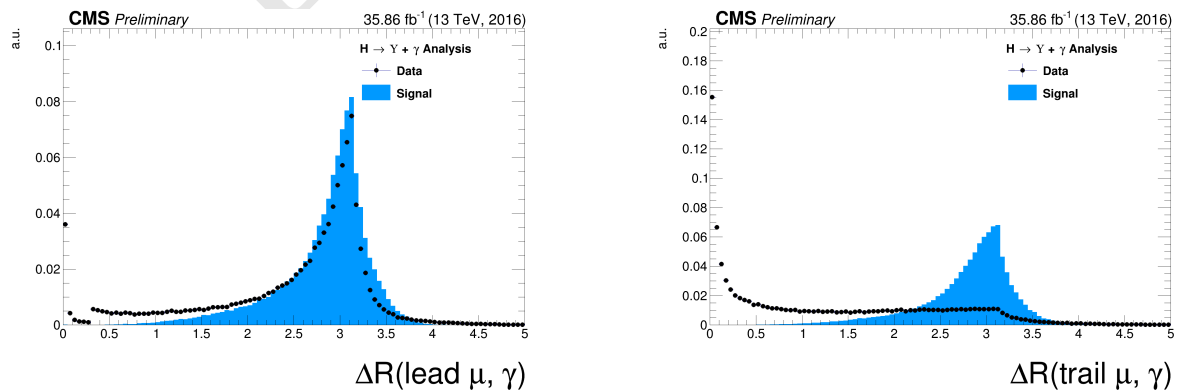


Figure 4.27: The ΔR distributions between the photon and the leading muon (left) and the trailing muon (right) for Higgs decaying in $\Upsilon(1S, 2S, 3S) + \gamma$ from data and signal events after Group I of selection cuts. The plots are normalized to the unit of area.

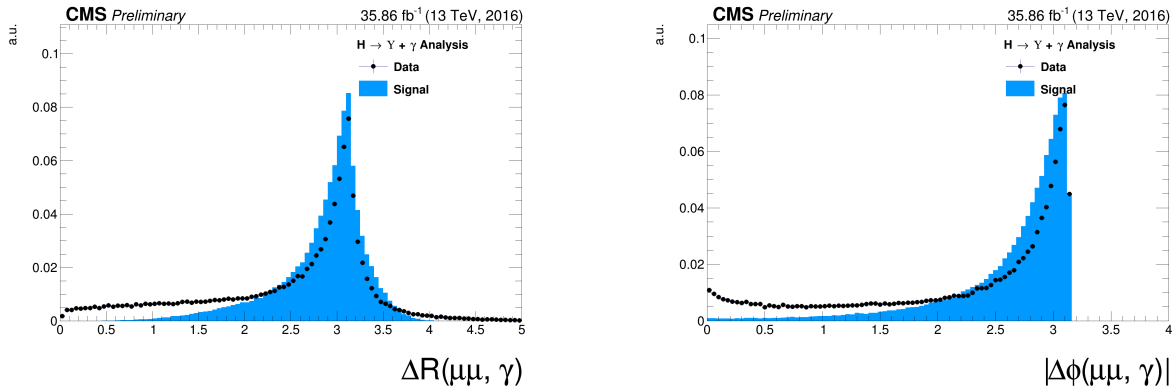


Figure 4.28: Left: The ΔR distributions between reconstructed dimuon ($\mu\mu$) system and the photon. Right: absolute value of the $\Delta\phi$ between the leading muon and the photon for for Higgs decaying in $\Upsilon(1S, 2S, 3S) + \gamma$ from data and signal events after Group I of selection cuts. The plots are normalized to the unit of area.

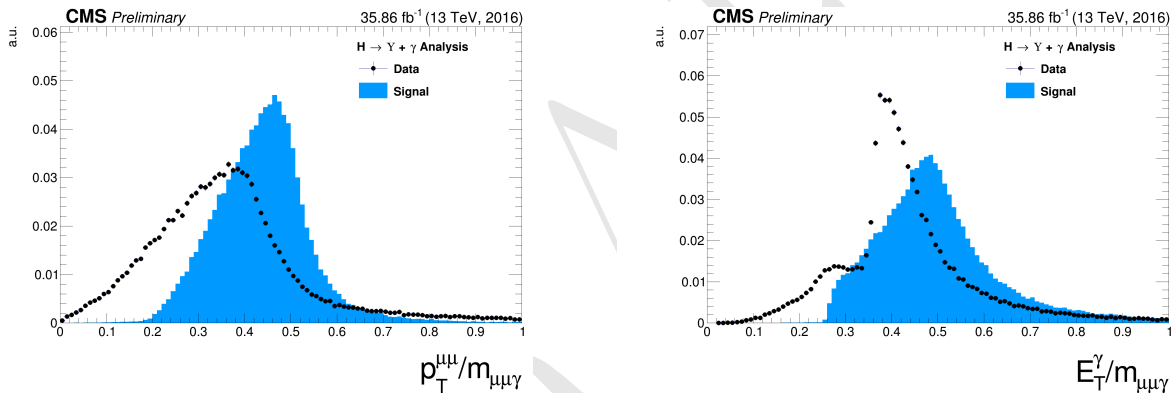


Figure 4.29: The ratio for the transverse momentum of the reconstructed Upsilon and the reconstructed Higgs mass ($p_T^{\mu\mu} / M_{\mu\mu\gamma}$ - left) and the ratio for the transverse energy of the reconstructed Photon and the reconstructed Higgs mass ($E_T^\gamma / M_{\mu\mu\gamma}$ - right) distribution for Higgs decaying in $\Upsilon(1S, 2S, 3S) + \gamma$ from data and signal events after Group I of selection cuts. The plots are normalized to the unit of area.

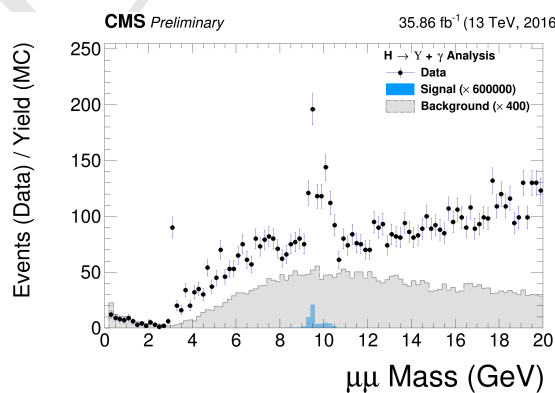


Figure 4.30: The dimuon mass distribution of the reconstructed $\Upsilon(1S, 2S, 3S)$ from data and signal events for Higgs decaying after Group I of selection cuts. This plot is normalized the expected number of events. "Signal" stands for the $H \rightarrow \Upsilon(1S, 2S, 3S) + \gamma$ sample (scaled by a factor of $\times 600000$) and "Background" corresponds to the peaking background (Higgs Dalitz Decay) sample (scaled by a factor of $\times 400$).

4.6 Kinematical selection (Group II)

After all Trigger and Object Identification cuts, described in before (**Group I**), a set of kinematical cuts are applied in order to improve the signal to background relation. They are

- $\Delta R(\text{leading } \mu, \gamma) > 1;$
- $\Delta R(\text{trailing } \mu, \gamma) > 1;$
- $\Delta R(\mu\mu, \gamma) > 2;$
- $|\Delta\phi(\text{leading } \mu, \gamma)| > 1.5;$
- $8.4 \text{ GeV} < M_{\mu\mu} < 11.1 \text{ GeV};$
- $E_T^\gamma/M_{\mu\mu\gamma} > 35/91.2 \text{ for the Z decay or } 35/125 \text{ for the Higgs decay};$
- $p_T^{\mu\mu}/M_{\mu\mu\gamma} > 35/91.2 \text{ for the Z decay or } 35/125 \text{ for the Higgs decay}.$

The choice of these thresholds were based on the visual inspection of the distributions (besides the invariant mass distribution of the dimuon system $M_{\mu\mu}$, which needs to be defined around the $v(1S, 2S, 3S)$ mass) and to keep this analysis in phase with other similar analysis within CMS.

Below it is shown the same set of plot shown before, but this time, taking into account the full selection (**Group I+II**).

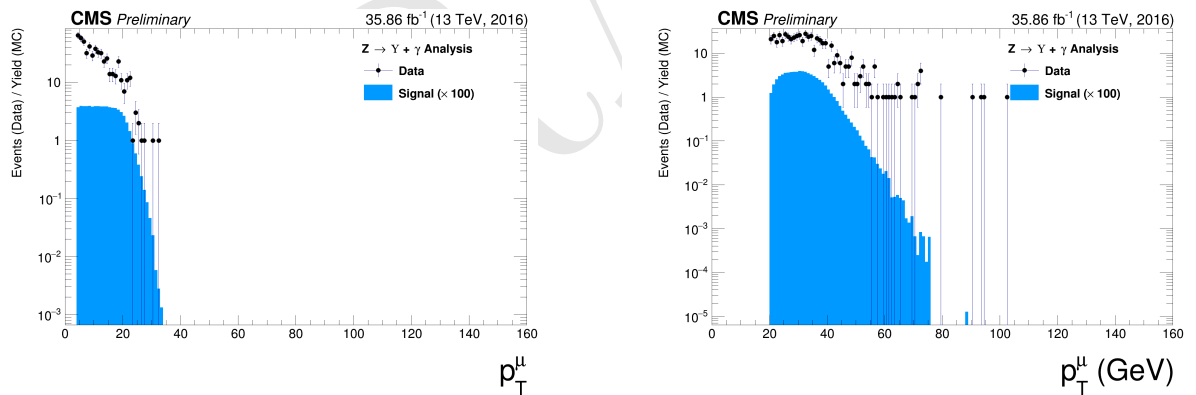


Figure 4.31: The p_T muon distributions from data and signal events for Z decaying in $\Upsilon(1S, 2S, 3S) + \gamma$ after Group I of selection cuts, where on left are presenting the trailing muons and on right are the leading muons. The plots are normalized to the number of events. Signal sample is scaled by a factor of $\times 100$.

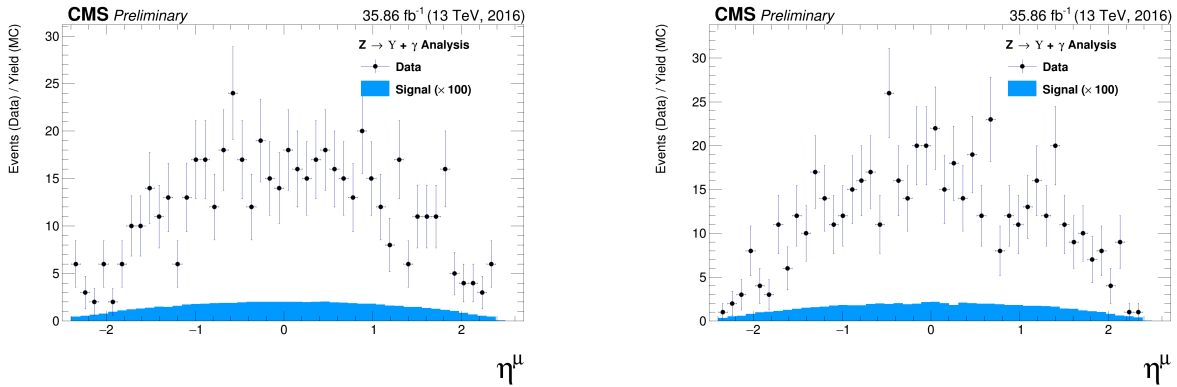


Figure 4.32: The η muon distributions from data and signal events of Z decaying in $\Upsilon(1S, 2S, 3S) + \gamma$ after Group I of selection cuts, where on left are presenting the trailing muons and on right are the leading muons. The plots are normalized to the number of events. Signal sample is scaled by a factor of $\times 100$.

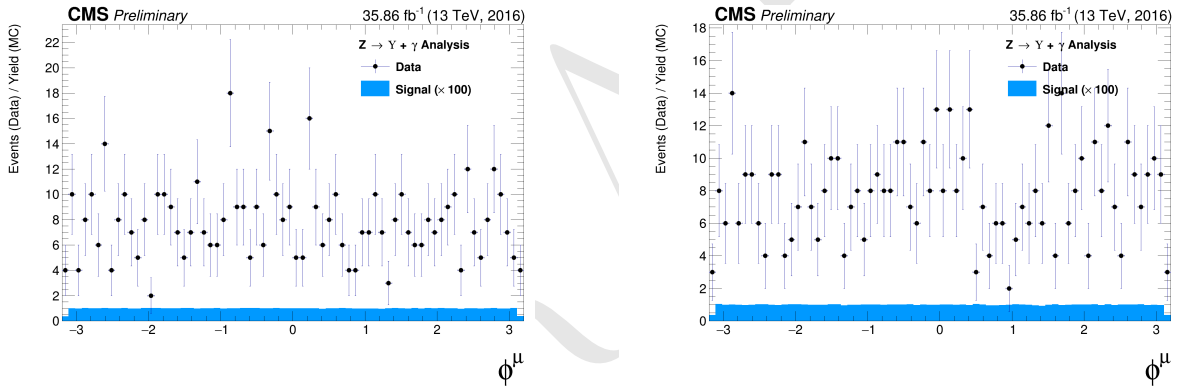


Figure 4.33: The ϕ muon distributions from data and signal events of Z decaying in $\Upsilon(1S, 2S, 3S) + \gamma$ after Group I of selection cuts, where on left are presenting the trailing muons and on right are the leading muons. The plots are normalized to the number of events. Signal sample is scaled by a factor of $\times 100$.

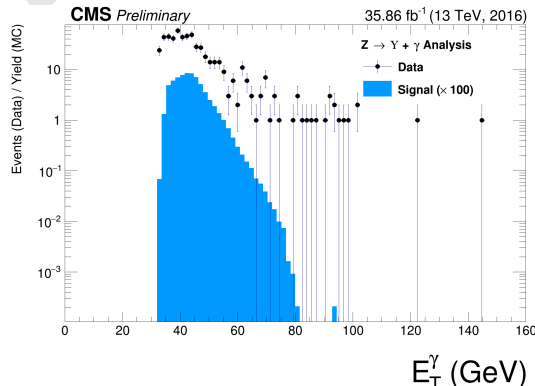


Figure 4.34: The p_T photon distributions from data and signal events for Z decaying in $\Upsilon(1S, 2S, 3S) + \gamma$ all (Group I+II) selection cuts. The plot is normalized to the number of events. Signal sample is scaled by a factor of $\times 100$.

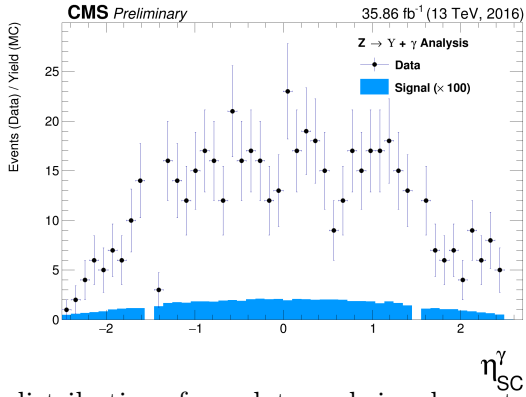


Figure 4.35: The η photon distributions from data and signal events of Z decaying in $\Upsilon(1S, 2S, 3S) + \gamma$ after all (Group I+II) selection cuts. The plot is normalized to the number of events. Signal sample is scaled by a factor of $\times 100$.

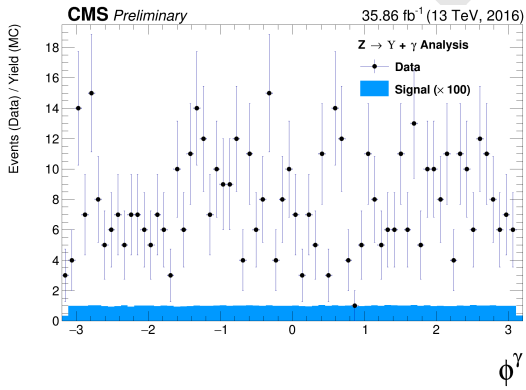


Figure 4.36: The ϕ photon distributions from data and signal events of Z decaying in $\Upsilon(1S, 2S, 3S) + \gamma$ after all (Group I+II) selection cuts. The plot is normalized to the number of events. Signal sample is scaled by a factor of $\times 100$.

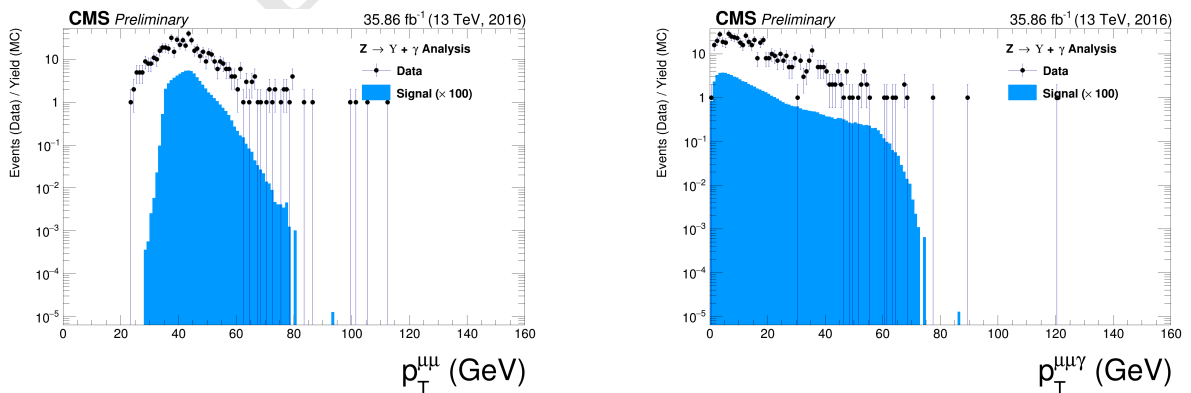


Figure 4.37: The p_T distributions for $\Upsilon(1S, 2S, 3S)$ in the left and for Z in the right from data and signal events for Z decaying in $\Upsilon(1S, 2S, 3S) + \gamma$ after all (Group I+II) selection cuts. The plots are normalized to the number of events. Signal sample is scaled by a factor of $\times 100$.

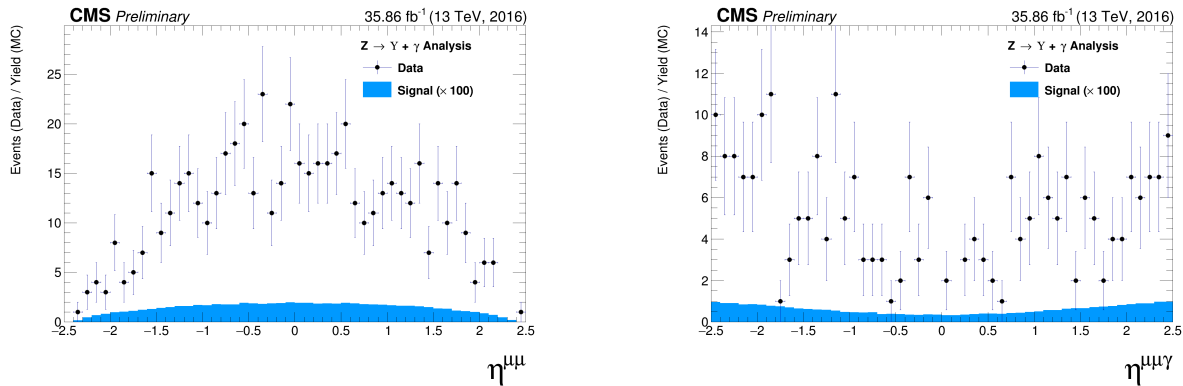


Figure 4.38: The η distributions for $\Upsilon(1S, 2S, 3S)$ in the left and for Z in the right from data and signal events for Z decaying in $\Upsilon(1S, 2S, 3S) + \gamma$ after all (Group I+II) selection cuts. The plots are normalized to the number of events. Signal sample is scaled by a factor of $\times 100$.

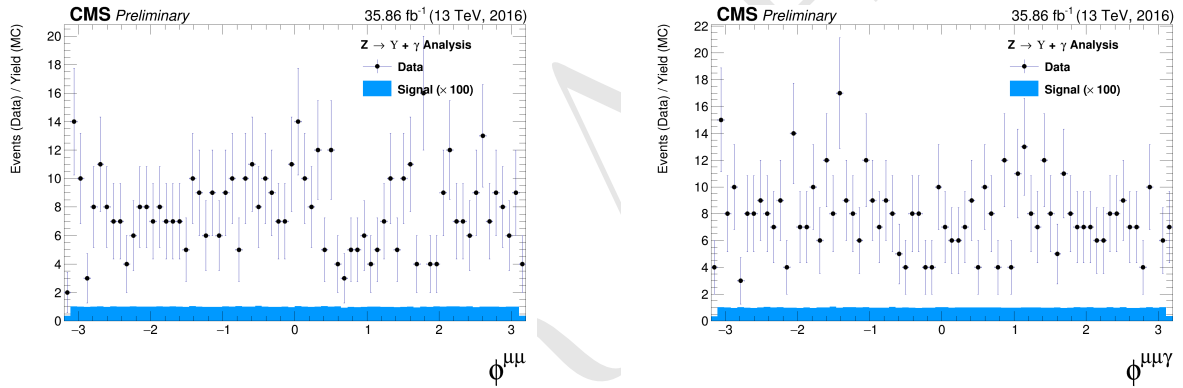


Figure 4.39: The ϕ distributions for $\Upsilon(1S, 2S, 3S)$ in the left and for Z in the right from data and signal events for Z decaying in $\Upsilon(1S, 2S, 3S) + \gamma$ after all (Group I+II) selection cuts. The plots are normalized to the number of events. Signal sample is scaled by a factor of $\times 100$.

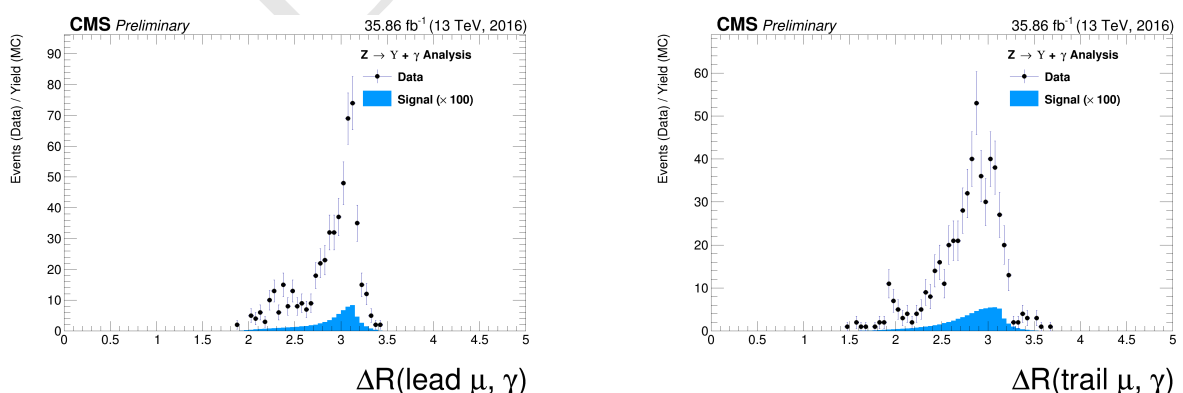


Figure 4.40: The ΔR distributions between the photon and the leading muon (left) and the trailing muon (right) for $\Upsilon(1S, 2S, 3S)$ from data and signal events for Z decaying after all (Group I+II) selection cuts. The plots are normalized to the number of events. Signal sample is scaled by a factor of $\times 100$.

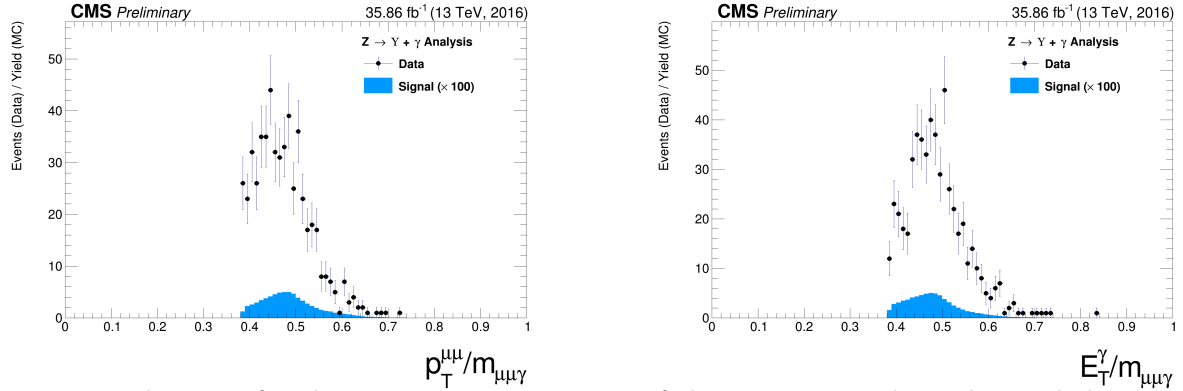


Figure 4.41: The ratio for the transverse momentum of the reconstructed Upsilon and the reconstructed Z mass ($p_T^{\mu\mu}/M_{\mu\mu\gamma}$ - left) and the ratio for the transverse energy of the reconstructed Photon and the reconstructed Z mass ($E_T^{\mu\mu}/M_{\mu\mu\gamma}$ - right) distribution for $\Upsilon(1S, 2S, 3S)$ from data and signal events for Z decaying after all (Group I+II) selection cuts. The plots are normalized to the number of events. Signal sample is scaled by a factor of $\times 100$.

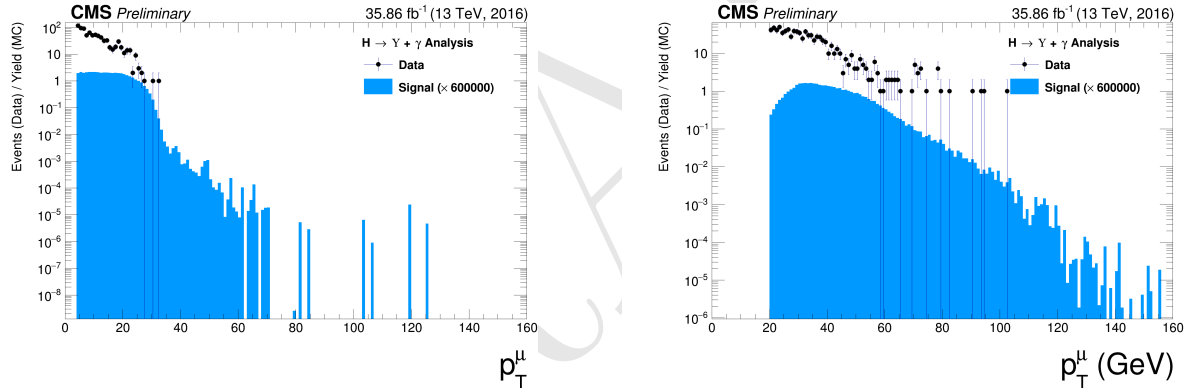


Figure 4.42: The p_T muon distributions from data and signal events for Higgs decaying in $\Upsilon(1S, 2S, 3S) + \gamma$ after Group I of selection cuts, where on left are presenting the trailing muons and on right are the leading muons. The plots are normalized to the number of events. Signal sample is scaled by a factor of $\times 600000$.

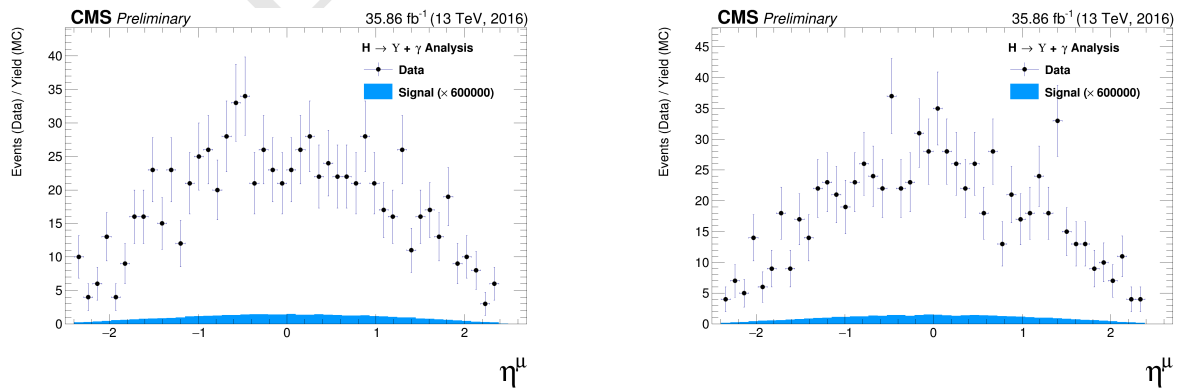


Figure 4.43: The η muon distributions from data and signal events of Higgs decaying in $\Upsilon(1S, 2S, 3S) + \gamma$ after Group I of selection cuts, where on left are presenting the trailing muons and on right are the leading muons. The plots are normalized to the number of events. Signal sample is scaled by a factor of $\times 600000$.

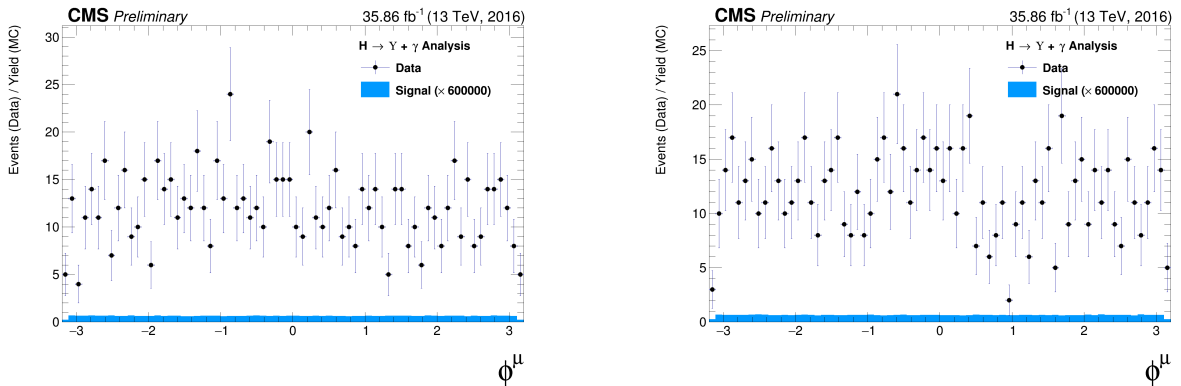


Figure 4.44: The ϕ muon distributions from data and signal events of Higgs decaying in $\Upsilon(1S, 2S, 3S) + \gamma$ after Group I of selection cuts, where on left are presenting the trailing muons and on right are the leading muons. The plots are normalized to the number of events. Signal sample is scaled by a factor of $\times 600000$.

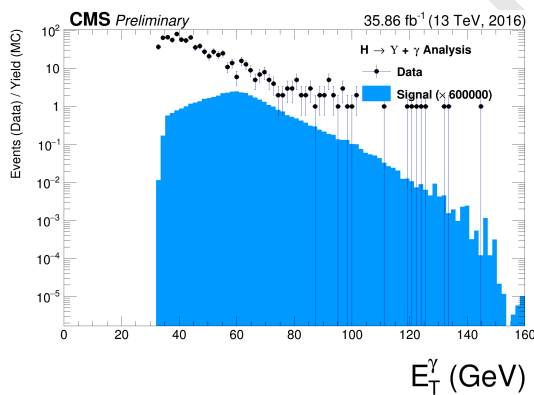


Figure 4.45: The p_T photon distributions from data and signal events for Higgs decaying in $\Upsilon(1S, 2S, 3S) + \gamma$ all (Group I+II) selection cuts. The plot is normalized to the number of events. Signal sample is scaled by a factor of $\times 600000$.

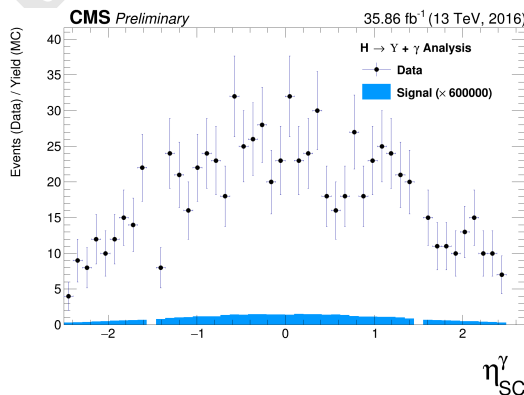


Figure 4.46: The η photon distributions from data and signal events of Higgs decaying in $\Upsilon(1S, 2S, 3S) + \gamma$ after all (Group I+II) selection cuts. The plot is normalized to the number of events. Signal sample is scaled by a factor of $\times 600000$.

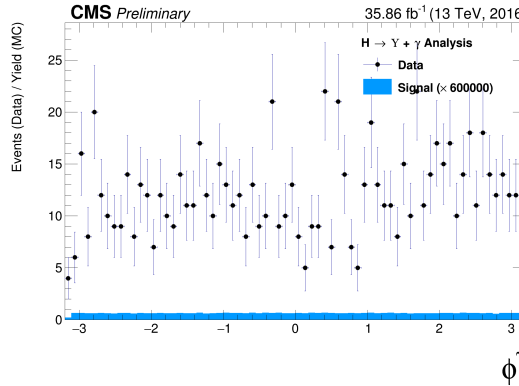


Figure 4.47: The ϕ photon distributions from data and signal events of Higgs decaying in $\Upsilon(1S, 2S, 3S) + \gamma$ after all (Group I+II) selection cuts. The plot is normalized to the number of events. Signal sample is scaled by a factor of c .

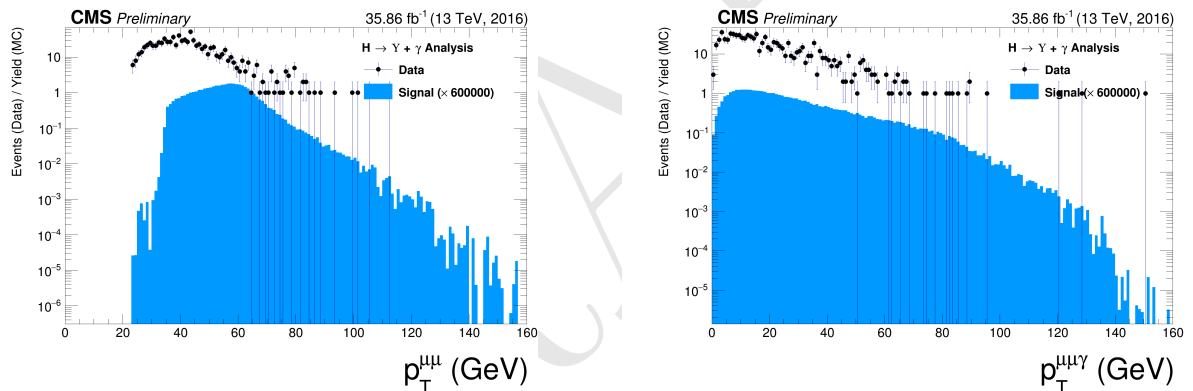


Figure 4.48: The p_T distributions for $\Upsilon(1S, 2S, 3S)$ in the left and for Higgs in the right from data and signal events for Higgs decaying in $\Upsilon(1S, 2S, 3S) + \gamma$ after all (Group I+II) selection cuts. The plots are normalized to the number of events. Signal sample is scaled by a factor of $\times 600000$.

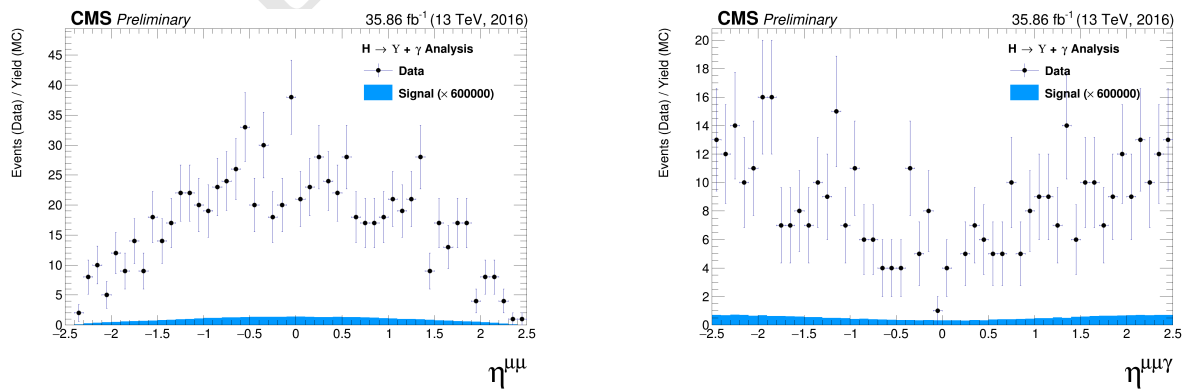


Figure 4.49: The η distributions for $\Upsilon(1S, 2S, 3S)$ in the left and for Higgs in the right from data and signal events for Higgs decaying in $\Upsilon(1S, 2S, 3S) + \gamma$ after all (Group I+II) selection cuts. The plots are normalized to the number of events. Signal sample is scaled by a factor of $\times 600000$.

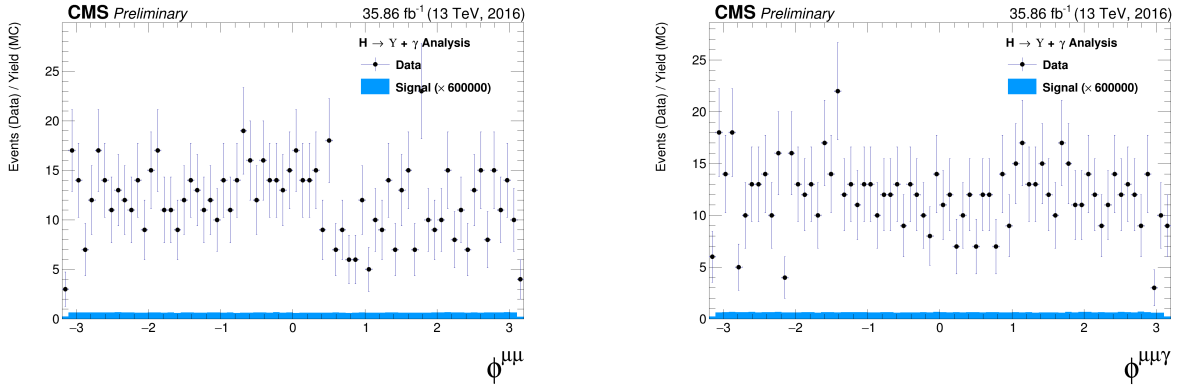


Figure 4.50: The ϕ distributions for $\Upsilon(1S, 2S, 3S)$ in the left and for Higgs in the right from data and signal events for Higgs decaying in $\Upsilon(1S, 2S, 3S) + \gamma$ after all (Group I+II) selection cuts. The plots are normalized to the number of events. Signal sample is scaled by a factor of $\times 600000$.

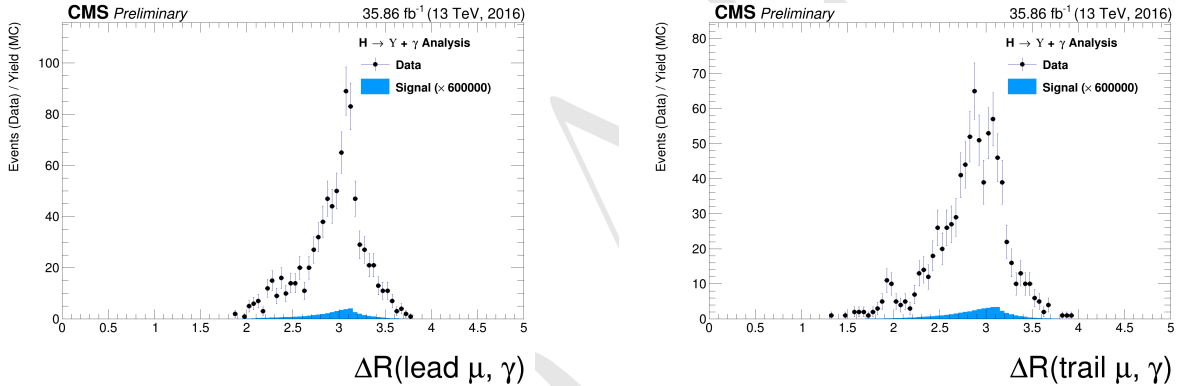


Figure 4.51: The ΔR distributions between the photon and the leading muon (left) and the trailing muon (right) for $\Upsilon(1S, 2S, 3S)$ from data and signal events for Higgs decaying after all (Group I+II) selection cuts. The plots are normalized to the number of events. Signal sample is scaled by a factor of $\times 600000$.

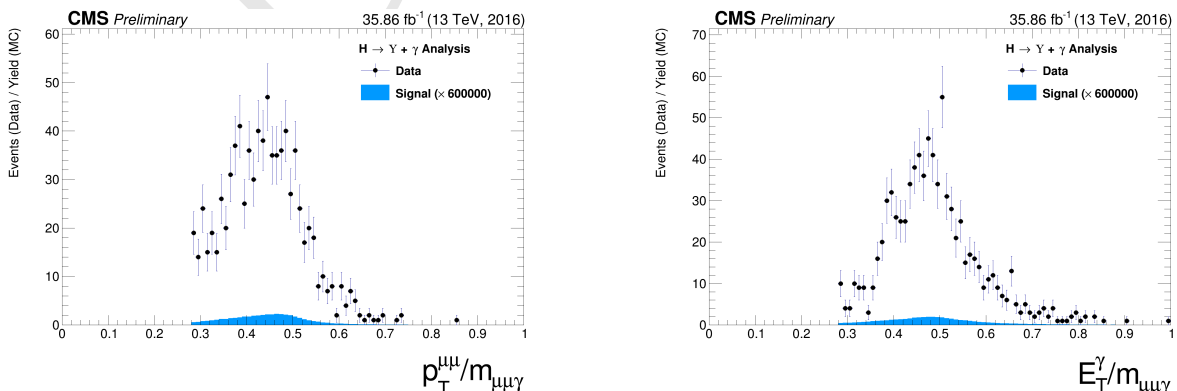


Figure 4.52: The ratio for the transverse momentum of the reconstructed Upsilon and the reconstructed Higgs mass ($p_T^{\mu\mu}/M_{\mu\mu\gamma}$ - left) and the ratio for the transverse energy of the reconstructed Photon and the reconstructed Higgs mass ($E_T^\gamma/M_{\mu\mu\gamma}$ - right) distribution for $\Upsilon(1S, 2S, 3S)$ from data and signal events for Higgs decaying after all (Group I+II) selection cuts. The plots are normalized to the number of events. Signal sample is scaled by a factor of $\times 600000$.

¹⁴⁹⁴ 4.7 Event categorization and yields

¹⁴⁹⁵ In order to increase the sensibility of the analysis, a categorization procedure was applied. They
¹⁴⁹⁶ are based on the η and R9 distribution of the reconstructed photon.

¹⁴⁹⁷ The photon R9 is a shower shape variable defined as the fraction of energy deposited in the 5x5
¹⁴⁹⁸ square surrounding the Super Cluster seed of the reconstructed photon. A photon that convert
¹⁴⁹⁹ before reaching the ECAL tend to have lower values of R9, in comparison with unconverted photons.
¹⁵⁰⁰ Converted photons have wider energy resolution and are more likely to be misidentified.

¹⁵⁰¹ Selected events with the photon reconstructed inside the barrel and with $R9 > 0.94$ are categorized
¹⁵⁰² as "EB High R9"⁶, selected events with the photon reconstructed inside the barrel and with
¹⁵⁰³ $R9 < 0.94$ are categorized as "EB Low R9" and selected events with the photon reconstructed
¹⁵⁰⁴ inside the endcap, regardless of its R9 value, categorized as "EE". This categorization is done in
¹⁵⁰⁵ view of increase the analysis sensitivity.

¹⁵⁰⁶ This categorization is implemented only for the Z decay. The Higgs does not present enough
¹⁵⁰⁷ statistics to make it profitable, so only the inclusive one is used.

¹⁵⁰⁸ 4.7.1 R9 reweighting

¹⁵⁰⁹ As spotted by the $H \rightarrow \gamma\gamma$ at $\sqrt{13}$ TeV analysis [113], there is a disagreement in the R9 distribution
¹⁵¹⁰ of photons in Data and MC. In order to mitigate this difference, a transformation factor is extracted
¹⁵¹¹ and applied to the reconstructed photons before the categorization.

¹⁵¹² The same approach of the $H \rightarrow \gamma\gamma$ analysis is applied, in which the nominal photon selection of this
¹⁵¹³ analysis (see section 4.5.3) is used to select photons on Data and MC. Then the two distributions
¹⁵¹⁴ are remapped and the transformation factors are extracted.

¹⁵¹⁵ Figure 4.53 show the R9 distribution before and after the reweighting, for the Barrel and the Endcap.

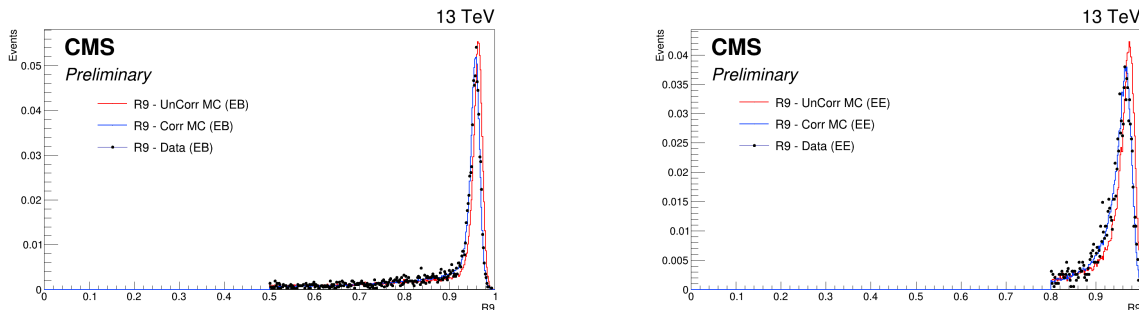


Figure 4.53: Data and MC of the R9 variable, before and after the reweighting. Barrel (left) and Endcap (right).

⁶EB stands for Electromagnetic Barrel

1516 **4.7.2 Event counting and yields**

1517 Tables 4.4 and 4.5 show the total number of events before and after the full selection. Two things
1518 are important to notice.

Table 4.4: Number of events for the Z decay, before and after the full selection, per categorization scenarios.

	Data	Signal			$Z \rightarrow \mu\mu\gamma_{FSR}$
		$Z \rightarrow \Upsilon(1S) + \gamma$	$Z \rightarrow \Upsilon(2S) + \gamma$	$Z \rightarrow \Upsilon(3S) + \gamma$	
Total (before selection)	169.84 M	3.54	1.4	1.22	3.33×10^3
Inclusive	447	0.393	0.157	0.136	176
EB High R9	197	0.172	0.0682	0.0597	78
EB Low R9	146	0.129	0.0519	0.0448	58.5
EE	104	0.0916	0.0365	0.032	39.8

Table 4.5: Number of events for the H decay, before and after the full selection.

	Data	Signal			$H \rightarrow \gamma\gamma^*$
		$H \rightarrow \Upsilon(1S) + \gamma$	$H \rightarrow \Upsilon(2S) + \gamma$	$H \rightarrow \Upsilon(3S) + \gamma$	
Total (before selection)	169.84 M	0.000257	5.43×10^{-5}	3.93×10^{-5}	136
Inclusive	231	5.23×10^{-5}	1.2×10^{-5}	8.96×10^{-6}	1.22

1519 The signal selection efficiency is between 20% and 21% for all Υ states and categories.

1520 When one compares the fraction of selected peaking background, with respect to the selected data
1521 events for the Higgs decay (1.22/231), the fraction obtained ($\sim 0.3\%$) is irrelevant. On the other
1522 hand, the same fraction for the Z decay (176/447) is far from irrelevant ($\sim 39\%$)⁷. The same relation
1523 is not found in the $H/Z \rightarrow J/\psi + \gamma$ analysis [60], where both decays (Higgs and Z) show neglectable
1524 estimations of peaking background contribution to data. The very same behavior was found by
1525 ATLAS [57]. It can be explained by the relatively larger cross-section of the Z peaking background
1526 ($Z \rightarrow \mu\mu\gamma_{FSR}$), with respect to the Higgs peaking background (Higgs Dalitz Decay). For the J/ψ
1527 channel, it is not an issue since its cross-section is way larger than the peaking background. The
1528 figures 4.17 and 4.30 help to clarify these affirmations, for the Z and Higgs decay, respectively. One
1529 can easily see how clear the J/ψ peak is in both decays and how minor the Higgs Dalitz Decay
1530 contributions is to the Υ peak, with respect to the $Z \rightarrow \mu\mu\gamma_{FSR}$ contribution. It is important to
1531 keep in mind the different scaling of the peaking background distributions, x3 for the Z and $\times 100$
1532 for the Higgs. The peaking background to the data due to $Z \rightarrow \Upsilon(1S, 2S, 3S) + \gamma$ channel is the
1533 main motivation to use a 2-dimensional modeling fitting of the signal and background events, in
1534 order to add one more layer of differentiation between many backgrounds contributions which will
1535 be detailed in the next section.

⁷It is worth to keep in mind that this is a estimation based on MC

1536 4.8 Background modeling

1537 The background modeling proposed for this analysis is a two dimensional unbinned maximum
 1538 likelihood fit on the $\mu\mu$ and the $\mu\mu\gamma$ invariant mass distributions. It is considered and modeled, as
 1539 briefly discussed in 4.1.2, three kinds of backgrounds:

- 1540 • **Full Combinatorial:** any combination of two muon and one photon that pass all the object
 1541 reconstruction and event selection criteria.
- 1542 • **Υ Combinatorial:** a $\Upsilon(1S, 2S, 3S)$, that decays to a dimuon system, combined with a
 1543 misidentified photon (misreconstructed, pileup photon, etc.), that pass all the object recon-
 1544 struction, identification and event selection criteria.
- 1545 • **Peaking background:** a Z (or Higgs) that decays straight to a $\mu\mu\gamma$, that pass all the object
 1546 reconstruction and event selection criteria, without passing through any intermediate state.
 1547 The main contributions considered for this background are $Z \rightarrow \mu\mu\gamma_{FSR}$ (a Z decaying to a
 1548 dimuon system with one of the muons irradiating a photon) or a Higgs Dalitz Decay.

1549 All of them will be modeled from data, with some inputs from the MC (simulated) samples, as
 1550 explained below. For both invariant mass spectra ($\mu\mu$ and $\mu\mu\gamma$) the full combinatorial background
 1551 is expected to behave like a non-peaking distribution. The same behavior is expected for the $\mu\mu\gamma$
 1552 mass distribution of the Υ Combinatorial background and for the $\mu\mu$ mass distribution of the
 1553 peaking background.

1554 On the other hand, the $\mu\mu$ distribution of the Υ Combinatorial background and the $\mu\mu\gamma$ mass
 1555 distribution for the peaking background are expected to behave like a peaking distribution, centered
 1556 around the $\Upsilon(1S, 2S, 3S)$ invariant mass (9.46 GeV, 10.02 GeV and 10.35 GeV) [13] and the Z boson
 1557 invariant mass (91.2 GeV) [13], respectively . Table 4.6 summarizes the background modeling
 1558 proposed for this analysis.

Table 4.6: Modeling for each background source and mass component.

	$m_{\mu\mu}$	$m_{\mu\mu\gamma}$
Peaking background	Bernstein 1 st order	Crystal Ball (Higgs decay) Double Crystal Ball (Z decay)
Υ Combinatorial	3 Gaussians (one for each Υ state)	
Full Combinatorial	Chebychev 1 st order	Polynomial

1559 For the $Z \rightarrow \Upsilon(1S, 2S, 3S) + \gamma$ analysis, the peaking background model parameters are extracted
 1560 by performing a simultaneous 2-dimensional fit over the invariant masses, $m_{\mu\mu}$ and $m_{\mu\mu\gamma}$, of the
 1561 simulated $Z \rightarrow \mu\mu\gamma_{FSR}$ MC sample of events that passes the selection described in Section 4.4, as in
 1562 figure 4.54. Once the parameters are extracted, they are fixed and the *pdf* (Probability Distributions
 1563 Function) of the 2-Dimensional modeling is stored, leaving only the normalization of the *pdf* as a
 1564 parameter free to float (this will be determined from data).

1565 In order to describe the 2-dimensional invariant mass distribution of the Peaking Background, as
 1566 stated in Table 4.6, the $m_{\mu\mu}$ component is described by a Bernstein polynomial of 1st order [114],
 1567 which is used here just a representation of a linear function. The $m_{\mu\mu\gamma}$ component is described

1568 by Double Crystal Ball function [115]. A Crystal Ball function is a *pdf* composed by a gaussian
 1569 distribution and a power-law tail to the left, before certain threshold. The Crystal Ball function was
 1570 named after the Crystal Ball Collaboration (first to use this *pdf*) and it is widely used in high-energy
 1571 physics to describe mass distributions that incorporate FSR (final state radiation) effects, via the
 1572 power-law tail. A Double Crystal Ball is a Crystal Ball function with the power-law tail on both
 1573 sides.

1574 A Crystal Ball function is defined as:

$$CB(x; \alpha, n, \bar{x}, \sigma) = N \cdot \begin{cases} \exp\left(-\frac{(x-\bar{x})^2}{2\sigma^2}\right), & \text{for } \frac{x-\bar{x}}{\sigma} > -\alpha \\ A \cdot (B - \frac{x-\bar{x}}{\sigma})^{-n}, & \text{for } \frac{x-\bar{x}}{\sigma} \leq -\alpha \end{cases}, \quad (4.4)$$

1575 where,

$$\begin{aligned} A &= \left(\frac{n}{|\alpha|}\right)^n \cdot \exp\left(-\frac{|\alpha|^2}{2}\right), \\ B &= \frac{n}{|\alpha|} - |\alpha|, \\ N &= \frac{1}{\sigma(C + D)}, \\ C &= \frac{n}{|\alpha|} \cdot \frac{1}{n-1} \cdot \exp\left(-\frac{|\alpha|^2}{2}\right), \\ D &= \sqrt{\frac{\pi}{2}} \left(1 + \operatorname{erf}\left(\frac{|\alpha|}{\sqrt{2}}\right)\right), \end{aligned}$$

1576 and erf is the error function.

1577 For the three gaussian functions fits, which represent the three Υ states (1S, 2S and 3S) from the Υ
 1578 Combinatorial background in the $m_{\mu\mu}$ component, we use a Υ control sample in order to extract the
 1579 fit parameters, including the relative normalization between each Υ state. This sample is composed
 1580 by dimuon candidates obtained from data, by selecting the events that passes the same trigger and
 1581 dimuon selection of the nominal selection and with $p_T^{\mu\mu} > 35$ GeV (this cut is done in order to
 1582 keep this selected dimuon candidates compatibles with the $p_T^{\mu\mu}/M_{\mu\mu\gamma}$ cut applied in the nominal
 1583 selection). No selection or cuts in the photon are required.

1584 This control sample is fitted with a Chebychev 1st order (linear polynomial) for the background
 1585 support and 3 gaussian with the following constraints:

- 1586 • the mean of each state should be the ones in the PDG [13], but allowed to shift by a float and
 1587 common (the same for all states) value.
- 1588 • the sigma should be based on the 1S fit of the MC. All other sigma should be the result of
 1589 the 1S sigma times the state mass over the 1S mass ($\sigma_{2S,3S} = \frac{m_{2S,3S}}{m_{1S}} \sigma_{1S}$).

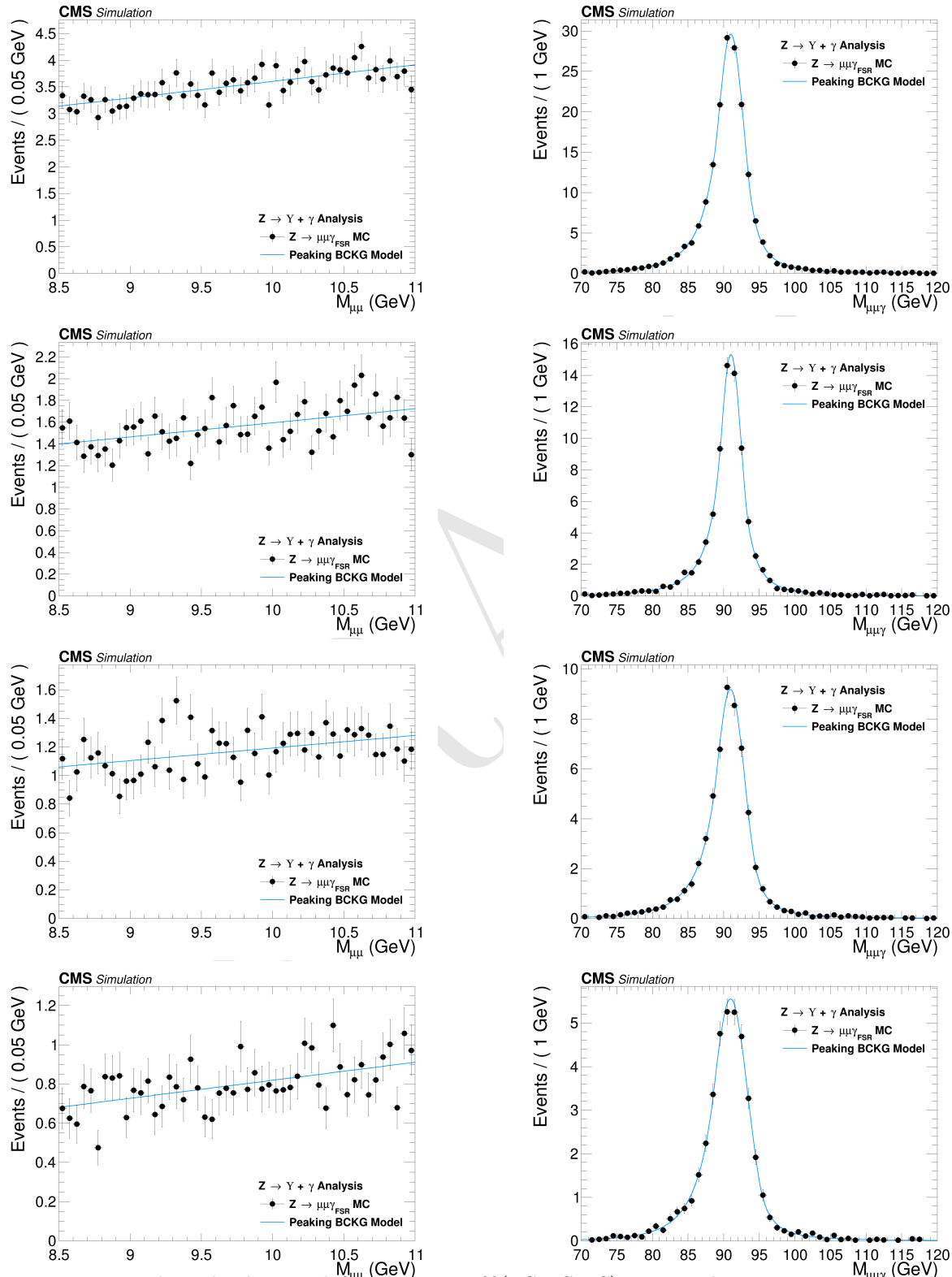


Figure 4.54: Peaking background for the $Z \rightarrow \Upsilon(1S, 2S, 3S) + \gamma$ analysis. $\mu\mu$ mass distribution (left) and $\mu\mu\gamma$ invariant mass distribution (right). From top to bottom categories: Inclusive, EB High R9, EB Low R9, EE.

1590 The idea behind this fit is that scale and resolution (mean and sigma, respectively, of the gaussians)
 1591 over a sample without a photon selection should be the same as over a sample with photon selection,
 1592 since these are detector only dependent effects. The fact that we exclude the photon from this control
 1593 sample, improves the statistics and gives a better measurement of these variables.

1594 The fit of the Υ control sample if shown in figure 4.55.

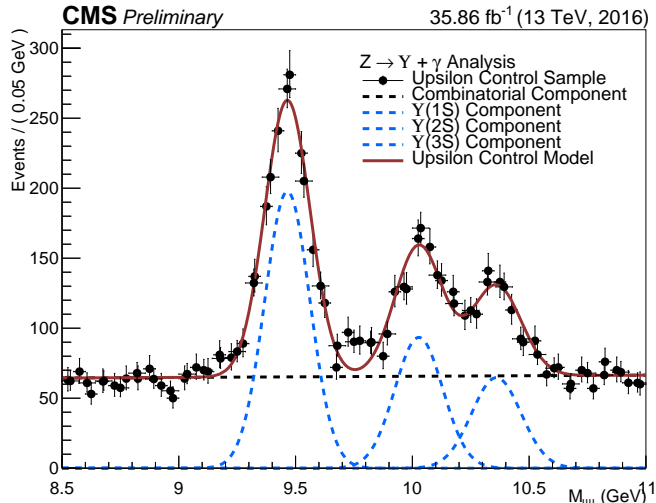


Figure 4.55: Υ control sample fit with Chebychev 1st order for the background support and 3 gaussian for the three $\Upsilon(1S, 2S, 3S)$ peaks.

1595 Once determined, the fit parameters are fixed, they are used to compose the 2-Dimensional *pdf*. The
 1596 $m_{\mu\mu}$ component of the full combinatorial background is derived fully from the data fit (described
 1597 below). In the same sense, the $m_{\mu\mu\gamma}$ component of the full combinatorial and the $\Upsilon(nS)$ Combin-
 1598 torial backgrounds are also fully derived from the data, but following a more complex procedure: a
 1599 composition with the *pdf* components described above, plus a statistical test, to avoid overfitting
 1600 within a Discrete Profiling (or "Envelope Method"), as described in [116] and also implemented
 1601 in [113].

1602 The statistical test consists of, for each category, different orders of a set of polynomial *pdfs* families
 1603 are tested: a sums of exponentials, sum of polynomials (in the Bernstein basis), a Laurent series
 1604 and a sums of power-law functions.

- Sums of exponentials:

$$f_N(x) = \sum_{i=1}^N p_{2i} e^{p_{2i+1}x},$$

- Sums of polynomials (in the Bernstein basis):

$$f_N(x) = \sum_{i=0}^N p_i b_{(i,N)}, \text{ where } b_{(i,N)} := \binom{N}{i} x^i (1-x)^{N-i},$$

- Laurent series:

$$f_N(x) = \sum_{i=1}^N p_i x^{-4+\sum_{j=1}^i (-1)^j(j-1)},$$

- Sums of power-law functions:

$$f_N(x) = \sum_{i=1}^N p_{2i} x^{-p_{2i+1}},$$

1605 where for all k , the p_k are a set of floating parameters in the fit.

1606 Twice difference in the negative log-likelihood (NLL) between the N^{th} and the $(N+1)^{th}$ order of
 1607 the same polynomial ($\Delta NLL = 2 \times (NLL_N - NLL_{N+1})$) is expected to follow a χ^2 distribution
 1608 with M degrees of freedom, where M is the increase in degrees of freedom when going from N^{th} to
 1609 $(N+1)^{th}$. This can be shown with the help of the Wilks' theorem [117].

1610 Starting from the lowest order possible, the best choice of order, for each family, is determined when
 1611 a increase in the order of the polynomial, does not brings a significant improvement in the quality
 1612 of the fit. Since a model with more fit parameters (higher order polynomials) will always perform,
 1613 if not the same, better than a simpler one, an optimal choice of the polynomial order, will be the
 1614 one right before the model becomes too flexible for the data.

1615 Consider a p -value defined as:

$$\begin{aligned} p\text{-value} &= \int_{\Delta NLL}^{\infty} \chi_M^2(\Delta) d\Delta \\ &= P(\chi_M^2 > \Delta NLL), \end{aligned} \tag{4.5}$$

1616 In the same spirit as the Wilks' theorem, this is the p -value for a likelihood ratio test between a
 1617 null hypotheses and an alternative model, where the null hypotheses is the N^{th} order and $(N+1)^{th}$
 1618 order is the alternative one.

$$\begin{aligned} \Delta NLL &= 2 \times (NLL_N - NLL_{N+1}) \\ &= -2 \times \log\left(\frac{\mathcal{L}_N}{\mathcal{L}_{N+1}}\right), \end{aligned} \tag{4.6}$$

1619 where \mathcal{L}_N is the likelihood for the N^{th} polynomial order.

1620 The alternative will present a statistically significant improvement, with respect to the null hypothe-
 1621 ses, if the p -value is smaller than 0.05, since the probability of obtaining, by chance, considering
 1622 the null hypotheses is true, a even higher ΔNLL is less than 5%. This will give support to chose
 1623 $(N+1)^{th}$ over N^{th} .

1624 If the p -value is greater than 0.05 a higher order is not supported, since the probability of obtaining
 1625 a ΔNLL greater than the one observed is statistically significant (more than 5%). A higher ΔNLL

means that another data sample, collected and analyzed with strictly the same conditions, would have a probability of more than 5% of giving a better fit improvement than the one observed, again assuming that the null hypotheses is true. This is an indication of overfitting, since the improvements are likely to come from just statistical fluctuations. When testing the $(N+1)^{th}$ order and this condition is reached, the optimal order should be the N^{th} .

At first, before any fit to data, the 2-Dimensional model is composed by the five components, as described in Table 4.6 (in which the $m_{\mu\mu\gamma}$ modeling for the Full Combinatorial Background and the Υ combinatorial are shared), then, the statistical test described before is ran for each family. It is important to stress that before the statistical test all the other fitting parameters have been fixed. This leaves only the normalizations of the model components and the polynomial coefficients free to float.

Once the optimal order for each *pdf* family is obtained, the composed *pdf* with each choice from statistical test is saved in the same model, providing a discrete variable that indexes the different polynomial *pdf* families. This method is called Discrete Profiling (or "*Envelope Method*") and it allows the analysis algorithm to treat the choice of the *pdf* as a systematics and incorporate its effect in the extracted upper limits. This model, with different choices of polynomial families is called envelope.

The implementation, used in the analysis, of the statistical test and the Discrete Profiling is based on the same algorithm used by the $H \rightarrow \gamma\gamma$ Run II analysis. An extensive documentation on these methods can be found in $H \rightarrow \gamma\gamma$ analysis note and physics analysis summary [118, 119] and in the specific reference of the Discrete Profiling [116]. The figures 4.56 and 4.57 show the projection for the $\mu\mu$ and $\mu\mu\gamma$ distribution after the statistical test.

For the $H \rightarrow \Upsilon(1S, 2S, 3S) + \gamma$ analysis, the same procedure is implemented, except for the peaking background modeling. Since the MC prediction for the contribution of the background is too small, according to the comparison between the final selected events for data and the Higgs Dalitz Decay sample, in order to avoid fitting over statistical fluctuations of the data sample, the Peaking Background, for the Higgs channel, is fully modeled from the MC sample, including its normalization, as shown in figure 4.58, hence it is not included the the statistical test, neither in the final background modeling envelope.

The results of the background modeling for the Full Combinatorial and Υ Combinatorial, can be found at Figures 4.59 and 4.60, for the $\mu\mu$ and $\mu\mu\gamma$ distribution, respectively. It is worth to remember that, for the Higgs channel, we are not implementing any categorization.

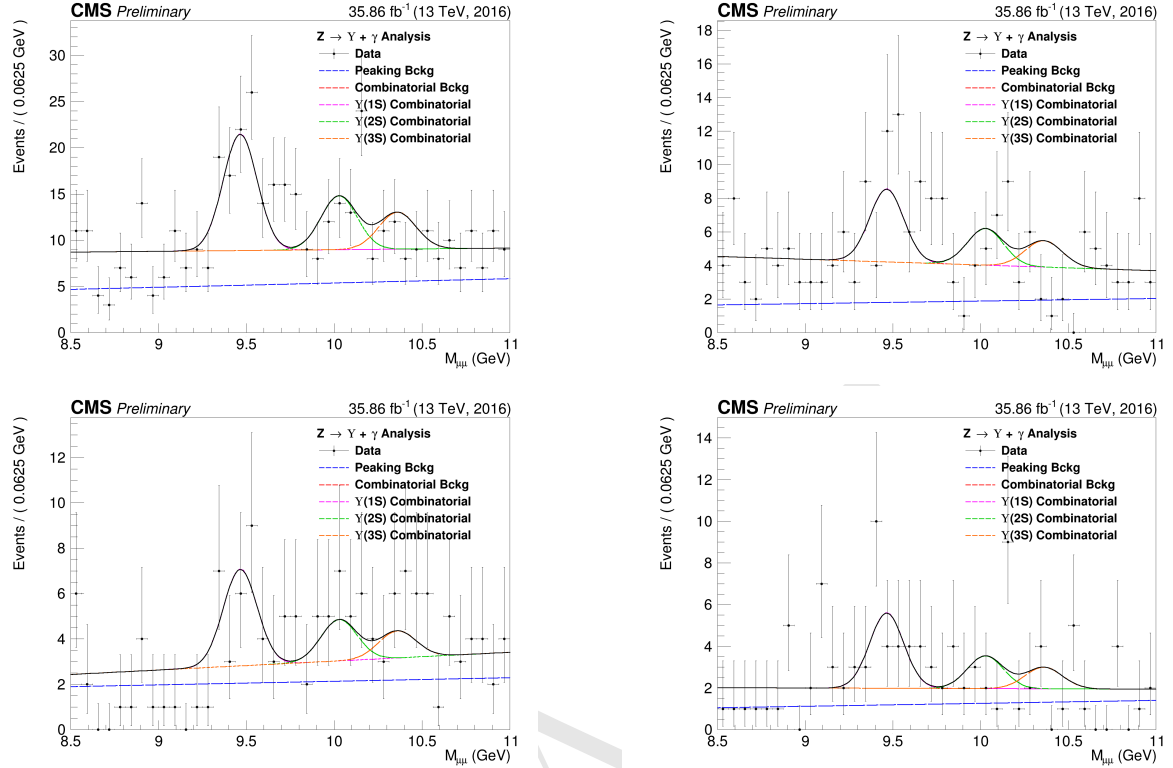


Figure 4.56: $Z \rightarrow \Upsilon(1S, 2S, 3S) + \gamma$ Background Modeling: $\mu\mu$ distribution. Inclusive (top left); EB High R9 (top right), EB Low R9 (bottom left), EE (bottom right). The pdfs projections are plotted with respect to the overall best choice of the statistica test.

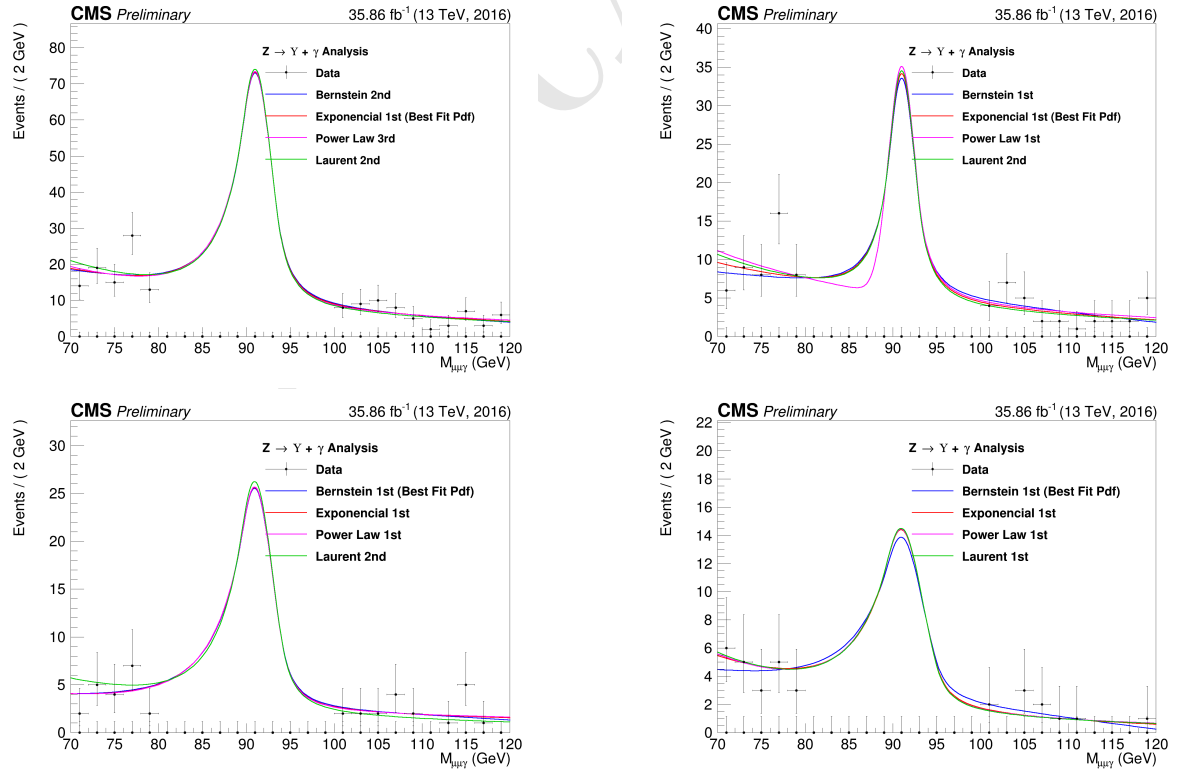


Figure 4.57: $Z \rightarrow \Upsilon(1S, 2S, 3S) + \gamma$ Background Modeling: $\mu\mu\gamma$ distribution. Inclusive (top left); EB High R9 (top right), EB Low R9 (bottom left), EE (bottom right). The plotted pdfs corresponds to the best choice by the statistical test for each family. The signal region, from 80 GeV to 100 GeV was blinded.

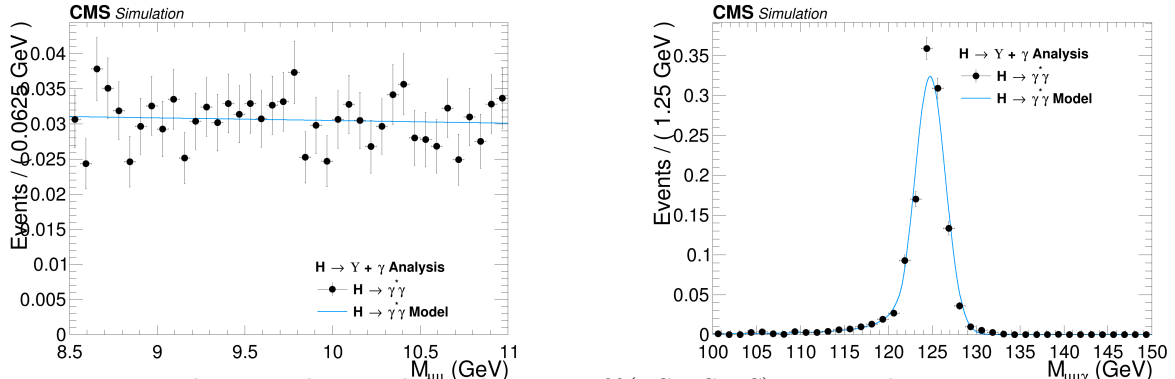


Figure 4.58: Peaking Background for the $H \rightarrow \Upsilon(1S, 2S, 3S) + \gamma$ analysis. $m_{\mu\mu}$ invariant mass distribution (left) and $m_{\mu\mu\gamma}$ invariant mass distribution (right).

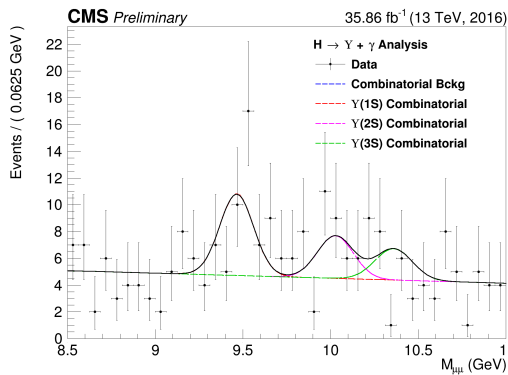


Figure 4.59: $H \rightarrow \Upsilon(1S, 2S, 3S) + \gamma$ Background Modeling: $m_{\mu\mu}$ distribution. The *pdfs* projections are plotted with respect to the overall best choice of the statistical test.

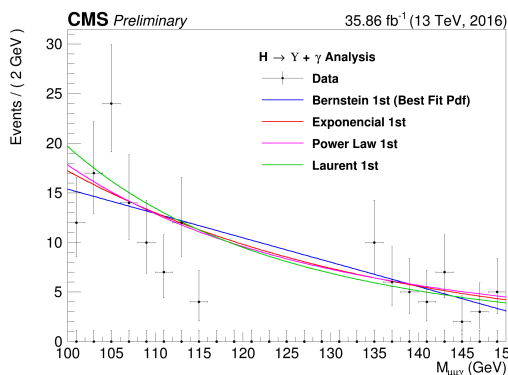


Figure 4.60: $H \rightarrow \Upsilon(1S, 2S, 3S) + \gamma$ Background Modeling: $\mu\mu\gamma$ distribution. The plotted *pdfs* corresponds to the best choice by the statistical test for each family. The signal region, from 115 GeV to 135 GeV was blinded.

₁₆₅₈ **4.9 Signal modeling**

₁₆₅₉ Along the same lines as the background modeling (Section 4.8), the signal modeling is implemented
₁₆₆₀ as a two dimensional unbinned maximum likelihood fit on the $m_{\mu\mu}$ and the $m_{\mu\mu\gamma}$ invariant masses
₁₆₆₁ distributions, but this time, only using the signal simulated MC samples 4.1.2. Since, for the two
₁₆₆₂ spectra, it is expected a peak-like distribution, one centered in the Z (or Higgs) boson mass and the
₁₆₆₃ other centered in the Υ mass, two also peak-like analytics *pdfs* were chosen to compose the signal
₁₆₆₄ model. The modeling is summarized in table 4.7.

Table 4.7: Modeling for each signal source and mass component.

	$m_{\mu\mu}$	$m_{\mu\mu\gamma}$
$Z \rightarrow \Upsilon(1S, 2S, 3S) + \gamma$	Double Crystal Ball	Double Crystal Ball
$H \rightarrow \Upsilon(1S, 2S, 3S) + \gamma$	Double Crystal Ball	Crystal Ball + Gaussian with the same mean

₁₆₆₅ The projections of the modeling for the Z boson decay channel analysis can be found at figures 4.61,
₁₆₆₆ 4.62, 4.63 and 4.64, for Inclusive, EB High R9, EB Low R9 and EE, respectively. The projection
₁₆₆₇ on the modeling for the Higgs boson signal can be found at Figure 4.65. A deeper discussion on the
₁₆₆₈ systematics uncertainties associated to them, will be presented in the next section.

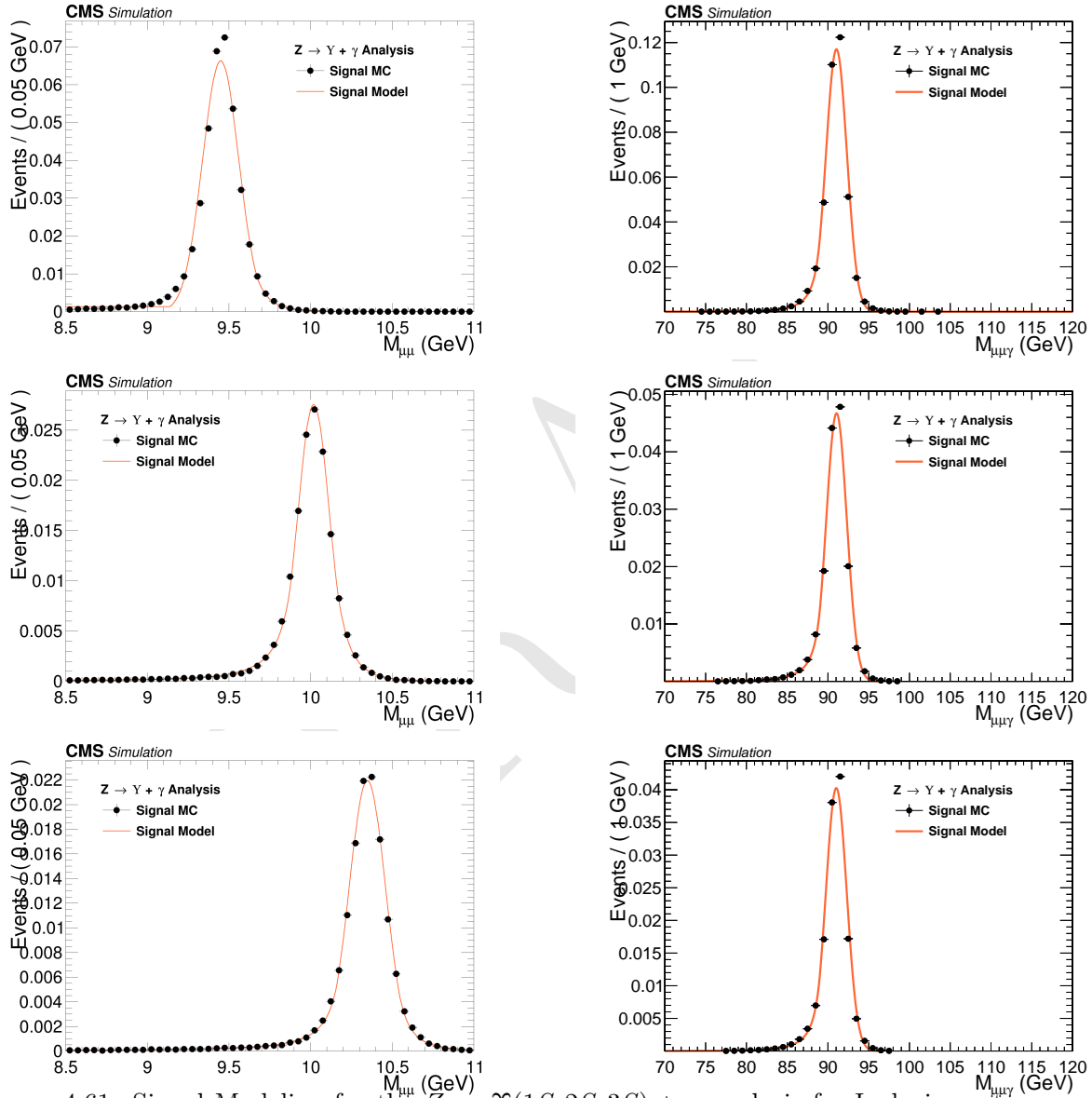


Figure 4.61: Signal Modeling for the $Z \rightarrow \Upsilon(1S, 2S, 3S) + \gamma$ analysis for Inclusive category. $m_{\mu\mu}$ mass distribution (left) and $m_{\mu\mu\gamma}$ mass distribution (right). From top to bottom: $\Upsilon(1S)$, $\Upsilon(2S)$, $\Upsilon(3S)$.

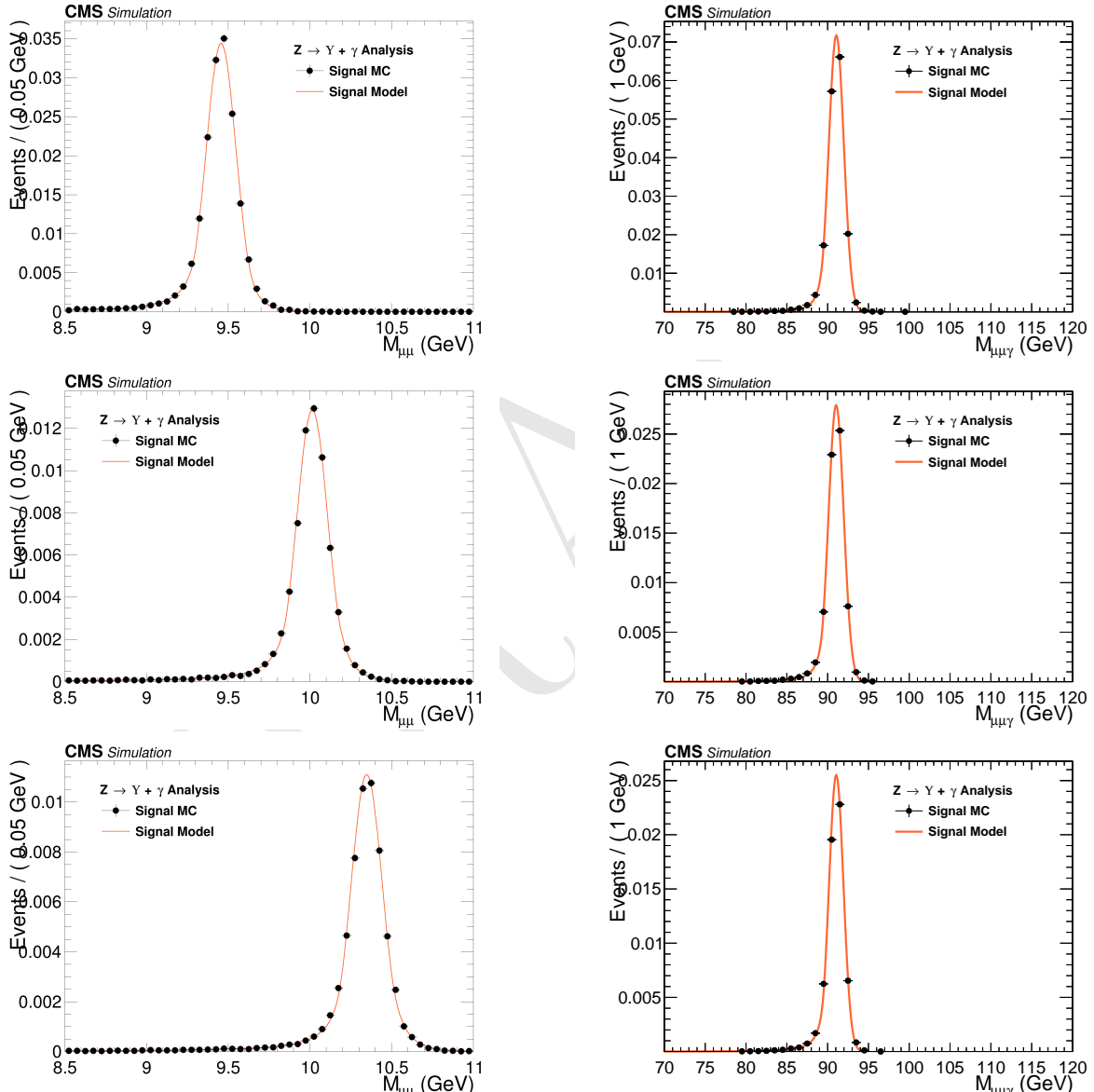


Figure 4.62: Signal Modeling for the $Z \rightarrow \Upsilon(1S, 2S, 3S) + \gamma$ analysis for EB High R9 category. $m_{\mu\mu}$ mass distribution (left) and $m_{\mu\mu\gamma}$ mass distribution (right). From top to bottom: $\Upsilon(1S)$, $\Upsilon(2S)$, $\Upsilon(3S)$.

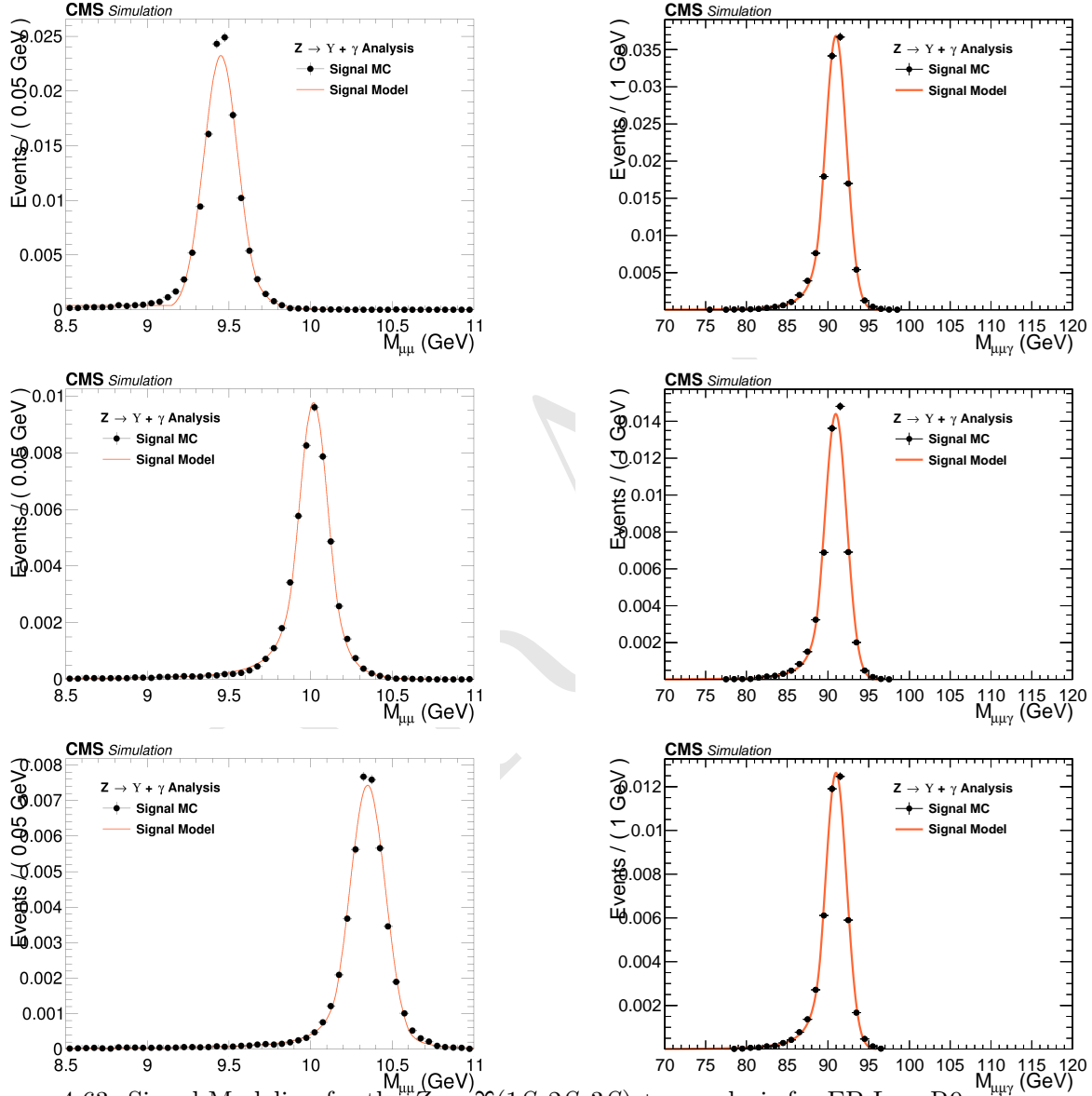


Figure 4.63: Signal Modeling for the $Z \rightarrow \Upsilon(1S, 2S, 3S) + \gamma$ analysis for EB Low R9 category. $m_{\mu\mu}$ mass distribution (left) and $m_{\mu\mu\gamma}$ mass distribution (right). From top to bottom: $\Upsilon(1S)$, $\Upsilon(2S)$, $\Upsilon(3S)$.

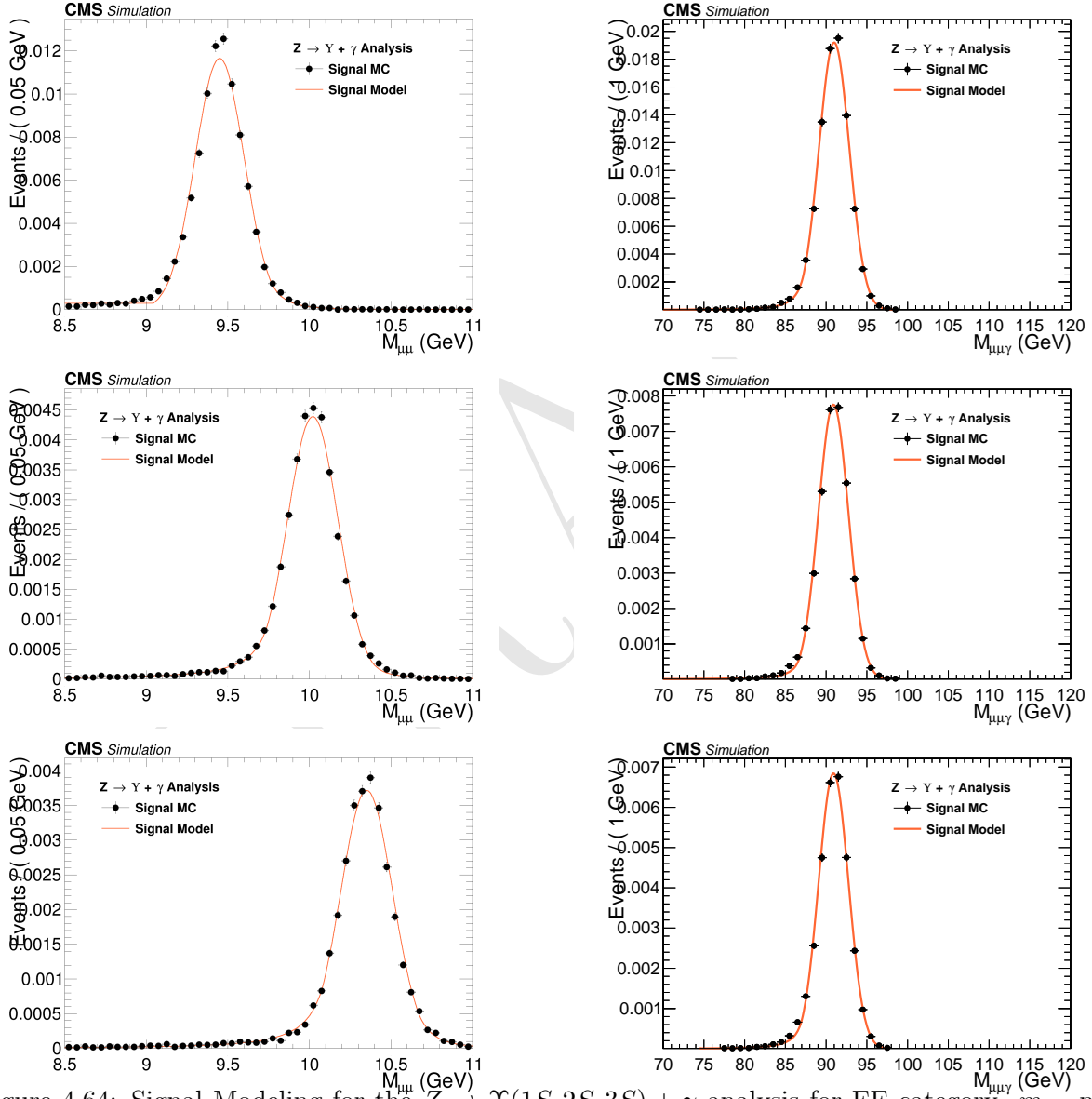


Figure 4.64: Signal Modeling for the $Z \rightarrow \Upsilon(1S, 2S, 3S) + \gamma$ analysis for EE category. $m_{\mu\mu}$ mass distribution (left) and $m_{\mu\mu\gamma}$ mass distribution (right). From top to bottom: $\Upsilon(1S)$, $\Upsilon(2S)$, $\Upsilon(3S)$.

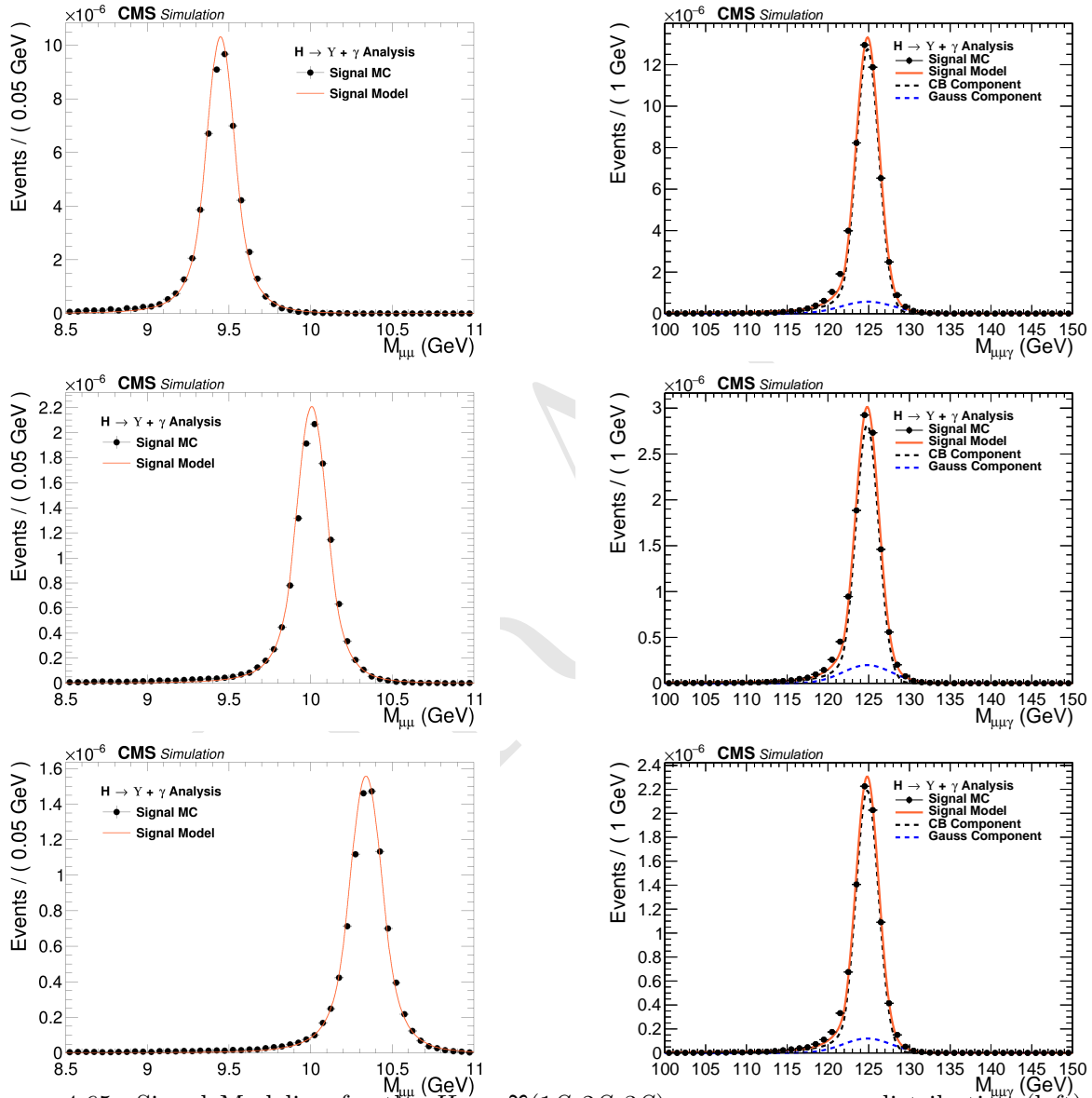


Figure 4.65: Signal Modeling for the $H \rightarrow \Upsilon(1S, 2S, 3S) + \gamma$. $m_{\mu\mu}$ mass distribution (left) and $m_{\mu\mu\gamma}$ mass distribution (right). From top to bottom: $\Upsilon(1S)$, $\Upsilon(2S)$, $\Upsilon(3S)$.

1669 4.10 Systematic uncertainties

- 1670 Two sources of systematics are considered: the ones that affect the predicted yields⁸ and the ones
 1671 that affect the shape of the pdfs used to compose the signal and background model.
- 1672 Those that affect the predicted yields, presented in Section 4.7.2, it is considered integrated lu-
 1673 minosity measurement [93], the pileup description in the Monte-Carlo simulations, the corrections
 1674 applied to the simulated events in order to compensate for the differences in performance of the some
 1675 selection criteria, such as trigger, object reconstruction and identification, the Υ polarization and
 1676 the theoretical uncertainties, such as the effects of the *parton density functions* (PDF) to the signal
 1677 cross section [28, 102, 120], the variations of the renormalization and factorization scales [121–125],
 1678 and the prediction of the decay branching ratios.
- 1679 For the systematics on the signal modeling, it is considered possible imprecisions of the momentum
 1680 scale and resolution. They are measured on how they affect the mean (μ) and the standard deviation
 1681 (σ) of the signal model. For the background modeling, since it is derived from data, the choice of
 1682 the *pdf* (Probability distribution function) is the only systematic uncertainties considered. It is
 1683 treated by the Discrete Profiling method, as described in section 4.8.
- 1684 The two kinds of systematics uncertainties are described in details below.

1685 4.10.1 Uncertainties on the predicted yields

- 1686 The theoretical sources of uncertainties includes: parton distribution functions uncertainties, strong
 1687 coupling constant (α_s) uncertainty and uncertainty on the $H \rightarrow \gamma\gamma$ branching fraction (used to derive
 1688 the Higgs Dalitz Decays cross-section). The values for these theoretical uncertainties are taken from
 1689 the Higgs Combination Group [105] and also from [124, 126].
- 1690 An uncertainty value of 2.5% is used on the integrated luminosity of the data samples, as recom-
 1691 mended by CMS [93]. To evaluate the impact of the pileup reweighting in the final result, the The
 1692 total inelastic cross section of 69.2 mb is varied by $\pm 4.6\%$ and the analysis is ran with these extreme
 1693 values. The systematic uncertainty quoted is the maximum difference in the yields with respect to
 1694 nominal value, as recommended by CMS.
- 1695 The impact of the trigger scale factor is evaluated by running this analysis with $\pm 1\sigma$ on the
 1696 Trigger Efficiency Scale factors (section 4.5.1). The systematic uncertainty quoted is the maximum
 1697 difference in the yields with respect to nominal value.
- 1698 For the final state object identification and isolation associated uncertainty, the scale factors, pro-
 1699 vided by CMS, to match the performance of MC and Data samples are varied in $\pm 1\sigma$. The
 1700 systematic uncertainty quoted is the maximum difference in the yields with respect to nominal
 1701 value. This procedure is applied on the scale factors for the Photon MVA ID and the Electron Veto
 1702 (section 4.5.3) and for Muon Identification and Isolation(section 4.5.2).

⁸Number of events, per process, after full selection and corrected by the expected SM cross sections.

Finally, the Υ Polarization is assessed applying the extremes scenarios of the Υ polarization (Transverse and Longitudinal Polarization to the signal samples (section 4.2). The systematic uncertainty quoted is the maximum difference in the yields with respect to nominal (Unpolarized) yield. This procedure is applied only for the Z decay. For the Higgs decay, the only polarization considered is the transverse polarization.

The effect of all systematic uncertainties in the signal and peaking background yields are summarized on table 4.8, for the Z decay and table 4.9, for the Higgs decay. Clearly, the main contribution to the systematics uncertainties on the yields is Polarization of the $\Upsilon(nS)$ (only for the Z decay), around 15%.

4.10.2 Uncertainties that affect the signal fits

Smearing and scaling corrections are applied on simulated events since the resolution of Monte Carlo is better than that on data and the detector might not catch all the possible differences in the detector performance, with respect to the data observation. They need to be estimated and included on the systematics. The corrections are:

- **Muon Momentum Scale and Resolution:** extracted by running the analysis with different setups of the official CMS Muon scaling and smearing package [127]. The deviations, with respect to the default correction are summed in quadrature. Once the nominal parameters (mean or sigma) are obtained, the default corrections are shifted by $\pm 1\sigma$ and the fits are re-done, with the parameters of interest free to float and all others fixed. The systematic uncertainty quoted is the maximum difference of the parameter with respect to nominal value.

- **Photon Energy Scale and Resolution:** extracted by running the analysis with different sets of corrections, provided by the CMS ⁹. Once the nominal mean is obtained, the sets are changed and the fits are re-done, with the mean free to float and all others parameters fixed. The corrections are shifted by $\pm 1\sigma$ on each source of systematics (following standard CMS recommendations). The quoted as systematic uncertainty is the quadrature sum of the maximum deviation within each set.

The effective systematic uncertainty associated with the scale and resolution are the quadrature sum of the muon and photon contributions. The effect of all systematic uncertainties in the Signal fits are summarized on table 4.10, for the Z and Higgs decay.

⁹CMS has not published, yet, a paper on the Run2 performance of the Photon reconstruction (This document is under internal review process.). Just as a reference, we cite the Run1 paper [128].

Table 4.8: A summary table of systematic uncertainties in the Z boson decaying in $\Upsilon(1S, 2S, 3S) + \gamma$, affecting the final yields of the MC samples.

Source	Uncertainty			
	Signal		Peaking Background	
	$Z \rightarrow \Upsilon(1S)\gamma$	$Z \rightarrow \Upsilon(2S)\gamma$	$Z \rightarrow \Upsilon(3S)\gamma$	$Z \rightarrow \mu\mu\gamma_{FSR}$
Integrated luminosity				
All Categories	2.5%			
SM Z boson σ (scale)				
All Categories	3.5%		5.0%	
SM Z boson σ (PDF + α_s)				
All Categories	1.73%		5.0%	
Pileup Reweighting				
Inclusive	0.65%	0.68%	0.71%	0.62%
EB High R9	1.01%	1.1%	1.04%	1.06%
EB Low R9	0.17%	0.08%	0.13%	0.11%
EE	1.07%	0.98%	1.26%	0.78%
Trigger				
Inclusive	4.45%	4.46%	4.49%	4.71%
EB High R9	3.5%	3.5%	3.52%	3.71%
EB Low R9	3.55%	3.54%	3.58%	3.72%
EE	7.52%	7.58%	7.56%	8.13%
Muon Identification				
Inclusive	4.82%	4.81%	4.8%	4.52%
EB High R9	4.45%	4.45%	4.44%	4.2%
EB Low R9	4.65%	4.62%	4.63%	4.32%
EE	5.75%	5.75%	5.74%	5.44%
Photon Identification				
Inclusive	1.1%	1.1%	1.09%	1.09%
EB High R9	1.1%	1.09%	1.09%	1.11%
EB Low R9	1.1%	1.1%	1.09%	1.08%
EE	1.1%	1.1%	1.1%	1.09%
Electron Veto				
Inclusive	1.02%	1.02%	1.02%	1.03%
EB High R9	1.2%	1.2%	1.2%	1.2%
EB Low R9	1.2%	1.2%	1.2%	1.2%
EE	0.45%	0.45%	0.45%	0.45%
Polarization				
Inclusive	15.36%	14.78%	14.84%	-
EB High R9	15.6%	14.88%	14.87%	-
EB Low R9	15.01%	14.31%	14.4%	-
EE	15.39%	15.27%	15.39%	-

Table 4.9: A summary table of systematic uncertainties in the Higgs boson decaying in $\Upsilon(1S, 2S, 3S) + \gamma$, affecting the final yields of the MC samples.

Source	Uncertainty			
	Signal			Peaking Background
	$H \rightarrow \Upsilon(1S)\gamma$	$H \rightarrow \Upsilon(2S)\gamma$	$H \rightarrow \Upsilon(3S)\gamma$	$H \rightarrow \gamma\gamma^*$
Integrated luminosity			2.5%	
SM Higgs σ (scale)			+4.6% / -6.7%	
SM Higgs σ (PDF + α_s)			3.2%	
SM BR $H \rightarrow \gamma\gamma^*$		-		6.0%
Pileup Reweighting	0.61%	0.68%	0.56%	0.9%
Trigger	5.61%	5.47%	5.5%	6.12%
Muon Identification	4.39%	4.36%	4.34%	4.33%
Photon Identification	1.21%	1.22%	1.22%	1.2%
Electron Veto	1.04%	1.04%	1.04%	1.04%

Table 4.10: A summary table of systematic uncertainties in the Z (H) decaying in $\Upsilon(1S, 2S, 3S) + \gamma$, affecting the signal fits.

	Z $\rightarrow \Upsilon(nS) + \gamma$				H $\rightarrow \Upsilon(nS) + \gamma$
	Inclusive	EB High R9	EB Low R9	EE	Inclusive
Mean - Scale					
$\Upsilon(1S)$	Muon Unc.	0.06%	0.05%	0.06%	0.11%
	Photon Unc.	0.21%	0.13%	0.19%	0.26%
	Total Unc.	0.22%	0.14%	0.2%	0.28%
Sigma - Resolution					
	Muon Unc.	1.12%	0.84%	1.55%	1.14%
	Photon Unc.	2.14%	2.48%	1.95%	2.79%
	Total Unc.	2.42%	2.61%	2.49%	3.01%
Mean - Scale					
$\Upsilon(2S)$	Muon Unc.	0.07%	0.05%	0.06%	0.13%
	Photon Unc.	0.25%	0.11%	0.2%	0.19%
	Total Unc.	0.26%	0.12%	0.21%	0.23%
Sigma - Resolution					
	Muon Unc.	1.21%	1.54%	2.65%	1.66%
	Photon Unc.	1.85%	2.67%	3.56%	3.6%
	Total Unc.	2.21%	3.08%	4.44%	3.97%
Mean - Scale					
$\Upsilon(3S)$	Muon Unc.	0.06%	0.06%	0.06%	0.09%
	Photon Unc.	0.22%	0.14%	0.25%	0.17%
	Total Unc.	0.23%	0.15%	0.26%	0.19%
Sigma - Resolution					
	Muon Unc.	1.78%	2.38%	2.1%	2.25%
	Photon Unc.	2.51%	4.14%	2.23%	4.08%
	Total Unc.	3.08%	4.77%	3.07%	4.66%

1732 4.11 Modeling Cross checks

1733 In order to test the applicability of the statistical (signal and background) modeling proposed
 1734 in this study, a cross-check procedure is performed by generating a set of pseudo-experiments
 1735 (toys datasets) based on the signal plus background model, for each decay channel ($H/Z \rightarrow$
 1736 $\Upsilon(1S, 2S, 3S,) + \gamma$) with some signal injected.

1737 The procedure consists of resampling from the signal plus background a number of events, including
 1738 some extra (injected signal). The amount of injected signal is controlled by the μ_{true} variable, where
 1739 $\mu_{true} = X$ means inject X times the expected signal.

1740 Once generated, the toy dataset is refitted to the signal plus background model and the signal
 1741 strength (μ_{fit}) and its error σ_{fit} are extracted. This procedure is repeated 10000 times and only
 1742 for the inclusive category. Figures 4.67, 4.66, 4.69 and 4.68 show examples of those fits for the
 1743 Higgs and Z decay.

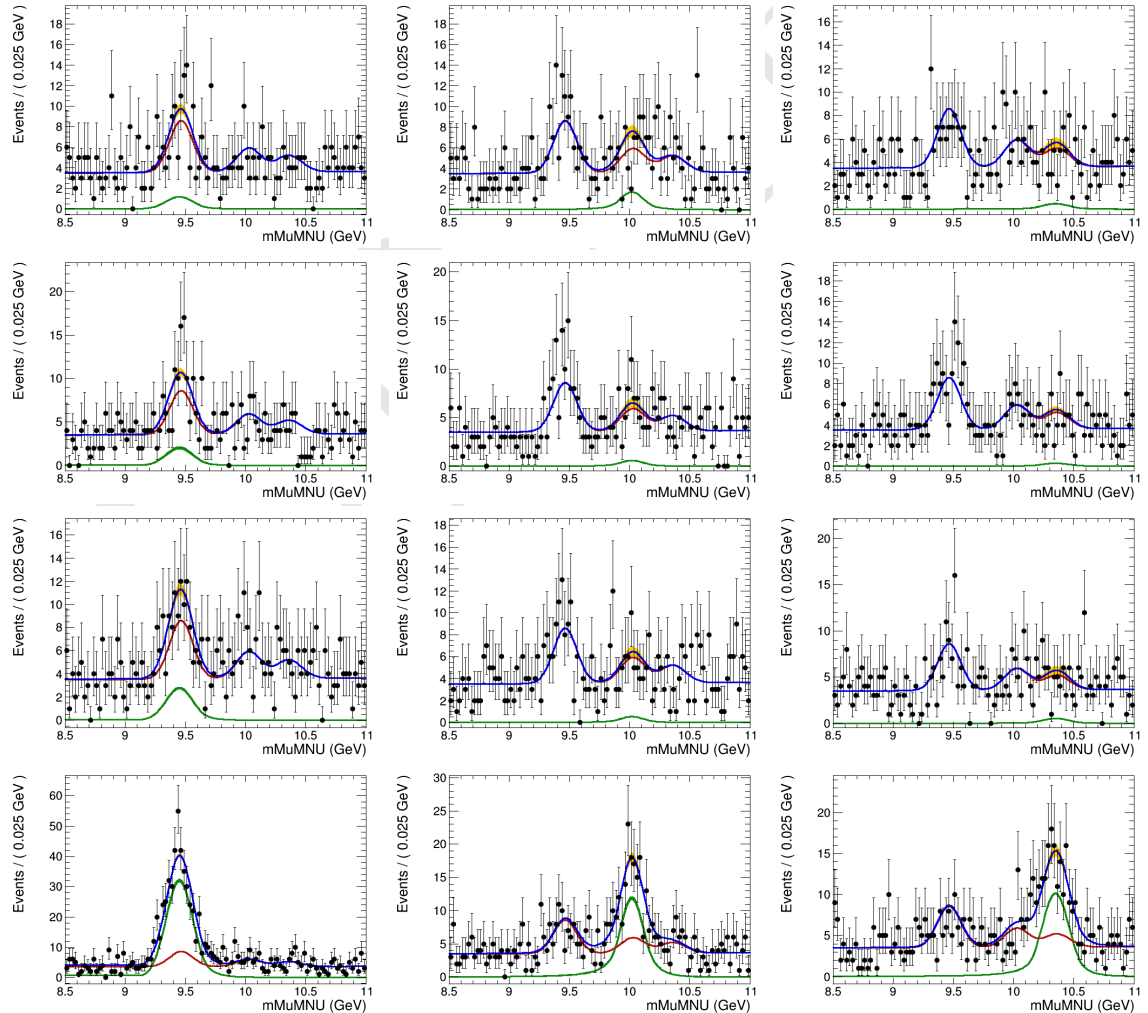


Figure 4.66: Examples of the toy datasets fit ($M_{\mu\mu}$), for the Z decay analysis, after the toy dataset refit, for 1S, 2S and 3S (left to right), with μ_{true} equals to 20, 50, 100, 1000 (top to bottom). The red lines corresponds to the background model (B), the green lines to signal model (S), the blue lines to the total (S+B) and the dots is the toy dataset.

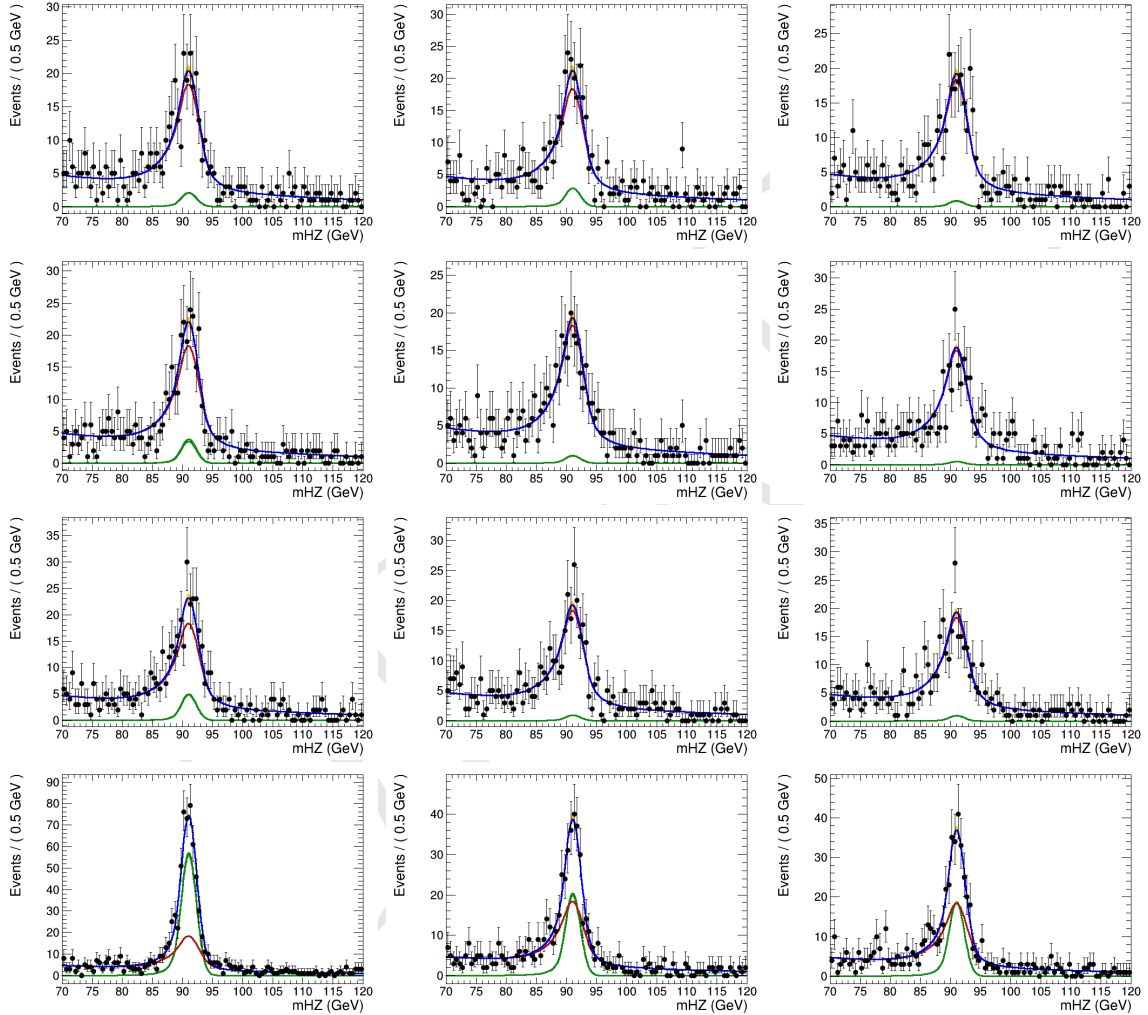


Figure 4.67: Examples of the toy datasets fit ($M_{\mu\mu\gamma}$), for the Z decay analysis, after the toy dataset refit, for 1S, 2S and 3S (left to right), with μ_{true} equals to 20, 50, 100, 1000 (top to bottom). The red lines corresponds to the background model (B), the green lines to signal model (S), the blue lines to the total (S+B) and the dots is the toy dataset.

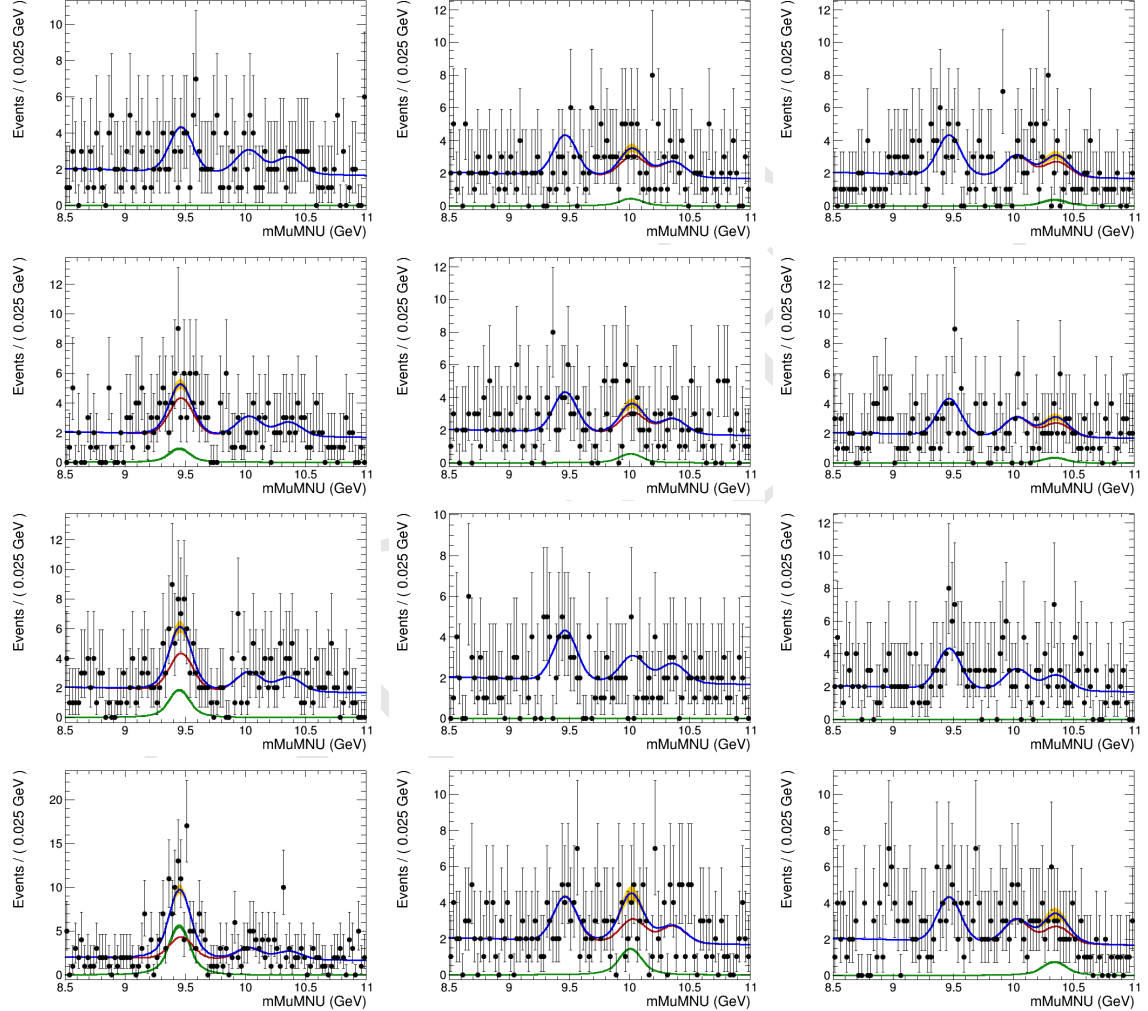


Figure 4.68: Examples of the toy datasets fit ($M_{\mu\mu}$), for the Higgs decay analysis, after the toy dataset refit, for 1S, 2S and 3S (left to right), with μ_{true} equals to 100000, 200000, 300000, 1000000 (top to bottom). The red lines corresponds to the background model (B), the green lines to signal model (S), the blue lines to the total (S+B) and the dots is the toy dataset.

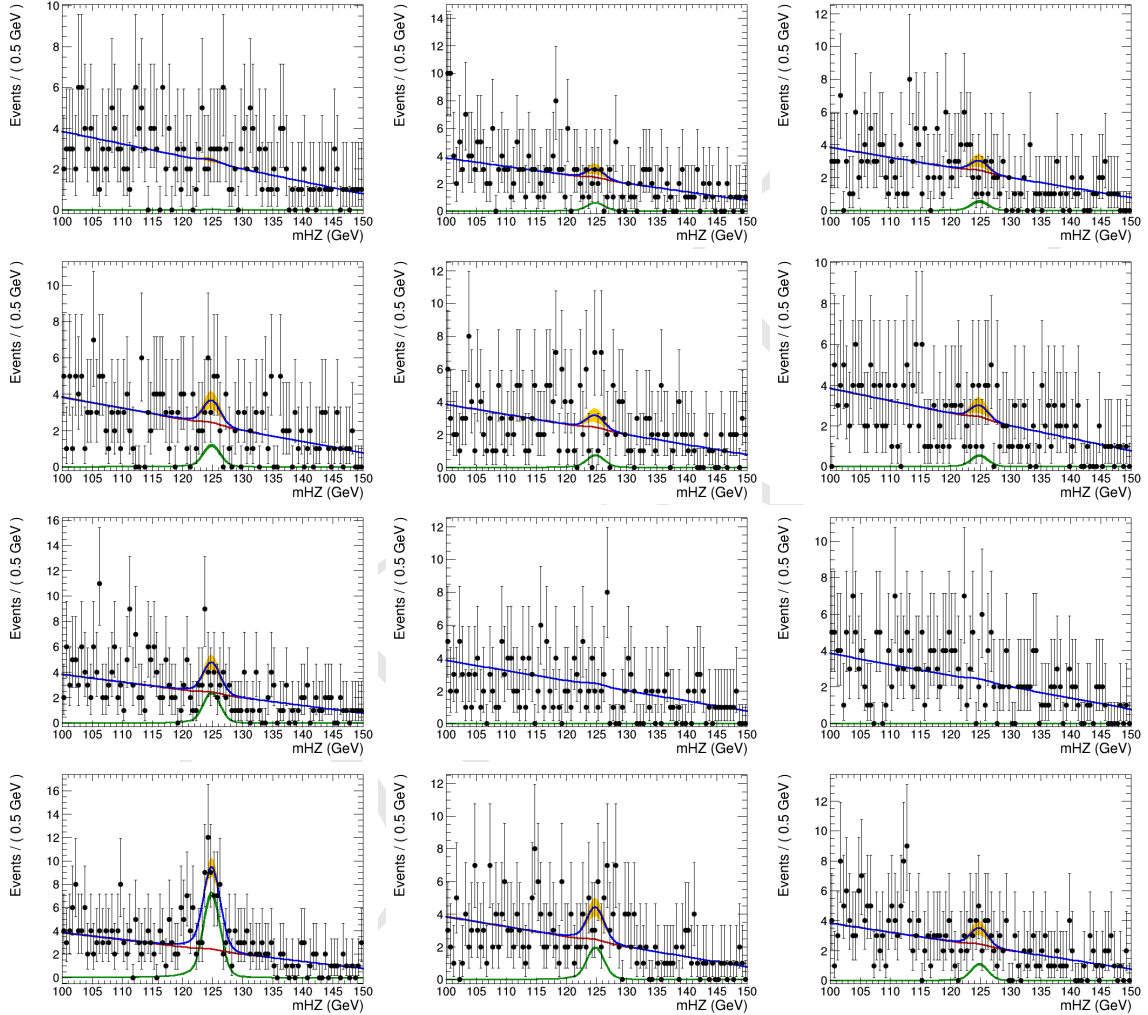


Figure 4.69: Examples of the toy datasets fit ($M_{\mu\mu\gamma}$), for the Higgs decay analysis, after the toy dataset refit, for 1S, 2S and 3S (left to right), with μ_{true} equals to 100000, 200000, 300000, 1000000 (top to bottom). The red lines corresponds to the background model (B), the green lines to signal model (S), the blue lines to the total (S+B) and the dots is the toy dataset.

1744 It is expected that the pulls distribution for the fitted signal strength ($\frac{\mu_{fit} - \mu_{true}}{\sigma_{fit}}$) should follow a
 1745 Gaussian distribution centered in 0 and with σ around 1. Figures 4.70 and 4.71 present those pulls
 1746 distributions for the Z and Higgs decays, respectively.

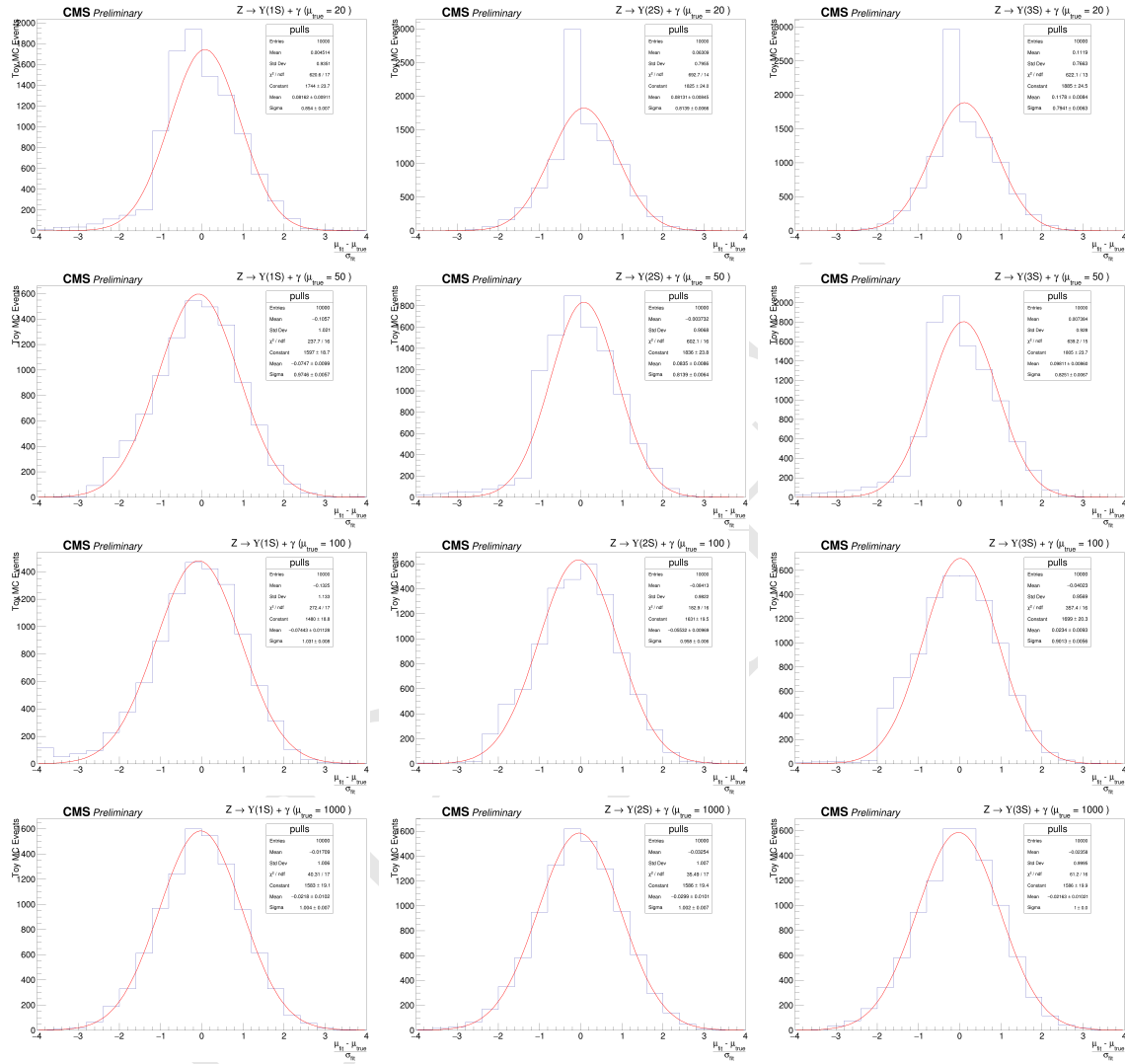


Figure 4.70: Distribution of pulls ($\frac{\mu_{fit} - \mu_{true}}{\sigma_{fit}}$), for the Z decay analysis, after the toy dataset refit, for 1S, 2S and 3S (left to right), with μ_{true} equals to 20, 50, 100, 1000 (top to bottom).

1747 As a general conclusion on this cross check, as long as the toy MC generation is able to inject enough
 1748 signal to be fit, the final modeling of this analysis is able to recover a Gaussian pulls distribution.
 1749 This, of course, depends on the Υ state to be considered. For the Z decay, between $\mu_{true} = 50$
 1750 and $\mu_{true} = 100$ (around a hundred of events passing full selection), while for the Higgs decay, it
 1751 is needed only a few events after full selection, even though it means hundreds of thousands times
 1752 the expected signal, since the very small cross sections for the decay, as shown in Table 4.1.

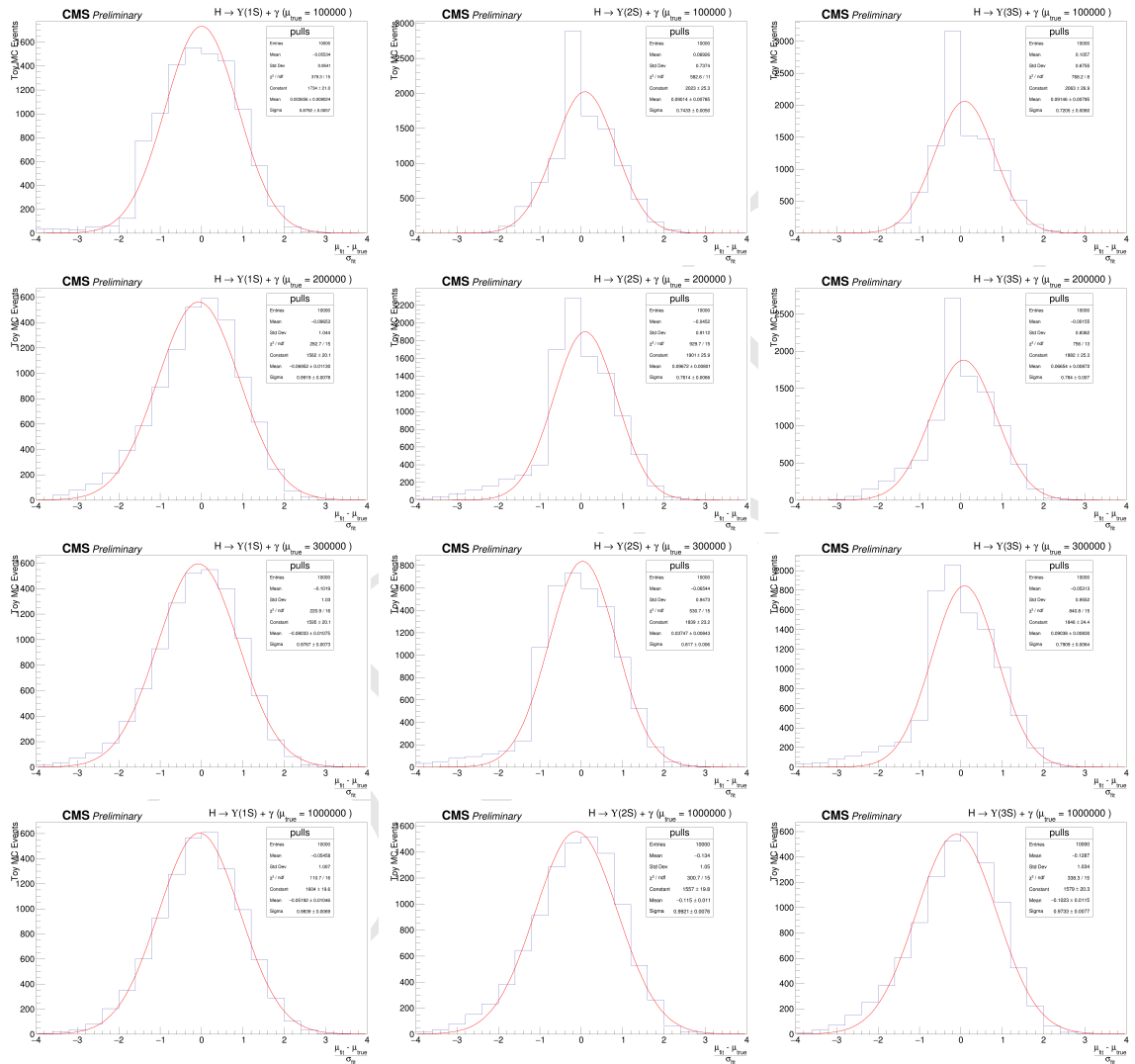


Figure 4.71: Distribution of pulls ($\frac{\mu_{fit} - \mu_{true}}{\sigma_{fit}}$), for the Higgs decay analysis, after the toy dataset refit, for 1S, 2S and 3S (left to right), with μ_{true} equals to 100000, 200000, 300000, 1000000 (top to bottom).

¹⁷⁵³ 5 Results and conclusion

¹⁷⁵⁴ A two-dimensional (2D) unbinned maximum-likelihood fit to the $m_{\mu^+\mu^-\gamma}$ and $m_{\mu^+\mu^-}$ distributions
¹⁷⁵⁵ was used to compare the data with background and signal predictions. Search has been performed for
¹⁷⁵⁶ a SM Higgs and Z boson decaying into a $\Upsilon(1S, 2S, 3S)\gamma$, with $\Upsilon(1S, 2S, 3S)$ subsequently decaying
¹⁷⁵⁷ into $\mu^+\mu^-$ using data obtained from 35.9 fb^{-1} of pp collisions at $\sqrt{s} = 13 \text{ TeV}$.
¹⁷⁵⁸ Since no excess has been observed above the background, the CL_s formalism is applied, in order to
¹⁷⁵⁹ establish an upper limit in the branching fractions for each channel.

¹⁷⁶⁰ 5.1 The CL_s formalism for upper limits setting at CMS

¹⁷⁶¹ The CL_s formalism [129] consists in a modified frequentist approach to obtain an upper limit for a
¹⁷⁶² certain parameter of a model, with respect to the data, when there is no significant excess that could
¹⁷⁶³ justify an observation. It is based on the profile-likelihood-ratio test statistic [130] and asymptotic
¹⁷⁶⁴ approximations [131]. It is a standard upper limit setting procedure for the LHC experiments [132].
¹⁷⁶⁵ When searching for non-observed phenomena, it is often usual to derive the results as a function of
¹⁷⁶⁶ the signal strength modifier μ , which is a free parameter of the full model (signal + background).
¹⁷⁶⁷ It can be defined such as, the expectation value for the number of events in a bin ¹ is:

$$E[n] = \mu s + b, \quad (5.1)$$

¹⁷⁶⁸ where, s and b are the expected number of signal and background events, respectively.
¹⁷⁶⁹ The Neyman–Pearson lemma [130] states the likelihood ratio is the optimal test between a null
¹⁷⁷⁰ hypothesis and an alternative one (i.e. background-only and signal-plus-background models). On
¹⁷⁷¹ top of this, one could build a likelihood ratio test as:

$$q(\mu) = -2 \ln \left(\frac{\mathcal{L}(\text{data}|\mu s + b)}{\mathcal{L}(\text{data}|b)} \right), \quad (5.2)$$

¹⁷⁷² where the denominator and numerator defines the likelihoods for the background-only and signal-
¹⁷⁷³ plus-background models, respectively. This was the hypothesis test used by LEP and Tevatron
¹⁷⁷⁴ experiments (the former one, with some modifications to include the nuisances effects).

¹A set of common analysis criteria.

With these two models, i.e. their *pdfs*, one can throw toy MC events in order to construct a distribution of $q(\mu)$, namely $f(q(\mu)|\mu)$. The *p*-value of $f(q(\mu)|\mu)$, as below, can be used to chose between each model.

$$p_\mu = \int_{q(\mu)_{\text{data}}}^{\infty} f(q(\mu)|\mu) dq(\mu), \quad (5.3)$$

where $q(\mu)_{\text{data}}$ is the observed value of $q(\mu)$ on data, for a given μ .

If p_μ is less than α (usually 0.05 or 0.1) the background-only model can be excluded in favor of the signal-plus-background model. For the propose of a confidence interval estimation, the argument can be reversed and one could look for all the values of μ that would not be excluded with Confidence Level (CL) $1 - \alpha$.

The problem with this definition is that, when the expected signal strength is very small, e.g. a invariant mass distribution in the TeV scale, the null hypothesis and the alternative one are almost indistinguishable. In this situation, a downward fluctuation of the background might lead us to exclude the alternative hypothesis (signal) in a region of low experimental sensitivity region. Putting in number, if we expect 50 background events and 2 signal events, but we observe 40 events, the signal would be easily excluded.

In order to take this effect into account, a modified frequentist approach for upper limits setting, the CL_s was proposed during the Higgs search era at LEP. Lets start by considering a profile likelihood ratio [133] as below:

$$\lambda(\mu) = \frac{\mathcal{L}(\text{data}|\mu, \hat{\theta})}{\mathcal{L}(\text{data}|\hat{\mu}, \hat{\theta})}, \quad (5.4)$$

where, $\mathcal{L}(\text{data}|\mu, \hat{\theta})$ is the profile likelihood function.

Defining μ and the investigated signal strength, $\hat{\theta}$ is the nuisances that maximizes the likelihood for a given μ (fixed) while $\hat{\mu}$ and $\hat{\theta}$ are the signal strength and nuisances that, overall, maximizes the likelihood. The advantage of the

CMS and ATLAS have a common set of statistical guidelines [134] to ensure the compatibility of the published results. Following these recommendations, the statistics test based on 5.4 is:

$$\tilde{q}_\mu = -2\ln[\lambda(\mu)], \text{ with } 0 \leq \hat{\mu} \leq \mu. \quad (5.5)$$

The left side restriction ($0 \leq \hat{\mu}$) ensure us the proper physical interpretation of μ as a positive define signal strength, i.e., the observation a process would, for a given bin, increase the number of events. The right side restriction $\hat{\mu} \leq \mu$ secure the interpretation of \tilde{q}_μ 's *p*-value as a one-sided confidence interval. This is required for a upper limit definition.

The advantage of using the profile likelihood ratio is that, even though it takes into account the effect of nuisances in the likelihood, it is possible to prove that, with the use of Wilk's Theorem [117],

that a statistic test defined as \tilde{q}_μ , asymptotically follows a chi-square distribution with one degree of freedom (the signal strength) [131]. Thus, \tilde{q}_μ is said to be approximately independent of any nuisance and allow a fast computation of its p -value without the need of toy MC strategies (which can computationally demanding, depending on the complexity of the models), event though this is not the standard CMS/ATLAS recommendation.

Based on \tilde{q}_μ , defined at 5.5, one should compute the $\tilde{q}_\mu^{\text{obs}}$, also the $\hat{\theta}_\mu^{\text{obs}}$ and $\hat{\theta}_{\mu=0}^{\text{obs}}$, which corresponds to the observed value of \tilde{q}_μ on data, the maximum likelihood estimator for the nuisances assuming some signal strength μ and assuming a background-only model, respectively. Then, the distributions of $f(\tilde{q}_\mu|\mu, \hat{\theta}_\mu^{\text{obs}})$ and $f(\tilde{q}_\mu|\mu = 0, \hat{\theta}_{\mu=0}^{\text{obs}})$ are generated tossing pseudo-random toy MC. Figure 5.1 presents an example of these two distributions.

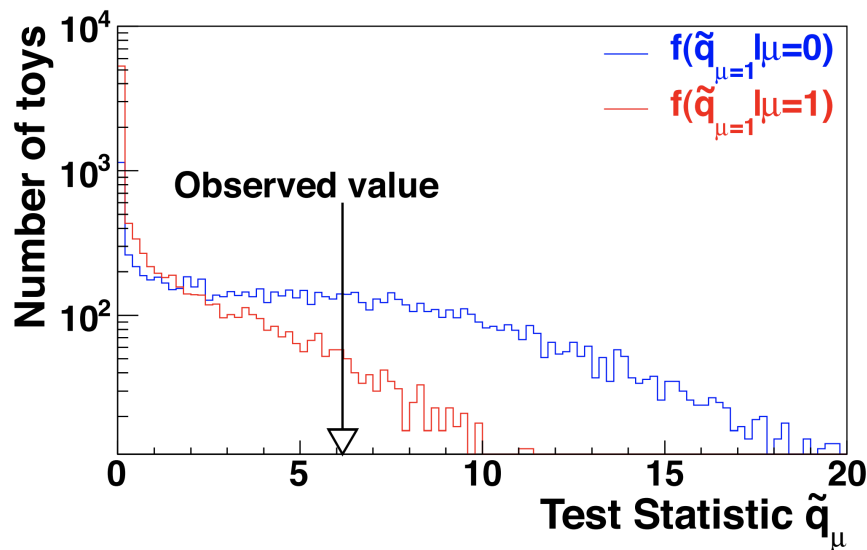


Figure 5.1: Example of $f(\tilde{q}_\mu|\mu, \hat{\theta}_\mu^{\text{obs}})$ $f(\tilde{q}_\mu|\mu = 0, \hat{\theta}_{\mu=0}^{\text{obs}})$ distributions generated with toy MC. Source: [134].

The CL_s value is defined as:

$$CL_s(\mu) = \frac{p_{s+b}(\mu)}{1 - p_b}, \quad (5.6)$$

where:

$$p_{s+b}(\mu) = \int_{\tilde{q}_\mu^{\text{obs}}}^{\infty} f(\tilde{q}_\mu|\mu, \hat{\theta}_\mu^{\text{obs}}) d\tilde{q}_\mu \quad (5.7)$$

and

$$p_b = \int_{-\infty}^{\tilde{q}_\mu^{\text{obs}}} f(\tilde{q}_\mu|\mu = 0, \hat{\theta}_{\mu=0}^{\text{obs}}) d\tilde{q}_\mu \quad (5.8)$$

Scanning different values of μ , within $0 \leq \hat{\mu} \leq \mu$, one would exclude the ones which $CL_s < \alpha$. CMS and ATLAS recommends a CL level $(1 - \alpha)$ of 95%.

1818 The main advantage of the CL_s approach is that the presence of the denominator $1 - p_b$ in 5.6
 1819 penalizes the exclusion of regions in which the experiment is no sensitive. Figure 5.2 helps to
 1820 illustrate this. One can notice that a small value of p_{s+b} (yellow area) is balanced by large value
 1821 of p_b (green area). When the experimental sensitivity is higher, the two distributions tend to be
 1822 far away from each other. Thus leading to a smaller compensation factor (p_b) and enhancing the
 1823 chance of a exclusive CL_s value.

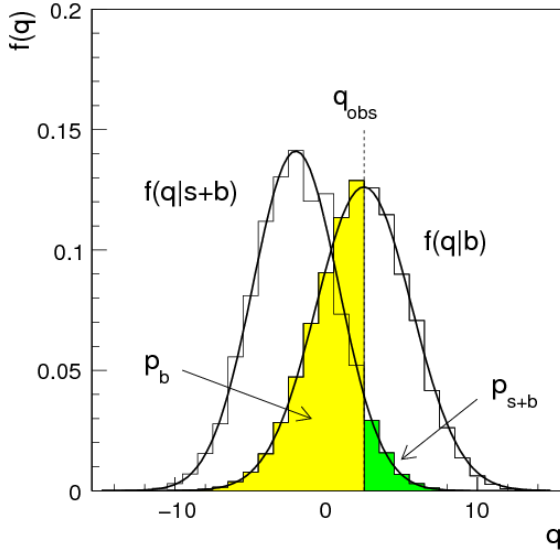


Figure 5.2: Example of $f(\tilde{q}_\mu | \mu, \hat{\theta}_\mu^{\text{obs}})$ $f(\tilde{q}_\mu | \mu = 0, \hat{\theta}_{\mu=0}^{\text{obs}})$ distributions generated with toy MC. In the figure, q must be read as \tilde{q} . The green area shows the p_{s+b} defined in 5.7, while the yellow one shows p_b defined in 5.8. Source: [131].

1824 The expected expected upper limit and its $\pm 1\sigma$ and $\pm 2\sigma$ are determined by generating a large
 1825 number of toy mc events, for the background-only model ($\mu = 0$), with nuisances free to float,
 1826 and for each simulation finding $\mu_{95\%}$, which defines the confidence level. Once enough samples are
 1827 generated, one should scan, from left to right, the cumulative distribution of $\mu_{95\%}$. The median
 1828 defines the expected value and the quantiles for 16%, 84% and 2.5%, 97.5% defines the $\pm 1\sigma$ and
 1829 $\pm 2\sigma$, respectively.

1830 5.2 Branching fraction upper limits

1831 The result are summarized on table 5.1.

1832 The observed(expected) exclusion limit at 95% confidence level on the $\mathcal{B}(Z \rightarrow \Upsilon(1S, 2S, 3S)\gamma) =$
 1833 $2.9, 2.7, 1.4$ ($1.6^{+0.8}_{-0.5}, 2.0^{+1.0}_{-0.6}, 1.8^{+1.0}_{-0.6} \times 10^{-6}$), and on the $\mathcal{B}(H \rightarrow \Upsilon(1S, 2S, 3S)\gamma) = 6.9, 7.4, 5.8$
 1834 ($7.3^{+4.0}_{-2.4}, 8.1^{+4.6}_{-2.8}, 6.8^{+3.9}_{-2.3} \times 10^{-4}$).

1835 As stated before, this analysis was done, for the Z decay, taking into account a mutually excludent
 1836 categorization of events, based on the reconstructed photon properties (η_{SC} and R9 value), as
 1837 described in section 4.7.

Table 5.1: Summary table for the limits on branching ratio of $Z \rightarrow \Upsilon(1S, 2S, 3S)\gamma$ and $H \rightarrow \Upsilon(1S, 2S, 3S)\gamma$ decays.

95% C.L. Upper Limit			
	$\mathcal{B}(Z \rightarrow \Upsilon\gamma) [\times 10^{-6}]$		
	$\Upsilon(1S)$	$\Upsilon(2S)$	$\Upsilon(3S)$
Expected	$1.6^{+0.8}_{-0.5}$	$2.0^{+1.0}_{-0.6}$	$1.8^{+1.0}_{-0.6}$
Observed	2.9	2.7	1.4
SM Prediction [$\times 10^{-8}$]	4.8	2.4	1.9
95% C.L. Upper Limit - $\mathcal{B}(H \rightarrow \Upsilon\gamma) [\times 10^{-4}]$			
	$\Upsilon(1S)$	$\Upsilon(2S)$	$\Upsilon(3S)$
Expected	$7.3^{+4.0}_{-2.4}$	$8.1^{+4.6}_{-2.8}$	$6.8^{+3.9}_{-2.3}$
Observed	6.9	7.4	5.8
SM Prediction [$\times 10^{-9}$]	5.2	1.4	0.9

1838 At table 5.2 we present the results obtained when there is no categorization of events (Inclusive
1839 category).

Table 5.2: Summary table for the limits on branching ratio of $Z \rightarrow \Upsilon(1S, 2S, 3S)\gamma$, for the two possible categorization scenarios.

95% C.L. Upper Limit - $\mathcal{B}(Z \rightarrow \Upsilon\gamma) [\times 10^{-6}]$			
	without categorization		
	$\Upsilon(1S)$	$\Upsilon(2S)$	$\Upsilon(3S)$
Expected	$1.7^{+0.9}_{-0.5}$	$2.1^{+1.1}_{-0.7}$	$1.9^{+1.0}_{-0.6}$
Observed	2.6	2.3	1.2
with categorization			
	$\Upsilon(1S)$	$\Upsilon(2S)$	$\Upsilon(3S)$
Expected	$1.6^{+0.8}_{-0.5}$	$2.0^{+1.0}_{-0.6}$	$1.8^{+1.0}_{-0.6}$
Observed	2.9	2.7	1.4

1840 It is worth to remember that the categorization takes places only for the Z decay. For the Higgs
1841 decay, no categorization is imposed.

1842 By taking, or not, into account any categorization, the numbers presented in both tables (5.1 and
1843 5.2), are compatible within themselves and with the results published by the ATLAS collabora-
1844 tion [135].

DRAFT

¹⁸⁴⁵ 6 CMS Resistive Plate Chambers - RPC

¹⁸⁴⁶ In the course of this PhD study, there were a lot of opportunities to work for the RPC project, in
¹⁸⁴⁷ the context of the CMS Collaboration. The main activities consists of shifts for the RPC operation
¹⁸⁴⁸ and data certification, upgrade and maintenance of the online software, R&D activities for the RPC
¹⁸⁴⁹ upgrade and detector maintenance during the LHC Long Shutdown 2 (2019 to 2020).

¹⁸⁵⁰ In this chapter, it is presented a summary of the Resistive Plate Chamber technology and the
¹⁸⁵¹ contributions to the RPC project at CMS.

¹⁸⁵² 6.1 Resistive Plate Chambers

¹⁸⁵³ The seminal paper on the Resistive Plate Chamber (RPC) technology was presented by R. Santonico
¹⁸⁵⁴ and R. Cardarelli, in which they described a "dc operated particle detector (...) whose constituent
¹⁸⁵⁵ elements are two parallel electrode Bakelite plates between" [136]. The key idea behind the RPC,
¹⁸⁵⁶ with respect to other similar gaseous detectors, is the use of two resistive plates as anode and
¹⁸⁵⁷ cathode, which makes possible to have a small localized region of dead time, achieving very good
¹⁸⁵⁸ time resolution.

¹⁸⁵⁹ The working principle for RPCs relies on the idea that an ionizing particle crossing the detector, tends
¹⁸⁶⁰ to interact with the gap between the two plates (filled with some specific gas mixture) and form a
¹⁸⁶¹ ionizing cascade process, in which the produced charged particles are driven by the strong uniform
¹⁸⁶² electrical field produced by the two plates.

¹⁸⁶³ The gas mixture is a key component of a RPC. Even though the first RPCs were produced with
¹⁸⁶⁴ a mixture of argon and butane, nowadays RPCs use a mixture of gases that would enhance an
¹⁸⁶⁵ ionization caused by the incident particle and quench secondary (background) effects.

¹⁸⁶⁶ Another feature of the RPCs is its construction simplicity and low cost. This allows the use of RPC to
¹⁸⁶⁷ cover larger areas at a reasonable cost.

¹⁸⁶⁸ An extensive review of the RPC technology and its applications can be found at [137].

¹⁸⁶⁹ 6.1.1 Principles and operation modes

¹⁸⁷⁰ The core of a RPC chamber is a gap made with two parallel high resistivity plates, separated
¹⁸⁷¹ by some regular distance (typically millimeters), filled with a proper gas mixture and under
¹⁸⁷² appropriate high voltage (HV) applied on the plates (electrodes, from here on). When an ionizing

1873 particle crosses the gap, there is a high enough chance the the particle will interact with the gas
 1874 and produce a newly created positive ion and a electron. This pair will travel in opposite directions,
 1875 according to the electric field from the electrodes. During this process, the electron will gain kinetic
 1876 energy and inelastically interact with other neighboring atoms/molecules, creating excitations in their
 1877 energy levels and, potentially, also ionizing them. The secondary ionization electrons will also follow
 1878 the same curse, creating an **Avalanche** of positive and negative particle/ions traveling towards the
 1879 electrodes. This process is proportional to the applied electric field. Figure 6.1 illustrates the
 1880 avalanche production.

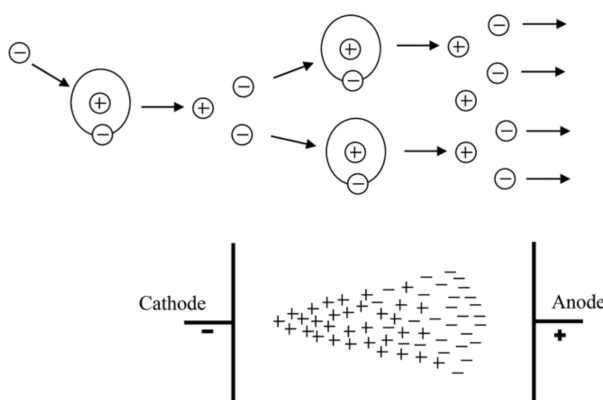


Figure 6.1: The Avalanche production process inside a RPC gap. (Top) The initial process and the secondary electron/ion generation. (Bottom) The overall charge distribution of an Avalanche between the electrodes. Source: [138].

1881 The number of particle composing the avalanche can be expressed as (assuming constant pres-
 1882 sure) [138]:

$$n_e = n_0 e^{\alpha d} = n_0 A, \quad (6.1)$$

1883 where n_0 is the number of initial electrons initiating the avalanche, A is the *gas gain*, or *multiplication*
 1884 *factor* and d is the distance since the avalanche creation. This is also known as Townsend theory
 1885 for discharges and α is the first Townsend coefficient.

1886 When the positive ions bunch reaches the cathode, under certain conditions (if the first ionization
 1887 energy of the ion is greater than the work function of the cathode), the recombination of the ion
 1888 with the electrode material might release electrons which will also follow the electric field. The
 1889 relative probability (with respect to the primary electron emission) of this emission to happen (γ_+)
 1890 is called the the second Townsend coefficient.

$$n_+ = n_0 A \gamma_+. \quad (6.2)$$

1891 Another process which can occur is the secondary photoelectron productions, described by a similar
 1892 equation as above: $n_{pe} = n_0 A \gamma_{ph}$. This production is mostly related to de-excitation of molecules
 1893 and atoms in vicinity of the avalanche. The produced photons might initiate new ionization process.

1894 As an alternative to the Townsend theory, Raether, Meek, and Loeb, proposed the *streamer-leader*
 1895 *theory* [139]. This theory is valid when there is a high enough concentration of ions
 1896 produced. This critical value is called Raether limit.

$$n_0 A > 10^8 \text{ electrons} \quad (6.3)$$

1897 In this limit, the electric field created by the space distribution is high enough to be same order
 1898 of the external field. In the vicinity of the head (or tail) of the avalanche the field gets disturbed
 1899 and intensified. The intensification of the field enhances the ionization effect and give rise to
 1900 secondary avalanches (photoelectrons). The intensified field also makes the photoelectrons produced
 1901 travel towards the head (positive ions). Their antikuaption generates more UV radiation and more
 1902 secondary avalanches. This whole process is called **Streamer**. If no quenching is imposed, the
 1903 streamer might evolve to a spark, fully discharging on the electrodes. If the concentration of
 1904 electrons is high enough, the avalanche tail (electrons) might also give rise to a streamer (namely,
 1905 negative streamer). Figure 6.2 illustrates the different subprocesses related to streamer production.

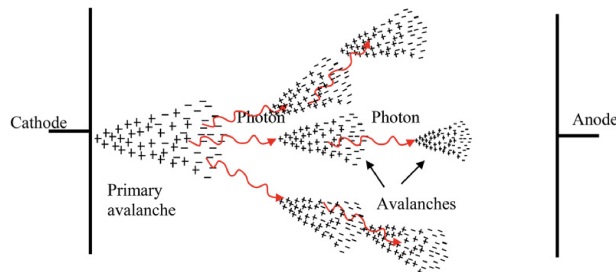


Figure 6.2: Streamer formation process. The distorted electric field around the high positive charge concentration enhances the ionization process, initiating secondary avalanches. Source: [138].

1906 A RPC where most of the charge multiplication process happens in the form of a streamer is said
 1907 to be working in **Streamer Mode**. The advantage of the of the streamer mode is the high induced
 1908 charge which is easily caught by non-sensitive readout electronics. On the other hand, the streamer
 1909 mode, because of its highly associated charge, will have a impact in the rate capability of the
 1910 detector (the local dead time will be higher).
 1911 Because of the high background environment of LHC, the CMS RPC operates in **Avalanche Mode**,
 1912 where de discharge is highly quenched and very well localized. On the other hand, a very sensitive
 1913 readout electronics is required to cope with the high rate demanded.
 1914 A good review of electrical discharge on gases can be found at [138].

1915 6.2 CMS Resistive Plate Chambers

1916 At CMS, the Resistive Plate Chamber are installed in both the barrel and endcap region, forming
 1917 a redundant system with the DT (barrel) and CSC (endcap). As described in the CMS Muon
 1918 Technical Design Report (Muon-TDR) [79], the RPC are composed of 423 Endcap chambers and

1919 633 barrel chambers. Figure 6.3 presents a picture of the CMS RPCs installed on station RE+4 of
 1920 the Endcap.

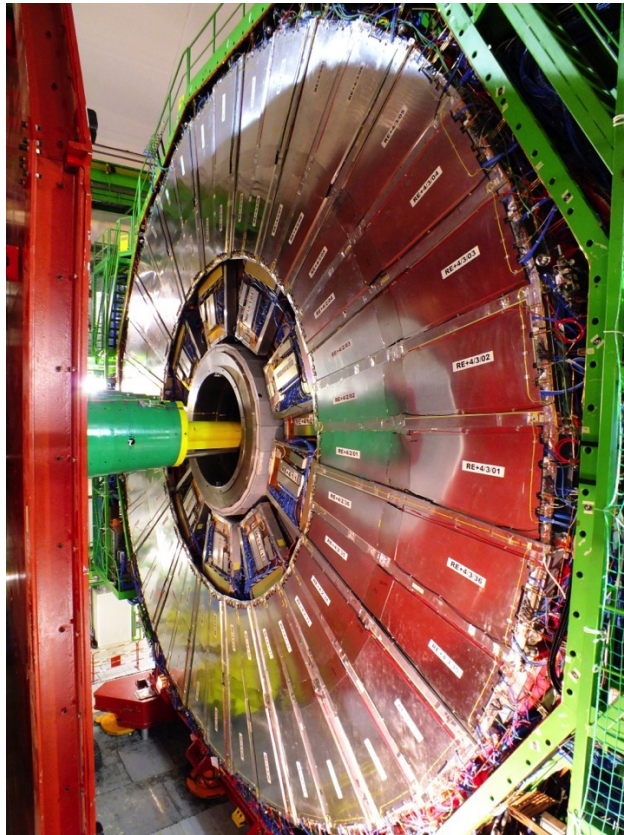


Figure 6.3: RPC chamber on installed on station RE+4 of CMS Endcap. Source: [140].

1921 Each chamber consists of two gas gaps (double gap), 2 mm tick each, made of Bakelite (phenolic
 1922 resin) with bulk resistivity of $10^{10} - 10^{11} \Omega m$. The choice of the bulk resistivity of the electrode has
 1923 high impact on the rate capability of the detector.

1924 Each gap has its external surface is coated with a thin layer of graphite paint, which acts as
 1925 conductive material, distributing the applied high-voltage (HV). On top of the graphite a PET
 1926 film is used for isolation. A sheet of copper strips is sandwiched between the gaps. Everything is
 1927 wrapped in aluminum case.

1928 The double gap configuration increases the efficiency of the chamber, since the signal is picked up
 1929 from the OR combination of the two gaps. A chamber with only one gap working, loses around
 1930 15% of efficiency, even though, this can be recovered by increasing the HV applied during operation
 1931 mode (working point - WP).

1932 A characteristic that differentiate the CMS RPC from previous RPC application in HEP is
 1933 the operation mode. A RPC at CMS, operates in avalanche mode, while previous experiments used
 1934 the streamer mode. Both modes are related to the applied HV, in commitment with the strength of
 1935 the generated signal, and are capable of generate a well localized signal, which can be picked up by
 1936 the readout electronics, but the avalanche mode offer a higher rate capability around 1 kHz/cm^2 ,

1937 while the streamer mode goes up to $100 \text{ Hz}/\text{cm}^2$. The high rate capability is a key factor in order
 1938 to cope with requirements of the LHC luminosity, specially in the high background regions.

1939 Besides the rate capability, the key factors that driven the CMS RPC design were: high efficiency ($>$
 1940 95%), low cluster size (> 2) for better spatial resolution (this reflects in the momentum resolution)
 1941 and good timing in order to do the readout of the signal within the 25 ns of a LHC bunch cross
 1942 (BX) and provide it to the CMS trigger system. These requirements have implications in the choice
 1943 of material, dimensions, electronics and gas mixture.

1944 In the barrel, along the radial direction, there are 4 muon layers (called stations), MB1 to MB4.
 1945 MB1 and MB2 is composed of a DT chamber sandwiched between two RPC chambers (RB1 and
 1946 RB2) with rectangular shape. The stations MB3 and MB4 have only one RPC (RB3 and RB4) are
 1947 composed by two RPC chambers (named - and + chambers with the increase of ϕ) attached to one
 1948 DT chamber, except in sector 9 and 11, where there is only one RPC. RE4, sector 10 is a special
 1949 case, since it is composed of four chambers (-, -, + and ++). These stations are replicated along
 1950 the z direction in five different wheels of the CMS (W-2, W-1, W0, W+1 and W+2) and in twelve
 1951 azimuthally distributed sectors (S1 to S12). Figure 6.4 show the different barrel stations and wheel.

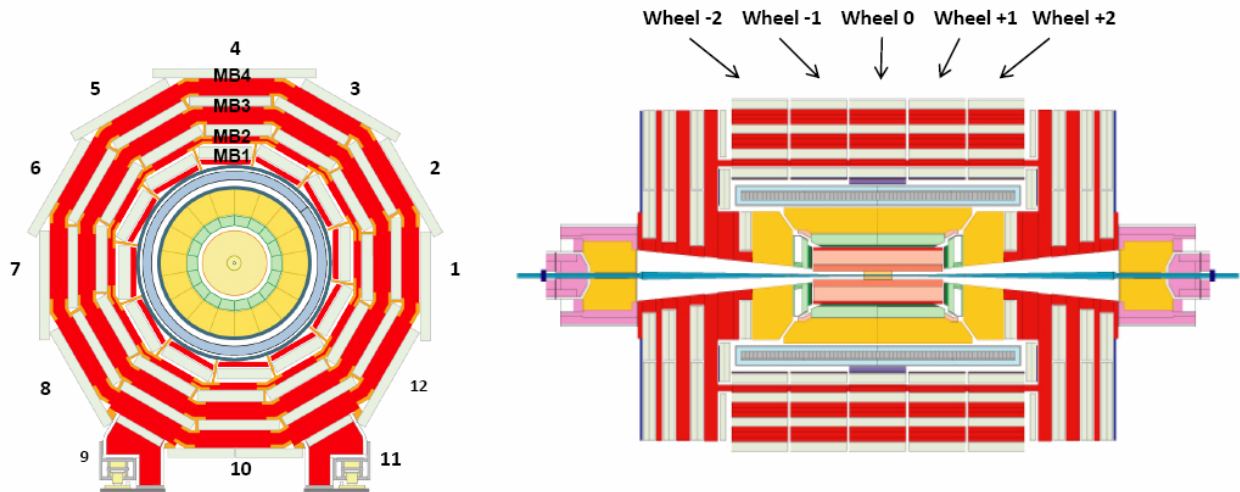


Figure 6.4: R- ϕ (left) and R-Z (right) projections of the barrel Muon System.

1952 In the endcap, the RPC chambers have a trapezoidal shape and are distributed in four disks (or
 1953 stations) each side ($RE \pm 4$, $RE \pm 3$, $RE \pm 2$, $RE \pm 1$), each one with 72 chambers. CMS split up its
 1954 disks in 3 rings, along the radial direction, and 36 sector in the azimuthal angle. RPCs are present
 1955 in the two outer rings ($R2$ and $R3$), in all 36 sectors. The $RE \pm 4$ are special cases, since these
 1956 chambers were installed only in 2014, a design choice was made the mechanically attached $R2$ and
 1957 $R3$ chambers, each sector, in what is called, a super-module. Figure 6.5 show the different endcap
 1958 disks.

1959 The length of the strips is chosen, for both barrel and endcap, in such a way to control the area of
 1960 each strip, in order to reduce the fake muons, due to random coincidence. This has to do with the
 1961 time-of-flight and signal propagation along the strip. In the barrel, each chamber readout is divided

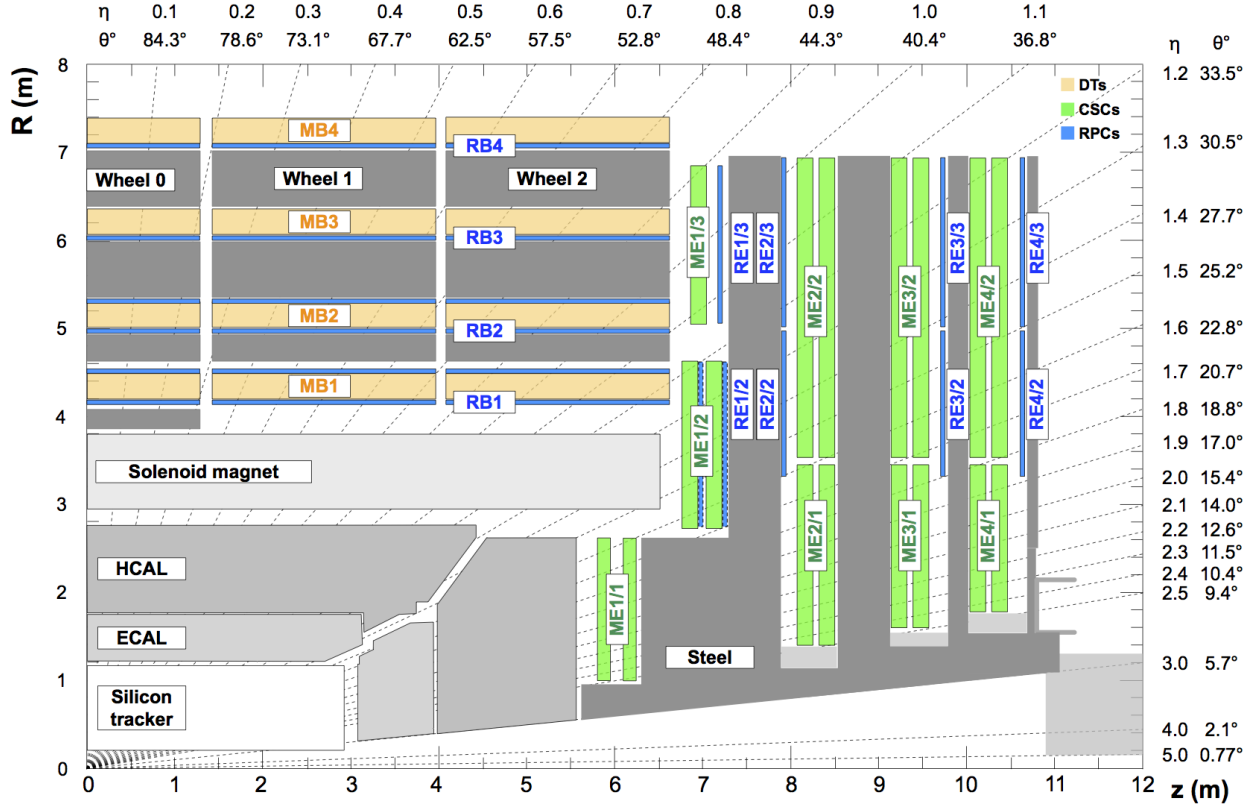


Figure 6.5: R-Z projections of the endcap Muon System (positive Z side). This is the same configuration for the 36 ϕ sectors.

in two regions (rolls), called forward and backward (along increasing $|\eta|$) ¹. In the endcap, the strips are divided in 3 regions, called partitions A, B and C (from inside the detector to outside).

The gas mixture used in the CMS RPCs is composed by C2H2F4 (Freon R-134a, tetrafluoroethane), C4H10 (isobutane), SF6 (sulphur hexafluoride) (95.2 : 4.5 : 0.3 ratio) and with controlled humidity of 40% at 20-22 °C. The Freon is used to enhance the ionization and charge multiplication that characterizes the avalanche, while the isobutane is introduced for quenching proposes, in order to reduce the secondary ionizations that could lead to formation of streamers and the SF6 is used to reduce the electron background. The choice of Freon over other gases, i.e. argon-based and helium-based, was motivated by previous studies [141, 142].

Since its R&D, the RPC have shown good performance over aging. This is even historical over previous RPC experiments [143–149]. Even the most recent studies of aging, taking into account future LHC conditions (High-Luminosity LHC - HL-LHC) plus a safety margin of 3 times the expected background (600 Hz/cm^2) have shown good aging hardness [150].

6.2.1 Performance

The RPCs, for the CMS experiment, contribute mainly with triggering inputs, due to its very good time resolution. The important parameters which are monitored to evaluate the RPC performance

¹Some chamber are divided in three rolls, forward, middle and backward, for trigger propose.

are the efficiency and cluster size. The former is related to the ratio of the registered hits over the number of muons that passed through the chamber, while the former one is the number adjacent strip (minimal readout unit) that were fired (activated) per hit. Figures 6.6 and 6.7 present the historical distribution of efficiency and cluster size as a function of the integrated luminosity collect during Run2.

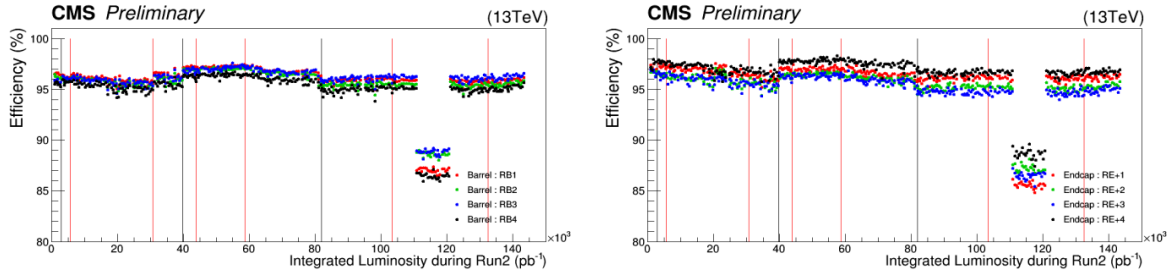


Figure 6.6: RPC efficiencies (per chamber) over Run2 Integrated Luminosity for Barrel (left) and Endcap (right). Red lines indicates technical stops (TS) while grey ones indicates Year-End-Technical stops (YETS). The drop in the efficiency around 110 pb^{-1} is related to a known operation mistake. Source: [151].

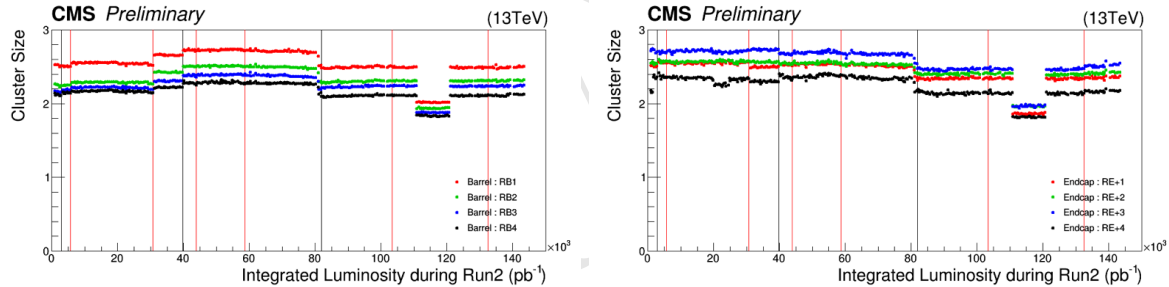


Figure 6.7: RPC cluster size (CLS - per chamber) over Run2 Integrated Luminosity for Barrel (left) and Endcap (right). Red lines indicates technical stops (TS) while grey ones indicates Year-End-Technical stops (YETS). The drop in the cluster size around 110 pb^{-1} is related to a known operation mistake. Source: [151].

In general, the RPC system operates with efficiency above 95% and cluster size smaller than 3 (a good parameter established during the design phase). The importance of the efficiency is a less complicated concept to catch, on the other hand, the cluster size might not be so straight forward. The optimal regime of RPCs operation at CMS is the avalanche mode, in which the electrical discharge is constrained in a millimeter level size region. Another operation mode is the streamer mode, in which the initial discharge might trigger secondary ones, e.g. by the emission of unquenched photons. A streamer discharge is capable of fire neighbor strips, increasing the cluster size. Operating in avalanche mode is fundamental to keep the RPCs capable of dealing with the high background environment of CMS.

To keep the mean cluster size under control (< 3) is important to guarantees enough spatial resolution for the measurements (the geometrical position of a hit is the midpoint of the cluster) and ensures that the system has enough rate capability to operate, since a RPC with a high sensitive front-end electronics (necessary for the avalanche mode operation) could be degraded by pileup of

dead time on many channels, including electronics noise, streamers, darks counts and other sources of background.

A third important parameter to be measured and controlled in a RPC system, under the LHC conditions, is the current due to the high voltage applied. This current is known to be proportional to the total charge released in each electrical discharges and to the hit rate on the chamber. The voltage applied is divided, as in a series circuit, between the electrodes and the gap. At increasing background, the current also increases and, since the applied voltage is constant, the voltage across the gap is reduced in favor of the voltage across the electrodes. This reduction of effective voltage on the gas, might have an impact on its gain, imposing a reduction on the detector sensitivity.

Figure 6.8 presents the ohmic currents ² in different regions of the detector, from 16th of April, 2018 to 2nd of December, 2018. It is clear how the stations subjected to higher background ($RE \pm 4$ - 40 Hz/cm^2) are subjected to a degrading factor that increases with the luminosity (background rate) and decreases when the detector is powered off. This effect is supposed to be related with the Hydrogen Fluoride (HF) production inside the gap, due to the electrical discharges. HF is a conductivity molecule, which can potentially attach to the internal surface of the gap, reducing the overall resistivity. The HF production can be controlled by properly tuning the gas flow as a function of the background that the chamber is subjected. HF concentration can also lead to permanent degradation of the gap, due to its chemical properties. Keeping the currents levels as low as possible is important for aging proposes.

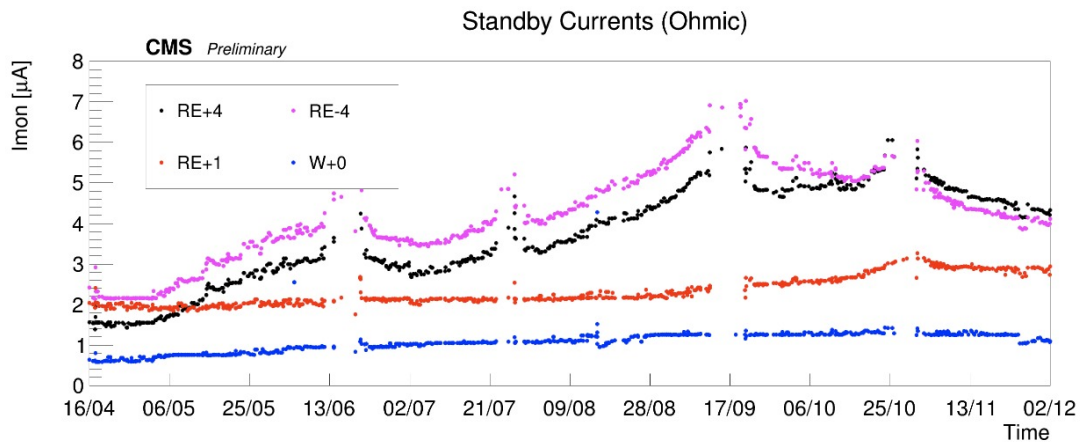


Figure 6.8: Ohmic current history of W+0, RE+1, RE+4 and RE-4. The blank regions, from time to time, corresponds to technical stops (TS), when the detector is off. Source: [151].

A review of the RPC performance during Run2 can be found at [151].

6.3 Contribution to the CMS RPC project

During the curse of this study, a head collaboration of our research group and the CMS RPC project was established. Many contributions were given to the project as part of the graduation as a

²Current at 6500 V, which is below the typical working point of a CMS RPC (around 9500 V). In this region, no charge multiplication effect take place and chamber current is governed only by Ohm's Law.

- 2019 experimental particle physicist, with focus on getting acquaintance with a subsystem technology and
 2020 give a meaningful collaboration to the detector operation. Those are considered by the community
 2021 important steps on the student graduation.
- 2022 Below it is described the contributions given to the CMS RPC project.

2023 **6.3.1 RPC Operation - Shifts and Data Certification**

- 2024 The first activities done for the CMS RPC project were shifts for data certification of data taken.
 2025 This certification is done by specialized people for different CMS subsystems and physics objects
 2026 groups³.
- 2027 This certification is done in order to ensure the quality of the date recorded based on the well
 2028 functionality of each system during the data taking and the reconstruction of the physics objects in
 2029 the expected matter. A certain collection of data (run) is said certificate when all subsystems and
 2030 object experts agrees on this.
- 2031 Figure 6.9 shows, as an example of the luminosity delivered by the LHC, recorded one by CMS and
 2032 the certified (validated), from the 22nd of April, 2016 to the 27th of October, 2016. Only certified
 2033 data is available for physics analysis.
- 2034 Shifts are a continuous weekly activity (specially during the data taking period), performed in a
 2035 weekly basis, in order to ensure the availability of certified data, as soon as possible.

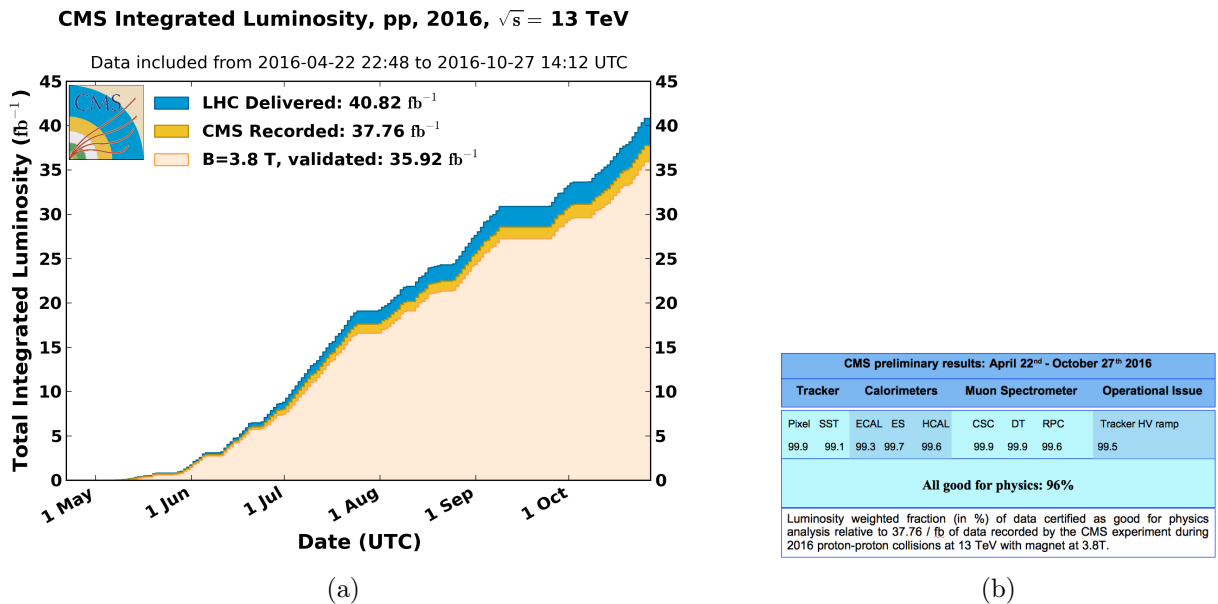


Figure 6.9: (a) Luminosity delivered by the LHC, recorded one by CMS and the certified (validated), from the 22nd of April, 2016 to the 27th of October, 2016. (b) Efficiency of the certification process for each subsystem, from the 22nd of April, 2016 to the 27th of October, 2016. Total CMS efficiency is above 90%. Source: [152]

³Groups of reconstruction and performance experts for different high-level reconstructed objects from CMS, i.e. muons, taus, jets/MET, electrons/photons

2036 6.4 RPC Online Software

2037 On what concerns the Online Software (OS) of the CMS RPC system, the main contribution given
 2038 was the upgrade of the Trigger Supervisor libraries.

2039 The Trigger Supervisor is a web-based software, which run over the xDAQ backend and provides,
 2040 through a modules organized in a tree system, called cells, a standard interface for the operation and
 2041 monitoring of different system at CMS. In principle only systems which contribute directly to the
 2042 L1 trigger should have a Trigger Supervisor implementation. This was the case for the RPC during
 2043 the Run1. Since Run2, RPC contributes to the trigger indirectly, by providing data to the muon
 2044 processors (CPPF, OMTF and TwinMux). The Trigger Supervisor implementation is a legacy from
 2045 that period.

2046 Each subsystem is responsible for its own implementation of the Trigger Supervisor, based on the
 2047 functionalities that it wants to have (requirements). The xDAQ [153] is a middleware, developed by
 2048 CERN and widely used at CMS, as a tool for control and monitoring of data acquisition system in
 2049 a distributed environment. It is capable of providing a software layer for direct access of hardware
 2050 functionalities and monitoring.

2051 The upgrade made (figure 6.10), consists in upgrade the higher level of the RPC online software.
 2052 In summary, up to 2017, the online software, was using Scientific Linux 6 as operational system,
 2053 which executed xDAQ 12, in turn, servers as backend for Trigger Supervisor 2. A upgrade of
 2054 the operational system to Centos 7, demanded the upgrade to xDAQ 14. On top of that, Trigger
 2055 Supervisor 2 would not work and had to be updated to Trigger Supervisor 5 in order to be functional
 2056 in 2018.

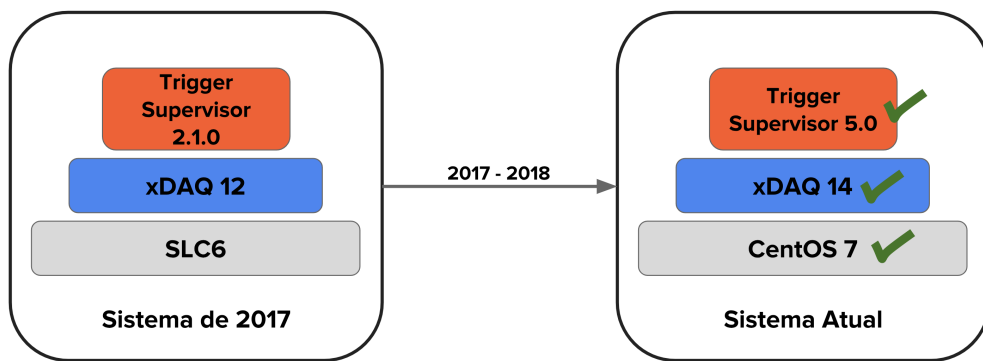


Figure 6.10: Upgrade of the RPC online software.

2057 Between versions 2 and 5 of Trigger Supervisor, part of the source-code had to be reworked, keep
 2058 the majority of the code structures. Most of the changes were made in the front-end of the system.
 2059 The standard JavaScript library Dojo [154], used in version2, was deprecated in favor of Google's
 2060 Polymer[155]. The main reason for this change was to isolate C++ code from HTML, which
 2061 was impossible with Dojo. This implied to rewrite all the screen of the RPC Trigger Supervisor
 2062 implementation, as in figure 6.11.

2063 The upgrade was done in time to ensure the control and operation of the RPC for 2018 data taking.

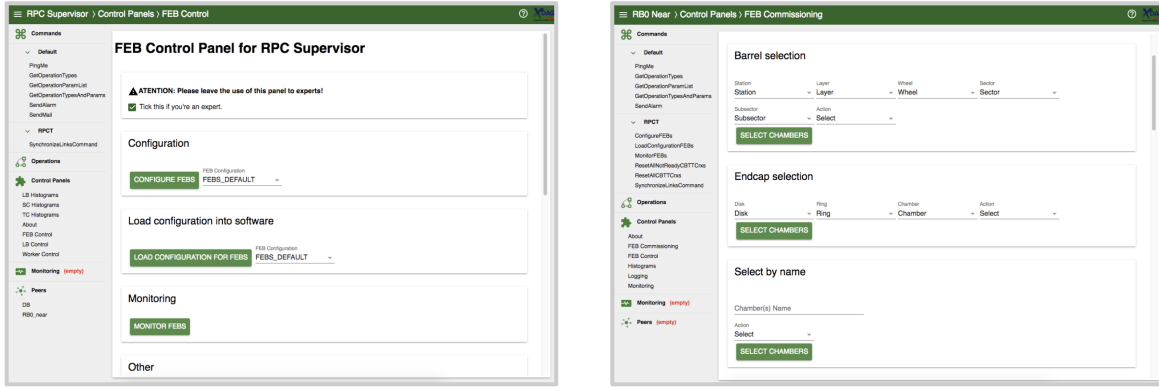
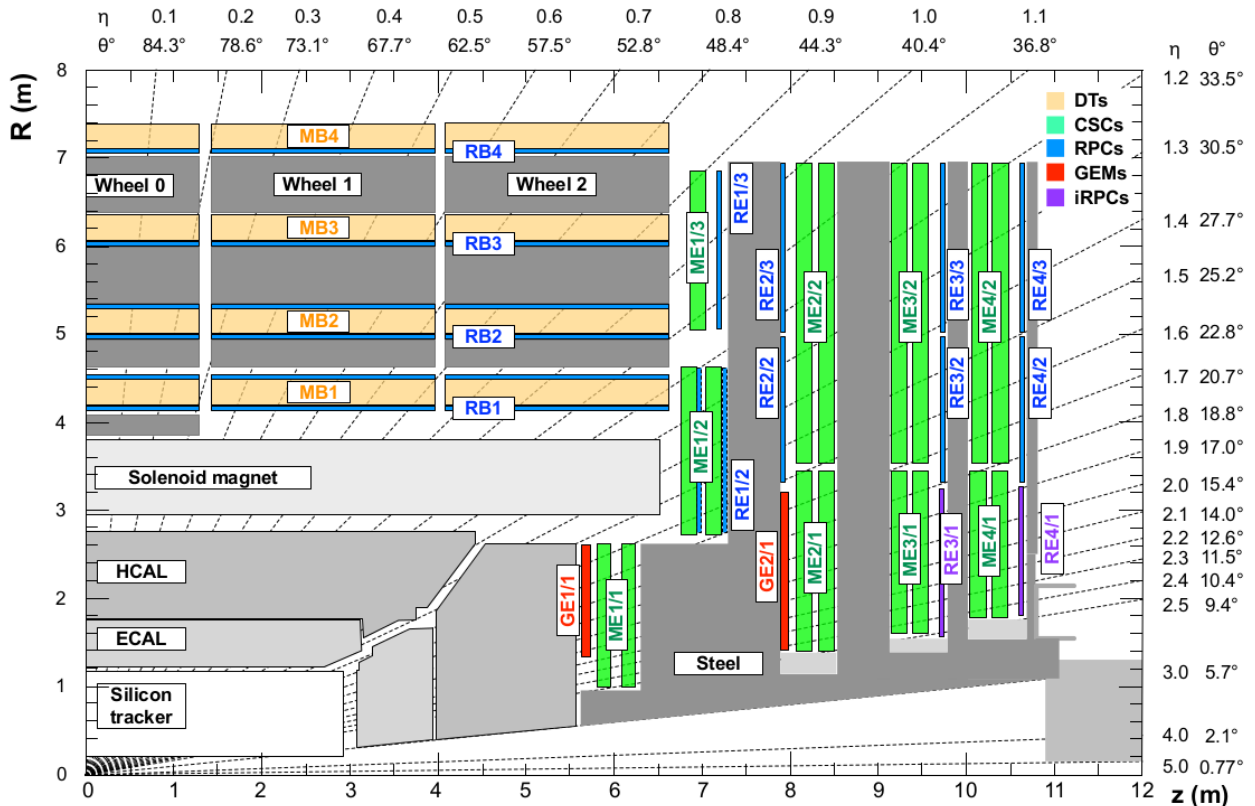


Figure 6.11: Example of the updated screens, using Trigger Supervisor 5.

6.4.1 iRPC R&D

For the next 4 year of CMS activities it is foreseen the upgrade of the the Muon Systems [79]. These upgrades are planed in order to extend the pseudorapidity coverage (η) and to guarantee the operation conditions of the present system in the HL-LHC (High Luminosity LHC) era. The RPC (Resistive Plate Chambers) [79] subsystem, it will have maintenance of the present chambers and installation of new chambers in the region of $|\eta| < 1,8$ para $|\eta| < 2,4$ [156]. These new chambers (iRPC) will be added in the most internal part of the muon spectrometer, RE3/1 e RE4/1, as in Figure 6.12.

Figure 6.12: η projection of the Muon System subdetectors. In purple, is labeled the iRPCs to be installed during the CMS upgrade.

Even thought this region is covered by the CSC detectors CSC (Cathode Strip Chambers), there are some loss of efficiency due the the system geometry. The installation of additional chambers will mitigate this problem and potentially increase the global efficiency of the muon system. The new chamber, called iRPC (*improved RPC*), will be different them the present one. For a luminosity of $5 \times 10^{34} cm^{-2}s^{-1}$ the neutrons, photons, electrons and positrons background in the high $|\eta|$ region is expected to be around $700 Hz/cm^2$ (for the chambers in RE3-4/1). Applying a safety factor of 3, the new chambers should support up to $2 Hz/cm^2$ of gamma radiation and still keep more than 95% of efficiency. Studies indicate, so far, that the use of High Pressure Laminates (HPL) for the double gap chambers is the most suitable choice. In order to reduce the aging and increase the rate capability, the electrodes and the gap size should be reduced in comparison with the present system.

One of the challenges for the R&D of the iRPC chambers is measuring the their performance in a high radiation environment, as the one for HL-LHC. For this, the CMS RPC project uses the Gamma Irradiation Facility (GIF++) [157], at CERN. The GIF++ is located at the H4 beam line in EHN1 providing high energy charged particle beams (mainly muon beam with momentum up to 100 GeV/c), combined with a 14 TBq 137-Cesium source. In the GIFF++ it is possible to achieve the HL-LHC total dose in a much reasonable amount of time. With the shutdown of LHC, the muon beam source is also off and will stay like this for 3 years. This means that the only muon sources for studies in GIF++ are cosmic muons.

In order to create a trigger system for iRPC R&D, the usual procedure is to use scintillators, on the top and on the bottom of the chamber. This is effective, but in a high gamma radiation environment, scintillators can be very sensitive which could lead to an undesirable amount of fake triggers which can degrade the measurements. Also, if one wants to covers a large area with scintillators, this can be expensive and they will not provide any means of tracking to measuring not only the global, but also the local chamber performance.

To provide a solution, the CMS RPC got in agreement with the LHCb [158] Muon Project to use their Multiwire Proportional Chambers (MWPC) [159], which were removed from LHCb, to be replaced by new chambers, and use them as trigger and/or tracking system at GIF++. This chambers, by design, have relatively low gamma sensitivity, already have some 1-dimensional resolution ($O(cm)$) and, the biggest advantage, with respect to any other gaseous particle detector option: LHCb has hundreds of vacant chambers. Any other detector would have to be build.

Not going in details of the MWPC technology nor the LHCb chamber construction [160], these chambers have a total active area of $968 \times 200 mm^2$ divided 2 layers (top and bottom) of 24 wire pads ($40 \times 200 mm^2$) composed of around 25 wires/channel, grouped by construction. Each chamber is equipped with 3 FEBs (Front-End Boards) with 16 pads each.

A channel is a logical combination of a top layer (pads) and a bottom layer readout. These readouts can be combined in AND or OR logics. One can have 8 channels per FEB, each channel being a logical combination of top and bottom pads. In this mode they are called AND2 and OR2. It is also possible to have the FEB configured in a 2 channels mode, each one corresponding to one sixth of the total readout pads. In this mode, all the pads can be combined in OR (called OR8) or they

2112 can be AND'ed in top and bottom pads and then group in OR (called OR4AND2). Figures 6.13
 2113 and 6.14 presents a logical diagram for each readout mode.

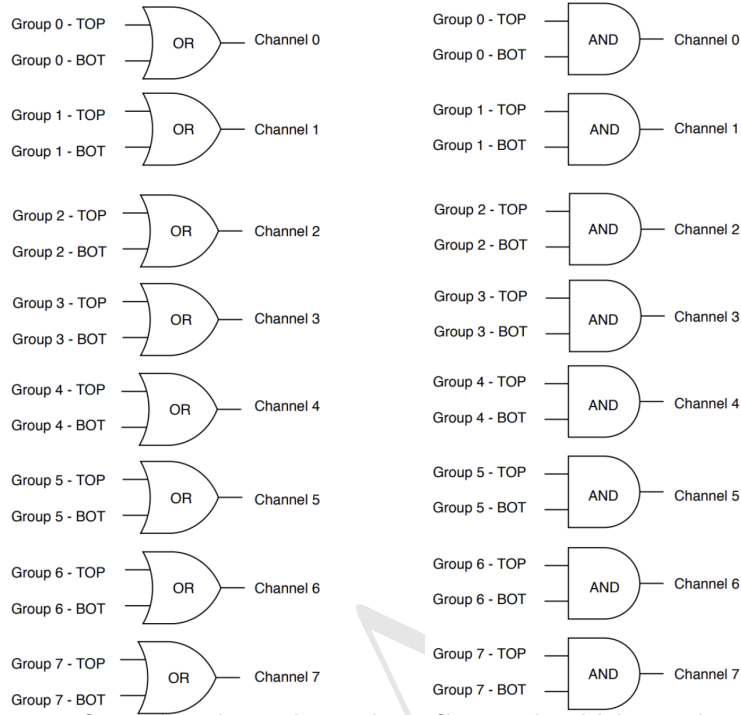


Figure 6.13: FEB configured 8 channels modes. Group should be understood as wire pad. Left: Logical diagram for OR2. Right: Logical diagram for AND2.

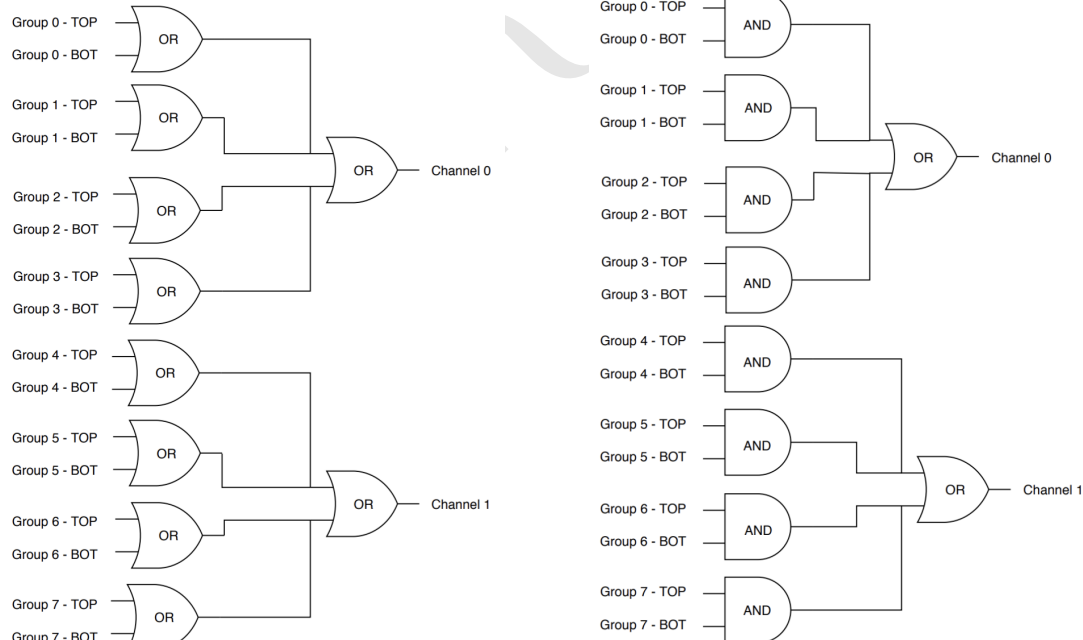


Figure 6.14: FEB configured 2 channels modes. Left: Logical diagram for OR8. Group should be understood as wire pad. Right: Logical diagram for OR4AND2.

2114 The nominal gas mixture for these chambers is Ar/CO₂/CF₄ (40:55:5). For a matter of simplicity,
 2115 it was used an already available similar gas line in the same building, used by CMS CSC (Cathode

2116 Strip Chamber) [79], which has a similar composition (40:50:10). Optimal conditions are obtained
 2117 with 2 to 4 liters/hour of gas flux and 2.65 kV of applied voltage.

2118 Figure 6.15 shows the setup that was prepared for commissioning of this chambers. It was mounted
 2119 two chambers on top of another (chambers A and B) above an RPC R&D chamber and two other
 2120 chambers on the bottom (chambers C and D). These four MWPC will be used as telescope for
 2121 the RPC chamber. All the services were mounted in rack, as in Figure 6.15. This includes power
 2122 supply (low voltage and high voltage), distribution panel, VME crate and boards for FEB control,
 2123 computer for control (high voltage, and FEB control) and NIM crate and boards for LVDS to NIM
 2124 signal conversion, logics and counting.

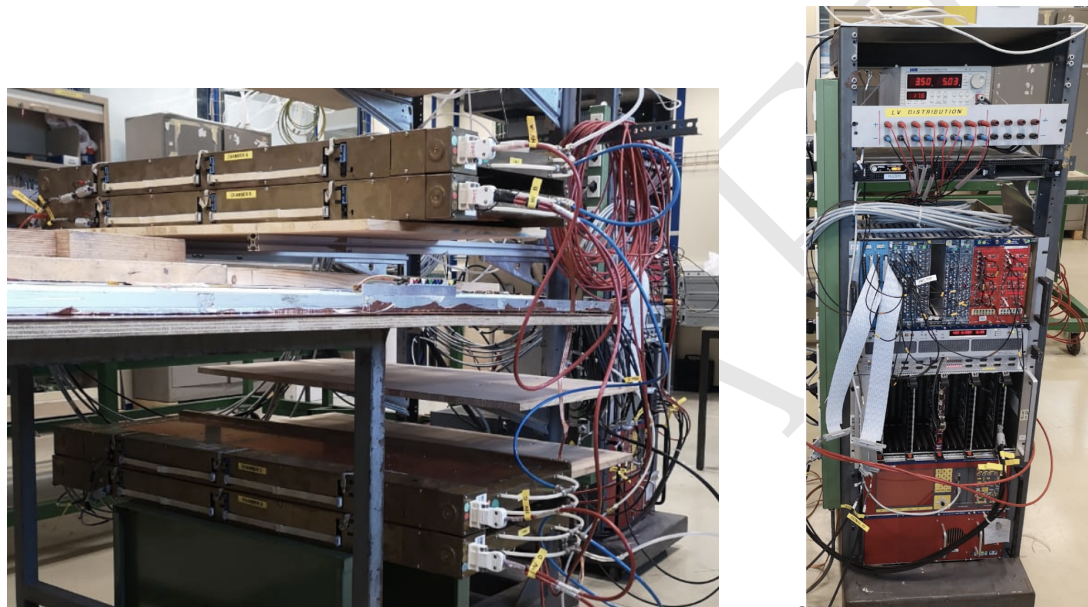


Figure 6.15: Left: Setup mounted for commissioning. Two MWPC chamber on the top (chambers A and B) and two (chambers C and D) on the bottom with a RPC R&D in the middle. Right: Rack with all the services for the operation of these chambers.

2125 Due to the short amount of time available for the commissioning, only two measurements mea-
 2126 surements were made with these chambers. They were meant to be a proof of concept for future
 2127 activities.

2128 The first measurement was to measure the coincidence rate of two chambers as a function of the
 2129 distance between the two top planes (Figure 6.16). This measurements were done with nominal
 2130 working point, with one FEB configured in 2 channels mode with 7 pC threshold, in (160 mm x
 2131 160 mm) area per chamber. One can observe that, if we go for a telescope trigger in the order of
 2132 1 meter of separation between the chamber, the logical combination chosen has negligible effect in
 2133 the coincidence rate. Also, the fits can be used to estimate the rate in a configuration with chamber
 2134 on the roof and under the floor. This could be the case of a universal trigger, to be mounted in
 2135 GIF++ with these chamber.

2136 The second measurement consist on evaluate the impact of γ background by placing a small Cs-137
 2137 source on top of the chamber A (Figure 6.17). For this measurement, the distance between top
 2138 planes of each pair of chamber (A to B and C to D) is 65 mm, while the distance between the top

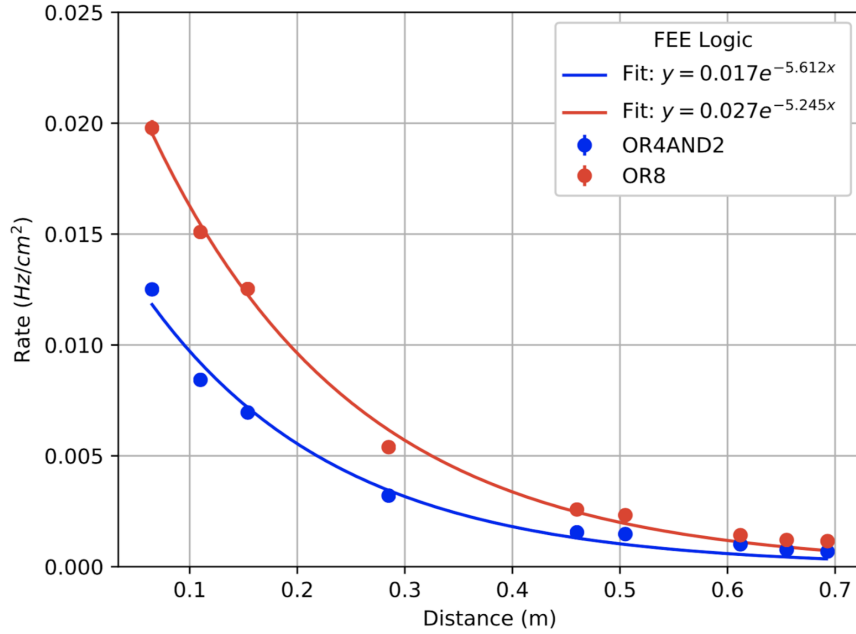


Figure 6.16: Coincidence rate of two chambers with respect to an arbitrary distance between the two top planes. Measured in 10 minutes, for 2 logical combinations (OR8 and OR4AND2). Applied high voltage: 2.65 kV. Threshold: 7 pC. Active area: readout of 160 mm x 160 mm per chamber.

2139 planes of A and C is 570 mm. It is clear the the γ source has an impact on chamber A rate, but
 2140 this is negligible when we take into account the coincidence between two chambers.

2141 This two measurements were enough to validate this chambers as possible trigger pro RPC R&D
 2142 with cosmic muons in the laboratory and at GIF++. The next steps would be use this MWPC
 2143 chamber to implement a tracking system from triggering. This would demand some developments,
 2144 since, due to bandwidth restrictions, the signal from each FEB would have to go to a programmable
 2145 fast electronics, i.e. a FPGA, which would reconstruct muon tracks and provide the trigger to the
 2146 DAQ system. This can be done by placing the two pair of chambers (AB and CD) in orthogonal
 2147 configuration and read the signal in a CAEN V2495 board [161].

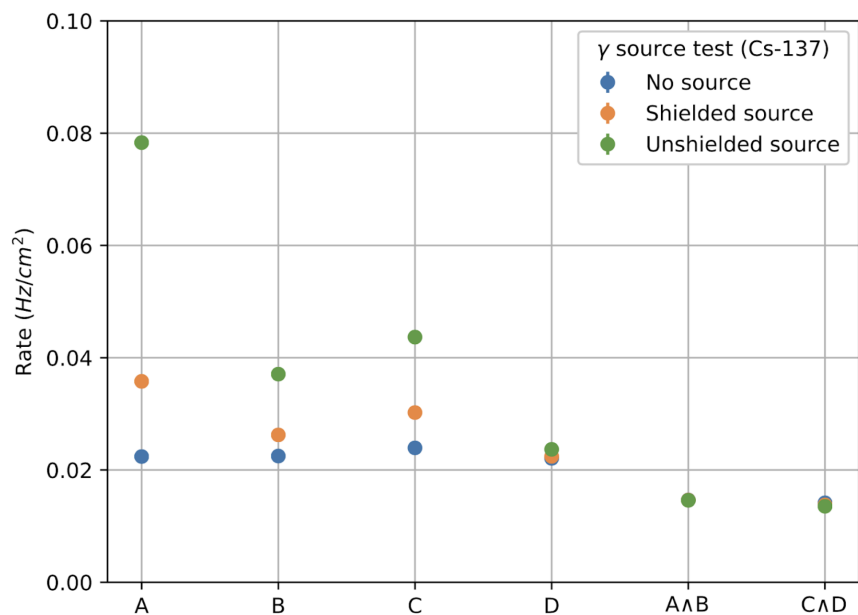


Figure 6.17: Individual rates (chambers A, B, C and D) and coincidence rates for two chambers (A AND B, C AND D), for without γ source (blue), a shielded γ source (orange) and an unshielded γ source (green). Source sitting on top of chamber A. Applied high voltage: 2.65 kV. Threshold: 7 pC. Active area: readout of 160 mm x 320 mm per chamber. Logical combination: AND2

2148 6.4.2 LS2 and the RPC Standard Maintenance

2149 In December 2018, the LS2 (Long Shutdown 2) was started. This a period in which the LHC and
2150 its detectors (CMS included) stop their operation for maintenance and upgrade. The LS2 will go
2151 up to 2021, when LHC and CMS restart the data taking with the Run3.

2152 During the LS2 it is being installed services for the new chambers (gas pipes, low voltage (LV), cables,
2153 signal and control optical fibers, high voltage (HV) cable and support equipment, and HV/LV power
2154 supplies), as well as continuity to the to the RPC R&D studies, besides the reparation of broken
2155 elements of the present system, i.e. chamber in the barrel region which present gas leak problems,
2156 maintenance of the LV and HV connectivity and power system, maintenance of the control system
2157 of problematic chambers (Front-Ends boards, cabling and Distribution Boards) and the dismount
2158 and reinstallation of four stations in the endcap (RE4) on both sides of CMS [162].

2159 What concerns the standard maintenance of the present RPC system, the main LS2 activities in
2160 which the student was involved, can be divided in three main tasks: (a) HV maintenance, (b) LV
2161 and control maintenance and (c) detector commissioning.

2162 HV maintenance

2163 A key factor of and RPC performance is the applied high voltage (HV). The CMS RPC achieve
2164 their optimal performance with, around, 9.5 kV applied in each gap. This voltage is in the range
2165 of the dielectric breakdown of many gases, which could lead to potential current leakages, if some
2166 part of the system is damaged, poorly operated or badly installed. If the currents are high enough
2167 this can make impossible the operation of the chamber. In cases like this, during the operation
2168 period (data taking), the problematic HV channel is identified and turned off (each chamber has
2169 two channels, one for each lawyer of gaps). Chambers in this situation are said to be operating in
2170 single gap mode (SG).

2171 The goal for the HV maintenance is to, now that the CMS is off and the chambers are accessible,
2172 identify which part of the HV supply system is causing the current leak and fix it the best way
2173 possible. Usually the problem is beyond the power supply, very often connectors or the gap itself
2174 are damaged.

2175 The CMS RPCs uses two kind of HV connectors, monopolar and tripolar connector. The monopolar
2176 are used to connect the chamber to the power supply. If mounted properly, rarely they present
2177 problems. The connection to the chamber is made by tripolar connectors, in which the ground and
2178 the HV for both gaps arrives to the chamber in a single connector, for simplicity and to save space in
2179 the patch panel. Unfortunately these connectors are relatively fragile, and they could be a potential
2180 source of leak, specially if they were poorly mounted, badly operated or with aging itself. Also,
2181 since this was a connector made exclusively for the CMS RPC system, some design choices had to
2182 be improved after the installation of other chamber. Those installed with old batches of tripolar
2183 connectors are sensitive ones. The reparation of this connectors consists in isolate the connector
2184 from the chamber and power it up to 15 kV (maximum voltage allowed by the system). If the tested

2185 connector is broken one will observe a very fast increase in the current of the HV channel. The only
 2186 solution to this kind of problem is to replace the connector.

2187 On the other hand, if the connector is powered isolated and pass the test, the problem beyond
 2188 the connector (assuming that the power system have already been tested), i.e. inside the chamber.
 2189 When a chamber is in SG mode it means that a full layer is off, but not necessarily all the gaps
 2190 in that layer are bad (a RPC can have up to three per layer). In this situation, the procedure
 2191 consists in cutting the cables that comes from the gaps to the chamber side connector one by one
 2192 and identify which gap of the problematic layer is the broken by powering it. Once identified, this
 2193 gap should isolated and the other ones reconnected. The broken gap is unrecoverable, since it is
 2194 inside the chamber, but 5% to 10 % of efficiency can be retaken, without changing the applied HV
 2195 and increasing the longevity of the chamber.

2196 Another contribution to the HV maintenance was the proposal of a procedure to replace the prob-
 2197 lematic tripolar connector by a monopolar (also called jupiter) connector, which are known for being
 2198 much more stable and reliable. The figure 6.18 (left) show the designed adapter for the chamber
 2199 patch panel which would made this change possible. Figure 6.18 (right) shows a tryout of a cham-
 2200 ber in which this procedure was tested. The proposal was presented to the RPC community and
 2201 approved to be used from now on. Technical drawings and instructions were provided.

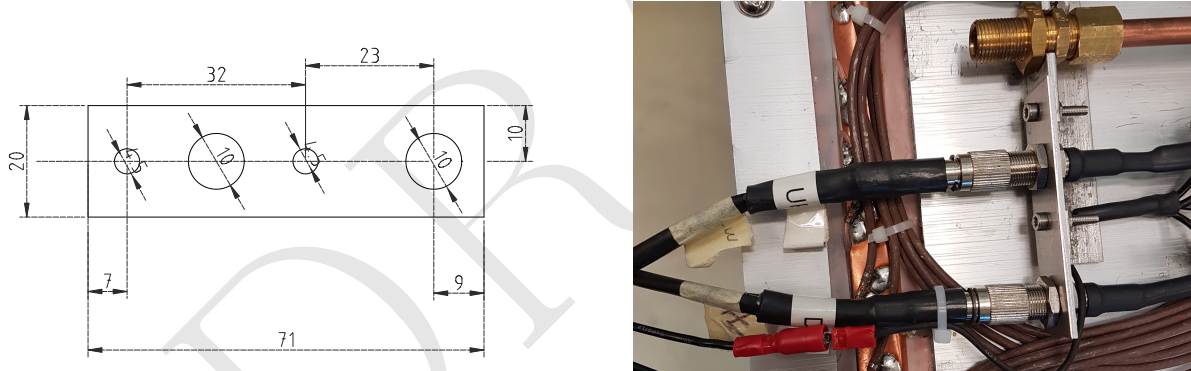


Figure 6.18: Left: Proposed adapter the chamber patch panel which make it possible to replace a tripolar by a jupiter HV connector. Right: Try out of the proposed HV connector replacement.

2202 LV and control maintenance

2203 The low voltage (LV) and control maintenance consists in make sure that the Front-End Boards
 2204 (FEBs) are powered and configurable, which means that the LV power system is working from
 2205 supply board to the cable, that the signal cables are in good state and properly connected to the
 2206 chamber and to the link boards and that the on-detector electronics (FEBs and Distribution Boards
 2207 - DBs) are working fine.

2208 Usually, this system is very reliable. The weak point, in most of the cases, is the detector electronics.
 2209 When a FEB [163] (as in Figure 6.19) is problematic it can present regions of very high noise or no
 2210 signal at all (silent), which can not be recovered by the threshold control. In cases like this, when
 2211 the FEB is accessible, it can be replaced in order to recover efficiency in the problematic chamber.

2212 This procedure is done by extracting the chamber from inside the detector (only for barrel chamber)
 2213 and opening its cover to have access to the problematic component. Removed boards are send back
 2214 to production labs for refurbishment.



Figure 6.19: RPC Front-end board (FEB) used in the barrel chambers.

2215 The most usual problem is a chamber in which the threshold control was lost. For those chamber,
 2216 most probably, the problem is in the distribution board of the chamber, which is a piece of hardware
 2217 responsible for distribute the LV power to the FEBs (3 to 6 per chamber) and send the threshold
 2218 control signal to the FEBs via I2C line. If a chamber has no threshold control, it means that the
 2219 RPC operation has no control over the signal selection, which can potentially induce performance
 2220 issues.

2221 For the barrel this maintenance happens concomitantly with the gas leak reparations on the barrel
 2222 chamber, since both demands the chamber extraction, which is a complex procedure in terms of
 2223 operation and demands specialized equipment and manpower. For technical reasons, the gas leak
 2224 extractions have precedence over LV ones.

2225 Detector commissioning

2226 All the LS2 activities demands uncabling of the chamber to be repaired and possibly some neighbor
 2227 chambers. Also, it can involve the replacement of components of the chamber. To avoid damage to
 2228 the system a compromising procedure is needed after all this activities. Given the responsibilities
 2229 of the commissioning it was necessary to: (a) make sure that the the RPC system keep tracks of all
 2230 the interventions, (b) maintain all the algorithms used in the commissioning procedure, (c) together
 2231 with the RPC Coordination, define a pool of people and a schedule to the commissioning of the
 2232 system and (d) follow-up, with other CMS RPC experts, the availability of materials and resources
 2233 for the commissioning operations.

2234 Besides the organizational tasks, the commissioning demanded to establish procedures to ensure the
 2235 connectivity and functionality of HV and LV connections. For the HV, it is needed to make sure
 2236 that the chambers are properly connected, without miscabling ⁴ and that the currents at stand-by

⁴Mixed cable connections.

2237 HV and working point HV are compatible with the ones in the end of last data-taking (end of
 2238 2018). This activity will start in November/2019, when the CMS RPC Standard Gas Mixture will
 2239 be available again.

2240 For the LV point of view, the LV power cable and signal cables should also be properly connected,
 2241 and presenting a noise profile compatible with last data-taking. One key point for this task is to
 2242 make sure that there are no miscabling of signal cable. One RPC chamber can have from 6
 2243 to 18 signal cable, which are connected very close one to another. There is a good chance that a
 2244 chamber, after reparation, have its signal cables mixed. In order to diagnose situations like this, it
 2245 was validated a algorithm present in the RPC Online Software, but never used since LS1, which,
 2246 by changing the threshold of each component of the RPC system, from very high to very low values
 2247 (component by component), can spot miscabled chambers. Since the control line is independent of
 2248 the signal line, a misclabeled will present a different noise from what is expected.

2249 Besides the validation of this algorithm, it was also implemented a web system (Figure 6.20),
 2250 developed in Flask [164] wich automatize the execution of the algorithm, making transparent to the
 2251 shifter (or the one performing the commissioning) the procedure to get miscabling report.

FEB Connectivity Test - Analysis

Worker	Date (YY-MM-DD)	Time (HH:MM:SS)	Hash	
RBP2_Far	2019-06-20	23:43:19	387534dst	Run Analyzer
RBP1_Far	2019-06-20	20:12:20	458306dst	Run Analyzer
RBP1_Far	2019-06-20	20:04:46	336162dst	Run Analyzer
RBP1_Near	2019-06-20	19:02:00	377883dst	Run Analyzer
RBP1_Near	2019-06-19	18:59:00	858950dst	Run Analyzer
RBP1_Far	2019-06-19	18:58:26	994787dst	Run Analyzer
YEN3_Far	2019-05-07	10:28:23	176278dst	Run Analyzer
YEN3_Near	2019-05-07	10:28:08	347504dst	Run Analyzer
YEN1_Far	2018-12-07	15:03:24	575561	Run Analyzer
RBO_Far	2018-12-07	14:45:42	101463	Run Analyzer
RBP1_Far	2018-12-07	09:12:00	477689	Run Analyzer

Figure 6.20: RPC FEB Commissioning Analyzer.

2252 The LV commissioning is ongoing, since it happens, as much as possible, right after the chamber
 2253 reparation.

2254 Bibliography

- 2255 [1] Stephen Myers. “The LEP collider, from design to approval and commissioning”. In: (Oct. 1991). DOI: [10.5170/CERN-1991-008](https://doi.org/10.5170/CERN-1991-008).
- 2256 [2] S. Chatrchyan et al. “The CMS experiment at the CERN LHC”. In: *JINST* 3 (2008), S08004. DOI: [10.1088/1748-0221/3/08/S08004](https://doi.org/10.1088/1748-0221/3/08/S08004).
- 2257 [3] The ATLAS Collaboration et al. “The ATLAS Experiment at the CERN Large Hadron Collider”. In: *Journal of Instrumentation* 3.08 (Aug. 2008), S08003–S08003. DOI: [10.1088/1748-0221/3/08/s08003](https://doi.org/10.1088/1748-0221/3/08/s08003). URL: <https://doi.org/10.1088%2F1748-0221%2F3%2F08%2Fs08003>.
- 2258 [4] Serguei Chatrchyan et al. “Observation of a new boson at a mass of 125 GeV with the CMS experiment at the LHC”. In: *Phys. Lett.* B716 (2012), pp. 30–61. DOI: [10.1016/j.physletb.2012.08.021](https://doi.org/10.1016/j.physletb.2012.08.021). arXiv: [1207.7235 \[hep-ex\]](https://arxiv.org/abs/1207.7235).
- 2259 [5] G. Aad et al. “Observation of a new particle in the search for the Standard Model Higgs boson with the ATLAS detector at the LHC”. In: *Physics Letters B* 716.1 (2012), pp. 1–29. ISSN: 0370-2693. DOI: <https://doi.org/10.1016/j.physletb.2012.08.020>. URL: <http://www.sciencedirect.com/science/article/pii/S037026931200857X>.
- 2260 [6] NobelPrize.org. *The Nobel Prize in Physics 2013*. 2013. URL: <https://www.nobelprize.org/prizes/physics/2013/summary/>.
- 2261 [7] CMS Collaboration. *Dimuon spectrum 2015*. Tech. rep. CMS-DP-2015-055. Dec. 2015. URL: <http://cds.cern.ch/record/2115428>.
- 2262 [8] Cliff Burgess and Guy Moore. *The Standard Model: A Primer*. Cambridge University Press, 2006. DOI: [10.1017/CBO9780511819698](https://doi.org/10.1017/CBO9780511819698).
- 2263 [9] M. Anselmino et al. *Introdução à QCD Perturbativa*. LTC, 2013. ISBN: 9788521622994.
- 2264 [10] F. Halzen and Alan D. Martin. *QUARKS AND LEPTONS: AN INTRODUCTORY COURSE IN MODERN PARTICLE PHYSICS*. Jan. 1984. ISBN: 978-0-471-88741-6.
- 2265 [11] I.J.R. Aitchison and A.J.G. Hey. *Gauge theories in particle physics: A practical introduction. Vol. 2: Non-Abelian gauge theories: QCD and the electroweak theory*. CRC Press, 2012. ISBN: 978-1-4665-1307-5.
- 2266 [12] Wikimedia Commons. *Standard Model*. 2020. URL: https://en.wikipedia.org/wiki/File:Standard_Model_of_Elementary_Particles.svg.
- 2267 [13] Particle Data Group et al. “Review of Particle Physics”. In: *Progress of Theoretical and Experimental Physics* 2020.8 (Aug. 2020). 083C01. ISSN: 2050-3911. DOI: [10.1093/ptep/ptaa104](https://doi.org/10.1093/ptep/ptaa104). eprint: <https://academic.oup.com/ptep/article-pdf/2020/8/083C01/33653179/ptaa104.pdf>. URL: <https://doi.org/10.1093/ptep/ptaa104>.

- [14] A. Salam and J. C. Ward. “On a gauge theory of elementary interactions”. In: *Il Nuovo Cimento (1955-1965)* 19.1 (1961), pp. 165–170. DOI: 10.1007/BF02812723. URL: <https://doi.org/10.1007/BF02812723>.
- [15] RH Dalitz. *Proceedings of the XIIIth International Conference on High Energy Physics*. 1967.
- [16] Wolfgang Ochs. “The Status of Glueballs”. In: *J. Phys. G* 40 (2013), p. 043001. DOI: 10.1088/0954-3899/40/4/043001. arXiv: 1301.5183 [hep-ph].
- [17] Peter W. Higgs. “Broken Symmetries and the Masses of Gauge Bosons”. In: *Phys. Rev. Lett.* 13 (1964). Ed. by J.C. Taylor, pp. 508–509. DOI: 10.1103/PhysRevLett.13.508.
- [18] Peter W. Higgs. “Broken symmetries, massless particles and gauge fields”. In: *Phys. Lett.* 12 (1964), pp. 132–133. DOI: 10.1016/0031-9163(64)91136-9.
- [19] Peter W. Higgs. “Spontaneous Symmetry Breakdown without Massless Bosons”. In: *Phys. Rev.* 145 (1966), pp. 1156–1163. DOI: 10.1103/PhysRev.145.1156.
- [20] F. Englert and R. Brout. “Broken Symmetry and the Mass of Gauge Vector Mesons”. In: *Phys. Rev. Lett.* 13 (1964). Ed. by J.C. Taylor, pp. 321–323. DOI: 10.1103/PhysRevLett.13.321.
- [21] G.S. Guralnik, C.R. Hagen, and T.W.B. Kibble. “Global Conservation Laws and Massless Particles”. In: *Phys. Rev. Lett.* 13 (1964). Ed. by J.C. Taylor, pp. 585–587. DOI: 10.1103/PhysRevLett.13.585.
- [22] T.W.B. Kibble. “Symmetry breaking in nonAbelian gauge theories”. In: *Phys. Rev.* 155 (1967). Ed. by J.C. Taylor, pp. 1554–1561. DOI: 10.1103/PhysRev.155.1554.
- [23] F. Abe et al. “Observation of top quark production in $\bar{p}p$ collisions”. In: *Phys. Rev. Lett.* 74 (1995), pp. 2626–2631. DOI: 10.1103/PhysRevLett.74.2626. arXiv: hep-ex/9503002.
- [24] S. Abachi et al. “Observation of the top quark”. In: *Phys. Rev. Lett.* 74 (1995), pp. 2632–2637. DOI: 10.1103/PhysRevLett.74.2632. arXiv: hep-ex/9503003.
- [25] John Ellis. “Outstanding questions: physics beyond the Standard Model”. In: *Philosophical Transactions of the Royal Society A: Mathematical, Physical and Engineering Sciences* 370.1961 (2012), pp. 818–830. DOI: 10.1098/rsta.2011.0452. eprint: <https://royalsocietypublishing.org/doi/pdf/10.1098/rsta.2011.0452>. URL: <https://royalsocietypublishing.org/doi/abs/10.1098/rsta.2011.0452>.
- [26] CMS Collaboration. *Summary of the cross section measurements of Standard Model processes*. 2020. URL: <https://twiki.cern.ch/twiki/bin/view/CMS/PhysicsResultsCombined> (visited on 08/21/2020).
- [27] M. Baak et al. “The global electroweak fit at NNLO and prospects for the LHC and ILC”. In: *Eur. Phys. J. C* 74 (2014), p. 3046. DOI: 10.1140/epjc/s10052-014-3046-5. arXiv: 1407.3792 [hep-ph].
- [28] LHC Higgs Cross Section Working Group. “Handbook of LHC Higgs Cross Sections: 4. Deciphering the Nature of the Higgs Sector”. In: (2016). DOI: 10.23731/CYRM-2017-002. arXiv: 1610.07922 [hep-ph].
- [29] Albert M Sirunyan et al. “Combined measurements of Higgs boson couplings in proton–proton collisions at $\sqrt{s} = 13$ TeV”. In: *Eur. Phys. J. C* 79.5 (2019), p. 421. DOI: 10.1140/epjc/s10052-019-6909-y. arXiv: 1809.10733 [hep-ex].

- [30] A. M. Sirunyan et al. “Observation of Higgs boson decay to bottom quarks”. In: *Phys. Rev. Lett.* 121.12 (2018), p. 121801. DOI: 10.1103/PhysRevLett.121.121801. arXiv: 1808.08242 [hep-ex].
- [31] CMS Collaboration. *Measurement of Higgs boson decay to a pair of muons in proton-proton collisions at $\sqrt{s} = 13$ TeV*. CMS Physics Analysis Summary CMS-PAS-HIG-19-006. 2019. URL: <http://cdsweb.cern.ch/record/1279362>.
- [32] Albert M Sirunyan et al. “Observation of the Higgs boson decay to a pair of τ leptons with the CMS detector”. In: *Phys. Lett. B* 779 (2018), pp. 283–316. DOI: 10.1016/j.physletb.2018.02.004. arXiv: 1708.00373 [hep-ex].
- [33] Albert M Sirunyan et al. “A search for the standard model Higgs boson decaying to charm quarks”. In: *JHEP* 03 (2020), p. 131. DOI: 10.1007/JHEP03(2020)131. arXiv: 1912.01662 [hep-ex].
- [34] Albert M Sirunyan et al. “Measurement and interpretation of differential cross sections for Higgs boson production at $\sqrt{s} = 13$ TeV”. In: *Phys. Lett. B* 792 (2019), pp. 369–396. DOI: 10.1016/j.physletb.2019.03.059. arXiv: 1812.06504 [hep-ex].
- [35] Albert M Sirunyan et al. “Measurement of the inclusive and differential Higgs boson production cross sections in the leptonic WW decay mode at $\sqrt{s} = 13$ TeV”. In: (July 2020). DOI: 10.3204/PUBDB-2020-02624. arXiv: 2007.01984 [hep-ex].
- [36] Albert M Sirunyan et al. “A measurement of the Higgs boson mass in the diphoton decay channel”. In: *Phys. Lett. B* 805 (2020), p. 135425. DOI: 10.1016/j.physletb.2020.135425. arXiv: 2002.06398 [hep-ex].
- [37] M. Spira et al. “Higgs boson production at the LHC”. In: *Nucl. Phys. B* 453 (1995), pp. 17–82. DOI: 10.1016/0550-3213(95)00379-7. arXiv: hep-ph/9504378.
- [38] CMS Collaboration. *List of CMS Higgs publications*. 2020. URL: <http://cms-results.web.cern.ch/cms-results/public-results/publications/HIG/index.html> (visited on 08/21/2020).
- [39] CMS Collaboration. *List of CMS Higgs public results*. 2020. URL: <http://cms-results.web.cern.ch/cms-results/public-results/preliminary-results/HIG/index.html> (visited on 08/21/2020).
- [40] CMS Collaboration. *Combined Higgs boson production and decay measurements with up to 137 fb⁻¹ of proton-proton collision data at $\sqrt{s} = 13$ TeV*. CMS Physics Analysis Summary CMS-PAS-HIG-19-005. 2019. URL: <http://cdsweb.cern.ch/record/1279362>.
- [41] L.D. Landau. “On the angular momentum of a system of two photons”. In: *Dokl. Akad. Nauk SSSR* 60.2 (1948), pp. 207–209. DOI: 10.1016/B978-0-08-010586-4.50070-5.
- [42] Chen-Ning Yang. “Selection Rules for the Dematerialization of a Particle Into Two Photons”. In: *Phys. Rev.* 77 (1950), pp. 242–245. DOI: 10.1103/PhysRev.77.242.
- [43] CMS Collaboration. *List of CMS Higgs publications involving spin-parity tests*. 2020. URL: <http://cms-results.web.cern.ch/cms-results/public-results/publications/HIG/SPIN.html> (visited on 08/21/2020).
- [44] Geoffrey Bodwin et al. “Higgs boson decays to quarkonia and the $H\bar{c}c$ coupling”. In: *Phys. Rev. D* 88 (5 Sept. 2013), p. 053003. DOI: 10.1103/PhysRevD.88.053003. URL: <https://link.aps.org/doi/10.1103/PhysRevD.88.053003>.

- [45] Geoffrey T. Bodwin et al. “Relativistic corrections to Higgs boson decays to quarkonia”. In: *Phys. Rev. D* 90 (11 Dec. 2014), p. 113010. DOI: 10.1103/PhysRevD.90.113010. URL: <https://link.aps.org/doi/10.1103/PhysRevD.90.113010>.
- [46] G. Aad, B. Abbott, et al. “Combined Measurement of the Higgs Boson Mass in pp Collisions at $\sqrt{s} = 7$ and 8 TeV with the ATLAS and CMS Experiments”. In: *Phys. Rev. Lett.* 114 (19 May 2015), p. 191803. DOI: 10.1103/PhysRevLett.114.191803. URL: <https://link.aps.org/doi/10.1103/PhysRevLett.114.191803>.
- [47] Cédric Delaunay et al. “Enhanced Higgs boson coupling to charm pairs”. In: *Phys. Rev. D* 89 (3 Feb. 2014), p. 033014. DOI: 10.1103/PhysRevD.89.033014. URL: <https://link.aps.org/doi/10.1103/PhysRevD.89.033014>.
- [48] M. A. PÉREZ, G. TAVARES-VELASCO, and J. J. TOSCANO. “NEW PHYSICS EFFECTS IN RARE Z DECAYS”. In: *International Journal of Modern Physics A* 19.02 (2004), pp. 159–178. DOI: 10.1142/S0217751X04017100.
- [49] Grossman, Yuval and König, Matthias and Neubert, Matthias. “Exclusive radiative decays of W and Z bosons in QCD factorization”. In: *Journal of High Energy Physics* 2015.4 (Apr. 2015), p. 101. ISSN: 1029-8479. DOI: 10.1007/JHEP04(2015)101. URL: [https://doi.org/10.1007/JHEP04\(2015\)101](https://doi.org/10.1007/JHEP04(2015)101).
- [50] Geoffrey T. Bodwin et al. “Z-boson decays to a vector quarkonium plus a photon”. In: *Phys. Rev. D* 97 (1 Jan. 2018), p. 016009. DOI: 10.1103/PhysRevD.97.016009. URL: <https://link.aps.org/doi/10.1103/PhysRevD.97.016009>.
- [51] Geoffrey T. Bodwin et al. “Addendum: New approach to the resummation of logarithms in Higgs-boson decays to a vector quarkonium plus a photon [Phys. Rev. D 95, 054018 (2017)]”. In: *Phys. Rev. D* 96 (11 Dec. 2017), p. 116014. DOI: 10.1103/PhysRevD.96.116014. URL: <https://link.aps.org/doi/10.1103/PhysRevD.96.116014>.
- [52] Gino Isidori, Aneesh V. Manohar, and Michael Trott. “Probing the nature of the Higgs-like boson via $h \rightarrow Vf$ decays”. In: *Physics Letters B* 728 (2014), pp. 131–135. ISSN: 0370-2693. DOI: <https://doi.org/10.1016/j.physletb.2013.11.054>. URL: <http://www.sciencedirect.com/science/article/pii/S037026931300960X>.
- [53] Alexander L. Kagan et al. “Exclusive Window onto Higgs Yukawa Couplings”. In: *Phys. Rev. Lett.* 114 (10 Mar. 2015), p. 101802. DOI: 10.1103/PhysRevLett.114.101802. URL: <https://link.aps.org/doi/10.1103/PhysRevLett.114.101802>.
- [54] Dao-Neng Gao. “A note on Higgs decays into Z boson and $J/\psi(\Upsilon)$ ”. In: *Physics Letters B* 737 (2014), pp. 366–368. ISSN: 0370-2693. DOI: <https://doi.org/10.1016/j.physletb.2014.09.019>. URL: <http://www.sciencedirect.com/science/article/pii/S0370269314006698>.
- [55] A. M. Sirunyan et al. “Observation of Higgs Boson Decay to Bottom Quarks”. In: *Phys. Rev. Lett.* 121 (12 Sept. 2018), p. 121801. DOI: 10.1103/PhysRevLett.121.121801. URL: <https://link.aps.org/doi/10.1103/PhysRevLett.121.121801>.
- [56] G Apollinari et al. *High-Luminosity Large Hadron Collider (HL-LHC): Preliminary Design Report*. CERN Yellow Reports: Monographs. Geneva: CERN, 2015. DOI: 10.5170/CERN-2015-005. URL: <https://cds.cern.ch/record/2116337>.

- [57] G. Aad et al. “Search for Higgs and Z Boson Decays to $J/\psi\gamma$ and $\Upsilon(nS)\gamma$ with the ATLAS Detector”. In: *Phys. Rev. Lett.* 114 (12 Mar. 2015), p. 121801. DOI: 10.1103/PhysRevLett.114.121801. URL: <https://link.aps.org/doi/10.1103/PhysRevLett.114.121801>.
- [58] Morad Aaboud et al. “Searches for exclusive Higgs and Z boson decays into $J/\psi\gamma$, $\psi(2S)\gamma$, and $\Upsilon(nS)\gamma$ at $\sqrt{s} = 13$ TeV with the ATLAS detector”. In: *Phys. Lett. B* 786 (2018), pp. 134–155. DOI: 10.1016/j.physletb.2018.09.024. arXiv: 1807.00802 [hep-ex].
- [59] S. Chatrchyan et al. “The CMS experiment at the CERN LHC”. In: *JINST* 3 (2008), S08004. DOI: 10.1088/1748-0221/3/08/S08004.
- [60] Albert M Sirunyan et al. “Search for rare decays of Z and Higgs bosons to J/ψ and a photon in proton-proton collisions at $\sqrt{s} = 13$ TeV”. In: *Eur. Phys. J. C* 79.2 (2019), p. 94. DOI: 10.1140/epjc/s10052-019-6562-5. arXiv: 1810.10056 [hep-ex].
- [61] Albert M Sirunyan et al. “Search for Higgs and Z boson decays to J/ψ or Υ pairs in proton-proton collisions at $\sqrt{s} = 13$ TeV”. In: *Phys. Lett. B* 797. arXiv:1905.10408. CMS-HIG-18-025-003 (May 2019). All figures and tables can be found at <http://cms-results.web.cern.ch/cms-results/public-results/publications/HIG-18-025> (CMS Public Pages), 134811. 31 p. DOI: 10.1016/j.physletb.2019.134811. URL: <https://cds.cern.ch/record/2676242>.
- [62] Albert M. Sirunyan et al. “Observation of the $Z \rightarrow \psi\ell^+\ell^-$ decay in pp collisions at $\sqrt{s} = 13$ TeV”. In: *Phys. Rev. Lett.* 121. arXiv:1806.04213. CMS-BPH-16-001-003 (June 2018). Submitted to Phys.Rev.Lett., 141801. 17 p. DOI: 10.1103/PhysRevLett.121.141801. URL: <https://cds.cern.ch/record/2623687>.
- [63] Albert M Sirunyan et al. “Search for decays of the 125 GeV Higgs boson into a Z boson and a ρ or ϕ meson”. In: (July 2020). DOI: 10.3204/PUBDB-2020-02812. arXiv: 2007.05122 [hep-ex].
- [64] “LHC Machine”. In: *JINST* 3 (2008). Ed. by Lyndon Evans and Philip Bryant, S08001. DOI: 10.1088/1748-0221/3/08/S08001.
- [65] Oliver Sim Brüning et al. *LHC Design Report*. CERN Yellow Reports: Monographs. Geneva: CERN, 2004. DOI: 10.5170/CERN-2004-003-V-1. URL: <http://cds.cern.ch/record/782076>.
- [66] Oliver Sim Brüning et al. *LHC Design Report*. CERN Yellow Reports: Monographs. Geneva: CERN, 2004. DOI: 10.5170/CERN-2004-003-V-2. URL: <http://cds.cern.ch/record/815187>.
- [67] Michael Benedikt et al. *LHC Design Report*. CERN Yellow Reports: Monographs. Geneva: CERN, 2004. DOI: 10.5170/CERN-2004-003-V-3. URL: <http://cds.cern.ch/record/823808>.
- [68] Christiane Lefèvre. “The CERN accelerator complex. Complexe des accélérateurs du CERN”. Dec. 2008. URL: <http://cds.cern.ch/record/1260465>.
- [69] S Baird. *Accelerators for pedestrians; rev. version*. Tech. rep. AB-Note-2007-014. CERN-AB-Note-2007-014. PS-OP-Note-95-17-Rev-2. CERN-PS-OP-Note-95-17-Rev-2. Geneva: CERN, Feb. 2007. URL: <http://cds.cern.ch/record/1017689>.
- [70] Jr. Alves A.Augusto et al. “The LHCb Detector at the LHC”. In: *JINST* 3 (2008), S08005. DOI: 10.1088/1748-0221/3/08/S08005.

- [71] K. Aamodt et al. “The ALICE experiment at the CERN LHC”. In: *JINST* 3 (2008), S08002. DOI: 10.1088/1748-0221/3/08/S08002.
- [72] “High-Luminosity Large Hadron Collider (HL-LHC): Technical Design Report V. 0.1”. In: 4/2017 (Nov. 2017). Ed. by G. Apollinari et al. DOI: 10.23731/CYRM-2017-004.
- [73] Tai Sakuma. “Cutaway diagrams of CMS detector”. In: (May 2019). URL: <http://cds.cern.ch/record/2665537>.
- [74] Serguei Chatrchyan et al. “Description and performance of track and primary-vertex reconstruction with the CMS tracker”. In: *JINST* 9 (2014), P10009. DOI: 10.1088/1748-0221/9/10/P10009. arXiv: 1405.6569 [physics.ins-det].
- [75] Vardan Khachatryan et al. “Performance of electron reconstruction and selection with the CMS detector in proton-proton collisions at $\sqrt{s} = 8$ TeV”. In: *JINST* 10 (2015), P06005. DOI: 10.1088/1748-0221/10/06/P06005. arXiv: 1502.02701 [physics.ins-det].
- [76] Vardan Khachatryan et al. “Performance of photon reconstruction and identification with the CMS detector in proton-proton collisions at $\sqrt{s} = 8$ TeV”. In: *JINST* 10 (2015), P08010. DOI: 10.1088/1748-0221/10/08/P08010. arXiv: 1502.02702 [physics.ins-det].
- [77] Matteo Cacciari, Gavin P. Salam, and Gregory Soyez. “The anti- k_t jet clustering algorithm”. In: *JHEP* 04 (2008), p. 063. DOI: 10.1088/1126-6708/2008/04/063. arXiv: 0802.1189 [hep-ex].
- [78] Matteo Cacciari, Gavin P. Salam, and Gregory Soyez. “FastJet User Manual”. In: *Eur. Phys. J.* C72 (2012), p. 1896. DOI: 10.1140/epjc/s10052-012-1896-2. arXiv: 1111.6097 [hep-ph].
- [79] *The CMS muon project: Technical Design Report*. Technical Design Report CMS. Geneva: CERN, 1997. URL: <https://cds.cern.ch/record/343814>.
- [80] A M Sirunyan et al. “Performance of the CMS muon detector and muon reconstruction with proton-proton collisions at $\sqrt{s} = 13$ TeV”. In: *JINST* 13 (2018), P06015. DOI: 10.1088/1748-0221/13/06/P06015. arXiv: 1804.04528 [physics.ins-det].
- [81] Serguei Chatrchyan et al. “The Performance of the CMS Muon Detector in Proton-Proton Collisions at $\sqrt{s} = 7$ TeV at the LHC”. In: *JINST* 8 (2013), P11002. DOI: 10.1088/1748-0221/8/11/P11002. arXiv: 1306.6905 [physics.ins-det].
- [82] Fabio Sauli. “The gas electron multiplier (GEM): Operating principles and applications. The gas electron multiplier (GEM): Operating principles and applications”. In: *Nucl. Instrum. Methods Phys. Res., A* 805 (2016), 2–24. 23 p. DOI: 10.1016/j.nima.2015.07.060. URL: <http://cds.cern.ch/record/2262884>.
- [83] Daniel Francois Teyssier. *CMS Drift Tubes performance*. Tech. rep. 2016, pp. 709–713.
- [84] Vardan Khachatryan et al. “The CMS trigger system”. In: *JINST* 12 (2017), P01020. DOI: 10.1088/1748-0221/12/01/P01020. arXiv: 1609.02366 [physics.ins-det].
- [85] A. M. Sirunyan et al. “Particle-flow reconstruction and global event description with the CMS detector”. In: *JINST* 12 (2017), P10003. DOI: 10.1088/1748-0221/12/10/P10003. arXiv: 1706.04965 [physics.ins-det].
- [86] Vardan Khachatryan et al. “Jet energy scale and resolution in the CMS experiment in pp collisions at 8 TeV”. In: *JINST* 12 (2017), P02014. DOI: 10.1088/1748-0221/12/02/P02014. arXiv: 1607.03663 [hep-ex].

- [87] Albert M Sirunyan et al. “Performance of missing transverse momentum reconstruction in proton-proton collisions at $\sqrt{s} = 13$ TeV using the CMS detector”. In: *JINST* 14 (2019), P07004. DOI: 10.1088/1748-0221/14/07/P07004. arXiv: 1903.06078 [hep-ex].
- [88] Jesse Thaler and Ken Van Tilburg. “Identifying Boosted Objects with N -subjettiness”. In: *JHEP* 03 (2011), p. 015. DOI: 10.1007/JHEP03(2011)015. arXiv: 1011.2268 [hep-ph].
- [89] Mrinal Dasgupta et al. “Towards an understanding of jet substructure”. In: *JHEP* 09 (2013), p. 029. DOI: 10.1007/JHEP09(2013)029. arXiv: 1307.0007 [hep-ph].
- [90] Jonathan M. Butterworth et al. “Jet substructure as a new Higgs search channel at the LHC”. In: *Phys. Rev. Lett.* 100 (2008), p. 242001. DOI: 10.1103/PhysRevLett.100.242001. arXiv: 0802.2470 [hep-ph].
- [91] Andrew J. Larkoski et al. “Soft drop”. In: *JHEP* 05 (2014), p. 146. DOI: 10.1007/JHEP05(2014)146. arXiv: 1402.2657 [hep-ph].
- [92] Albert M Sirunyan et al. “Pileup mitigation at CMS in 13 TeV data”. In: *JINST* 15 (2020), P09018. DOI: 10.1088/1748-0221/15/09/p09018. arXiv: 2003.00503 [hep-ex].
- [93] CMS Collaboration. *CMS Luminosity Measurements for the 2016 Data Taking Period*. CMS Physics Analysis Summary CMS-PAS-LUM-17-001. 2010. URL: <http://cdsweb.cern.ch/record/1279362>.
- [94] S. Agostinelli et al. “GEANT4—a simulation toolkit”. In: A506 (2003), pp. 250–303. DOI: 10.1016/S0168-9002(03)01368-8.
- [95] Paolo Nason. “A New method for combining NLO QCD with shower Monte Carlo algorithms”. In: *JHEP* 11 (2004), p. 040. DOI: 10.1088/1126-6708/2004/11/040. arXiv: hep-ph/0409146 [hep-ph].
- [96] Stefano Frixione, Paolo Nason, and Carlo Oleari. “Matching NLO QCD computations with Parton Shower simulations: the POWHEG method”. In: *JHEP* 11 (2007), p. 070. DOI: 10.1088/1126-6708/2007/11/070. arXiv: 0709.2092 [hep-ph].
- [97] Simone Alioli et al. “A general framework for implementing NLO calculations in shower Monte Carlo programs: the POWHEG BOX”. In: *JHEP* 06 (2010), p. 043. DOI: 10.1007/JHEP06(2010)043. arXiv: 1002.2581 [hep-ph].
- [98] Abdelhak Djouadi. “The anatomy of electroweak symmetry breaking: Tome I: The Higgs boson in the Standard Model”. In: *Physics Reports* 457.1 (2008), pp. 1–216. ISSN: 0370-1573. DOI: <https://doi.org/10.1016/j.physrep.2007.10.004>. URL: <http://www.sciencedirect.com/science/article/pii/S0370157307004334>.
- [99] Torbjörn Sjöstrand, Stephen Mrenna, and Peter Skands. “A brief introduction to PYTHIA 8.1”. In: *Computer Physics Communications* 178.11 (2008), pp. 852–867. ISSN: 0010-4655. DOI: <https://doi.org/10.1016/j.cpc.2008.01.036>. URL: <http://www.sciencedirect.com/science/article/pii/S0010465508000441>.
- [100] Torbjörn Sjöstrand et al. “An Introduction to PYTHIA 8.2”. In: *Comput. Phys. Commun.* 191 (2015), pp. 159–177. DOI: 10.1016/j.cpc.2015.01.024. arXiv: 1410.3012 [hep-ph].
- [101] Vardan Khachatryan et al. “Event generator tunes obtained from underlying event and multiparton scattering measurements”. In: *Eur. Phys. J. C*76.3 (2016), p. 155. DOI: 10.1140/epjc/s10052-016-3988-x. arXiv: 1512.00815 [hep-ex].

- [102] The NNPDF collaboration et al. “Parton distributions for the LHC run II”. In: *Journal of High Energy Physics* 2015.4 (Apr. 2015), p. 40. ISSN: 1029-8479. DOI: 10.1007/JHEP04(2015)040. URL: [https://doi.org/10.1007/JHEP04\(2015\)040](https://doi.org/10.1007/JHEP04(2015)040).
- [103] J. Alwall et al. “The automated computation of tree-level and next-to-leading order differential cross sections, and their matching to parton shower simulations”. In: *Journal of High Energy Physics* 2014.7 (July 2014), p. 79. ISSN: 1029-8479. DOI: 10.1007/JHEP07(2014)079. URL: [https://doi.org/10.1007/JHEP07\(2014\)079](https://doi.org/10.1007/JHEP07(2014)079).
- [104] Ali Abbasabadi et al. “Radiative Higgs boson decays $H \rightarrow f\bar{f}\gamma$ ”. In: *Phys. Rev. D* 55 (9 May 1997), pp. 5647–5656. DOI: 10.1103/PhysRevD.55.5647. URL: <https://link.aps.org/doi/10.1103/PhysRevD.55.5647>.
- [105] D. de Florian et al. *Handbook of LHC Higgs Cross Sections: 4. Deciphering the Nature of the Higgs Sector*. CERN Yellow Reports: Monographs. 869 pages, 295 figures, 248 tables and 1645 citations. Working Group web page: <https://twiki.cern.ch/twiki/bin/view/LHCPhysics/LHCHXSWG>. Oct. 2016. DOI: 10.23731/CYRM-2017-002. URL: <https://cds.cern.ch/record/2227475>.
- [106] Ye Li and Frank Petriello. “Combining QCD and electroweak corrections to dilepton production in the framework of the FEWZ simulation code”. In: *Phys. Rev. D* 86 (9 Nov. 2012), p. 094034. DOI: 10.1103/PhysRevD.86.094034. URL: <https://link.aps.org/doi/10.1103/PhysRevD.86.094034>.
- [107] John M. Campbell and R.K. Ellis. “MCFM for the Tevatron and the LHC”. In: *Nuclear Physics B - Proceedings Supplements* 205-206 (2010). Loops and Legs in Quantum Field Theory, pp. 10–15. ISSN: 0920-5632. DOI: <https://doi.org/10.1016/j.nuclphysbps.2010.08.011>. URL: <http://www.sciencedirect.com/science/article/pii/S0920563210001945>.
- [108] Vardan Khachatryan et al. “Search for a Higgs boson decaying into $\gamma^*\gamma \rightarrow \ell\ell\gamma$ with low dilepton mass in pp collisions at $\sqrt{s} = 8$ TeV”. In: *Phys. Lett. B* 753 (2016), pp. 341–362. DOI: 10.1016/j.physletb.2015.12.039. arXiv: 1507.03031 [hep-ex].
- [109] N. Brambilla, S. Eidelman, B.K. Heltsley, et al. “Heavy quarkonium: progress, puzzles, and opportunities”. In: *The European Physical Journal C* 71.2 (Feb. 2011), p. 1534. ISSN: 1434-6052. DOI: 10.1140/epjc/s10052-010-1534-9. URL: <https://doi.org/10.1140/epjc/s10052-010-1534-9>.
- [110] Sandro Palestini. “Angular distribution and rotations of frame in vector meson decays into lepton pairs”. In: *Phys. Rev. D* 83 (3 Feb. 2011), p. 031503. DOI: 10.1103/PhysRevD.83.031503. URL: <https://link.aps.org/doi/10.1103/PhysRevD.83.031503>.
- [111] A.M. Sirunyan et al. “Particle-flow reconstruction and global event description with the CMS detector”. In: *Journal of Instrumentation* 12.10 (2017), P10003. URL: <http://stacks.iop.org/1748-0221/12/i=10/a=P10003>.
- [112] Albert M Sirunyan et al. “Measurements of properties of the Higgs boson decaying into the four-lepton final state in pp collisions at $\sqrt{s} = 13$ TeV”. In: *JHEP* 11 (2017), p. 047. DOI: 10.1007/JHEP11(2017)047. arXiv: 1706.09936 [hep-ex].
- [113] V. Khachatryan et al. “Observation of the diphoton decay of the Higgs boson and measurement of its properties”. In: *The European Physical Journal C* 74.10 (Oct. 2014), p. 3076. ISSN: 1434-6052. DOI: 10.1140/epjc/s10052-014-3076-z. URL: <https://doi.org/10.1140/epjc/s10052-014-3076-z>.

- 2576 [114] S. Bernstein. “Démonstration du théorème de Weierstrass fondée sur le calcul des probabilités”. In: *Commun. Soc. Math. Kharkov* 13.1–2 (1912).
- 2577
- 2578 [115] John Erthal Gaiser. “Charmonium Spectroscopy From Radiative Decays of the J/ψ and ψ'' ”.
2579 PhD thesis. SLAC, 1982. URL: <http://www-public.slac.stanford.edu/sciDoc/docMeta.aspx?slacPubNumber=slac-r-255.html>.
- 2580
- 2581 [116] P. D. Dauncey et al. “Handling uncertainties in background shapes: the discrete profiling
2582 method”. In: *JINST* 10.04 (2015), P04015. DOI: 10.1088/1748-0221/10/04/P04015. arXiv:
2583 1408.6865 [[physics.data-an](#)].
- 2584 [117] S. S. Wilks. “The Large-Sample Distribution of the Likelihood Ratio for Testing Composite
2585 Hypotheses”. In: *Ann. Math. Statist.* 9.1 (Mar. 1938), pp. 60–62. DOI: 10.1214/aoms/1177732360. URL: <https://doi.org/10.1214/aoms/1177732360>.
- 2586
- 2587 [118] Higgs to Gamma Gamma Working Group. *Further measurement of $H \rightarrow \gamma\gamma$ at $\sqrt{s} = 13$ TeV*.
2588 CMS Note 2016/209. CERN, 2016. URL: http://cms.cern.ch/iCMS/jsp/db_notes/noteInfo.jsp?cmsnoteid=CMS%20AN-2016/209.
- 2589
- 2590 [119] *Updated measurements of Higgs boson production in the diphoton decay channel at $\sqrt{s} = 13$ TeV in pp collisions at CMS*. CMS Physics Analysis Summary CMS-PAS-HIG-16-020.
2591 Geneva: CERN, 2016. URL: <http://cds.cern.ch/record/2205275>.
- 2592
- 2593 [120] Jon Butterworth et al. “PDF4LHC recommendations for LHC Run II”. In: *J. Phys.* G43
2594 (2016), p. 023001. DOI: 10.1088/0954-3899/43/2/023001. arXiv: 1510.03865 [[hep-ph](#)].
- 2595 [121] A. D. Martin et al. “Parton distributions for the LHC”. In: *Eur. Phys. J.* C63 (2009), pp. 189–
2596 285. DOI: 10.1140/epjc/s10052-009-1072-5. arXiv: 0901.0002 [[hep-ph](#)].
- 2597 [122] Hung-Liang Lai et al. “New parton distributions for collider physics”. In: *Phys. Rev.* D82
2598 (2010), p. 074024. DOI: 10.1103/PhysRevD.82.074024. arXiv: 1007.2241 [[hep-ph](#)].
- 2599 [123] Sergey Alekhin et al. “The PDF4LHC Working Group Interim Report”. In: (2011). arXiv:
2600 1101.0536 [[hep-ph](#)].
- 2601 [124] Michiel Botje et al. “The PDF4LHC Working Group Interim Recommendations”. In: (2011).
2602 arXiv: 1101.0538 [[hep-ph](#)].
- 2603 [125] Richard D. Ball et al. “Impact of Heavy Quark Masses on Parton Distributions and LHC
2604 Phenomenology”. In: *Nucl. Phys.* B849 (2011), pp. 296–363. DOI: 10.1016/j.nuclphysb.
2605 2011.03.021. arXiv: 1101.1300 [[hep-ph](#)].
- 2606 [126] Giampiero Passarino. “Higgs Boson Production and Decay: Dalitz Sector”. In: *Phys. Lett.*
2607 B727 (2013), pp. 424–431. DOI: 10.1016/j.physletb.2013.10.052. arXiv: 1308.0422
2608 [[hep-ph](#)].
- 2609 [127] A.M. Sirunyan et al. “Performance of the CMS muon detector and muon reconstruction with
2610 proton-proton collisions at $\sqrt{s}=13$ TeV”. In: *Journal of Instrumentation* 13.06 (June 2018),
2611 P06015–P06015. DOI: 10.1088/1748-0221/13/06/p06015. URL: <https://doi.org/10.1088%2F1748-0221%2F13%2F06%2Fp06015>.
- 2612
- 2613 [128] Vardan Khachatryan et al. “Performance of photon reconstruction and identification with the
2614 CMS detector in proton-proton collisions at $\sqrt{s} = 8$ TeV”. In: *JINST* 10.CMS-EGM-14-001.
2615 CMS-EGM-14-001. CERN-PH-EP-2015-006 (Feb. 2015). Comments: Submitted to JINST,
2616 P08010. 59 p. DOI: 10.1088/1748-0221/10/08/P08010. URL: <http://cds.cern.ch/record/1988093>.
- 2617

- [129] A L Read. "Presentation of search results: theCLstechnique". In: *Journal of Physics G: Nuclear and Particle Physics* 28.10 (Sept. 2002), pp. 2693–2704. DOI: 10.1088/0954-3899/28/10/313. URL: <https://doi.org/10.1088/0954-3899/28/10/313>.
- [130] J. Neyman and E. S. Pearson. "On the Problem of the Most Efficient Tests of Statistical Hypotheses". In: *Philosophical Transactions of the Royal Society of London. Series A, Containing Papers of a Mathematical or Physical Character* 231 (1933), pp. 289–337. ISSN: 02643952. URL: <http://www.jstor.org/stable/91247>.
- [131] Glen Cowan et al. "Asymptotic formulae for likelihood-based tests of new physics". In: *The European Physical Journal C* 71.2 (Feb. 2011), p. 1554. ISSN: 1434-6052. DOI: 10.1140/epjc/s10052-011-1554-0. URL: <https://doi.org/10.1140/epjc/s10052-011-1554-0>.
- [132] *Procedure for the LHC Higgs boson search combination in Summer 2011*. Tech. rep. CMS-NOTE-2011-005. ATL-PHYS-PUB-2011-11. Geneva: CERN, Aug. 2011. URL: <https://cds.cern.ch/record/1379837>.
- [133] David H. Annis. "Kendall's Advanced Theory of Statistics, Vol. 1: Distribution Theory (6th ed.). Alan Stuart and J. Keith Ord; Kendall's Advanced Theory of Statistics, Vol. 2A: Classical Inference and the Linear Model (6th ed.). Alan Stuart and J. Keith Ord, and Steven F. Arnold". In: *Journal of the American Statistical Association* 101 (2006), pp. 1721–1721. URL: <https://EconPapers.repec.org/RePEc:bes:jnlasa:v:101:y:2006:p:1721-1721>.
- [134] *Procedure for the LHC Higgs boson search combination in Summer 2011*. Tech. rep. CMS-NOTE-2011-005. ATL-PHYS-PUB-2011-11. Geneva: CERN, Aug. 2011. URL: <https://cds.cern.ch/record/1379837>.
- [135] M. Aaboud et al. "Searches for exclusive Higgs and Z boson decays into $J/\psi\gamma$, $\psi(2S)\gamma$, and $\Upsilon(nS)\gamma$ at $\sqrt{s} = 13\text{TeV}$ with the ATLAS detector". In: *Physics Letters B* 786 (Nov. 2018), pp. 134–155. ISSN: 0370-2693. DOI: 10.1016/j.physletb.2018.09.024. URL: <http://dx.doi.org/10.1016/j.physletb.2018.09.024>.
- [136] R. Santonico and R. Cardarelli. "Development of resistive plate counters". In: *Nuclear Instruments and Methods in Physics Research* 187.2 (1981), pp. 377–380. ISSN: 0167-5087. DOI: [https://doi.org/10.1016/0029-554X\(81\)90363-3](https://doi.org/10.1016/0029-554X(81)90363-3). URL: <http://www.sciencedirect.com/science/article/pii/0029554X81903633>.
- [137] Marcello Abbrescia, Paulo Fonte, and Vladimir Peskov. *Resistive gaseous detectors: designs, performance, and perspectives*. Weinheim: Wiley-VCH, 2018. DOI: 10.1002/9783527698691.
- [138] A Beroual and I Fofana. "The background of air gap discharge theory". In: *Discharge in Long Air Gaps*. 2053-2563. IOP Publishing, 2016, 2-1 to 2-22. ISBN: 978-0-7503-1236-3. DOI: 10.1088/978-0-7503-1236-3ch2. URL: <http://dx.doi.org/10.1088/978-0-7503-1236-3ch2>.
- [139] Leonard B. Loeb and John M. Meek. "The Mechanism of Spark Discharge in Air at Atmospheric Pressure. I". In: *Journal of Applied Physics* 11.6 (1940), pp. 438–447. DOI: 10.1063/1.1712792. eprint: <https://doi.org/10.1063/1.1712792>. URL: <https://doi.org/10.1063/1.1712792>.
- [140] Dong Hyun, Kim. "Work on CMS Muon Detector (RPC) during Long Shutdown 1 (LS1) - Point 5, Cessy, CMS cavern". CMS Collection. May 2015. URL: <https://cds.cern.ch/record/2016815>.

- [141] P. Bernardini et al. "Precise measurements of drift velocities in helium gas mixtures". In: *Nuclear Instruments and Methods in Physics Research Section A: Accelerators, Spectrometers, Detectors and Associated Equipment* 355.2 (1995), pp. 428–433. ISSN: 0168-9002. DOI: [https://doi.org/10.1016/0168-9002\(94\)01144-3](https://doi.org/10.1016/0168-9002(94)01144-3). URL: <http://www.sciencedirect.com/science/article/pii/0168900294011443>.
- [142] E. Gorini et al. "Drift velocity measurements in C₂H₂F₄ based mixtures". In: *Proceedings of the 4th International Workshop on Resistive Plate Chamber and Related Detectors, in Napoli, Italy, 15-16 October* (1997).
- [143] G. Bressi et al. "AN APPARATUS TO SEARCH FOR FREE NEUTRON ANTI-NEUTRON OSCILLATIONS". In: *Nucl. Instrum. Meth. A* 261 (1987), pp. 449–461. DOI: 10.1016/0168-9002(87)90353-6.
- [144] H.L. Ge et al. "The production of residual nuclides in Pb irradiated by 400 MeV/u carbon ions". In: *Nucl. Instrum. Meth. B* 337 (2014), pp. 34–38. DOI: 10.1016/j.nimb.2014.07.024.
- [145] M. Abbrescia et al. "A Horizontal muon telescope implemented with resistive plate chambers". In: *Nucl. Instrum. Meth. A* 336 (1993), pp. 322–329. DOI: 10.1016/0168-9002(93)91116-5.
- [146] L. Antoniazzi et al. "The E771 RPC muon detector". In: *Nucl. Instrum. Meth. A* 315 (1992), pp. 92–94. DOI: 10.1016/0168-9002(92)90686-X.
- [147] A. Di Ciaccio et al. "Muon tracking and hadron punchthrough measurements using resistive plate chambers". In: *Nucl. Instrum. Meth. A* 315 (1992), pp. 102–108. DOI: 10.1016/0168-9002(92)90688-Z.
- [148] R. de Asmundis. "Performances of the RPC trigger system in the L3 experiment". In: *3rd International Workshop on Resistive Plate Chambers and Related Detectors (RPC 95)*. 1995, pp. 139–155.
- [149] D. Boutigny et al. "BaBar technical design report". In: (Mar. 1995).
- [150] Andrea Gelmi. *Longevity studies for the CMS-RPC system*. Tech. rep. CMS-CR-2018-136. Geneva: CERN, July 2018. URL: <https://cds.cern.ch/record/2634505>.
- [151] M.A. Shah et al. "Experiences from the RPC data taking during the CMS RUN-2". In: *15th Workshop on Resistive Plate Chambers and Related Detectors*. May 2020. arXiv: 2005.12532 [physics.ins-det].
- [152] *Public CMS Data Quality Information*. twiki.cern.ch/twiki/bin/view/CMSPublic/DataQuality. Acessado em: 20/02/2018.
- [153] Johannes Guteleber, Steven Murray, and Luciano Orsini. "Towards a homogeneous architecture for high-energy physics data acquisition systems". In: *Computer Physics Communications* 153.2 (2003), pp. 155–163. ISSN: 0010-4655. DOI: [https://doi.org/10.1016/S0010-4655\(03\)00161-9](https://doi.org/10.1016/S0010-4655(03)00161-9). URL: <http://www.sciencedirect.com/science/article/pii/S0010465503001619>.
- [154] *Dojo*. <https://dojotoolkit.org/>. Acessado em: 20/02/2018.
- [155] *Polymer Project*. Acessado em: 20/02/2018.
- [156] M. I. Pedraza-Morales. *RPC upgrade project for CMS Phase II*. 2018. arXiv: 1806.11503 [physics.ins-det].
- [157] Dorothea Pfeiffer et al. "The radiation field in the Gamma Irradiation Facility GIF++ at CERN". In: *Nuclear Instruments and Methods in Physics Research Section A: Accelerators*,

- 2702 *Spectrometers, Detectors and Associated Equipment* 866 (2017), pp. 91–103. ISSN: 0168-9002.
2703 DOI: <https://doi.org/10.1016/j.nima.2017.05.045>. URL: <http://www.sciencedirect.com/science/article/pii/S0168900217306113>.
- 2704
2705 [158] A. Augusto Alves Jr. et al. “The LHCb Detector at the LHC”. In: *JINST* 3 (2008), S08005.
2706 DOI: 10.1088/1748-0221/3/08/S08005.
- 2707 [159] Georges Charpak et al. “The Use of Multiwire Proportional Counters to Select and Localize
2708 Charged Particles”. In: *Nucl. Instrum. Meth.* 62 (1968), pp. 262–268. DOI: 10.1016/0029-
2709 554X(68)90371-6.
- 2710 [160] *LHCb Muon Group Home Page*. [Online; accessed 1-October-2019]. 2019. URL: <http://lhcb-muon.web.cern.ch/lhcb-muon/>.
- 2711
2712 [161] *CAEN Programmable Logic Unit - V2495*. [Online; accessed 1-October-2019]. 2019. URL:
2713 <https://www.caen.it/products/v2495/>.
- 2714 [162] *Resistive Plate Chambers are getting dolled up*. <https://cms.cern/news/resistive-plate-chambers-are-getting-dolled>. Acessado em: 20/09/2019.
- 2715
2716 [163] C. Binetti et al. “A new Front-End board for RPC detector of CMS”. In: (Sept. 1999).
- 2717 [164] *Flask (web framework)*. [Online; accessed 1-October-2019]. 2019. URL: <https://palletsprojects.com/p/flask/>.
- 2718